



ELSEVIER

Thermodynamics of dynamic nuclear polarization

W.Th. Wenckebach

Faculty of Applied Physics, Delft University of Technology, P.O.B. 5046, 2600 GA Delft, The Netherlands

Abstract

Dynamic nuclear polarization is presented as a Carnot cycle where the high temperature bath consists of the crystal lattice and the low temperature bath consists of the nuclear spin system. It is explained how modulation of the magnetic field or microwave frequency can be interpreted as improvements leading to a more ideal Carnot cycle.

1. Entropy and polarization

Basically, the method of dynamic nuclear polarization (DNP) to obtain a high polarization $P_I = \langle I_z \rangle / I$ of nuclear spins consists of using a microwave field to transfer the polarization $P_S = \langle S_z \rangle / S \approx \pm 1$ of electron spins to these nuclei [1]. Many limitations of this process are best understood if it is realized that the electron spin polarization P_S and the nuclear spin polarization P_I are directly related to the electron spin entropy S_S and the nuclear spin entropy S_I . Thus, DNP corresponds to using a microwave field to transfer entropy from the nuclear spins to the electron spins.

To appreciate this point in a more quantitative manner, we consider N_I non-interacting nuclear spins I in an externally applied magnetic field. Their $2I + 1$ energy levels are equidistant and separated by $\hbar \omega_I$, where ω_I is the Larmor frequency. The entropy S_I of this spin system is given by

$$S_I = N_I k_B \sum_{m=-I}^{+I} N_m \ln N_m, \quad (1)$$

where k_B is Boltzmann's constant and N_m is the number of spins in the m th level. On the other hand, the occupations N_m are directly related to the nuclear polarization. Here we consider the special cases of proton spins $I = \frac{1}{2}$ and deuteron spins $I = 1$. For the former:

$$P_I = \frac{N_{-1/2} - N_{+1/2}}{N_I}. \quad (2)$$

Thus, after some arithmetic [1]:

$$S_I = N_I k_B \left[\ln 2 - \frac{1}{2}(1 + P_I) \ln(1 + P_I) - \frac{1}{2}(1 - P_I) \ln(1 - P_I) \right]. \quad (3)$$

This result is shown in Fig. 1 as the solid curve I. Here we plot the nuclear polarization P_I for $I = \frac{1}{2}$ as a function of the reduced entropy $S_I / N_I k_B$. As an example the figure

shows that a polarization of 64% corresponds to a reduction of reduced entropy by 0.23.

For deuteron spins with $I = 1$ the situation is slightly more complicated. Now two parameters determine the level occupation, the nuclear polarization

$$P_I = \frac{N_{-1} - N_{+1}}{N_I} \quad (4)$$

and the nuclear alignment

$$A_I = \frac{N_{-1} + N_{+1} - 2N_0}{N_I}. \quad (5)$$

As a result, after some more arithmetic [2],

$$S_I = N_I k_B \left[\ln 3 - \frac{1}{3} \left(1 + \frac{1}{2} A_I + \frac{3}{2} P_I \right) \ln \left(1 + \frac{1}{2} A_I + \frac{3}{2} P_I \right) - \frac{1}{3} \left(1 + \frac{1}{2} A_I - \frac{3}{2} P_I \right) \ln \left(1 + \frac{1}{2} A_I - \frac{3}{2} P_I \right) - \frac{1}{3} \left(1 - \frac{1}{2} A_I \right) \ln \left(1 - \frac{1}{2} A_I \right) \right]. \quad (6)$$

Now the relation between the entropy and the nuclear polarization is not unambiguous. However, this ambiguity is lifted if we assume a Boltzmann distribution over the energy levels:

$$N_m \propto \exp \left(\frac{m \hbar \omega_I}{k_B T_I} \right), \quad (7)$$

where T_I is the nuclear spin temperature. First, we note that this Boltzmann distribution will be justified in the next section where the DNP process is described as a Carnot cycle. Secondly, we note that a two-level system corresponding to $I = \frac{1}{2}$ can always be described by such a Boltzmann distribution.

The solid curve II in Fig. 1 shows the nuclear polarization as a function of the reduced entropy for this latter case. Moreover the dashed curve III shows the corresponding alignment A_I as a function of the reduced entropy. As an example we again consider the case that the entropy is reduced by 0.23. Now the nuclear polarization is only 50% while the nuclear alignment is barely 20%.

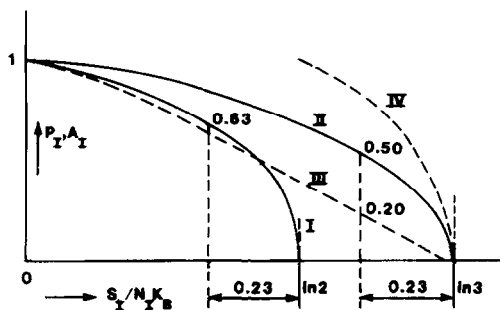


Fig. 1. Polarization P_I and alignment A_I as a function of entropy I . I: P_I for proton spins. II: P_I for deuteron spins. III: A_I for deuteron spins. IV: A_I for deuteron spins if $P_I = 0$.

What is to be learned from Fig. 1? First, that the same reduction of entropy leads to a much higher proton spin polarization than deuteron spin polarization. Secondly, that it leads to even less deuteron spin alignment. This difference originates in the larger number of degrees of freedom of the deuteron spin system and constitutes a fundamental limitation for the creation of simultaneous deuteron spin polarization and alignment.

However, for many applications it is not necessary to have a high deuteron spin polarization and alignment simultaneously. If one puts $P_I = 0$ and subsequently calculates the maximum obtainable alignment for a given value of the entropy one obtains the dashed curve IV. Now an entropy reduction of 0.23 may lead to considerable alignment $A_I = 0.83$!

2. DNP as a Carnot cycle

Fig. 2 shows the currents of entropy during the DNP process. Central to the DNP process are the electron spins. It is important to realize that their individual resonance frequencies may differ due to crystal field effects, hyperfine interactions etc. Consider the electron spins with a resonance frequency ω_S^i . They are surrounded by a few nearby nuclear spins, also called the local or "abnormal" nuclear spins [1]. In the solid effect a microwave field with a frequency $\omega = \omega_S^i \pm \omega_j$ induces flip-flop transitions between the electron spins and one of these local nuclear spins.

Next, two processes occur simultaneously: nuclear spin diffusion transfers the polarization of the local nuclear spins to the bulk nuclear spins far from the electron spins. Furthermore, electron spin-lattice relaxation repolarizes the electron spin. Under the normal circumstances of DNP for polarized targets, this occurs via the direct process where the electron emits an acoustical phonon with a frequency ω_S^i . Finally these monochromatic phonons scatter by non-linear phonon processes or exit the crystal.

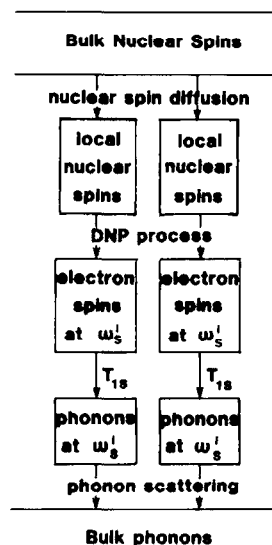


Fig. 2. Diagram showing the various processes involved in DNP.

The processes shown in Fig. 2 can be interpreted as a Carnot cycle [3]. For this purpose we use the diagram given in Fig. 3 where the P_S is plotted as a function of the effective field $\omega_S^i - \omega$ in a frame of reference rotating with the microwave frequency ω . Adiabatic processes follow dotted curves $S_S = \text{const.}$, while isothermal processes follow dashed curves where the electron spin temperature $T_S = \text{const.}$ The curves are obtained for electron spins $S = \frac{1}{2}$ using Eqs. (2), (3) and (7).

The Carnot cycle corresponding to an idealized DNP process is given by a solid line. We start with a highly polarized electron spin in a strong field (A in Fig. 3). We apply a microwave field and sweep its frequency, thus adiabatically demagnetizing to a small effective field (A \rightarrow B in Fig. 3). As result the electron spin temperature is lowered. Furthermore, after this step the electron spin is on speaking terms with the nuclear spins, leading to isother-

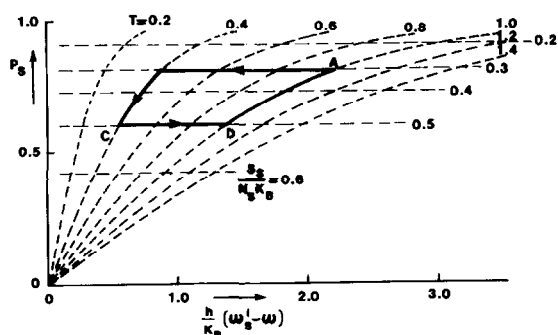


Fig. 3. The electron spin polarization P_S as a function of the effective field $\omega_S^i - \omega$. Dashed curves represent constant entropy. Dotted curves represent constant temperature. The drawn curve represent a Carnot cycle.

mal transfer of polarization to this nuclear spin ($B \rightarrow C$ in Fig. 3). Note that the description of the polarization process as an isothermal process automatically justifies the assumption (7) of a Boltzmann distribution over the nuclear spin levels. Then, the microwave field is swept adiabatically back to its original large value ($C \rightarrow D$ in Fig. 3) where it regains its large polarization by isothermal electron spin–lattice relaxation ($D \rightarrow A$ in Fig. 3).

Thus, the Carnot cycle is operated between a high temperature bath consisting of the crystal lattice and a low temperature bath consisting of the bulk nuclear spins. The low temperature bath is cooled through work performed by the microwave field on the electron spins. Evidently, as in any refrigerator isolation between the high and low temperature bath should be as good as possible, i.e., nuclear spin–lattice relaxation should be slow.

Of course, in practical DNP the cycle is less ideal than shown in Fig. 3. In particular, in standard DNP the microwave field is applied continuously and the adiabatic and isothermal steps are mixed up. Much cleaner cases with the corresponding much greater efficiencies are obtained by separating the adiabatic steps involving the microwave field from the isothermal steps involving nuclear spin diffusion and electron spin–lattice relaxation. This is achieved in nuclear orientation via electron spin locking (NOVEL) [4–6] as well as the integrated solid effect (ISE) [7,8] where great care is taken to demagnetize the electron spins adiabatically to the field where they are on speaking terms with the nuclear spins.

Modulating the microwave frequency (or the magnetic field) can be considered as a partial improvement of the Carnot cycle. Now, for given electron spins with a resonance frequency ω_S^i the resonance condition for polarization transfer to the nuclei is fulfilled during part of the modulation cycle only. Thus, this isothermal step ($B \rightarrow C$ in Fig. 3) is well separated from the other steps. Also ample time is now available for the isothermal step corresponding to electron spin lattice relaxation ($D \rightarrow A$ in Fig. 3). The rate of change of the microwave frequency can be adjusted to optimize these two steps. This does not automatically imply that the other two steps are adiabatic, however. Thus, the Carnot cycle is still imperfect.

3. Modulation effects

The above improvement of the Carnot cycle is only obtained if one of the two isothermal steps is bottlenecking the polarization process and moreover electron spins with different resonance frequencies ω_S^i are not or badly coupled to each other. To explain this we refer again to Fig. 2. If the electron spins are not coupled to each other, a microwave field with a frequency ω induces flip-flop transitions between electron spins with a resonance frequency $\omega_S^i = \omega \pm \omega_j$ and its neighbouring local nuclear spins. However, it does not induce such transitions involv-

ing electron spins with a different frequency ω_S^j . Hence the parallel process involving these latter spins is not operating. Effectively, one operates the DNP process using a reduced number of electron spins, local nuclear spins and phonon modes.

This situation alters significantly if electron spin–spin interactions are strong enough to induce flip-flop interactions between electron spins with different resonance frequencies ω_S^i on a time scale of the order of or faster than the electron spin–lattice relaxation time T_{1S} and the time scale of the DNP process. Then the microwave field acts on all electron spins and the DNP processes uses all electron spins, local nuclear spins and phonon modes in the bandwidth of electron spin resonance frequencies. Note that under those circumstances, thermal mixing processes might dominate DNP [1].

If electron spin–spin interactions are weak, one might try to increase the number of electron spins involved in the DNP process by modulating the microwave frequency and/or the static magnetic field [1]. This does not have any effect if the DNP process itself or electron–spin lattice relaxation are the bottleneck. Then, one simply shifts from one electron spin to another, one group of local spins to another and one phonon mode to another, but the process goes on with the same rate. It does have a dramatic effect, however, if either nuclear spin diffusion or phonon scattering are bottlenecking the process. Then, one improves the efficiency of the isothermal processes in the Carnot cycle described in the previous section.

In the former case, modulation of either the microwave frequency or the magnetic field implies shifting from one set of local nuclear spins to another. Then, while the new set is polarized, the old set transfers its polarization to the bulk nuclear spins. Similarly, in the latter case modulation of the microwave field implies shifting to a new phonon mode allowing the old phonon mode to scatter to the bulk phonon bath. Furthermore, shifting the magnetic field implies shifting the old electron spins to a different frequency allowing them to relax to a new phonon mode.

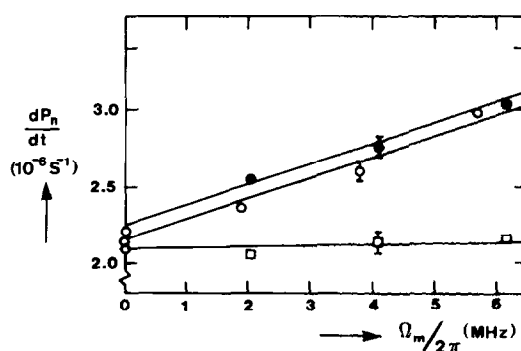


Fig. 4. Polarization rate at 9 GHz as function of modulation amplitude. Open circles: magnetic field modulation. Closed circles: frequency modulation. Squares: simultaneous modulation.

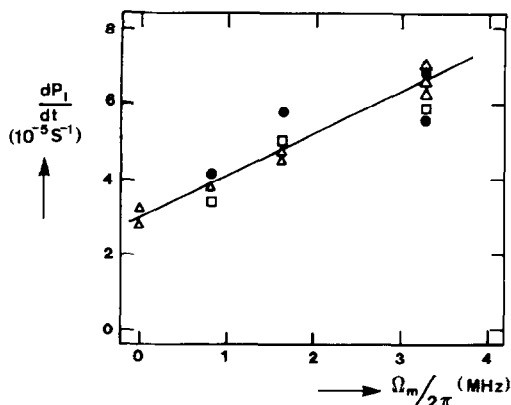


Fig. 5. Polarization rate at 9 GHz as function of modulation amplitude. Squares: magnetic field modulation. Closed circles: frequency modulation. Triangles: simultaneous modulation.

In practice it is possible to distinguish between the two cases by applying microwave frequency and magnetic modulation simultaneously. Then, the DNP process involves the same electron spins and local spins continuously, but as ω_S^i is modulated, one involves more phonon modes than without modulation. Hence, if such modulation improves the rate of the DNP processes, clearly a phonon bottleneck occurs. On the other hand, if modulation does not improve DNP, but simultaneous modulation does not, nuclear spin diffusion bottlenecks the DNP process.

Both cases are illustrated in Figs. 4 and 5 showing such modulation experiments for DNP of proton spins in a molecular crystal of fluorene. The sample was doped with phenanthrene molecules replacing fluorene and the photoexcited triplet state of the dopant provided the electron spin for DNP. The experiments were performed at 1.2 K. Fig. 4 shows the polarization rate as a function of the modulation amplitude at a magnetic field of 3 T and a microwave frequency of 9 GHz [9]. In the case of field modulation, the amplitude is reduced to frequency units. The dots give the results for frequency modulation, the triangles for field modulation and the squares for simultaneous modulation. As modulation does not improve the polarization rate in the latter case, one concludes that nuclear spin diffusion bottlenecks the DNP process.

Fig. 5 shows the results at a magnetic field of 3.5 T and a microwave frequency of 75 GHz [10]. Again, the polarization rate is plotted as a function of the modulation amplitude. The same symbols are used for the same cases. Now, simultaneous modulation does improve the polarization rate in the same way as field or frequency modulation alone. Hence, here we have a clear case of phonon bottleneck limitation of DNP. The difference between 9 GHz and 75 GHz is easily understood. In the former case the direct process creates phonons of 9 GHz, which are abundant at 1.2 K and scatter easily, while in the second case

phonons of 75 GHz are created which are rare at this temperature.

The fact that modulation improves the DNP rate also implies that the coupling between the electron spins is weak. This was confirmed by performing a hole burning experiment. After a short microwave pulse at frequency ω , only electron spins with $\omega_i = \omega$ were saturated [2]. Because of the weak coupling the DNP process should be governed by the solid effect, which is confirmed by a study of the polarization rate as a function of the microwave frequency. Here one observes a well resolved solid effect [11].

4. Conclusions

It is important to realize that DNP should obey the laws of thermodynamics. The amount of entropy reduction needed to polarize deuteron spins is larger than needed for proton spins. Taking into account that DNP can be interpreted as a Carnot cycle, this leads to a fundamental limitation in deuteron spin polarization. The use of a Carnot cycle to describe DNP also allows a better understanding of modulation effects on DNP. More importantly, it shows that present methods for DNP do not correspond to optimal thermodynamic processes.

Acknowledgements

The work is part of the research programme of the "Stichting Fundamenteel Onderzoek der Materie (FOM)" and financially supported by the "Nederlandse Organisatie voor Wetenschappelijk Onderzoek".

References

- [1] A. Abragam and M. Goldman, *Nuclear Magnetism: Order and Disorder* (Clarendon, Oxford, 1982).
- [2] P.F.A. Verheij, Thesis, Leiden (1990).
- [3] C.J. Adkins, *Equilibrium Thermodynamics* (Cambridge University Press, Cambridge, 1983).
- [4] H. Brunner, R.H. Fritsch and K.H. Hausser, *Z. Naturforsch.* 42a (1987) 1456.
- [5] A. Henstra, P. Dirksen, J. Schmidt and W.Th. Wenckebach, *J. Magn. Res.* 77 (1988) 389.
- [6] D.J. van den Heuvel, A. Henstra, T.-S. Lin and W.Th. Wenckebach, *Chem. Phys. Lett.* 188 (1992) 194.
- [7] A. Henstra, P. Dirksen and W.Th. Wenckebach, *Phys. Lett. A* 134 (1988) 134.
- [8] A. Henstra, T.-S. Lin, J. Schmidt and W.Th. Wenckebach, *Chem. Phys. Lett.* 165 (1990) 6.
- [9] H.W.J. van Kesteren, W.Th. Wenckebach and J. Schmidt, *Chem. Phys. Lett.* 121 (1985) 440.
- [10] P.F.A. Verheij, W.Th. Wenckebach and J. Schmidt, *Appl. Magn. Reson.* 5 (1993) 187.
- [11] H.W.J. van Kesteren, W.Th. Wenckebach and J. Schmidt, *Phys. Rev. Lett.* 55 (1985) 1642.



ELSEVIER

Behaviour of polarized ammonia in an intense electron beam [☆]

A. Thomas ^{*}, Ch. Bradtke, H. Dutz, R. Gehring, S. Goertz, H. Hainer, W. Meyer,
M. Plückthun, G. Reicherz, K. Runkel

Universität Bonn, Physikalisches Institut, Nussallee 12, 5300 Bonn 1, Germany

Abstract

Polarized target experiments with intense particle beams suffer from the depolarization effects due to radiation damage and beam heating. The local depolarization of the target material $^{14}\text{NH}_3$ at the electron beam spot has been investigated by hitting it with 1.2 GeV electrons. This beam has been delivered from the electron stretcher accelerator ELSA of the Bonn University.

The polarized target consists of a 4 T superconducting magnet with a Helmholtz configuration and a ^4He evaporation cryostat which operates at a temperature around 1 K. The heating of the target chips by the electron beam has been measured up to an intensity of 70 nA using a specific set-up of the nuclear magnetic resonance apparatus for the polarization measurements.

1. Introduction

Deep inelastic scattering experiments with intense electron beams at SLAC have been performed with the polarized alcohol target material butanol ($\text{C}_4\text{H}_9\text{OH}$) to investigate the spin structure function of the proton [1]. In these measurements the main problem with the polarized target has been its depolarization due to radiation damage. In the 1980s the target material ammonia (NH_3 and ND_3) has been developed and shows a much better behaviour in this regard. [2] (Fig. 1). Therefore recent experiments with intense electron beams use NH_3 and ND_3 to investigate the spin structure of the proton and of the neutron as well. In intermediate energy physics the deuteron form factors were measured in Bonn using ND_3 as target material [3].

Polarized solid state targets work on the principle of Dynamic Nuclear Polarization (DNP). The target material has to be cooled to the temperature of ≈ 1 K and placed in a magnetic field of a few tesla (2.5–5 T). For the DNP process one needs a diluted assembly of electrons (paramagnetic radicals). In our case ammonia $^{14}\text{NH}_3$ was used. It was doped with paramagnetic radicals by irradiation at the Bonn 20 MeV electron injection linear accelerator (linac) [2]. The sample is exposed to microwaves of a frequency near to the electron spin resonance frequency to

drive the forbidden hyperfine transition. This allows the nuclear spins to be aligned. By this process protons can be polarized to nearly 100% and deuterons up to 50%. The target material is made of small beads or chips with a dimension of 1–2 mm, which are cooled by the surrounding helium bath in order to have a homogeneous temperature and hence a homogeneous polarization across the entire target. All polarized targets operating in intense particle beams use superfluid ^4He at about 1 K as coolant due to its excellent cooling properties. Nevertheless, beam spot sizes of some millimeters can locally depolarize the material by the energy deposition. The investigation of the local depolarization caused by temperature effects from the beam is the subject of this paper.

First a brief description of the Bonn polarized target for electron scattering experiments is given. Then some details of the specific set-up nuclear magnetic resonance (NMR) are described. These allow the investigation of the local depolarization due to beam heating [4]. Finally the results of the temperature distribution in the target material obtained by measuring the thermal equilibrium polarization during the electron irradiation are shown.

2. The Bonn polarized target for electron scattering experiments

The Bonn polarized target consists of a superconducting 4 T split pair magnet and a vertical ^4He refrigerator with a cooling power of 0.6 W at 1.2 K (Fig. 2). The homogeneity $\Delta B/B$ of the magnet is better than 5×10^{-5} over the target volume. This system is designed to allow

[☆] Supported by Bundesministerium für Forschung und Technologie.

^{*} Corresponding author.

¹ Made by duPont.

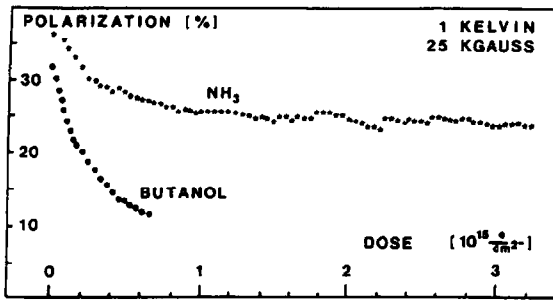


Fig. 1. Comparison of the depolarization due to radiation damage of ammonia and butanol. The polarization decrease can be fitted exponentially with $P = P_0 e^{-D/\phi_0}$, where P_0 is the initial polarization, D is the dose and ϕ_0 is the critical dose. The critical dose of ammonia is approximately 30 times higher than that of butanol.

the detection of scattered electrons over an angular range from 0° to 26° in connection with the electrons at nucleons (ELAN) magnetic electron spectrometer at the Bonn electron stretcher accelerator ELSA, which produces a continuous electron beam. The energy of the incident electrons has been 1.2 GeV and the intensity was measured by using a totally absorbing Faraday cup.

The ammonia sample with a volume of 5 cm^3 was placed inside a cylindrical microwave cavity of 90 cm^3

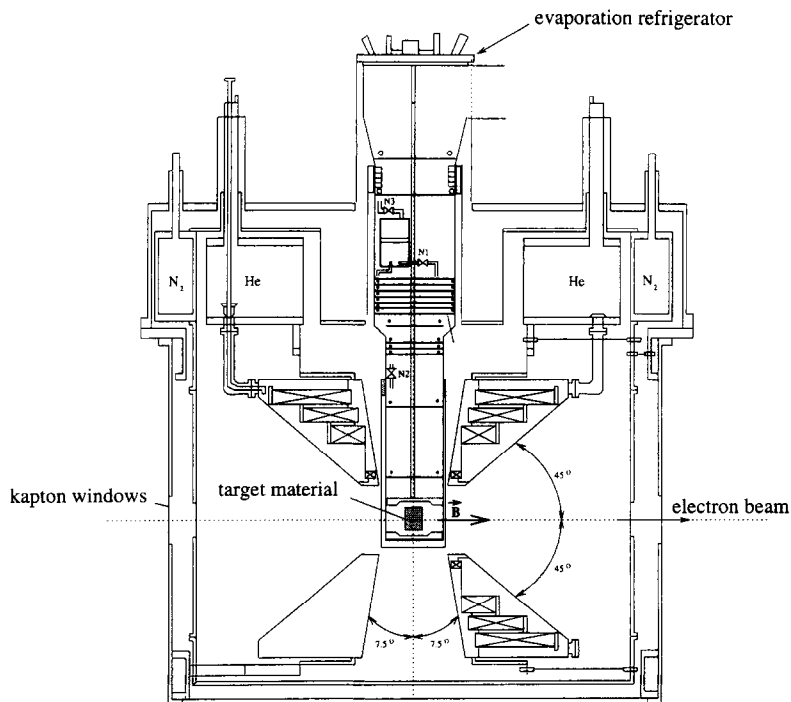


Fig. 2. The superconducting 4 T magnet with the ^4He cryostat. The cooling power of this refrigerator with a $3000 \text{ m}^3/\text{h}$ roots pumping system is 0.6 W at 1.2 K.

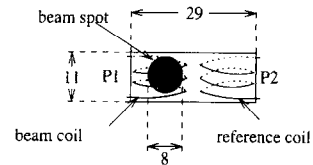


Fig. 3. Cross section of the target container with the two NMR coils. The dimensions are given in mm. The electron beam spot is indicated.

volume. The target container, made of Kapton¹, had the dimensions of $29 \times 11 \times 15 \text{ mm}^3$ (Fig. 3). The electron beam with a diameter of 8 mm (FWHM) was directed onto one part of the target, where the polarization was measured by the so called “beam coil”. The second coil was used as “reference coil” to determine the polarization decrease due to the helium bath heating. Both coils were situated inside the material and consisted of three turns. They are connected by a $\lambda/2$ cable to a Q -meter, which is part of a phase sensitive NMR system. The proton polarization has been measured at a resonance frequency of 106 MHz, which corresponds to a field of 2.5 T. The readout of the proton polarization, detected by the two coils, was made alternate every 30 s.

3. Depolarization caused by beam heating

The depolarization of the target material due to radiation damage is a well known phenomenon. In addition, there is a temperature dependent depolarization due to the beam heating. The dependence of the maximum polarization on radiation damage was very similar to that reported in Ref. [2] (Fig. 1) The polarization decrease can be fitted exponentially by $P = P_0 e^{-D\phi_0}$, where P_0 is the initial polarization, D is the dose and ϕ_0 in the critical dose. To avoid the superposition of the two effects the measurements were made at doses higher than 2×10^{15} electrons/cm² electrons, where the radiation damage is a weak effect.

Some typical curves for the temperature dependent depolarization in the region of both NMR coils are shown in Fig. 4. The average beam intensity was 44 nA as measured with a Faraday cup. The normalized polarizations detected with both coils are displayed in Fig. 5. The depolarization determined with the “reference coil” is caused by the heating of the helium bath, whereas the depolarization determined with the “beam coil” comes from the additional heating of the target chips due to the thermal conductivity of the material and the Kapitza resistance. These temperature dependent depolarizations were measured for different intensities (Fig. 6). During the measurements the microwave power, the microwave frequency, the helium filling of the cryostat, and the parameters of the NMR system were kept constant. The time constant for the temperature dependent depolarization was of the order of 300 s.

4. Determination of the target material temperature

For spin $\frac{1}{2}$ particles, e.g. protons, the polarization P in the thermal equilibrium (TE) is given by

$$P = \tanh\left(\frac{\mu B}{kT}\right), \quad (1)$$

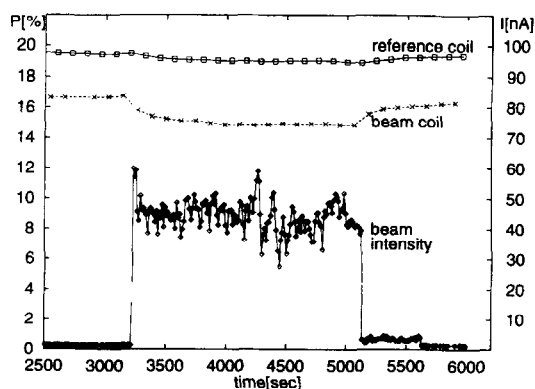


Fig. 4. Depolarization behaviour measured with each NMR coil at an average beam intensity of 44 nA. The beam intensity and both polarizations were recorded simultaneously.

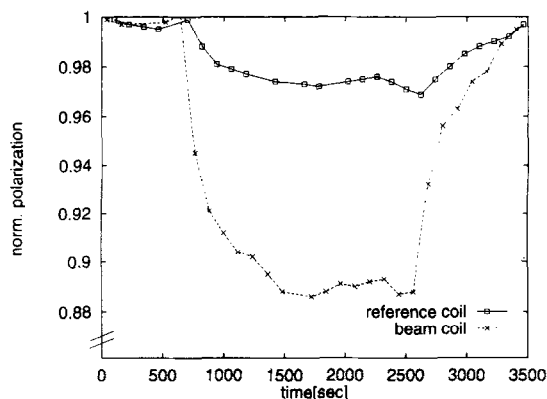


Fig. 5. The normalized polarization at a beam intensity of 44 nA. The polarization was normalized to 1 to compare the measurements at different starting conditions.

where μ is the magnetic moment, B is the magnetic field, k is the Boltzmann constant and T is the target temperature. Formula (1) can be used to determine the temperature differences in the target material caused by local beam heating. The temperature scale is calibrated with a resistor while the target material has the same temperature as the helium bath. This is the case when the beam and the microwaves are switched off.

During the electron irradiation the temperature of the target material located in the beam and the temperature of the entire helium bath increases. Hence the polarization measured with each coil decreases to its new thermal equilibrium value (see Section 3). Using formula (1) the new temperatures of the target material can be calculated. This method requires an excellent precision of the polarization measurement at a low sweep number (≈ 100) to

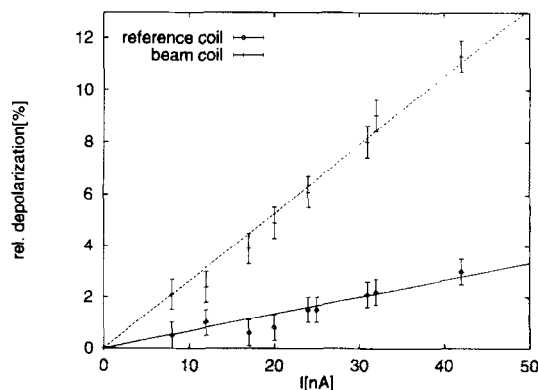


Fig. 6. Depolarization dependence of the beam intensity. The depolarization of the material in the reference coil is caused by the heating of the helium bath. The target material (irregularly formed chips with typical dimensions of 2 mm) shows a stronger depolarization in the beam region due to the Kapitza resistance and the thermal conductivity of the material.

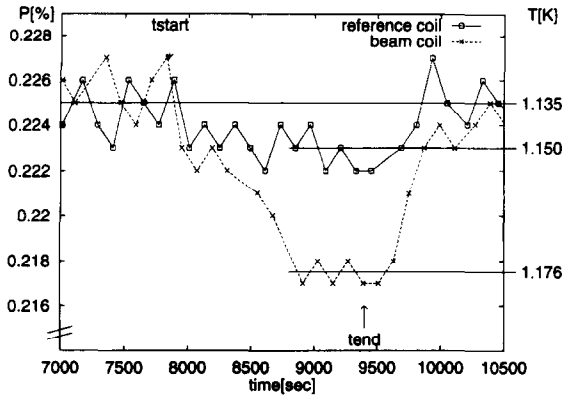


Fig. 7. Depolarization measured with both NMR coils in the thermal equilibrium at an average beam intensity of 35 nA. The beam has been switched on at the time indicated by t_{start} and has been switched off at the time indicated by t_{stop} . The temperature was calculated by formula (1) and corresponds to the thermal equilibrium polarizations measured in both coils.

get a sufficient time resolution for the subsequent measurements. Details about the NMR system can be found in Ref. [5]

The TE polarization behaviour during the electron irradiation (1.2 GeV) at an intensity of 35 nA is shown in Fig.

Table 1
Heating of the target material and the helium bath

I [nA]	Beam coil		Reference coil	
	dP1 [%]	ΔT_{probe} [mK]	dP2 [%]	ΔT_{bath} [mK]
6	0.02	10	0.00	0
25	0.06	31	0.02	10
35	0.08	41	0.03	15

7. The beam was switched on at the time indicated by “ t_{start} ” and switched off at the time indicated by “ t_{end} ”. Again the heating of the material in the “beam coil” is caused by the thermal conductivity and the Kapitza resistance, the heating of the material in the “reference coil” is caused by the heating of the helium bath only. The measured heating of the target material and the heating of the bath for several electron beam intensities is plotted in Table 1. Details can be found in Ref. [4].

5. Conclusions

Polarized solid targets with ^4He cooling at about 1 K can accept electron beam intensities of more than 50 nA with only a small, temperature dependent, depolarization. A local relative depolarization of 12.5% at a beam intensity of 50 nA with a beam spot diameter of 8 mm was measured using a ^4He cryostat with a cooling power of 0.6 W at 1.2 K. The temperature of the solid target chips hit by the beam and the helium bath heating were separately determined by measuring the thermal equilibrium polarization.

References

- [1] M.J. Alguard et al., Phys. Rev. Lett. 37 (1976) 1261, and (1978) 70.
- [2] W. Meyer, Proc. 4th Int. Workshop on Polarized Target Materials and Techniques, Bonn, 1984, p. 23.
- [3] H.-D. Schablitzky, Thesis BONN-IR-89-32.
- [4] A. Thomas, Thesis BONN-IR-94-15.
- [5] G. Reicherz et al., these Proceedings (7th Workshop on Polarized Target Materials and Techniques, Bad Honnef, Germany, 1994) Nucl. Instr. and Meth. A 356 (1995) 74.

The Virginia/Basel/SLAC polarized target: operation and performance during experiment E143 at SLAC

D.G. Crabb^{*}, D.B. Day¹

Physics Department, University of Virginia, Charlottesville, VA 22901, USA

1. Introduction

Several experiments are currently investigating the spin structure of the proton and neutron [1–4]. These experiments all measure a scattering asymmetry when the target and beam have their spins parallel, compared to them being anti-parallel, along the beam momentum direction. Thus a polarized nucleon target as well as a polarized lepton beam is required.

Experiment NA47 (SMC) at CERN [1,2] uses a low intensity muon beam incident on a very thick (1.2 m long) target of butanol or deuterated butanol, which is cooled by a powerful dilution refrigerator. Polarization is achieved by the technique of dynamic nuclear polarization (DNP). Several aspects of this target are presented in these proceedings.

In contrast experiment E142 at SLAC [3] used a very intense electron beam incident on a gaseous ³He target polarized through spin exchange from polarized rubidium.

Experiment E143 at SLAC [4] used a less intense electron beam than E142 together with a DNP style polarized solid target. The operation and performance of this target during the running of E143 is presented here.

2. Polarized target system

Fig. 1 shows a schematic of the polarized target. It operated in End Station A (ESA) with all measurement, control and monitoring done remotely from the counting house outside ESA.

The target was required to operate in as high a beam intensity as possible. Consequently this meant that the target material be as radiation resistant as possible and that the refrigerator has high cooling power to minimize the effects of beam heating on the polarization. The target performance was optimized by the use of ammonia as the

polarizeable material in conjunction with a ⁴He evaporation refrigerator, a large pumping system, a magnetic field of 5 T, and a high power microwave tube operating at a frequency around 140 GHz.

2.1. Magnet

The magnet is a 5.1 T superconducting Helmholtz pair obtained from Oxford Instruments. The field is uniform to 10⁻⁴ over a 3 cm DSV. The bore is 20 cm diameter with a clear output angle of 100°. The split is 8 cm at the narrowest point with clear output angles of 34° horizontally and 50° vertically. It took about 35 min to ramp to 5 T and operated in persistent mode. The liquid helium and nitrogen tanks were fed on demand from nearby dewars.

2.2. Refrigerator

The refrigerator is of the ⁴He evaporation type and is installed vertically along the center of the magnet. Liquid helium from the magnet tank was fed into the separator via a very short transfer line. The cold vapor in the separator was pumped away by a small pump and cooled the radiation baffles. The liquid helium from the separator flowed through a tube and plate heat exchanger and was metered into the nose by a needle valve. The heat exchanger could be bypassed, by opening another needle valve, for precooling. Liquid helium filled the nose so that the targets were covered and was pumped on by a 12 000 m³/h roots pump assembly to reach temperatures < 1 K. A cooling power of 1.3 W at 1.06 K was measured in the beam.

2.3. Insert

An insert was slid along the central bore of the refrigerator and carried the targets, microwave guide and horn, NMR coils and cables and cryogenic instrumentation. Several inserts were made and all carried four targets: the top one, closest to the horn, was ND₃; the next one was NH₃ followed by an empty target; and finally a carbon or aluminum target (Fig. 2). The target insert could be moved

^{*} Corresponding author.

¹ On behalf of the E143 polarized target group.

up and down by a remotely driven air motor to position any target in the beam.

2.4. Microwaves

The microwaves at around 140 GHz were provided by an EIO tube from Varian Canada. The layout of the microwave components is shown in Fig. 2. They were mounted on a table which moved up and down with the

target insert. Our primary tube failed at the beginning of the experiment and the back-up EIO (137 GHz) was used for the whole experiment. Measurement of the microwave power was made with a calibrated thermistor while the frequency was measured with an EIP frequency counter and appropriate mixer.

Before entering the cryostat several waveguide transitions were made to allow transmission along oversized circular waveguide. Finally a horn broadcast the mi-

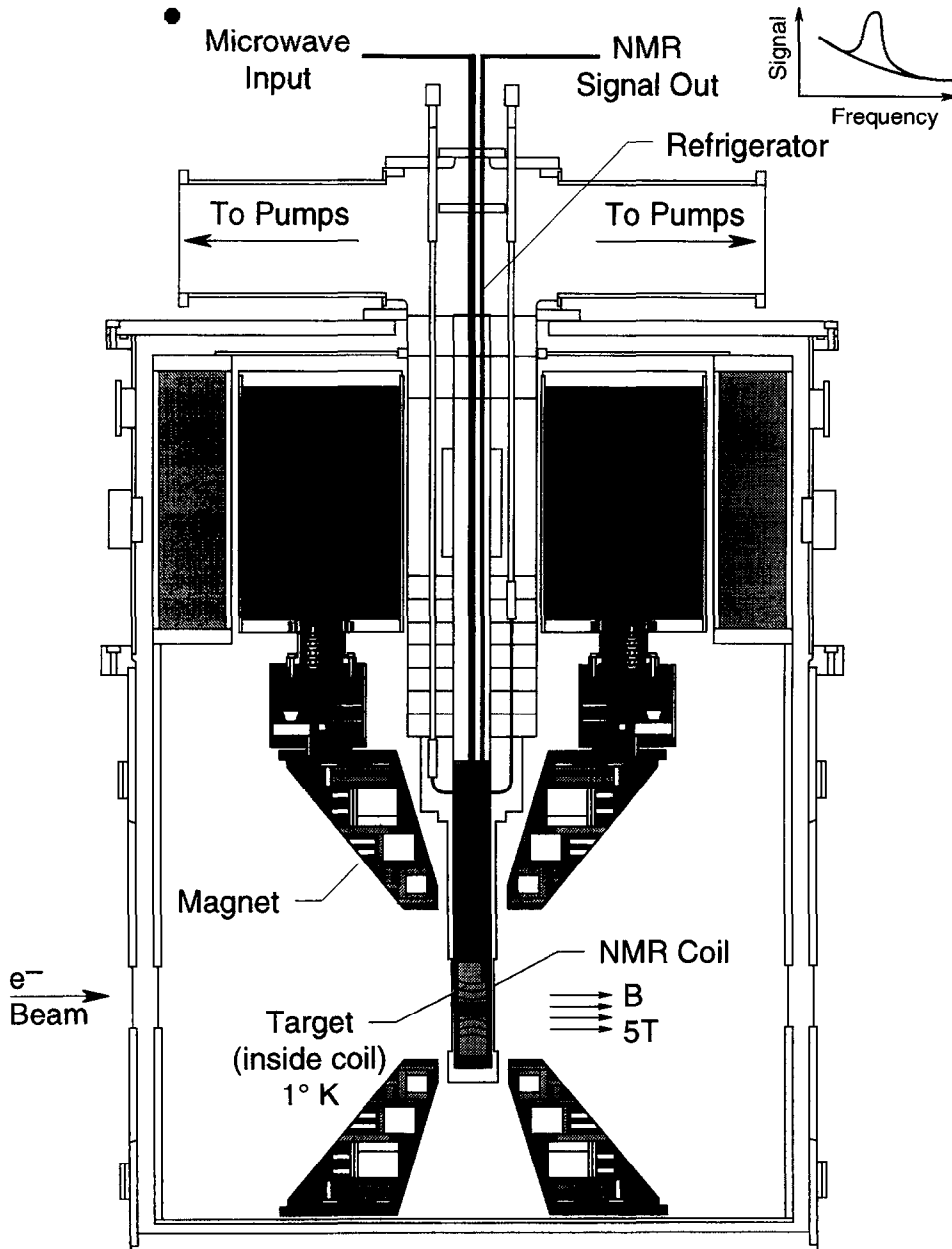


Fig. 1. Schematic of the E143 polarized target.

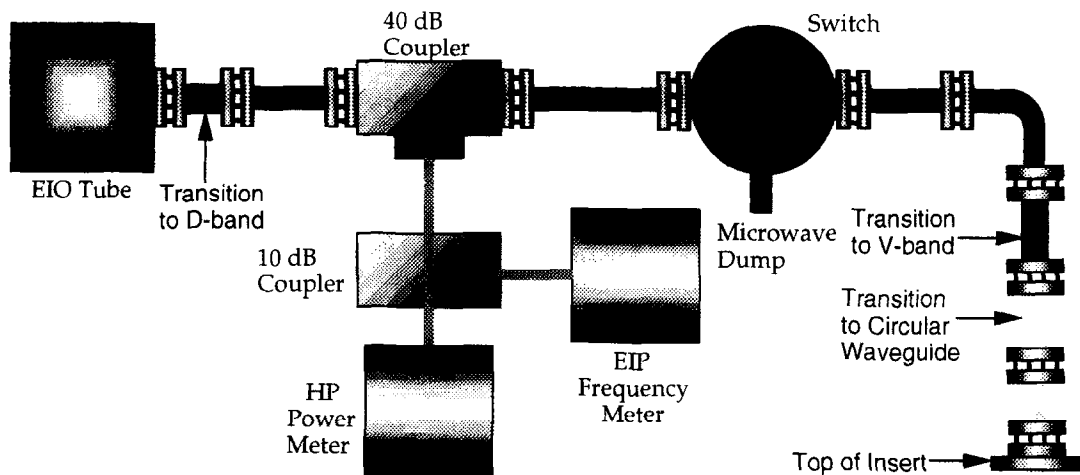
crowaves onto the targets below it. Approximately 1 W of microwave power (as measured by He boil-off) was delivered to the target region.

2.5. NMR

Each target contained two NMR measurement coils as shown in the panel in Fig. 2. In the NH₃ target there was a large coil for measuring the ¹⁵N polarization and a small

one for measuring the proton polarization. Similar coils in the ND₃ target were used to measure the deuteron and residual proton polarizations; the deuteron coil could be switched to measure the ¹⁵N polarization. Each coil was made from 0.040 in. diameter, 0.007 in. wall CuNi tubing.

Five Q-meter modules of the Liverpool type [5] were used to measure the five possible polarizations. The method of measurement has been well documented elsewhere [6]. The rest of the system, including the PTS frequency



- F-band Waveguide (90-140 GHz)
- D-band Waveguide (110-170 GHz)
- V-band Oversized Waveguide (50-75 GHz)

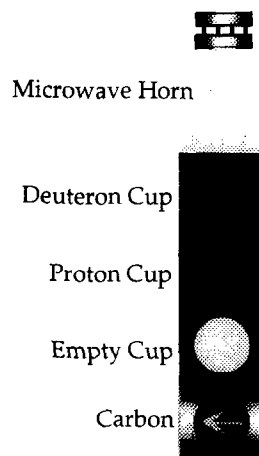
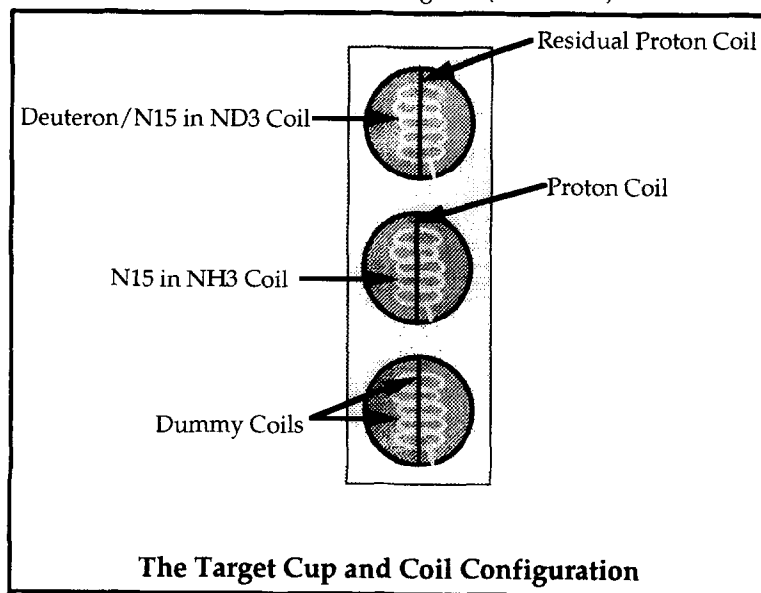


Fig. 2. Microwave assembly. The panel inset shows the configuration of the NMR coils in different targets.

synthesizer and STAC modules were similar to that used by SMC [6]. Measurement of the NMR signals and control of the hardware used the commercial software package LabView running on a Macintosh Quadra.

The $\lambda/2$ (or $n\lambda/2$) cable carrying the NMR rf signal between coil and Q -meter was of two different types: inside the cryostat the signal was carried by 0.085 cryogenic semi-rigid cable; outside, the signal was carried by Isocore semi-rigid cable. The use of Isocore cable and its encasement in a temperature controlled enclosure considerably reduced the drift problems encountered in measuring the very small deuteron thermal equilibrium (TE) signal [7].

2.6. Instrumentation

Temperature sensors consisting of RuO chip resistors, Pt resistors and thermocouples were used to monitor the temperature in different parts of the cryostat. These were read out to commercially available bridges and controllers.

Of particular importance was the measurement of the ^4He vapor pressure in the nose and a ^3He vapor pressure measurement with a sealed tube of ^3He positioned between the ammonia targets.

There also was the standard array of pressure sensors, vacuum gauges, mass flowmeters and level meters. All instruments were read out to the Macintosh/Labview for monitoring and display. A parallel, custom built, system also monitored all the instruments for the SLAC technical support groups and also controlled the cryogen filling.

Finally two color TV cameras were mounted to scan the target area.

3. Target materials

Ammonia was chosen as the target material because it has the highest resistance to degradation of polarization by radiation damage. In addition $^{15}\text{NH}_3$ and $^{15}\text{ND}_3$ were used rather than the usual ^{14}N ammonia because the lack of a

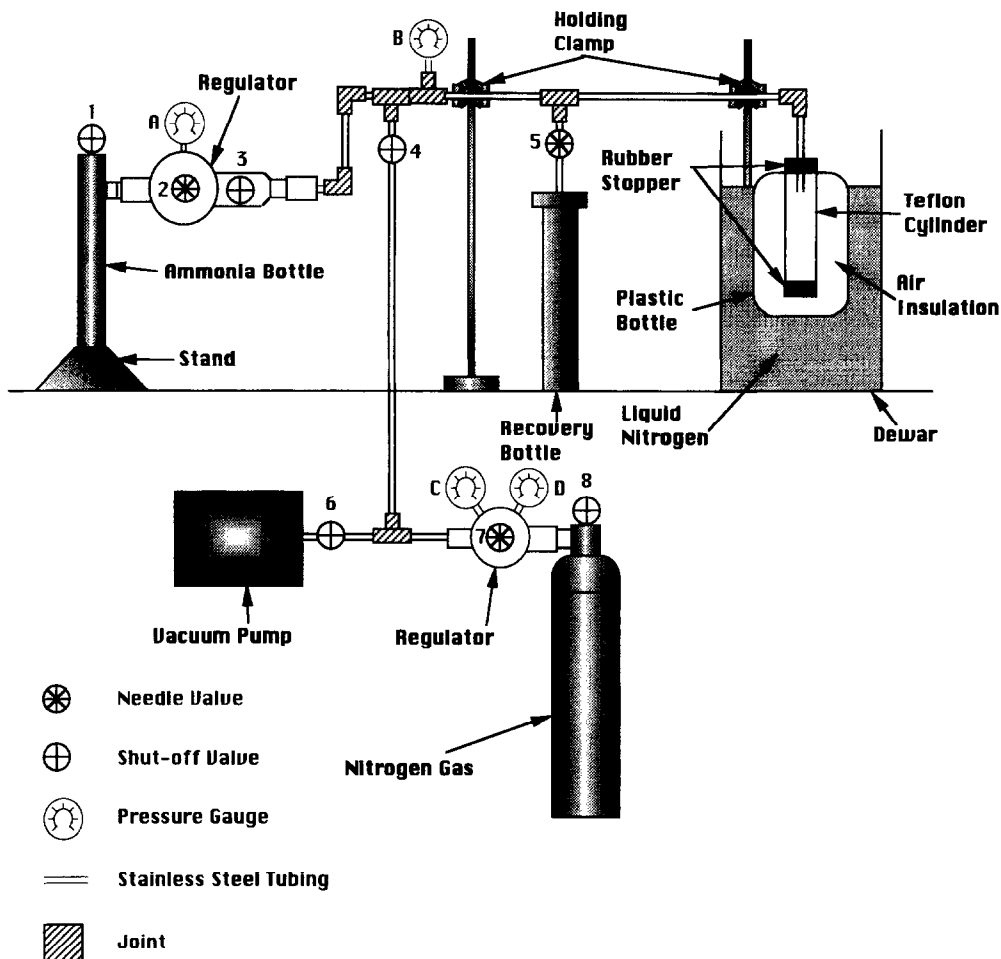


Fig. 3. Layout of ammonia freezing apparatus. The procedure is described in the text.

polarized neutron in ^{15}N leads to a smaller correction and error on the spin asymmetry measurement.

The $^{15}\text{NH}_3$ and $^{15}\text{ND}_3$ were obtained from Cambridge Isotopes Ltd. with ^{15}N purities of better than 98% and D purities of 99% or better. The actual purities for each batch were supplied by CIL after NMR measurements.

3.1. Preparation

The ammonia was slowly frozen, using the apparatus shown in Fig. 3 and afterwards crushed and the appropriate size fragments selected by sifting. In Fig. 3, all the tubing was first flushed and evacuated before ammonia gas from the cylinder was frozen into the test tube by the surrounding "isolated" liquid nitrogen bath. After removal from the test tube the solid ammonia was carefully crushed and sifted through layers of different size mesh to obtain fragments of the right size. Provision was made for recycling and refreezing the ammonia which "escaped" the crushing and sifting by using the recovery bottle. The fragments were stored in sample bottles under LN_2 .

3.2. Irradiation

The technique for obtaining polarizable ammonia by radiation doping is now standard. Though any source of ionizing radiation appears to work, the use of electrons or gamma rays is preferred, as the problems of residual

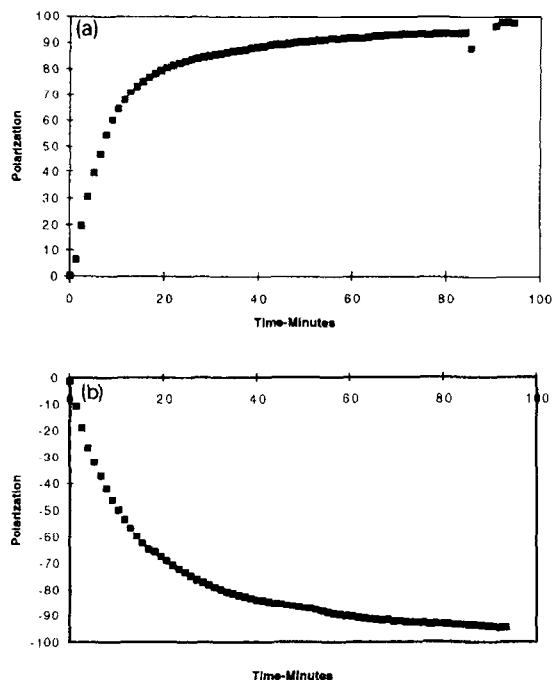


Fig. 4. (a) Positive polarizations and (b) negative polarizations for protons in $^{14}\text{NH}_3$. The warm irradiation dose was a total of 10^{17} electrons through the material.

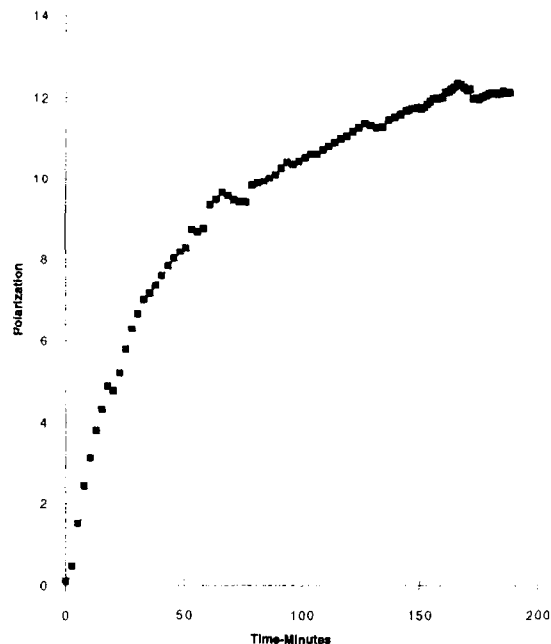


Fig. 5. Positive deuteron polarization in $^{14}\text{ND}_3$. The warm irradiation dose was a total of 10^{17} electrons through the material.

activity in the irradiation equipment (dewars, target holders etc.) are much less compared to that with proton beams for example. In order to get the required dose in a reasonable time, the use of electron beams at operating accelerators is preferred, though the availability and scheduling of these accelerators sometimes presents a problem. In our case we irradiated $^{15}\text{NH}_3$ and $^{15}\text{ND}_3$ at Bates (350 MeV), Naval Post Graduate School, Monterey (65 MeV) and Stanford University (35 MeV). We also irradiated batches of ^{14}N ammonia at Saskatoon (250 MeV).

All these irradiations were done in the same way. The ammonia to be irradiated was poured into a mesh basket which was then immersed in a dewar of liquid argon and put into the beam. Past experience has shown that doses of around 10^{17} electrons cm^{-2} gave very good results [8,9] and this is the approximate dose that most batches of ammonia received at the various accelerators. Also the irradiation current was limited to about $1 \mu\text{A}$ at Saskatoon and Bates, 0.5 at Monterey and 2–3 at Stanford [9].

3.3. Initial performance

The first batches of ammonia were irradiated at Saskatoon and were $^{14}\text{NH}_3$ and $^{14}\text{ND}_3$ except for one batch of 10% ^{15}N NH_3 . These were used in the initial setting up and testing stage at the University of Virginia to establish target performance. Initial proton polarizations of greater than 90% were obtained and are shown in Fig. 4 and were comparable to that obtained previously by Crabb et al. [9]. Proton polarizations from 10% ^{15}N NH_3 were similar to those obtained from $^{14}\text{NH}_3$ with the same dose.

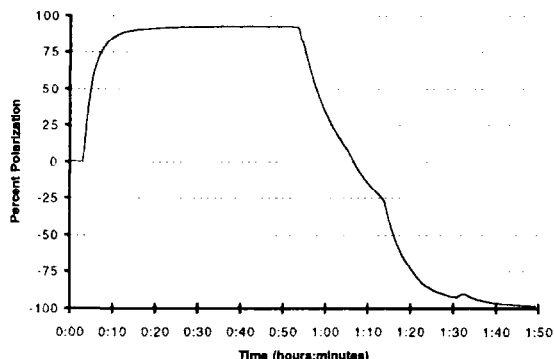


Fig. 6. Example of proton polarization in $^{14}\text{NH}_3$ just before moving the target into the beam line. The $^{15}\text{NH}_3$ had similar behaviour.

On the other hand the deuteron polarization reached only 12%–13%, Fig. 5, and seemed to be very dose dependent. It was known from previous measurements [10] that in-situ irradiation increased the deuteron polarization, by at least a factor of 2, to as much as 49% and substantially decreased the polarizing time. However these measurements were made with a dilution refrigerator operating at 200–300 mK in a magnetic field of 2.5 T. No such data existed for 1 K and 5 T although the SLAC/Yale target operated for E130 [11], had achieved polarizations up to 30% after in-situ irradiation only, on virginal $^{14}\text{ND}_3$.

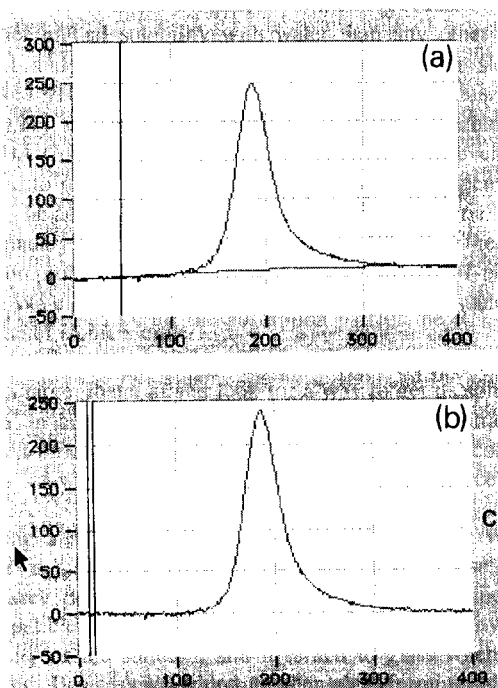


Fig. 7. (a) Proton TE signal after baseline subtraction. The second order fit to the wings of the spectrum is shown. (b) Proton TE signal after subtraction of fitted background. The vertical cursor lines should be ignored.

Attempts were made to investigate the effects of dose on the deuteron polarization by further irradiating some of the ammonia in a gamma beam derived from a 5 MeV electron beam at CEBAF. This only reduced the maximum polarization.

After this the target was moved and set up at SLAC. Tests were carried out with both ^{14}N and ^{15}N ammonia. Fig. 6 shows the proton polarization performance in $^{14}\text{NH}_3$. The $^{15}\text{NH}_3$ was similar. The deuteron polarization in $^{15}\text{ND}_3$ reached 12% as it did in $^{14}\text{ND}_3$.

4. In-beam performance

4.1. Thermal equilibrium measurements

The proton TE calibrations were carried out in the standard way. After thermalizing, without beam or microwaves, a baseline spectrum was taken by moving off-resonance through shifting the magnetic field by 1%. Then the magnetic field was moved back on resonance and the baseline + TE signal spectrum measured. Subtraction of the baseline from the baseline + TE gave the TE signal. To compensate for drifts, the first and last 50 channels of the

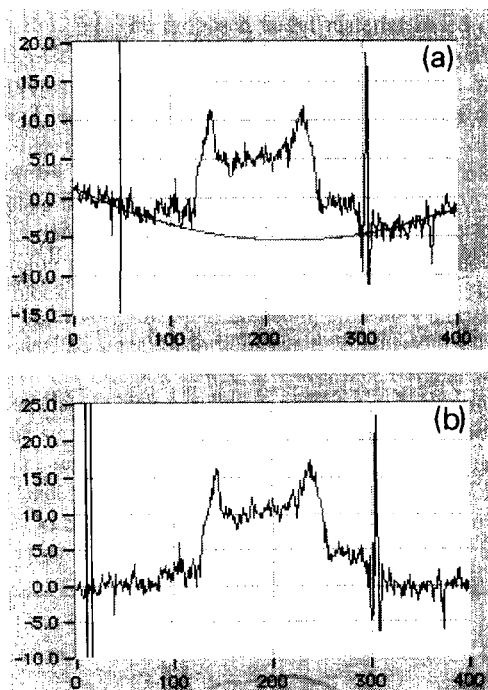


Fig. 8. (a) Deuteron TE signal after baseline subtraction. The second order fit to the wings of the spectrum is shown. (b) Deuteron TE signal after the subtraction of fitted background. In both graphs the noise spike on the RHS of the signal comes from the synthesizer and was filtered in off-line processing. The vertical cursor lines should be ignored.

TE spectrum were used for a second order fit to the background which was then subtracted to give the final TE spectrum. The sequence is shown in Fig. 7. Generally the system was so stable that only one baseline was taken and subtracted from 20 to 25 subsequent measurements of baseline + signal. Typically each measurement took 50 s using 500 rf sweeps. A very accurate measurement of the temperature was made with the ^3He and ^4He vapor pressure thermometers discussed above.

As is well known, the deuteron TE signal is very small and difficult to measure and requires many hours of measurement to obtain the most accurate results. During the course of the experiment there was not time to make the optimum measurement so a compromise procedure was adopted which was similar to that described above for the proton. However, whenever the quadratic fit became unreliable due to drifts in the signal compared to the original baseline another baseline was taken and the procedure repeated. Typically 2000 rf sweeps were used for each measurement with the magnetic field shifted by 3% for the baseline. Fig. 8. shows the deuteron TE signal. The spectra were also treated off-line to improve the fits and to filter out noise spikes from the synthesizer.

At the end of the experiment a full TE calibration was taken on each ND_3 target used. In these calibrations alternating measurements at baseline and on-resonance of 5000 rf sweeps each were made and continued for twelve to fifteen hours.

4.2. Torlon

The ammonia target containers were fabricated from Torlon which contains a small amount of hydrogen. There was a small (3%) contribution to the proton TE signal from this hydrogen, mainly because a short section of the NMR coil was in close contact with the Torlon. Later in the paper we discuss how the correction for this effect was made. At the end of the experiment the NH_3 target material was removed and the TE signal from Torlon was measured and is shown in Fig. 9 and can be compared with the proton TE signal in Fig. 7b.

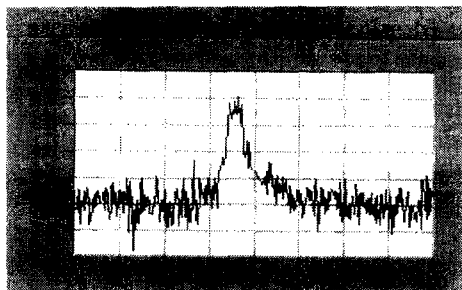


Fig. 9. The TE signal from protons in Torlon.

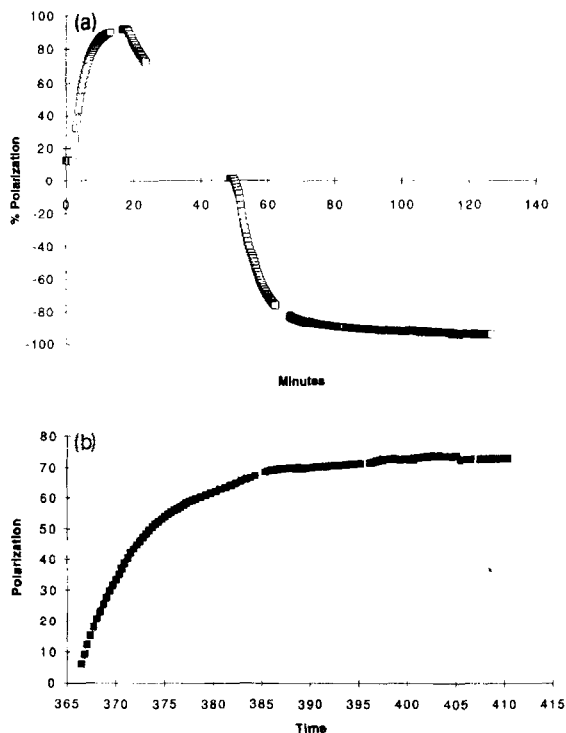


Fig. 10. (a) Proton polarization with no ND_3 in top target. (b) Proton polarization with ND_3 in top target.

4.3. Polarization

4.3.1. NH_3

In the pre-experiment tests it was established that proton polarizations of $> 90\%$ could be achieved. However in the target configuration of the experiment the polarizations were $< 80\%$ before beam was established. This was attributed to there being insufficient microwave power reaching the NH_3 target, with enough being absorbed in the upper ND_3 target to compromise the performance of the NH_3 target. This was confirmed at the end of the experiment when the ND_3 was removed and the NH_3

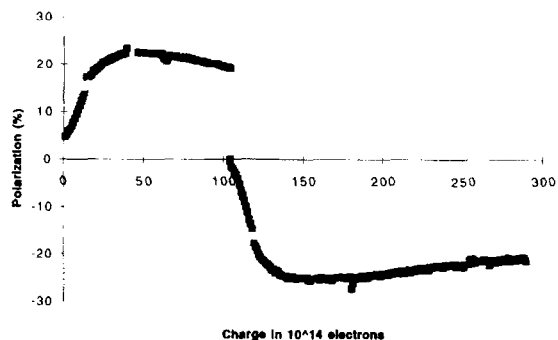


Fig. 11. Growth and decay of deuteron polarization in the first 16 hours of beam irradiation.

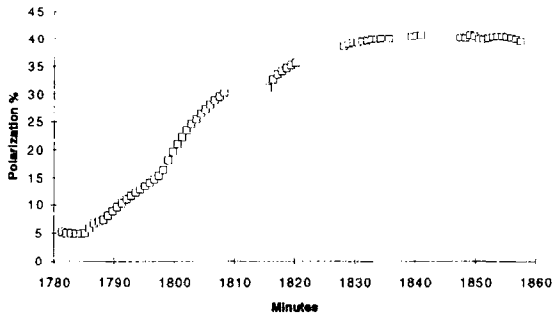


Fig. 12. Deuteron polarization rise to > 40% vs. time.

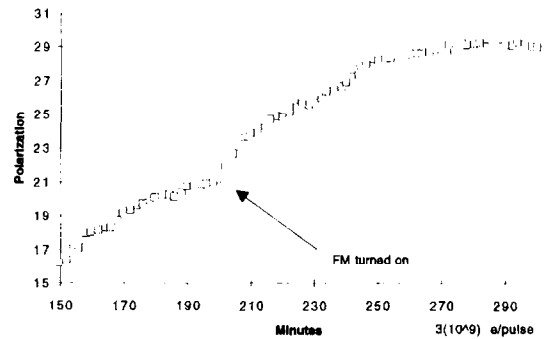


Fig. 13. Effect on deuteron polarization of turning on fm.

polarized. The result is shown in Fig. 10 compared to that obtained during the experiment.

4.3.2. ND_3

As discussed above, the deuteron polarizations achieved after the warm irradiations were at the level of 12–13%. But in contrast to the proton polarizations the deuteron polarizations were substantially improved by in-situ irradiation. Fig. 11 shows the growth of polarization when first put into the ESA beam. The polarization grows quite rapidly, with beam dose, to about 25% and then the effects of radiation damage take over. Also the values are suppressed because of beam heating in the target. Eventually polarizations of < 40% were reached, Fig. 12 and also Fig. 15, meaning more than a factor of 3 increase over the warm irradiation values.

4.3.3. Frequency modulation

The deuteron polarizations were achieved with frequency modulation of the microwaves. It had been known for many years that applying fm had improved the polarization of some target materials. Then in 1992 this effect was accidentally rediscovered by SMC [12] when the deuteron polarization, in butanol, was found to have increased by 80%. Subsequently a smaller effect was found with the proton polarization. In our case we find that once the maximum value without fm had been reached, turning on the fm increased the polarization by an absolute 3–5%. Applying the fm early improves the rate of rise by at least a factor of 2, Fig. 13.

There did not appear to be any significant fm effect on the proton polarization in NH_3 .

For this microwave system the fm was applied with a high voltage isolation transformer, the secondary of which was placed in the high voltage cathode line of the EIO. For these targets a fm voltage of 80 V p-p corresponding to a total fm frequency of about 44 MHz was applied. The fm sweep rate was at 1 kHz.

4.4. Radiation damage

The behaviour of $^{15}NH_3$ and $^{15}ND_3$ in an intense beam of ionizing particles is similar to that seen with ^{14}N

ammonia. Figs. 14 and 15 show proton and deuteron polarizations as a function of accumulated beam dose. The pattern is that the polarization decays with accumulated dose as the ammonia is radiation damaged and allowed to fall to a value dictated by the conditions of the experiment at that time. Generally data was taken on the ND_3 target until the lower limit of polarization was reached; then the NH_3 target was moved into the beam and data taken with it. Once the lower limit on the proton polarization had been reached both targets were annealed by raising their temperature to about 80 K by means of a heating coil wrapped on the support between the two targets. Heat conduction along the aluminum supports and through the He gas in the target chamber allowed the temperature to rise to 80 K in 45 min. The temperatures were read out by a thermocouple (chromel–Au/0.07% Fe) buried in each target and controlled by an Oxford Instruments ITC4 temperature controller.

As shown in Figs. 14 and 15, the pattern of exponential decay of polarization with dose is different for the two materials. For NH_3 there appear to be at least two regions of decay as seen previously [9,13]. The two regions have characteristic values for decay of $0.7 \times 10^{16} e^-/cm^2$ and $1.3 \times 10^{16} e^-/cm^2$. These values are in agreement with those measured by Seely et al. [13] with 20 GeV electrons and Crabb et al. [19] with 24 GeV/c protons, both for

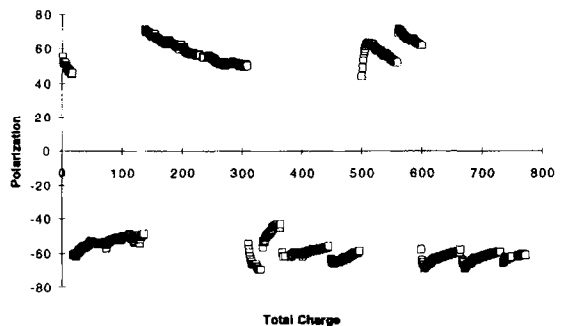


Fig. 14. Polarization history of one $^{15}NH_3$ target as a function received charge.

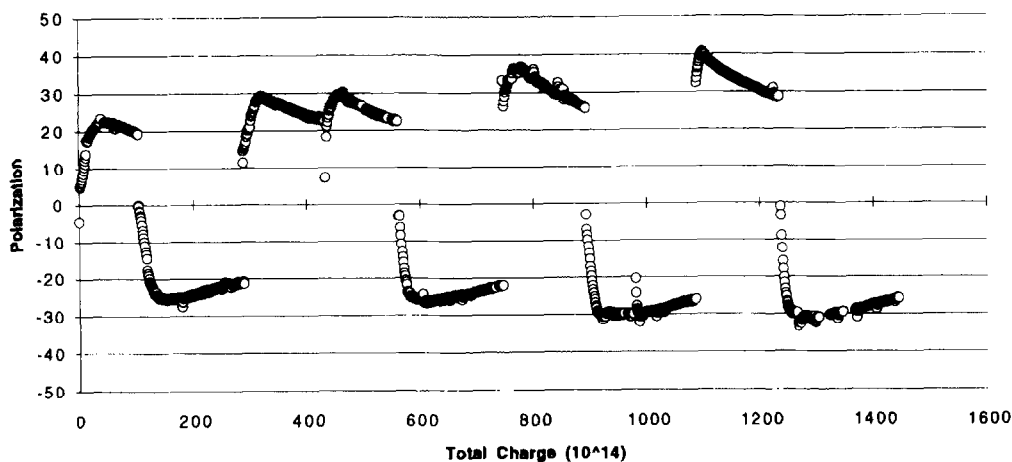


Fig. 15. Polarization history of one $^{15}\text{ND}_3$ target as a function received charge.

$^{14}\text{NH}_3$. The positive and negative polarizations behave in approximately the same way. On the other hand, for ND_3 there is only one region of exponential decay and the characteristic values for positive and negative polarizations are, respectively, $1.4 \times 10^{16} \text{ e}^-/\text{cm}^2$ and $2.5 \times 10^{16} \text{ e}^-/\text{cm}^2$.

Most of the experiment was run with beam intensities of about 5×10^{11} electrons/s, with the beam rastered over the face of the target. An increase of the intensity from 2 to 5×10^{11} lost a relative 15% of the polarization because of beam heating. So the increase in intensity improved the Figure of Merit (P^2I) for the target.

As discussed above, the target holders were made of Torlon which contains a small amount of hydrogen and which contributed 3% to the proton TE signal. After irradiation it was found that the Torlon could be polarized. At the end of the experiment the target cells were emptied and the Torlon polarization studied. Fig. 16 shows the polarization growth to about 5%.

4.5. Other effects

A long term effect noticed during the course of the experiment was one of mechanical damage to the ammonia

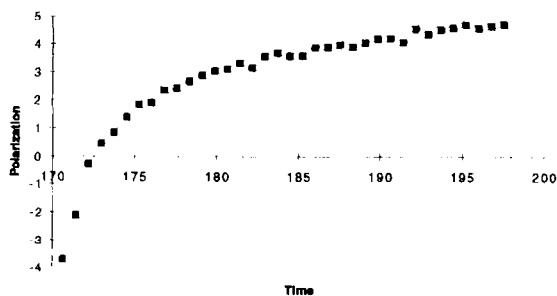


Fig. 16. Polarization growth of protons in Torlon vs. time (min).

fragments. It was noted during and after the experiment, from X-raying and monitoring event rates from different parts of the target that there was a slight settling of the material. The X-rays and subsequent inspection of the material showed a smaller granularity. When the targets were unloaded after the experiment small amounts of ammonia dust were seen. It appears that the granules are being broken up and this is consistent with the much more dramatic effects seen during experiment E130 at SLAC [10] when fast-frozen ammonia beads completely disintegrated.

5. Polarization error

A correction to all the on-line proton polarization values was made to account for the Torlon contribution. The 3% contribution to the TE signal meant that the polarizations were undervalued by 3%. But the enhanced Torlon signal contribution meant that the proton polarization was overvalued by up to 0.3%. Therefore all on-line proton polarization values were multiplied by 1.027%.

The error on the polarization measurement for both protons and deuterons comes mainly from the TE calibration. For protons the statistical error is small but systematic effects such as movement of the target material around the NMR coil can lead to substantial variations in the measured TE constants. For the deuteron the statistical error tends to dominate. The systematic effects were estimated by taking as many separate TE calibrations as possible throughout the lifetime of the target.

A single TE calibration consisted of 20 to 25 measurements of the TE area. From these measurements were calculated the mean area and the error on the mean, typically 0.2% for the proton and 3% for the deuteron.

Fig. 17 shows a plot of all the proton calibration constants. Obviously the scatter is much worse than ex-

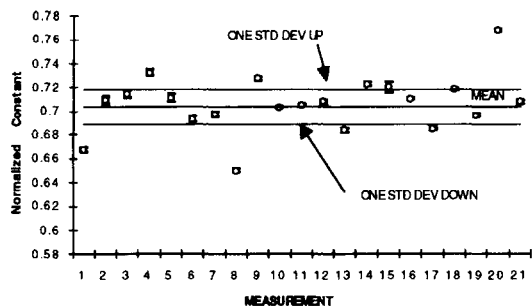


Fig. 17. Proton TE constants plotted against measurement number.

pected from statistics and is a measure of systematic effects. The one sigma line is drawn on the graph. As a check the TE area was plotted against $1/T$ (Curie Law) and of course should go to zero as $1/T$ goes to zero. The deviation from the Curie law is then a measure of overall error. In our case there was not a wide range of temperatures but the results from this analysis were in good agreement with the previous analysis. Any significant error from the enhanced proton signal comes from line shape distortion due to large signals. In our case the signal size was modest (modulation at 80% polarization was $< 10\%$) and leads to an error of $< 1\%$ from a simulation study [14].

The total relative error on the measurement of the proton polarization was estimated to be 2.5%.

A similar analysis was done for the deuteron, Fig. 18, though there were less measurements. This led to a total relative error on the measured deuteron polarization of 4%.

5.1. Other polarizations

Because spin structure measurements are inclusive, only the scattered lepton is detected, there is no way of telling whether the detected lepton was scattered from a polarized nucleon or from a nucleon in the ^{15}N or from a residual proton in the deuteron target. If the background nucleons are polarized then those scatters will contribute to the measured asymmetry. Therefore the composition and po-

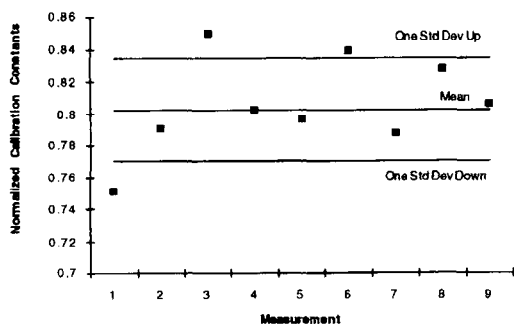


Fig. 18. Deuteron TE constants plotted against measurement number.

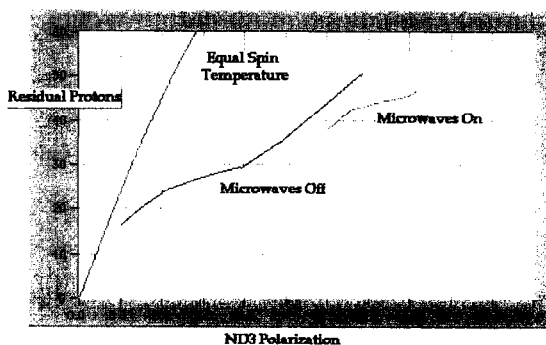


Fig. 19. Measured residual proton polarizations vs. deuteron polarizations with microwaves on and off and EST relation.

larization of the background material must be measured or estimated. In the DNP process the assumption can be made that the polarization of all spin species in the material follow the equal spin temperature hypothesis (EST) i.e. they are all at the same spin temperature so that the individual polarizations depend only on the individual magnetic moments. Most materials in use seem to follow EST but it has been long known that for ammonia the residual protons in ND_3 do not. More recently there have been two measurements [15,16] on the polarization of ^{15}N in $^{15}\text{NH}_3$. In Ref. [15] there is agreement with EST, in Ref. [16] there is not. For these reasons it was decided to measure the residual proton polarization as well as the ^{15}N polarizations in $^{15}\text{NH}_3$ and $^{15}\text{ND}_3$.

5.1.1. Residual protons

In Fig. 19 is plotted the residual proton polarization against deuteron polarization. It is clear that the polarizations are far away from the EST curve and confirm the measurement of Court et al. [15] for $^{14}\text{ND}_3$. At the higher polarizations there is a difference depending on whether the microwaves are on. We have no explanation for this effect.

5.1.2. ^{15}N

Figs. 20 and 21 show the magnitude of the ^{15}N polarizations in $^{15}\text{ND}_3$ plotted against the proton and deuteron

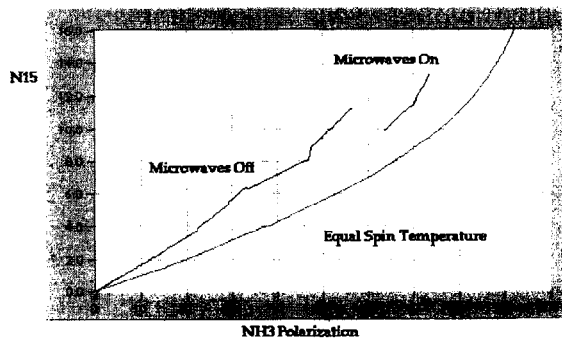


Fig. 20. Measured ^{15}N polarizations vs. proton polarization for microwaves on and off and the EST relation.

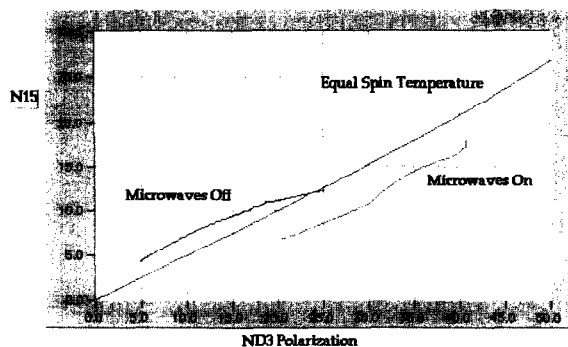


Fig. 21. Measured ^{15}N polarization vs. deuteron polarization for microwaves on and off and the EST relation.

polarizations. Because of its negative magnetic moment the ^{15}N will have negative polarization when the proton and deuteron polarizations are positive. In neither case does the polarization agree with EST and again there is a significant difference between microwaves on and off. The data of van den Brandt et al. [16] from PSI is in good agreement with our data. The exact same material was first measured by Court et al. [15] at Liverpool where they found good agreement with EST. The only known difference between the PSI and Liverpool measurements is that the ammonia was used in a beam at PSI, albeit a weak one, 10^6 to 10^7 pions/s compared to our 5×10^{11} electrons/s. So any beam effects which might cause disagreement with EST would have to saturate very quickly to allow the agreement between our data and PSI's.

6. Conclusions and improvements

We have built and operated a polarized target in a beam of 5×10^{11} electrons/s while maintaining substantial polarizations. To our knowledge this is the highest beam intensity in which a polarized target has run in a routine manner.

^{15}N ammonia has been shown to have the same polarization and radiation damage properties as ^{14}N ammonia. We have confirmed the observations of Crabb et al. [9]

regarding proton polarizations and are in agreement with the Bonn group [10] as to the necessity of in-situ irradiation to gain in deuteron polarization. In our case (5 T/1 K) the gain is more than a factor of 3 compared to a factor of 2 with the Bonn target (2.5–3.5 T/0.3 K).

There are some improvements to be made in operational and instrumental efficiency; in annealing for example. However the biggest gain will come from increasing the microwave power coupled into the NH_3 target. This perhaps could be done by feeding the microwaves directly to each target rather than using a horn to broadcast to both. Another place for improvement is in the NMR control system where it would be advantageous to measure the ^{15}N polarization simultaneously with the proton or deuteron.

We will investigate these and other ideas in the next year before our next experiment comes on line.

References

- [1] B. Adeva et al., Phys. Lett. B 302 (1993) 553.
- [2] B. Adeva et al., Phys. Lett. B 329 (1994) 399.
- [3] P.L. Anthony et al., Phys. Rev. Lett. 71 (1993) 959.
- [4] K. Abe et al., Phys. Rev. Lett., to be published.
- [5] G. Court et al., Nucl. Instr. and Meth. A 324 (1993) 433.
- [6] B. Adeva et al., Nucl. Instr. and Meth. A 349 (1994) 334.
- [7] D. Crabb et al., Proc. 10th Int. Symp. on High Energy Spin Physics, eds. T. Hasegawa, N. Horikawa, A. Masaike and S. Sawada, Nagoya (1992) p. 375.
- [8] R. Dostert et al., Proc. 4th Int. Workshop on Polarized Target Materials and Techniques, ed. W. Meyer, Bonn (1984) p. 33.
- [9] D.G. Crabb, Proc. 9th Int. Symp. on High Energy Spin Physics, Vol. 2, W. Meyer, E. Steffens and W. Thiel, Bonn (1990) p. 289.
- [10] B. Boden et al., Particles and Fields 49 (1991) 175.
- [11] M.L. Seely et al., Nucl. Instr. and Meth. 201 (1982) 303.
- [12] T. Niinikoski, in Ref. [7], 249.
- [13] M. Seely et al., Proc. 5th Int. Symp. on High Energy Spin Physics, ed. G. Bunce, Brookhaven National Lab. (1982) p. 526.
- [14] Y. Semertzidis and T. Niinikoski, SMC Report SMC/94/8 (1994).
- [15] G. R. Court et al., in Ref. [8], 53.
- [16] B. van den Brandt et al., in Ref. [9], 307.



ELSEVIER

Investigations in high temperature irradiated $^{6,7}\text{LiH}$ and ^6LiD , its dynamic nuclear polarization and radiation resistance

St. Goertz ^{*}, Ch. Bradtke, H. Dutz, R. Gehring, W. Meyer, M. Plückthun, G. Reicherz, K. Runkel, A. Thomas

Universität Bonn, Physikalisches Institut, Nussallee 12, 53115 Bonn, Germany

Abstract

Samples of ^7LiH , ^6LiD , ^6LiH have been irradiated at the Bonn 20 MeV electron preaccelerator under various temperatures and with different radiation doses. The most important paramagnetic defect, the so-called F-center, created during these irradiations has been studied in a conventional EPR spectrometer at liquid nitrogen temperature. Also several samples have been dynamically polarized in both a ^4He evaporation cryostat (1 K) and in a $^3\text{He}/^4\text{He}$ dilution refrigerator (200 mK) at a magnetic field of 2.5 and 5 T. Finally some selected samples have been exposed to an intense (up to 70 nA) and high energy (1.2 GeV) electron beam at the Bonn Electron Stretcher and Accelerator ELSA.

1. Introduction

The first successful Dynamic Nuclear Polarization (DNP) in lithium hydride ^7LiH has already been observed in 1978 with maximum polarizations of 95% (H) and 80% (^7Li) [1]. In 1980 a deuteron polarization of 71% could be obtained in ^6LiD , dynamically polarized in a $^3\text{He}/^4\text{He}$ dilution refrigerator at about 200 mK in a magnetic field of 6.5 T [2]. This result was the highest deuteron polarization ever reached in a solid state material. Initially investigated as substances to study nuclear ordering processes, these very high polarizations as well as the high deuteron content in ^6LiD made these materials a potential polarized solid state target material of great interest [2]. The paramagnetic impurities, necessary for the dynamic nuclear polarization process, have been produced by irradiation of small chips of these materials with 2 to 3 MeV electrons. To avoid recombinations of the created defects, the samples have been cooled by mounting them above a liquid argon surface [3].

For the use as a polarized target a preparation method for larger amounts of the material was needed. As has been shown [4], samples irradiated under liquid argon (87 K) could not be polarized to more than a few percent. To provide a reasonable cooling power during the intense preirradiation, a special argon gas cryostat has been built [5]. Samples of some cm^3 , irradiated at temperatures between 180 K and 190 K, showed again very high polariza-

tion values, but with rather long polarization build-up times. For a summary of the polarization results see [6]. The intention of the present work was threefold:

- 1) Finding a physically satisfactory explanation of the dependence of the polarization behaviour on the preirradiation conditions (especially the temperature).
- 2) On the basis of this knowledge shortening of the long polarization build-up times.
- 3) Investigations in the polarization behaviour of the materials under an intense particle beam in order to test ^6LiD as a possible polarized deuteron material in high current scattering experiments.

2. The irradiation cryostat

An irradiation cryostat providing a continuous temperature adjustment has been built in Bonn. This allows systematic investigations in the polarizability of the lithium hydrides in dependence on the preirradiation temperature [7]. With this apparatus 10 cm^3 of these materials, broken in small crystalline pieces (2–4 mm length of side), can be irradiated at an arbitrary temperature between 120 K and 200 K.

The cryostat consists of a closed ^4He gas circuit surrounded by an isolation vacuum (see Fig. 1). The helium gas, used as the sample coolant, is pumped counter-clockwise through a liquid nitrogen heat exchanger by a special high speed turbine which is capable to operate at environment temperatures down to 150 K. The gas is cooled down roughly to the desired temperature which can be varied by means of the filling height in the heat exchanger. Then the

^{*} Corresponding author.

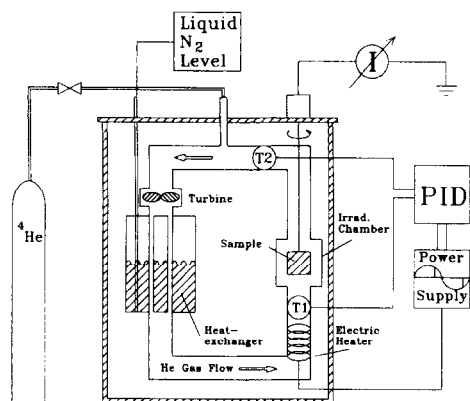
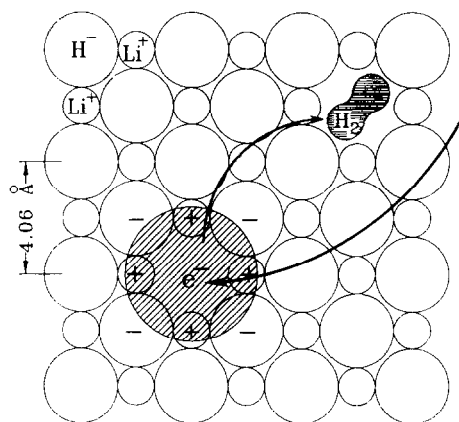


Fig. 1. Block diagram of the irradiation cryostat.

Fig. 2. Mechanism of F-center production in ${}^7\text{LiH}$.

gas stream enters an additional electric heater in order to adjust exactly the operating temperature. Finally the gas passes the irradiation chamber. There the sample contained in an aluminium net is irradiated by the intense ($\bar{I} = 15 \mu\text{A}$) 20 MeV electron beam from the linac. T1 and T2 indicate the positions of two PT-100 temperature resistors monitoring the gas temperature in front of and behind the irradiation chamber. A proportional integral differential (PID) controller drives the power supply of the heater in order to keep the average temperature $(T1 + T2)/2$ constant. With this steering the irradiation temperature can be controlled within 0.1 K, independent of the actual heat load of the electron beam or other influences. The sample container itself is fixed at the end of a slowly rotating axis in order to irradiate the sample homogeneously. The secondary emitted electrons which are ejected by the electron beam from the aluminum walls of the sample container are used as a monitor for the accumulated radiation dose.

For irradiations at 90 K the liquid argon cryostat which has been constructed for the irradiation of solid ammonia [8] is used.

3. Sample preparation

At room temperature the lithium hydrides are in their solid state phase (melting point $\approx 680^\circ\text{C}$), which makes them easy to handle. Crystals of ${}^7\text{LiH}$, ${}^6\text{LiD}$ and ${}^6\text{LiH}$ have been broken under an inert atmosphere into monocrystalline pieces of 2 to 4 mm length of side and

stored in darkness to avoid the creation of unwanted paramagnetic impurities caused by the natural UV light. 10 cm^3 of each sample prepared in this way were loaded into the irradiation cryostat and exposed to the electron beam. After the irradiation the samples have been stored under liquid nitrogen to prevent the paramagnetic centers from recombination.

The Bonn electron preaccelerator is a pulsed linac with 20 MeV final energy, a maximum beam current $I_{\text{puls}} \approx 300 \text{ mA}$ and 50 Hz repetition rate. Thus the average beam intensity is about $15 \mu\text{A}$. With these parameters the heat deposition in the sample, caused by ionization and excitation, is of the order of 10 to 15 W. The cooling power of the irradiation cryostat is between 20 and 25 W/K, depending on the actual operation temperature. Consequently the irradiation temperature in the sample is defined within 0.5 K.

To produce the required density of the paramagnetic impurities of the order of some 10^{19} spins per cm^3 , the samples have to be irradiated with about $10^{17} \text{ e}^-/\text{cm}^2$. This takes an irradiation time of some hours. Table 1 summarizes the performed irradiations.

4. The structure of the F-center

The lattice structure of the lithium hydrides is face-centered cubic. The most important paramagnetic lattice defect is the so called F-center, already detected in 1960 in these materials by Pretzel et al. [9].

Table 1
Samples irradiated at 90 to 200 K with different radiation doses

T_{irrad} [K]	90	120	140	160	180	190	200
${}^7\text{LiH} [\times 10^{17} \text{ e}^-/\text{cm}^2]$	1	1	1	1	1/2/4	1	1
${}^6\text{LiD} [\times 10^{17} \text{ e}^-/\text{cm}^2]$	–	–	–	–	1/4	–	–
${}^6\text{LiH} [\times 10^{17} \text{ e}^-/\text{cm}^2]$	–	–	–	–	1	–	–

Fig. 2 shows a cut through a ${}^7\text{LiH}$ crystal parallel to the (100) and (010) axes. The picture shown here is chosen only for the simplicity of the arguments. As already mentioned by Mulliken in 1936, the lattice is a mixture of an ionic and a homopolar binding rather than a pure ionic state [10].

The electronic structure of the F-center consists of a vacancy in the anion sublattice in combination with a trapped electron. This defect can be regarded as a quasi hydrogen atom with an unpaired electron. The anion, freed from its original lattice site, can be bound e.g. by another H atom to form an interstitial H_2 molecule. Although there are generally several ways of creating these anion vacancies, e.g. additional coloration, exposition to UV-light or X-rays, the most effective production method is the bombardment of the crystal with “high energy” particles. In the case of the lithium hydrides an incoming particle ionizes an H atom. It becomes unstable and will be ejected from its lattice site. The produced vacancy has an effective positive charge and can trap a free electron. It depends on the actual temperature during the ionization process, whether the ionized atom is able to leave its lattice site or not [11].

At low temperatures the ejection probability of the ionized atom is comparatively low so that an electron is trapped before any lattice defect can be produced. With increasing temperatures the ion is able to move away from its lattice site, which leads to an anion vacancy and possibly to an F-center. Evidence for a critical temperature of the F-center formation in ${}^7\text{LiH}$ is given later in this report. If the energy of the ionizing radiation is high enough, this vacancy can also be produced by a direct knock out of the anion.

5. The F-center paramagnetic resonance

The paramagnetic resonances of all samples have been investigated in a conventional EPR spectrometer operating at 9 GHz with a magnetic field of 3 to 3.5 kG. The measurements have been carried out under liquid nitrogen temperature in order to avoid destruction of the paramagnetic centers caused by thermal annealing. Fig. 3 shows a typical F-center resonance structure in ${}^7\text{LiH}$ centered at a g -factor of 2.00. This sample has been irradiated at 180 K with $1 \times 10^{17} \text{ e}^-/\text{cm}^2$. The structure in the left tail of the F-center resonance line has a g -factor of about 2.05 and is caused most probably by some impurities in the material. This interpretation is supported by the intensity dependence of this resonance on the original crystal color before the irradiation. The integrated curve shows a Gaussian lineshape with a FWHM of 56 G. The width of the resonance line is caused mainly by hyperfine interaction of the unpaired electron with its surrounding nuclei. In the case of ${}^7\text{LiH}$ the nearest six ${}^7\text{Li}$ nuclei surrounding the electron play the most important part although the influ-

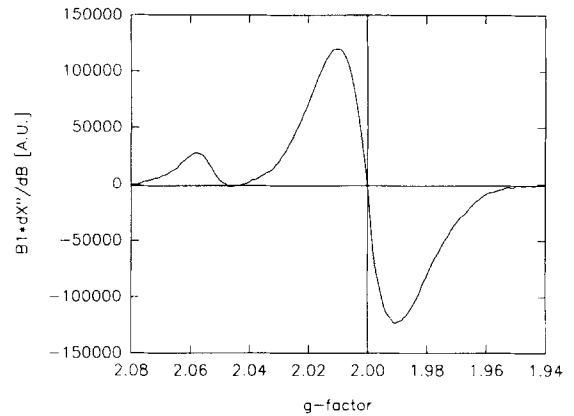


Fig. 3. Paramagnetic resonance of irradiated ${}^7\text{LiH}$.

ence of the nuclei in the second shell around the F-center is not negligible. The rms width of the resonance line is then given by

$$\langle (\Delta H)^2 \rangle = \frac{64\pi^2}{27} \sum \mu_i^2 \frac{I_i + 1}{I_i} |\psi(i)|^4, \quad (1)$$

μ_i and I_i being the magnetic moment and the spin quantum number of the neighbour nucleus i . $|\psi(i)|$ is the probability of the electron staying at the position of this nucleus. For a detailed discussion of EPR lines broadened by hyperfine interaction see Ref. [12]. In contrast to LiH in some alkali halides like CsCl, NaF or LiF these additional hyperfine transitions can be resolved. This is also the case for the alkali hydride NaH.

The EPR resonances of samples of ${}^6\text{LiD}$ and ${}^6\text{LiH}$, prepared under the same conditions, have also been measured. Fig. 4 shows the corresponding resonance structure in ${}^6\text{LiD}$. The “impurity resonance” at the lower magnetic field side is not present in these samples. Here the main structure consists of two superimposed resonances, a broader one belonging to the F-center and a more narrow one caused by an EPR resonance due to free conduction

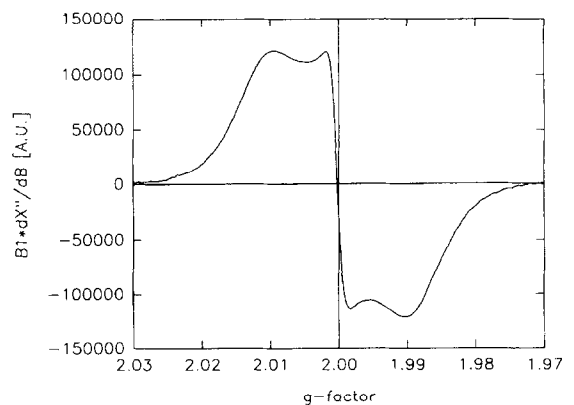


Fig. 4. Paramagnetic resonance of irradiated ${}^6\text{LiD}$.

electrons in small clusters of lithium metal. Such “cluster centers” have also been observed in neutron irradiated LiF [13]. In the case of ${}^6\text{LiD}$, the FWHM of the F-center resonance is with 30 G almost a factor of 2 smaller than in ${}^7\text{LiH}$. This can be understood by taking into account the smaller magnetic moments of the surrounding nuclei in the deuterated material. The F-center resonance of ${}^6\text{LiH}$ is similar to that in ${}^6\text{LiD}$ with the exception of a 10% wider EPR line due to the presence of hydrogen instead of deuterium.

6. Thermal mixing

The so-called Equal Spin Temperature (EST) theory is the most successful picture describing the mechanism of DNP in a macroscopic, that means thermodynamic way. A comprehensive overview of polarization and relaxation mechanisms can be found in Ref. [14]. Furthermore the EST theory provides the possibility to calculate the polarizations of all nuclei in the same material with nonvanishing spin by the Brillouin function B_I :

$$P = B_I \left(\frac{\hbar \omega_I}{kT_{SS}} \right). \quad (2)$$

This function depends only on the spin I and the Larmor frequency ω_I of the corresponding nucleus and on the common spin–spin temperature T_{SS} which is a measure of the dipolar energy of the unpaired electrons. Under the influence of microwaves having a frequency slightly deviating from the electron larmor frequency ω_e the dipolar temperature can be much smaller than the actual lattice temperature T_L . This leads to nuclear polarizations much higher than in the thermal equilibrium case, determined by Eq. (2) with T_L instead of T_{SS} . To test the validity of this picture, also known as thermal mixing, one has to measure the dynamic polarizations of different nuclei in the same material simultaneously. A second check can be made by measuring the thermal coupling time of these nuclei after the destruction of one of the nuclear polarizations. This can be done by applying a strong resonant rf field to the sample. The latter test exhibits the idea of a common thermodynamic equilibrium among the different spins very clearly because no driving microwave field is used.

Both measurements have been carried out with a ${}^6\text{LiD}$ sample prepared under our standard conditions ($T_B = 180$ K, $Q = 1 \times 10^{17} \text{ e}^-/\text{cm}^2$) and polarized in a ${}^4\text{He}$ evaporation cryostat at about 1 K with a magnetic field of 2.5 T. We monitored at the same time both the deuteron polarization and the polarization of the unsubstituted ${}^7\text{Li}$ nuclei ($\approx 15\%$) in the same sample. The upper part of Fig. 5 shows both polarizations plotted vs. time. In stage I the deuteron polarization grew until 11%, whereas in the same time the ${}^7\text{Li}$ polarization reached 37%. During the polarization build-up the ratio of both polarizations correspond

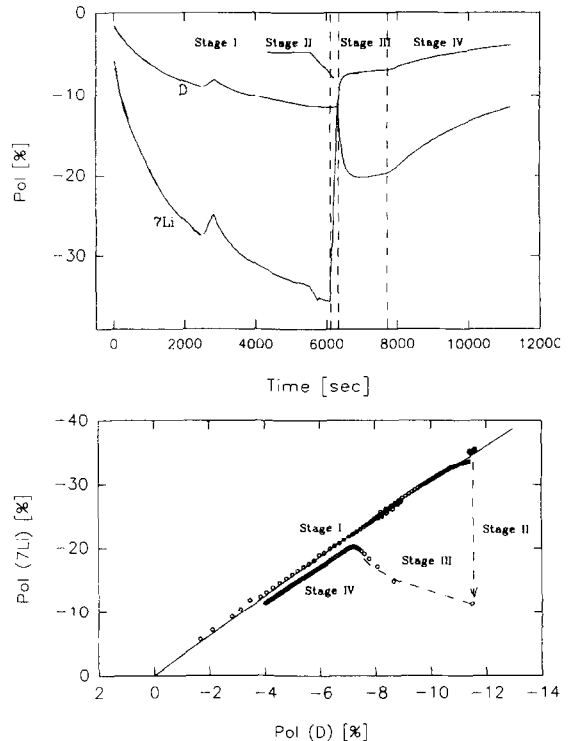


Fig. 5. Thermal mixing of D and ${}^7\text{Li}$ in ${}^6\text{LiD}$.

to the curve predicted by the EST theory (see the almost straight line in the lower part of Fig. 5.) Then (stage II) a strong rf burst at the larmor frequency of the ${}^7\text{Li}$ nucleus has been applied to the sample. This leads to a reduction of the ${}^7\text{Li}$ polarization to about 10%, whereas the deuteron polarization remained almost unchanged. Immediately after that, both nuclei start to establish their equilibrium polarization value again with a time constant of about 1 min (stage III). However, the original EST polarization ratio (stage I) could not be reached completely. Not even in stage IV, where at a slightly higher temperature both polarizations commonly decreased to their thermal equilibrium values. With the exception of the latter effect, suggesting a second process in the material with a much larger time constant, the result of this experiment is a good proof of the validity of the EST theory in this material.

7. Polarization results

7.1. Influence of the additional low temperature irradiation

In order to test the polarization resistance of the polarized lithium hydrides against damage caused by the particle beam of a scattering experiment, ${}^7\text{LiH}$ has been polarized at 2.5 T and about 1 K. The ${}^4\text{He}$ -cryostat is able to accept the heat load caused by the intense electron beam

(1.2 GeV, up to 70 nA). Before any additional irradiation 11.5% proton polarization was reached with a build-up time of 50 min. Already after 10^{14} e⁻/cm² of additional low temperature irradiation the polarization build-up time was decreased to 8 min, which is a reduction by a factor of 6. At the same time the maximum polarization was increased from 11.5% to 14.5%. The experiment was stopped at an accumulated dose of 5×10^{15} e⁻/cm². Up to this dose the build-up time remained constant at about 8 min and no reduction in the maximum polarization could be observed. With this result ⁷LiH even surpasses the excellent properties of NH₃. This standard material for experiments with intense particle beams has however to be thermally annealed after each 10^{15} e⁻/cm² [15]. Furthermore additional low temperature irradiation could be a helpful tool in order to reduce the long polarization build-up times which make the lithium hydrides unfit for the use as a polarized target material in asymmetry experiments. Here a fast and frequent polarization reversal is demanded to reduce the systematic errors.

The experiment described above was also performed with ⁶LiD. In addition the sample container was divided into two parts, each containing about 1 cm³ of material. Two separated NMR coils allowed the simultaneous measurements of the deuteron polarization of such material located directly in the beam or 1 cm away from it in the halo of the beam. Therefore changes in the maximum polarization as well as in the polarization build-up time could be measured in narrow steps and at very low radiation doses. Fig. 6 shows in the upper part the maximum deuteron polarizations and in the lower part the nuclear

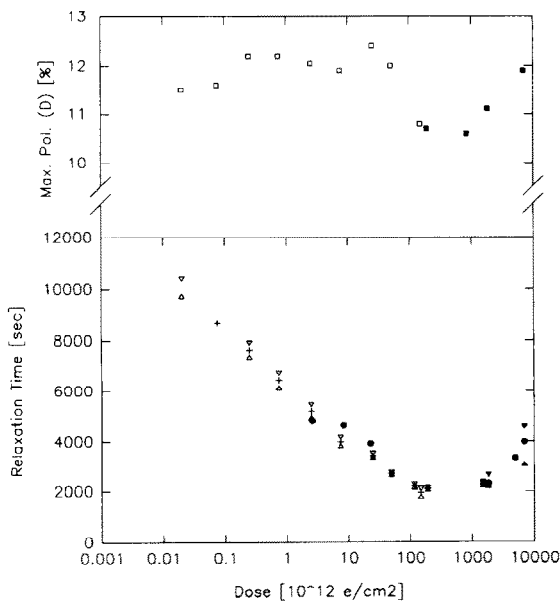


Fig. 6. Polarizability of ⁶LiD during additional low temperature irradiation.

Table 2

Summary of the polarization results under various conditions

Material	Temperature	Magnetic field	Maximum Polarization	Build-up time
⁷ LiH	1.0 K	2.5 T	11.5/14.5% ^a	50/8 min ^a
⁶ LiD	1.0 K	2.5 T	12.5%	50/23 min ^b
	1.0 K	5.0 T	22%	4.2/2.8 h ^c
	200 mK	2.5 T	> 30%	1.6 h ^a
	200 mK	5.0 T	> 50% ^d	4.4 h
⁶ LiH	1.3 K	2.5 T	16%	20 min
	200 mK	2.5 T	> 40% ^a	1.4 h

^a After additional 10^{15} e⁻/cm² at 1 K.

^b After 5 min at room temperature.

^c Cryostat in single shot mode, full microwave power.

^d Preirradiation dose 4×10^{17} e⁻/cm².

relaxation times plotted vs. the total radiation dose. The full points correspond to the sample directly hit by the beam, whereas the open points were obtained from the sample somewhat beside the beam spot. The results of both parts are scaled by means of a comparison of the dose rates with equal relaxation times. In this experiment the relaxation times were monitored instead of the polarization build-up times because the latter depend on the actual microwave parameters like power or frequency. The relaxation curves are not exactly exponential. In particular the initial relaxation time at high polarizations is slightly shorter than the final one at lower polarization values. Both time constants as well as the average values are indicated by the triangles and the crosses, respectively. As in the case of the hydrogen in ⁷LiH the deuteron polarization growth in ⁶LiD also became faster by a factor of 5 to 6 after about 2×10^{14} e⁻/cm². The maximum polarization, however, remained constant with 12% during the whole run with the exception of the region between 2×10^{14} and 1×10^{15} e⁻/cm². The run was stopped at a total dose of 10^{16} e⁻/cm². The range from 2×10^{14} to 1×10^{15} e⁻/cm² corresponds to the minimum observed in the relaxation times. But this local decrease in the polarization values is only supported by three data points so that possibly the effect is only an artificial one.

7.2. Polarization results under varied conditions

Table 2 summarizes the results obtained with the lithium hydrides under various conditions. With one exception (^d) all samples have been irradiated under our standard conditions (see above).

“Build-up time” means the time needed to reach 63% of the maximum polarization. In the second line of Table 2 two build-up times are given for the deuteron polarization in ⁶LiD. The second and shorter time constant was obtained after exposing the sample to room temperature for 5 min. This warming up procedure was done under dry He

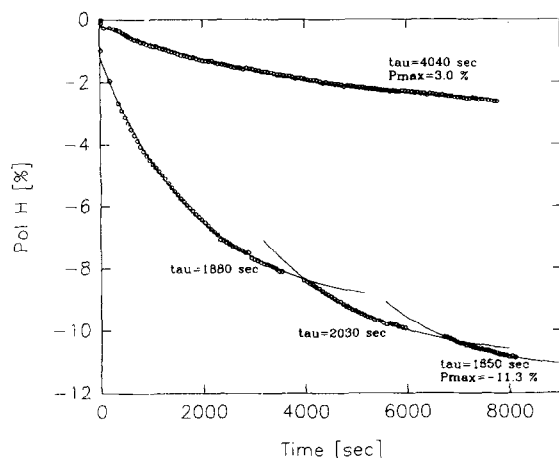


Fig. 7. Influence of tempering on the polarizability.

gas in order to avoid the formation of lithium hydroxyl on the sample surface. We supposed that the thermal annealing leads to some changes in the physical properties of the paramagnetic centers, making them more useful for the DNP process¹.

We also performed this experiment with a sample of ⁷LiH under the same conditions. The sample was originally irradiated with the standard dose but at a temperature of 160 K being too low for a reasonable proton polarization. Fig. 7 shows the build-up curves of the proton polarization. The upper curve was obtained with the originally prepared sample indicating only a poor maximum polarization of about 3% with a build-up time of 67 min. The lower curve was obtained with the same sample stored for 5 min at room temperature. The build-up time was reduced again by a factor of 2 with a maximum polarization almost the same as in the case of a sample preirradiated at our standard temperature (180 K, see Table 2). This effect is a new approach in the understanding of the irradiation temperature dependence of the polarizability and may become a further method to minimize the polarization build-up time.

8. Sample preparation and polarizability, evidence from EPR

As already mentioned, the temperature during preirradiation is a crucial parameter for the polarizability of the samples. The optimum temperature has been found empirically to be between 180 K and 190 K [6]. In this section it

is tried to give some simple arguments for the existence of such an optimum irradiation temperature.

In a first step the polarizability at 1 K and 2.5 T was measured for several samples of ⁷LiH preirradiated between 160 K and 200 K with our standard dose of 1×10^{17} e⁻/cm². The results of this rough survey are shown in Fig. 8a, where the open points correspond to proton polarization values reached with samples irradiated at the indicated temperatures without any additional treatment. The full points show the polarization values obtained with the same samples but after an additional exposition to room temperature. Figs. 8b and c show the corresponding maximum intensities of the differentiated EPR absorption line and the magnetic field difference between these maximum values and the line center, respectively (for an illustration see also Fig. 3). The latter quantity is the line width in the case of a pure Gaussian resonance. The data (open and full points) are obtained from samples with and without additional warming-up. At first sight the polarization values seem more or less to reproduce the shape of the EPR intensity curve. This could be easily understood if the number of the created F-centers was the main parameter for the polarizability of the samples. But a comparison of the sample preirradiated at 180 K with the one preirradiated at 160 K shows a factor of 4 in the maximum

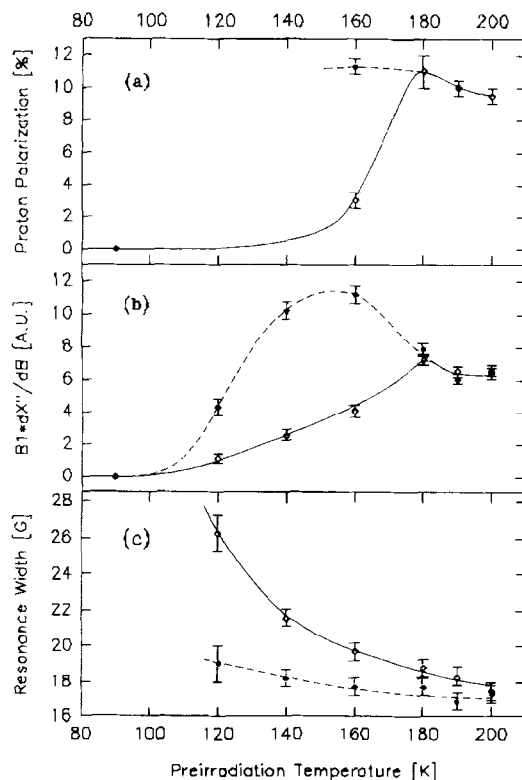


Fig. 8. Proton polarizations (a), EPR absorption intensities (b) and EPR line widths (c) as functions of the preirradiation temperature. The curves are drawn only to guide the eye.

¹ In Section 8 a rough picture of the relation between the temperature during irradiation and the polarizability will be outlined.

polarizations but only a factor of 2 in the EPR signal height. This, together with the warming-up experiment (see Section 7.2), indicates that not only the F-center density is responsible for the polarizability but also some changes in the atomic structure of the color-centers. These changes occur either at higher preirradiation temperatures or during the warming-up procedure after the preirradiation. This supposition is also supported by changes in the EPR width. Firstly, the EPR width decreases with increasing preirradiation temperature and, secondly, the resonance line becomes narrower when a sample preirradiated at temperatures ≤ 160 K is warmed up in the way described above (see Fig. 8c). Fig. 9 shows the EPR line width of the “160 K-sample” in dependence on the applied microwave field B_1 in its original state (open circles) and after the heat treatment (full circles). The line width in dependence on the applied microwave field decreases strongly at lower power levels, shows a minimum in the intermediate region and slightly increases at higher power levels. In contrast to this behaviour the width of a pure inhomogeneously broadened line should be independent of the degree of saturation [22]. Therefore the observed power dependence of the line width can only be explained under the assumption that the electron paramagnetic resonance structure in ^7LiH centered at $g = 2.00$ with a Gaussian width of about 20 G is a superposition of at least three broader components ($\sigma \geq 15$ G) and one narrower component ($\sigma \approx 5$ G). The latter is caused by the conduction electrons of metallic lithium. In order to extract the EPR line of the particular resonance responsible for the DNP mechanism the derivatives of the EPR lines of the original and the warmed sample preirradiated at 160 K were subtracted from each other. Because of the possible influence of the impurity center on the lower field side only the negative part of the differentiated

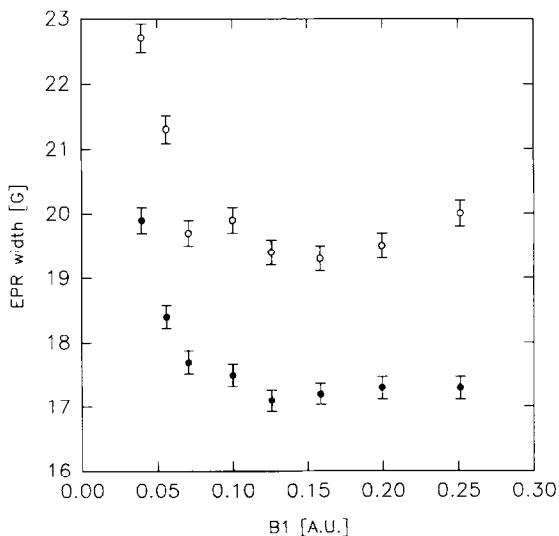


Fig. 9. EPR Line widths ($B(I = I_{\max}) - B_0$) vs. microwave field B_1 for ^7LiH irradiated at 160 K.

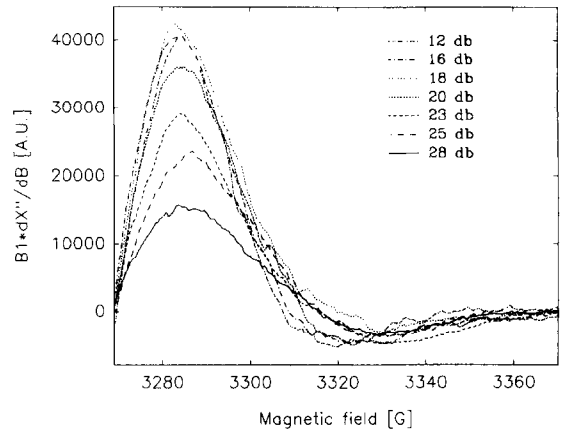


Fig. 10. Difference of the negative part of the differentiated EPR resonance line between the original irradiated sample and the additional warmed sample for different microwave attenuations vs. magnetic field.

resonance line was taken into account. This difference is shown in Fig. 10 for several microwave power attenuations. Two important features can be seen from this figure. Firstly, the position of the maximum is independent of the microwave field within the experimental errors. This corresponds to a power independent width of the integrated resonance line. Secondly, the resonance saturates at some intermediate microwave power level corresponding to the minimum in the line width in Fig. 9. Both facts indicate the presence of a single paramagnetic structure with a line width of about 15 G being much narrower than the composite one of the original sample (≈ 20 G). There is a good reason to believe that in addition to the isolated F-centers also some kind of F-cluster centers are formed. This can happen either if the temperature is high enough during the irradiation procedure to allow the F-centers to migrate in the crystal and therefore to coagulate or if the crystal is thermally annealed after the irradiation. This phenomenon has also been observed by many authors in the alkali halides KCl and LiF colored either by additional coloration or by ionizing radiation [11,16–21]. Therefore the following picture of the dependence of the DNP process on the preirradiation temperature can be outlined:

The process of DNP requires paramagnetic centers with a sufficient coupling strength to the phonons of the crystalline lattice as well as to the nuclear magnetic moments in order to satisfy the assumptions of the EST theory. Separate F-centers possess only a very weak coupling to the lattice. This is caused by the large energetic distance of the electronic ground state to the first excited state with nonvanishing angular momentum. This leads to very long longitudinal and transversal relaxation times so that the DNP process is slowed down. The DNP mechanism in the irradiated lithium hydrides is enabled by the existence of loosely bound clusters of F-centers with strongly reduced relaxation times caused by the so-called exchange narrow-

ing (see e.g. Refs. [16,17]). The physical origin of the preirradiation temperature dependence of the DNP process is the temperature dependent efficiency of the F-cluster center production during irradiation. At preirradiation temperatures of

≤ 90 K: No F-centers are produced due to the low probability that the ionized anion leaves its lattice site before an electronic recombination process takes place (see also Ref. [11]).

≈ 120 K: The crystal temperature is high enough to allow some ionized anions to escape from their lattice site and to migrate far enough so that an electron can be trapped by the vacancy forming a separate F-center. The EPR shows a relatively weak and broad resonance ($\sigma \approx 26$ G). Warming-up of the sample causes a narrowing to 19 G and a growth of the resonance line by a factor of 4 due to the clustered color centers which saturate less readily and possibly due to an additional conversion of some diamagnetic F-aggregate centers (e.g. F²-centers) into F-centers.

≈ 140 K: The F-center production efficiency increases with increasing irradiation temperature and the resonance becomes smaller, a sign for the beginning mobility of the F-center itself. The resonance of the F-cluster centers is narrowed to 22 G caused by the starting exchange interaction. The warming-up procedure leads again to a further narrowing (18 G) and to a growth of the resonance.

≈ 160 K: The F-center production efficiency and their mobility further increase leading to a higher gain of cluster centers. DNP becomes possible but can be improved by means of additional thermal annealing. This raises the number and possibly the size of the F-cluster centers which corresponds again to an increase and a narrowing of the resonance ($\sigma \approx 20$ G \rightarrow $\sigma \approx 18$ G).

≈ 180 K: F-center production efficiency and agglomeration probability during irradiation becomes optimum for the DNP process. The EPR resonance reaches its maximum intensity with a line width of about 18 G. Thermal annealing has only a minor influence on the EPR properties.

≥ 190 K: Further increasing temperatures lead to stronger clustering and possibly to recombinations of the F-centers with some interstitial atoms and therefore to a healing up of the paramagnetic defects. The DNP becomes still faster but the maximum polarization decreases. A warming-up of the sample causes no change in the EPR line width and height, but the DNP process is slightly slowed down.

9. Summary

The idea of the EST as a valid picture of the DNP in the lithium hydrides could be verified by means of observation of the thermal mixing process between the deuteron and the ⁷Li magnetic moment in ⁶LiD.

With more than 50% and 22% very high deuteron polarizations could be obtained in ⁶LiD at a magnetic field of 5 T in a ³He/⁴He-dilution refrigerator ($T \approx 200$ mK) and in a ⁴He-evaporation cryostat ($T \approx 1$ K), respectively.

No significant loss in the polarizability was observed during the irradiation of the lithium hydrides under the conditions of an electron scattering experiment up to an accumulated radiation dose of 10^{16} e/cm², a result even better than the radiation resistance of ammonia. In addition, subsequent low temperature irradiation shortens the polarization build-up time by a factor 5 to 6 (all lithium compounds) and increases the maximum polarization by about 25% (⁷LiH).

With the extremely helpful tool of EPR studies some new aspects could be demonstrated in order to explain the preparation requirements for an efficient DNP process in the lithium hydrides. Adequate paramagnetic centers can be created in the material by means of irradiation with "high energy" electrons at temperatures allowing the formed point defects to coagulate to larger paramagnetic structures possessing a sufficiently strong coupling of their magnetic moment to the lattice phonons. A rough scheme is outlined showing the physical processes which take place during the preirradiation at different temperatures.

However, some uncertainties have remained in the interpretation of the EPR spectra. They were mainly caused by the presence of several resonance lines superimposing to an "F like"-center. Thus the common saturation curves which were used to determine the electronic relaxation times could not be unambiguously analysed in contrast to samples colored by the additional coloration method [16]. Moreover the magnetic field used for the EPR studies is about a factor of 10 lower than the one used for the DNP experiments. Thus during DNP the energy of each spin flip transferred to the lattice is higher and the corresponding phonon wavelength is lower by this factor. Therefore the results of the EPR measurements need not hold exactly under DNP conditions. Nevertheless the main idea that DNP is made possible by F-cluster centers seems to be an encouraging way to understand the preparation formula given some years ago [6].

For further improvement of the polarization characteristics of the lithium hydrides (maximum polarization and polarization build-up time) other coloration methods should be tested. Their gain of proper paramagnetic impurities should be controlled with "in situ" EPR measurements under the DNP conditions. Secondly, more detailed investigations in the effect of polarization enhancement and shortening of the build-up times due to additional low temperature irradiation should be undertaken. Here the main idea consists in the introduction of crystalline displacements caused by the particle beam which should be stable at temperatures of 1 K and below. Possibly these defects supply the necessary interaction between the electron magnetic moment and the lattice.

References

- [1] Y. Roinel, V. Bouffard and P. Roubeau, *J. Phys. (Paris)* 39 (1978) 1097.
- [2] A. Abragam, V. Bouffard, Y. Roinel and P. Roubeau, *J. Phys. Lett.* 41 (1980) 309.
- [3] V. Bouffard, D. Pasquette and Y. Roinel, *Rev. Phys. Appl.* 13 (1978) 304.
- [4] J. Ball, P. Chaumette, J. Deregel, G. Durand, J. Fabre and J. Movchet, *Proc. 4th Int. Workshop on Polarized Target Materials and Techniques*, ed. W. Meyer, Bad Honnef, Germany (1984) p. 81.
- [5] P. Chaumette et al., *Int. Workshop on Polarized Sources and Targets*, Montana, Switzerland (1986).
- [6] P. Chaumette, J. Deréglé, G. Durand, J. Fabre and L. van Rossum, *Proc. 8th Int. Symposium on High Energy Spin Physics*, Minneapolis, 1988 (*Am. Inst of Phys.*) Conf. Proc. No. 187 Vol. 2 p. 1275.
- [7] S. Goertz, Ph.D. thesis, to be published.
- [8] S. Brown, G. Court, G. Hayes, W. Meyer, J.M. Rieubland, A. Rijllart, E. Schilling and D. Williams, *Proc. 4th Int. Workshop on Polarized Target Materials and Techniques*, ed. W. Meyer, Bad Honnef, Germany (1984) p. 81. p. 66.
- [9] W. Burton Lewis and F.E. Pretzel, *J. Phys. Chem. Solids* 19 (1961) 139.
- [10] R.S. Mulliken, *Phys. Rev.* 50 (1936) 1028.
- [11] E. Sonder, *J. Physique Colloque C9* (1973) 32.
- [12] A.F. Kip, C. Kittel, R.A. Levy, and A.M. Portis, *Phys. Rev.* 91 (1953) 1066.
- [13] Y.W. Kim, R. Kaplan and P.J. Bray, *Phys. Rev.* 117 (1960) 740.
- [14] A. Abragam and M. Goldman, *Rep. Prog. Phys.* 41 (1978) 395.
- [15] K.H. Althoff, V. Burkert, U. Harfiel, T. Hewel, G. Knop, M. Leenen, W. Mehnert, W. Meyer, H.D. Schablitzky, E. Schilling, and W. Thiel, *Proc. 4th Int. Workshop on Polarized Target Materials and Techniques*, ed. W. Meyer, Bad Honnef, Germany (1984) p. 81. p. 23.
- [16] M. Schwoerer and H.C. Wolf, *Z. Phys.* 175 (1963) 457.
- [17] R. Kaplan and P.J. Bray, *Phys. Rev.* 129 (1963) 1919.
- [18] M. Misakian and Y.W. Kim, *Phys. Rev.* 137 (1965) A1226.
- [19] S.C. Jain and G.D. Sootha, *Phys. Rev.* 171 (1968) 1075.
- [20] G. Goldberger and F.J. Owens, *Phys. Rev. B* 4 (1971) 3927.
- [21] E. Sonder, *Phys. Rev. B* 5 (1972) 3259.
- [22] A.M. Portis, *Phys. Rev.* 91 (1953) 1071.



ELSEVIER

New investigations of organic compounds for targets with polarized hydrogen nuclei

E.I. Bunyatova

Joint Institute for Nuclear Research, Dubna, Head P.O. Box 79, 101000 Moscow, Russian Federation

Abstract

Pentanol $C_5H_{12}O$, polyethylene $(CH_2)_n$ and their deuterated analogues $C_5D_{12}O$ and $(CD_2)_n$ are proposed as target materials. Particular attention is paid to the production of materials in a glass-like (amorphous) state.

1. Target material based on glass-like solutions of 1-pentanol

1.1. Introduction

1-pentanol is an interesting substance to use in targets with polarized hydrogen nuclei in terms of its better resistance to radiation and relatively high hydrogen content in comparison with ordinary alcohols [1–4].

The first experiment with pentanol was described in Ref. [5] and later experiments in Refs. [3,6–8]. Aqueous solutions were used. The authors of Refs. [5,9] and of later papers pointed out that a small water admixture increased the proton polarization in alcohol solutions. It was also found that the highest values of the proton polarization for ethanol were obtained in a water–ethanol solution of eutectic composition. To understand the role of water, binary alcohol–water solutions were studied by viscosimetric [10] and calorimetric [19] methods. It was stressed that the glass-forming ability of the target material is the main reason for the increase of the polarizability. The nature of the phenomenon is not yet clear; it is probably due to microscopic properties of glasses. Only macroscopic properties of glasses with hydrogen bonds have been partially explained. For example, alcohols have relatively strong hydrogen bonds between molecules even in the liquid state and thus they are capable of glass-forming. A macroscopic explanation of the “eutectic effect” is that the glass-forming ability of solutions increases in the region of the eutectic composition. In this case it is difficult for solution components to be isolated into separate phases. Apart from organic glasses with hydrogen bonds inorganic substances were also used in polarized proton targets [11,12]. In Ref. [11] the relation between glassy state and polarizability of protons in inorganic polar glasses based on amines, boron hydrides and ammonia was proved. Investigations described in the above papers suggest that glass-like solutions should be used as target materials. Noteworthy is that

rapid solidification is one of the best ways to get a glass. In this way a solid is created with the composition of the liquid phase out of which it has been made. However, such a solid is always in a non-equilibrium state and sometimes an insignificant variation in the external conditions is enough to trigger crystallization. Another type of glass is given by substances or solutions where crystallization is avoided by relatively slow cooling ($\sim 5\text{--}8$ K/min) down to their changing to a solid amorphous state.

We began the work on a target material based on 1-pentanol, whose melting point is 194.5 K, and tried to get this very type of glass. The question arose whether water is an obligatory glass-forming admixture to pentanol. Undoubtedly, water benefits from the solution of the paramagnetic admixture. However, there may occur hydrolysis, for example, of $EHBA-Cr^V$. The presence of water also reduces the radiation resistance of the target material. Aqueous solutions of such alcohols as methanol, ethanol, and propanol from typical glasses with hydrogen bonds because they mix with water in any proportion. The mutual solubility of butanol and water is 10%, but the mutual solubility of pentanol and water is very low. Up to now, however, 1-pentanol with a water admixture has been used as a target material [5–8].

1.2. Results and discussion

The goal of the investigation was to create a target material based on 1-pentanol without water, which would change to glass when cooled. A complex compound of pentavalent chromium synthesized in 1,2-propanediol ($PD-Cr^V$) was used as a paramagnetic admixture. The concentration of paramagnetic centres was $2.5 \times 10^{20}/\text{cm}^3$ [13]. The complex content of the solution was 18.5 wt.%. When the $PD-Cr^V$ complex is added to pentanol at room temperature, the solution becomes turbid. However, we managed to avoid turbidity at 223 K and to quickly freeze the

solution in liquid nitrogen. No signs of crystallization were seen. The solid solution was transparent. This solution was investigated by the method of electron paramagnetic resonance (EPR). The EPR spectrum of the PD-Cr^V complex in 1-pentanol is a symmetric singlet with $g = 1.980 \pm 0.001$. The spectrum line width of the solid solution is $\Delta B = 14 \times 10^{-4}$ T. The concentration of paramagnetic centres was $3 \pm 0.3 \times 10^{19}/\text{cm}^3$. For the experiments on dynamic polarization of nuclei (DPN) the solid solution was ground. The size of the particles was $\sim 2 \text{ nm}^3$. The proton polarization obtained in the only experiment with this sample was 44% at a temperature of 0.3 K in a magnetic field of 2.6 T.

Thus, we have managed to get a water-free target material based on the PD-Cr^V solution in pentanol. The frozen material was transparent after rapid cooling, which may well suggest a glass-like state. The target material contains 13 wt.% of hydrogen; its liquid state density is 0.89 g/cm^3 . The corresponding values for pentanol are 13.6 wt.% and 0.81 g/cm^3 . A disadvantage of the material is the difficulty of making frozen bead targets out of it by a regular method. Yet, it can be used in block targets [14,15].

Continuing the work in view of a glass-like pentanol-based target material, we carried out experiments with the 1-pentanol isomers 2-pentanol and 3-pentanol, which do not have a melting point. Amyl alcohols, including 1-pentanol, 2-pentanol and 3-pentanol are poor solvents. We chose 2-pentanol for the first experiments, because it has a higher mutual solubility with water than any other pentanol and forms an amorphous structure when slowly cooled [16]. Following recommendations of Refs. [6–8,10,17] we took the pentavalent chromium complex EHBA-Cr^V as the paramagnetic admixture. However, we failed to make a stable EHBA-Cr^V solution in 2-pentanol with the adequate concentration for the target material [18]. Secondary alcohols are more readily oxidized, so the oxidation probability for 2-pentanol is larger than for 1-pentanol. We did not have information on radiation resistance of pentanol isomers either.

All the aforesaid made us turn back to 1-pentanol as the main target material and look for a way to get its solution with an adequate paramagnetic admixture concentration, which forms an amorphous structure when slowly cooled. It is known that the solubility of a polar substance, the EHBA-Cr^V complex in our case, can be improved by adding a solvent with a high dielectric constant. Water with $\epsilon_{\text{water}} = 80.4$ is often used for this purpose. We replaced it by 1,2-propanediol with $\epsilon_{\text{PD}} = 32$, which is compatible with 1-pentanol. It increased the viscosity and density of the solution, and it turned to glass when fast cooled. Besides, we added another glass-forming admixture 3-pentanol to the solution.

A sample was prepared in the following way. A solution of 1,2-propanediol and 3-pentanol was mixed with the EHBA-Cr^V complex to get 5×10^{19} spins/cm³. The solu-

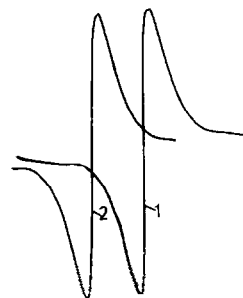


Fig. 1. EPR spectrum of EHBA-Cr^V solutions (concentration $5 \times 10^{19}/\text{cm}^3$ at 295 K) (1) solvent: 1-pentanol (83%), 3-pentanol, 1-propanediol. (2) solvent: 1-pentanol (95%), water (5%).

tion was immediately coloured, the complex was partially dissolved. Then 1-pentanol was added to make up 83 wt.%. The solution was intensely stirred until the complex was completely solved. A sample described in Refs. [6–8] was also prepared for comparison. It was a solution of the EHBA-Cr^V complex in 1-pentanol mixed with 5% of water. Both solutions were examined by the EPR method. Parameters of EPR signals from the two samples were the same (Fig. 1). The samples were also analyzed by the method of differential scanning calorimetry (DSC) (Fig. 2). The heating rate was 8 K/min. The water sample curve showed melting at 185–194 K. The result is in agreement with Ref. [9]. The proposed target material based on the EHBA-Cr^V complex solution in 1-pentanol mixed with 1,2-propanediol and 3-pentanol has no endothermic melting peak. The DSC curve of the solution is typical of a good glass.

In 1992 this material was examined in the polarized targets group at the Paul Scherrer Institute (PSI), Villigen, Switzerland. The target was a block of $18 \times 18 \times 3 \text{ mm}^3$. A proton polarization of more than 73% was achieved in this block at 0.5 K in a magnetic field of 2.5 T [25].

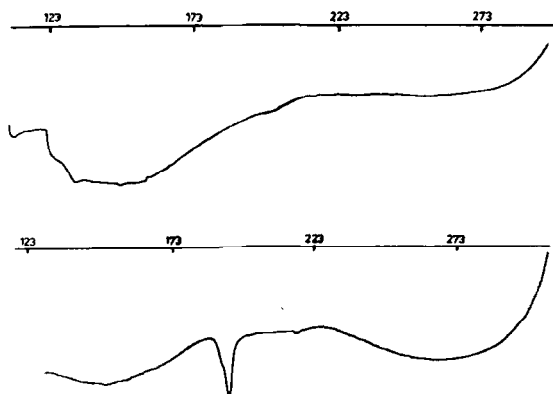


Fig. 2. Differential calorimeter scans of EHBA-Cr^V solutions (conc. $5 \times 10^{19}/\text{cm}^3$). upper part solvent: 1-pentanol (83%), 3-pentanol, 1-propanediol; lower part solvent: 1-pentanol (95%), water (5%).

A target based on 1-pentanol-D₁₂ is of interest from the point of view of creating a polarized deuteron target material with higher radiation resistance. The Russian Research Centre ‘‘Applied Chemistry’’ (RRCAC) at St. Petersburg has developed a relevant technique on our request and synthesized 1-pentanol-D₁₂. The DSC-study of solutions showed that one could get a glass-like substance based on 1-pentanol-D₁₂ with an admixture of 1,2-propanediol-D₈. Finally it should be mentioned that the ultimate conclusion about the efficiency of using pentanol-based glass solutions as targets with polarized hydrogen nuclei should be drawn from the study of DPN, relaxation phenomena and other characteristics of targets after their exposure to a particle beam of high intensity.

2. Polyethylene-based target material

2.1. Introduction

Apart from low-molecular glasses, a quite wide class of substances called organic glasses also includes high-molecular ones, e.g. polymethylmethacrylate. Moreover, while low-molecular glasses can be obtained only at fast or slow cooling, some polymers are glasses at room temperature. If one finds a way to introduce a paramagnetic chemical admixture to the polymers, the resulting ‘‘solution’’ will be of interest as a material for polarized targets. Perhaps, a system like this will allow the microscopic nature of the glass to be elucidated by studying the phenomenon of increasing nuclear polarization. However, polymers are a more complicated subject of investigations than other compounds. Polymers feature two types of bonds, chemical and molecular, which are sharply different in energy and length. Most polymers are nonuniform in phase composition and molecular weight distribution. Despite all that, polymers with high hydrogen content are of interest. That is why they were studied already in the first investigations on the choice of suitable target materials [9,20]. Our main objective in the experiments with polymers was to look for a target material that is hard at room temperature and adequately rich in hydrogen. From this point of view polyethylene (PE) is a suitable substance. Then it was necessary to choose a method of introducing a paramagnetic admixture to PE. We paid attention to Refs. [21,22], where migration of nitroxyl radicals into polymers was discovered. In the mean time this discovery has become a method of investigation. Nitroxyl radicals are used as a paramagnetic probe in all fields requiring investigation of molecular organization and dynamics: physics and chemistry of condensed matter, molecular biology, the science of polymers. In polymers the part accessible for the probe coincides with the degree of amorphism. The behaviour of a paramagnetic molecule in a polymeric medium was studied by EPR. Particularly, a highly stable and volatile radical 2,2,6,6-tetramethyl-piperidine-1-oxyl (TEMPO)

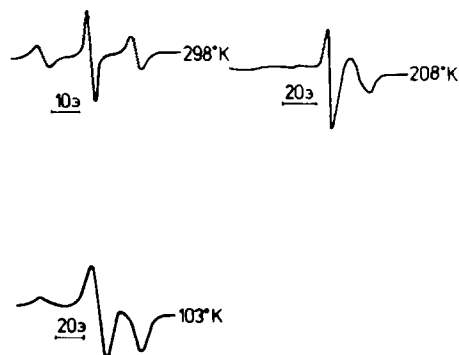


Fig. 3. EPR spectrum of the free radical TEMPO in PE at different temperatures. The concentration of the radical is $5 \times 10^{18}/\text{cm}^3$.

was studied. It was found that there was no significant interaction between unpaired electrons at the radical concentration $5 \times 10^{18}/\text{cm}^3$, and the EPR spectrum of the radical was a well-resolved triplet resulting from the hyperfine interaction (HFI) of an unpaired electron with the nitrogen nucleus (Fig. 3).

At room temperature the EPR spectrum of the radical in PE looks like the spectrum of TEMPO in glycerin, which is a typical glass-forming matrix with hydrogen bonds. Near the temperature of liquid nitrogen the EPR spectrum of the radical takes a form typical for vitrified liquids. The radical is not isolated into a separate phase. This observation is of special interest to us. We have a glass-like solution of the paramagnetic radical TEMPO in PE, a polymer with a high hydrogen content.

2.2. Results and discussion

The first investigation with PE was carried out in 1972 [23]. TEMPO was used as a paramagnetic admixture. The PE structure is similar to the crystal structure of regular paraffins. Yet, the crystallinity of low-density PE after polymerization of ethylene at high pressure with radical-type initiators does not reach 100%. Besides the crystalline phase there is over 50% of the amorphous phase in the polymer. That is why powdered PE of density $d = 0.910 \pm 0.002 \text{ g/cm}^3$ and molecular weight $M = 15\,000\text{--}20\,000$ was chosen. To have diffusion of the radical into the polymer an appropriate amount of TEMPO and PE was put into a sealed glass test-tube. The test-tube was heated to 353 K and kept for 8–10 hours at this temperature. As a result, the PE was uniformly coloured, i.e. the radical had diffused into the polymer. Annealing the polymer is known to result in a higher amorphous phase percentage. Therefore, prior to the DNP experiments at very low temperatures, the PE powder was annealed in vacuum (10^{-5} mbar) for 5–6 days at 353 K. Then pure helium was added to the test-tube with the powder, and the polymer was saturated with radical vapour in this atmosphere. The EPR

Table 1
Polarization obtained at 0.2 K and 2.5 T

Substance	Nominal spins/mm ³	Maximum polarization
Polyethylen + TEMPO	6×10^{19}	-28% +32%
Polyethylene + TEMPO	2×10^{19}	-56% +60%

spectrum of this sample with a TEMPO concentration of $2 \times 10^{19}/\text{cm}^3$ at room temperature was a typical well-resolved triplet with a distance of 15×10^{-4} T between the SFS components. A proton polarization of 50% was achieved in this sample at 0.1 K in a magnetic field of 2.7 T. The sample weighed 0.15 g [23].

At a temperature below 1 K the EPR spectrum is transformed into a line with $\Delta B = 80 \times 10^{-4}$ T with indistinct SFS. To simplify the EPR spectrum of the radical in PE we tried to replace TEMPO with ¹⁴N (nuclear spin $I = 1$) by the same radical with ¹⁵N ($I = \frac{1}{2}$) in the same concentration. The replacement did not increase the maximum polarization achievable.

In 1993 polarization tests in PE with TEMPO were carried out at the Paul Scherrer Institute [24]. PE with a density of 0.915 g/cm^3 and TEMPO were purchased from Sigma Chemie, CH-9470 Buchs. The diffusion of the radical into the polymer was carried out at 353 K for 22 hours. As a result of the diffusion process, the white polymer powder became of a uniform yellow colour. Several samples with different TEMPO concentrations were prepared (see Table 1)

Fig. 4 shows an EPR spectrum of the sample with a concentration of $2 \times 10^{19}/\text{cm}^3$ at room temperature. In Fig. 5 an EPR absorption spectrum is given of the same sample at 0.3 K.

Deuterated polyethylene (CD₂)_n (DPE) is of interest as a material for a polarized deutron target. We used DPE with a deuterium content of 98%, synthesized at RRCAC by suspension polymerization of deuterated ethylene at a

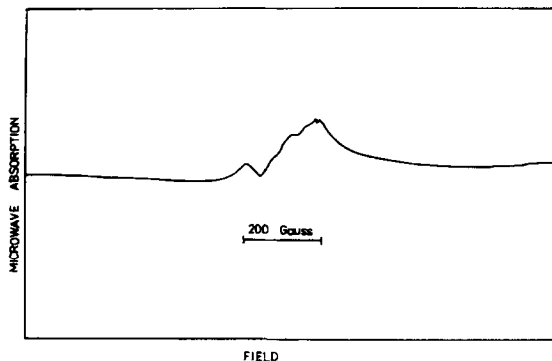


Fig. 5. EPR spectrum (microwave absorption) of TEMPO in PE at 0.3 K. The radical concentration is $2 \times 10^{19}/\text{cm}^3$.

low pressure in the presence of an alumino-organic catalyst. The DPE density is 1.1 g/cm^3 , its melting point is 403 K. It is practically a crystalline polymer with the degree of crystallinity being over 80%. We tried to introduce the TEMPO radical into DPE. The polymer at our disposal was a single block. We needed DPE powder. Yet, the nature of the polymer is such that we failed to grind it in a ball mill at 77 K. So, we cut the polymer with a sharp knife and used the resulting chips in our experiments. To provide diffusion of the radical into the polymer we put the appropriate amount of TEMPO into a glass ampoule, heated it up to 120°C and kept it for 5 h at that temperature. Two samples with the TEMPO concentration $2 \times 10^{20}/\text{cm}^3$ and $2 \times 10^{19}/\text{cm}^3$ were prepared. The samples were studied by EPR. The EPR spectrum of DPE with a TEMPO concentration $2 \times 10^{20}/\text{cm}^3$ was a single line, which indicated a too high local concentration of the radical. The EPR spectrum of DPE with a TEMPO concentration $2 \times 10^{19}/\text{cm}^3$ was a typical well-resolved triplet (Fig. 6) similar to the EPR spectrum of TEMPO in non-deuterated PE (Fig. 4).

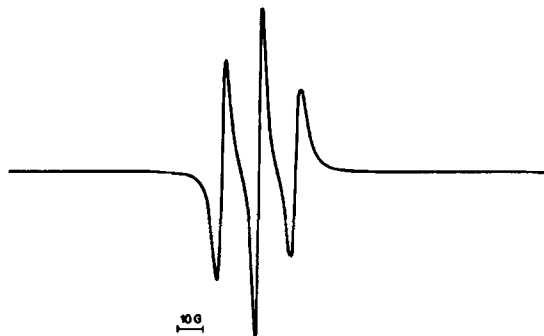


Fig. 4. EPR spectrum of TEMPO in PE at 293 K. The concentration of the radical is $2 \times 10^{19}/\text{cm}^3$.

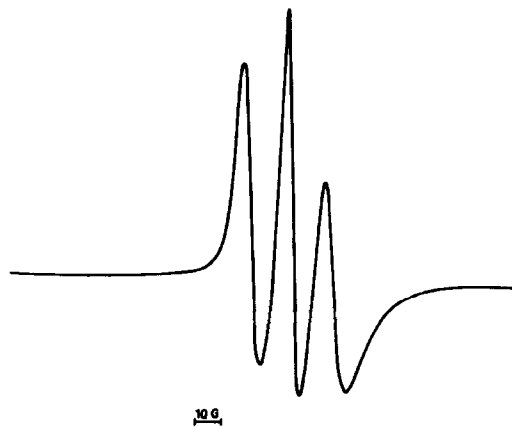


Fig. 6. EPR spectrum of TEMPO in DPE at 293 K. The concentration of the radical is $2 \times 10^{19}/\text{cm}^3$.

We have studied two different sorts of PE, a highly amorphous and a highly crystalline one. The fact that the EPR spectra of the two polymers are similar reflects the complicated dynamic behaviour of TEMPO in such inhomogeneous polymers. It seems to be due to segment mobility of the polymer macromolecules. Diffusion of the radical is most affected by the motion of polymer molecules at a scale comparable with the size of the radical. Hence the cavities in which radicals reside (and migrate) are probably distributed all over the volume of the polymer [22]. We intend to investigate the DPN process in deuterated polyethylene in the near future [24]. It seems also possible to introduce TEMPO by diffusion into glass-like polymers such as polymethylmethacrylate, polystyrene and others.

3. Conclusions

The reported results allow the conclusion that the proposed materials based on glass-like solutions of pentanol, polyethylene and their deuterated analogues contain the highest percentage of hydrogen nuclei in comparison with organic substances used in polarized targets and ensure a high polarization of the protons. We hope that they will find a proper application.

Acknowledgements

Part of this work was carried out during a stay at the Paul Scherrer Institute, Villigen, Switzerland. It is a pleasure to thank Drs. S. Mango, B. van den Brandt, P. Hautle and J.A. Konter for their hospitality and for stimulating discussions.

The test of the 1-pentanol sample was kindly performed by Dres. N. Bubnov, Yu. Kisselev and A. Prugkoglyad.

References

- [1] C.C. Morehouse, DESY preprint F-34-72/1, Hamburg (1972).
- [2] R.C. Fernow, Nucl. Instr. and Meth. 148 (1978) 311.
- [3] R.C. Fernow, Nucl. Instr. and Meth. 159 (1979) 557.
- [4] R.C. Fernow, Proc. 2nd Workshop on Polarized Target Materials, October 1–5, 1979, Rutherford Lab. RL80-0880, p. 49.
- [5] G. Hartmann et al., Proc. 2nd Int. Conf. on Polarized Targets, 30 August–2 Sept. 1971, Berkeley, LBL-500, UC-34, Physics (1972) p. 289.
- [6] J. Ball, Saturne preprint LNS-SSG 81.06/A Ph01, Saclay (1981).
- [7] J. Ball et al., Proc. 4th Int. Workshop on Polarized Target Materials and Techniques, 3–6 Sept. 1984, Bad Honnef, Bonn Univ., 1985, p. 112.
- [8] R. Bernard et al., Nucl. Instr. and Meth. A 249 (1986) 176.
- [9] M. Borghini et al., Proc. Int. Conf. on Polarized Targets and Ion Sources, 1966 CEN Saclay, p. 387.
- [10] T.O. Niinikoski, Proc. 2nd Workshop on Polarized Target Materials, 1–5 Oct. 1979, Rutherford Lab., RL80-0880 (1980) p. 69.
- [11] D. Hill and M. Krumpolc, Proc. Conf. on High Energy Spin Physics, Brookhaven, 1982, AIP Conf. Proc. (1983) p. 479.
- [12] D. Hill et al., Proc. 4th Int. Workshop on Polarized Target Materials and Techniques, 3–6 Sept. 1984, Bad Honnef, Bonn Univ., 1985 p. 84.
- [13] N.S. Borisov, E.I. Bunyatova et al., PTEZ (1978) 32.
- [14] B. Van den Brandt et al., Int. Conf. on High Energy Spin Physics, 1988, Minneapolis, AIP Conf. Proc. 187 (1989) p. 1251.
- [15] S. Ishimoto et al., J. Appl. Phys. 25 (1986) L 246.
- [16] E.I. Bunyatova et al., Solid State Commun. 75 (1990) 125.
- [17] M. Krumpolc and J. Rocek, J. Am. Chem. Soc. 101 (1978) 3206.
- [18] E.I. Bunyatova, JINR Comm. E1-92-5-18, Dubna (1992).
- [19] S. Takala and T.O. Niinikoski, Proc. 9th Int. Symp. on High Energy Spin Physics, 6–15 Sept. 1990, Bonn (Springer, 1991) Vol. 2, p. 347.
- [20] C.F. Hwang et al., Nucl. Instr. and Meth. 51 (1967) 254
- [21] V.B. Strykov et al., Vysokomol. soedin. 7B (1967) 493.
- [22] E.G. Rosantsev, Free Nitroxyl Radicals, (Plenum, New York, London, 1970).
- [23] N.S. Borisov, E.I. Bunyatova et al., JINR preprint P6-7408, Dubna (1973).
- [24] B. Van den Brandt et al., these Proceedings (7th Workshop on Polarized Target Materials and Techniques, Bad Honnef, Germany, 1994) Nucl. Instr. and Meth. A 356 (1995) 36.
- [25] C. Joram et al., Proc. 5th Int. Symp. on Meson–Nucleon Physics and the Structure of the Nucleon, Boulder, Colorado, Sept. 6–10 1993.

Dynamic nuclear polarization in perfluorodimethylcyclohexane doped with a perfluoralkyl free radical

B. van den Brandt ^{a,*}, N.N. Bubnov ^c, E.I. Bunyatova ^b, P. Hautle ^a, J.A. Konter ^a,
 S. Mango ^a, S.P. Solodovnikov ^c, B.L. Tumanski ^c

^a Paul Scherrer Institute, CH-5232 Villigen PSI, Switzerland

^b Joint Institute for Nuclear Research, Dubna, Head P.O. Box 79, 101000 Moscow, Russian Federation

^c A.N. Nesmeyanov Institute of Organo-element Compounds, Russian Academy of Science, 117813 Moscow, Russian Federation

Abstract

First results of DNP at 2.5 T and below 0.3 K in F-dimethylcyclohexane (C₈F₁₆), doped with F-2,4-dimethyl-3-ethyl-3-pentyl (C₉F₁₉), are presented. A polarization of the ¹⁹F-nuclei of up to 54% was obtained.

1. Introduction

For a pion scattering experiment to be performed on the SUSI spectrometer at the PSI medium energy accelerator, a target material containing only ¹⁹F and light, non-polarizable “background” nuclei was requested. Irradiated LiF [1], CaF₂ + Tm²⁺ [2], and C₃H₂FO + EHBA – Cr^V [3], in which high ¹⁹F polarizations have been achieved, were in fact not considered suited for that particular experiment. We present here preliminary results obtained with a target material which would fulfill the conditions mentioned.

2. The free radical

At present the only stable perfluoralkyl radical that can be synthetically produced with 100% yield is F-2,4-dimethyl-3-ethyl-3-pentyl [4]. A colourless, transparent liquid with elemental composition C 23.15%, F 76.94% (found), C 23.03% and F 76.97% (calculated), this radical is stable at room temperature to dimerization, disproportionation, O₂, Cl₂, Br₂, I₂ or aqueous acid or base [5]. Since the radical is a derivative of the paraffin series, it is remarkably compatible with perfluorocarbon compounds.

The radical has a practically isotropic *g*-factor close to the *g*-factor of the free electron. In accordance with the results of the spectrum simulation (see Fig. 1), we have determined the following hyperfine interaction constants

(HFI) between an unpaired electron and a fluorine nucleus in the radical ((CF₃)₂CF)₂ĊCF₂CF₃:

$$a_{F_{4-\beta}} = 45 \text{ G},$$

$$a_{F_{1,2,3-\beta}}(3F) = 3.47 \text{ G},$$

$$a_{F-\gamma}(15F) = 2.55 \text{ G}.$$

The HFI constant increases from $F_{4-\beta} = 45 \text{ G}$ to 54 G in a solid matrix at 77 K, due to some variation in the radical conformation shown in Fig. 2. A specific feature of the radical is the spin density on all fluorine atoms, which should be favourable for the polarization of the fluorine nuclei in a fluorine containing base material like F-dimethyl-cyclohexane.

3. Polarization tests

We investigated four samples of F-dimethyl-cyclohexane with different concentrations of the free radical (see Table 1). Since we had only a limited quantity of the free

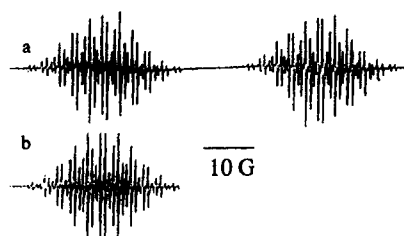


Fig. 1. ESR spectrum of F-2,4-dimethyl-3-ethyl-3-pentyl (a) and computer-simulated spectrum (b).

* Corresponding author.

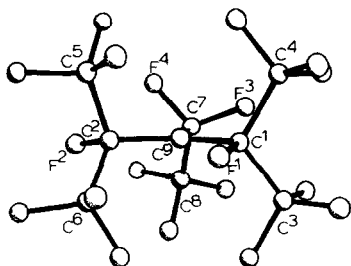


Fig. 2. Radical conformation corresponding to the minimum energy.

radical, we first prepared sample no. 1 with a volume of 0.7 cm^3 , loaded it in the mixing chamber of our standard polarized target test cryostat [6,7] and measured the polarizability at 2.5 T and below 0.3 K the relaxation time around 1 K. Then we took it out of the cryostat, warmed it up in a sealed plastic bag to avoid as much as possible the condensation of water, diluted the liquid by adding F-dimethylcyclohexane until the concentration quoted under sample no. 2 was obtained, loaded this material, and measured it. We repeated this process three times. The maximum polarization of 54% was obtained with a spin concentration of $2 \times 10^{19}/\text{cm}^3$. The relaxation time of this sample was 49 s at 1.05 K. The optimum microwave frequencies were in this case 190 MHz apart. The results for the other three samples are listed in Table 1. All polarizations quoted assume a Boltzmann distribution of

Table 1
Summary of polarization measurements on F-dimethylcyclohexane

	Spins/ cm^3	Polarization freq. (GHz) ^a	Pol. (%)	T_n (s)
1	1.2×10^{20}	$f_+ = 69.660$ $f_- = 70.180$	+35 -35	5 (at 0.98 K)
2	5.8×10^{19}	$f_+ = 69.790$ $f_- = 70.080$	+42 -42	20 (at 0.98 K)
3	2×10^{19}	$f_+ = 69.820$ $f_- = 70.010$	+54 -54	49 (at 1.05 K)
4	9×10^{18}	$f_+ = 69.825$ $f_- = 69.990$	+39 -43	64 (at 1.05 K)

^a At 2.4490 T.

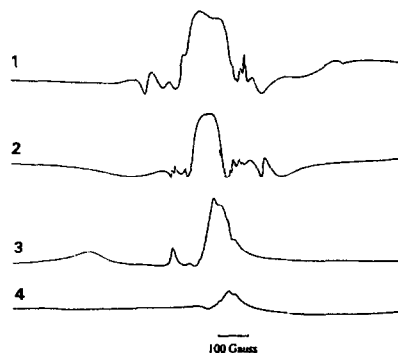


Fig. 3. EPR spectra of the free radical F-2,4-dimethyl-3-ethyl-3-pentyl in F-dimethylcyclohexane. (The numbers refer to the sample numbers in Table 1.)

independent spins for the thermal equilibrium polarization signal, measured at 1 K.

To estimate the concentration of the paramagnetic centers in our samples we recorded the value of a 100Ω Matsushita resistor in the mixing chamber while sweeping the magnetic field through the electron resonance at 0.3 K and 70 GHz (see Fig. 3).

In conclusion, for the first time ^{19}F nuclei have been polarized to an appreciable degree in a substance with only C nuclei as background.

References

- [1] A. Abragam, M. Chapellier, J.F. Jacquinot and M. Goldman, *J. Magn. Res.* 10 (1973) 322.
- [2] A. Abragam and M. Goldman, *Nuclear Magnetism: Order and Disorder* (Clarendon, Oxford, 1982).
- [3] D. Hill et al., *Proc. 8th Int. Symp. on High Energy Spin Physics*, Minneapolis, 1988, ed. K.J. Heller, AIP Proc 187 (New York, 1989) vol. 2, p. 1268.
- [4] S.R. Sterlin et al., to be published in the *Bull. Russian Acad. Sci.*
- [5] K.V. Scherer et al., *J. Am. Chem. Soc.* 107 (1985) 718.
- [6] B. van den Brandt, J.A. Konter and S. Mango, *Nucl. Instr. and Meth. A* 289 (1990) 526.
- [7] B. van den Brandt, J.A. Konter, S. Mango and M. Wessler, *Proc. 9th Int. Symp. on High Energy Spin Physics*, Bonn, 1990, eds. W. Meyer et al., (Springer, Berlin, 1991) vol. 2, p. 320.



ELSEVIER

Dynamic nuclear polarization in thin polymer foils and tubes

B. van den Brandt ^{a,*}, E.I. Bunyatova ^b, P. Hautle ^a, J.A. Konter ^a, S. Mango ^a^a Paul Scherrer Institute, CH-5232 Villigen PSI, Switzerland^b Joint Institute for Nuclear Research, Dubna, Head P.O. Box 79, 101000 Moscow, Russian Federation

Abstract

First results of DNP at 2.5 T and below 0.3 K in thin polymer foils and tubes with the chemical composition $(CX_2)_n$, [$X = {}^1\text{H}, {}^2\text{D}, {}^{19}\text{F}$], doped with TEMPO, are presented. Appreciable polarizations of protons, deuterons, and ${}^{19}\text{F}$ -nuclei were obtained. The samples can be handled at room temperature for several hours, and therefore they are suitable for new applications.

1. Introduction

DNP (dynamic nuclear polarization) requires the presence of paramagnetic centers in the vicinity of the nuclear spins to be polarized. In practice, these centers are introduced either by solution of free radicals in liquids (e.g. 1-butanol, propanediol), which are then quickly cooled to less than ~ 100 K and solidified, and must be handled under liquid nitrogen, or produced by irradiating a solid (e.g. ${}^6\text{LiD}$, NH_3) at low temperature, again requiring handling under liquid nitrogen. These methods have been used extensively to prepare polarized targets for spin-dependent scattering experiments, but polarizable substances which are solid and can be handled at room temperature for at least a few hours would provide, besides obvious practical advantages, a wealth of new experimental possibilities in nuclear and particle physics.

The introduction via diffusion in polymers of the stable free nitroxyl radical 2,2,6,6-tetramethyl-piperidine-1-oxyl, also known as TEMPO [1], had given in powders interesting results described elsewhere in these proceedings [2]. Encouraged by the data available for the process of translational diffusion of TEMPO into samples of polyethylene [3], we have performed further tests and introduced TEMPO by diffusion into thin polymer foils, viz. in normal polyethylene (12.5 μm thickness), in deuterated polyethylene (~ 100 μm) and in PTFE (25 μm). The nuclear polarizations achieved so far can be defined appreciable. An attempt to polarize a polyethylene tube, 0.28 mm I.D. \times 0.51 mm O.D., doped with TEMPO using the same procedure, has given the best polarizations so far in our polymer samples, and suggests further investigations.

2. Preparation of the samples

The polymer foils were – as received – cut to strips, the capillary to 2 cm long pieces, and placed in a glass test tube, sealable with a glass lid. This hollow lid was filled with the amount of TEMPO necessary to obtain the desired concentration of electron spins (see Table 1). The sealed tube was then placed in horizontal position in an oven at 80°C. The operation was done in air. After waiting for 20 or 40 h, the TEMPO had disappeared from its original place and the polymer had acquired a slightly yellow or brown colour.

3. Foils

The samples were placed in a 18 \times 18 \times 5 mm cavity and loaded in the mixing chamber of our standard polarized target test cryostat [4,5]. The magnetic field homogeneity was about 10^{-4} over the target volume. The weight of the samples was approximately 0.5 g, giving a filling factor of ~ 0.25 .

The results of the polarization tests are summarized in Table 2. The polarization values were calculated from NMR signals (see Figs. 1–3) and calibrated against the thermal equilibrium polarization signal, assuming a Boltzmann distribution of independent spins for ${}^1\text{H}$ and ${}^{19}\text{F}$ at

Table 1
Samples

	Substance	Foil thickness (μm)	Hours at 80°C	Spins/ cm^3 nom.
a	n-polyethylene	12.5	20	2×10^{19}
b	d-polyethylene	~ 100	20	2×10^{19}
c	PTFE	25	40	7×10^{19}

* Corresponding author.

Table 2
Summary of polarization measurements

Substance	Spins/cm ³ nom.	polarization freq. (GHz) ^a	pol. (%)
a n-polyethylene	2 × 10 ¹⁹	f ₊ = 69.840	+48
		f ₋ = 70.200	-47
b d-polyethylene	2 × 10 ¹⁹	f ₊ = 69.840	+10
		f ₋ = 70.180	-10
c PTFE	7 × 10 ¹⁹	f ₊ = 69.990	+15
		f ₋ = 70.156	-22

^a At 2.494 T (a,c), or normalized to this field (b).

2.17 K and 0.85 K, respectively. It was not possible to measure the thermal equilibrium signal of the deuterons, so the deuteron polarization was estimated from the asymmetry of the NMR signals.

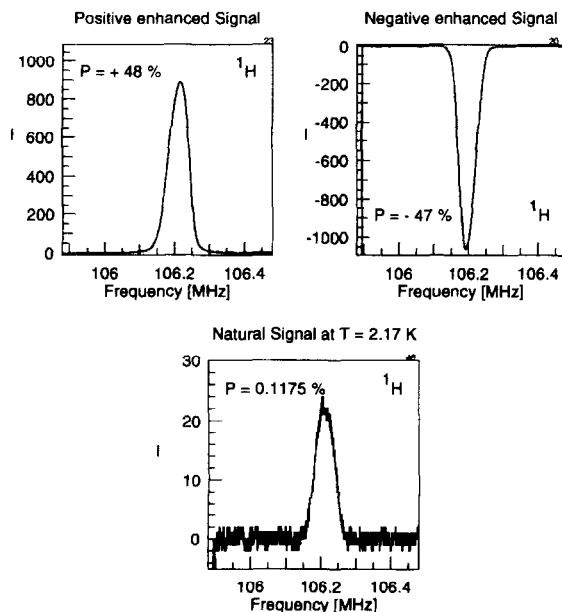


Fig. 1. NMR signals of polyethylene foil (12.5 μm) doped with TEMPO (2 × 10¹⁹ spins/cm³).

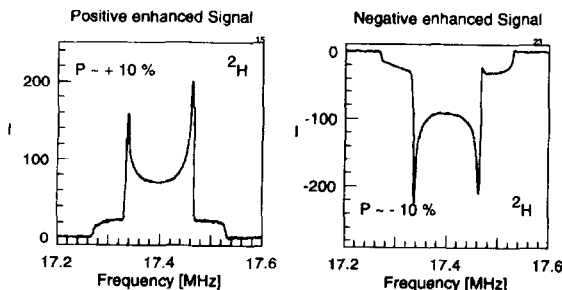


Fig. 2. NMR signals of deuterated polyethylene foil (100 μm) doped with TEMPO (2 × 10¹⁹ spins/cm³).

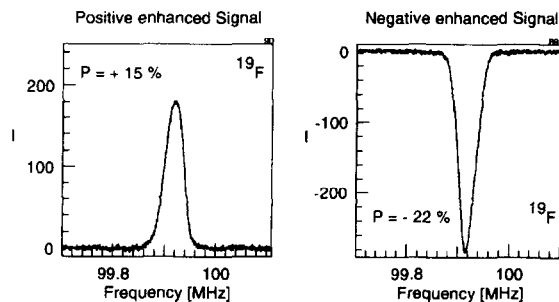


Fig. 3. NMR signals of polytetrafluoroethylene foil (25 μm) doped with TEMPO (7 × 10¹⁹ spins/cm³).

Relaxation times were measured at 2.5 T: the relaxation time of the protons in normal polyethylene was 5 min at 2.1 K, 43 min at 0.9 K, the relaxation time of ¹⁹F in PTFE was 6 min at 0.85 K, 18 h at 0.20 K.

4. Tube

Three pieces of tube (0.07 g), doped with nominal 2 × 10¹⁹ spins/cm³, were slid over the NMR coil, and polarized under the same conditions as the foils. Proton polarizations of +70% and ~65% have been achieved, if the assumption of an independent proton spins system made above is valid, although the optimum polarizing frequencies have still to be determined. The relaxation times at 2.5 T were measured to be 8 min at 1.14 K and ~1 min at 2.17 K, and TEP signals have been taken at these temperatures. Polarization measurements at 1 K and 5 T will be performed soon.

5. Conclusions

The nuclei in thin polymer foils and tubes can be polarized using the stable nitroxyl radical TEMPO. The radical can be easily introduced via a diffusion process. The samples can be stored at room temperature at least for several hours.

Acknowledgements

The deuterated polyethylene was kindly provided by Prof. E. Boschitz, Karlsruhe University, the PTFE-foil by Maag Technic AG, CH-8600 Dübendorf.

References

- [1] E.I. Bunyatova, Proc. 9th Int. Symp. on High Energy Spin Physics, Bonn, 1990, eds. W. Meyer et al. (Springer, Berlin, 1991) vol. 2, p. 333, and references therein.

- [2] B. van den Brandt, E.I. Bunyatova, P. Haulte, J.A. Konter, A.I. Kovalev and S. Mango, these Proceedings (7th Workshop on Polarized Target Materials and Techniques, Bad Honnef, Germany, 1994) *Nucl. Instr. and Meth. A* 356 (1995) 138.
- [3] E.G. Rozantsev, *Free Nitroxyl Radicals* (Plenum, New York, 1970).
- [4] B. van den Brandt, J.A. Konter, S. Mango and M. Wessler, Proc. 9th Int. Symp. on High Energy Spin Physics, Bonn, 1990, eds. W. Meyer et al. (Springer, Berlin, 1991) vol. 2, p. 320.
- [5] B. van den Brandt, J.A. Konter and S. Mango, *Nucl. Instr. and Meth. A* 289 (1990) 526.



ELSEVIER

New investigations of polarized solid HD targets [☆]

A. Honig ^{a,*}, Q. Fan ^a, X. Wei ^a, A.M. Sandorfi ^b, C.S. Whisnant ^c^a *Physics Department, Syracuse University, Syracuse, NY 13244, USA*^b *LEGS Project, Brookhaven National Laboratory, Upton, NY 11973, USA*^c *Dept. of Physics and Astronomy, University of S. Carolina, Columbia, SC 29208, USA*

Abstract

Polarized solid HD targets in a frozen-spin mode, with superior nuclear physics characteristics and simple operational configurations, have previously been restricted in their deployment due to a disproportionate target production time with respect to utilization time. Recent investigations have yielded frozen-spin polarization lifetimes, at a convenient target temperature of 1.5 K, of nearly a year for both H and D at high holding fields, and of more than a week at sub-Tesla holding fields. These results, taken together with the advent of new interesting spin-physics using relatively weakly ionizing beams, such as polarized photon beams, remove the above impediment and open up the use of polarized solid HD to long duration nuclear spin-physics experiments. Large, multiple targets can be produced, retrieved from the polarization-production apparatus with a cold-transport (4 K) device, stored for very long times in inexpensive (1.5 K, 7 T) cryostats, and introduced “off-the-shelf” into in-beam cryostats via the portable cold-transport apparatus. Various modes for achieving polarized H and/or D, as well as already achieved and expected polarization values, are reported. Experimental results are given on Kapitza resistance between the solid HD and the cooling wires necessary to obtain low temperatures during the heat-evolving polarization process. 15 mK is achievable using gold-plated aluminum wires, which constitute 15% extraneous nucleons over the number of polarizable H or D nucleons. Application to more highly ionizing beams is also given consideration.

1. Introduction

Polarized HD targets have very desirable properties. The fraction of free protons exceeds that of any other operational target, the H and D polarizations are independent of each other and independently reversible, allowing a polarized neutron configuration, and H and D vector polarizations, exceeding 95% and 70%, respectively, are attainable with present low temperature and high magnetic field technology. Easy transportability of the polarized target, which is in the frozen-spin condition for temperatures below about 5 K, is made possible by the cold-transport systems which have been devised. Thus, the polarization production system is completely separable from the target usage environment. A target of several moles (20 cm³/mole) is feasible in a single production cycle. In addition, as a consequence of the recent discovery of proton and deuteron relaxation times of the order of a year, long term inexpensive storage of a passive polarized target

in a simple 1.5 K cryostat under unattended conditions has been made feasible. This allows “off-the-shelf” target availability, and assemblage of stored moderate-sized targets into very large ones.

The new relaxation results obtained within the past year which are reported in this paper have led to a decision to employ this target in a long-duration mode, previously seen as impractical because of the disparity between production and usage times. Thus, it joins the ranks of contemporary operational targets. The first nuclear experiments which it will serve will be at the Laser Electron Gamma Source (LEGS project) at Brookhaven National Laboratory. In view of this debut, a brief history of the development of the solid HD frozen-spin polarized target may be in order before presenting the new results.

2. Historical background of frozen-spin polarized solid HD

The history of this frozen-spin molecular HD target begins almost 40 years ago. In an early paper, Bloom [1] showed that an important relaxation mechanism for the protons in solid HD near the melting point was via “impurity” ortho-H₂ molecules, whose protons relaxed to the

[☆] Work supported by NSF, through the University of S. Carolina, and by the US Dept. of Energy, under contract #DE-AC02-76-CH00016.

* Corresponding author.

lattice efficiently because of the $J = 1$ molecular rotation state, and then cross-relaxed with the protons in the HD, which have the same Larmor frequency. H polarization is then distributed throughout the HD host by spin-diffusion. Several years later, Hardy and Gaines [2] carried out relaxation time measurements in very pure HD with small traces of o-H_2 at temperatures between 4.2 and 1.2 K, and showed the above relaxation mechanism was the only one responsible for proton relaxation in HD. Consequently, by aging a solid HD sample containing a small o-H_2 impurity concentration at a temperature below about 5 K, one obtained proton relaxation times of many hours, since over the course of a few weeks the o-H_2 concentration decreased due to conversion from the $J = 1$ ortho state to the non-magnetic $J = 0$ para state with a temperature independent conversion time constant of 6.5 days. A proposal for a frozen-spin target was next put forward by Honig [3] based on polarizing the HD at high magnetic field (> 10 T) and low temperature (near 10 mK) under conditions of relatively high initial o-H_2 concentration, c_1^{H} , typically of the order of 0.05%. Even though relaxation times at 1.5 K and sub-Tesla magnetic fields for that c_1^{H} are of the order of seconds, at mK temperatures and high fields, the relaxation times were expected to be many orders of magnitude longer, hopefully adjustable by means of choice of c_1^{H} to values of a few days, so that near-equilibrium polarization could be obtained within a reasonable waiting time. After polarization, the target would be aged at the polarizing field-temperature until c_1^{H} was sufficiently reduced for the relaxation time to be very long even at frozen-spin usage conditions of 1–4 K, with holding fields of a fraction of a Tesla. This was one of the earliest suggested frozen-spin target systems, and is still among the few which use a relaxation mechanism “switch” other than lowering of the temperature after (usually dynamic) polarization. Its main advantage is that the frozen-spin temperature is at convenient liquid helium temperatures, so that physical separation of polarization-production and usage apparatuses, using cold-transport devices, is relatively easy to implement. A secondary advantage is that the target operates at a relatively high temperature of 1.5 K, where the heat capacity and thermal conductivity are much larger than in the mK temperature region, and local heating from particle beams will be much reduced. The disadvantage is that an aging process of the order of 30–50 days appeared to be required to reduce c_1^{H} by the more than 3 orders of magnitude estimated as necessary for sufficient polarization holding times at the 1.5 K, sub-Tesla usage conditions. The actual resultant H relaxation time at liquid helium temperature, sub-Tesla field usage conditions was an extrapolation since continuous ageing over such long periods was difficult, and quasi-continuous ageing (short intervals at room temperature) always involved some para \rightarrow ortho back conversion during the few minutes room temperature residencies. During the 15 years following this HD target proposal, explorations of the relaxation times

were undertaken at Syracuse University, mostly in the 0.4 to 16 K temperature and 0–1 T magnetic field regions [4–7], and at the Stony Brook campus of SUNY, in the 35 mK to 4 K temperature and 1.5 T–10 T magnetic field region [8–10]. These studies built up a phenomenological map of T_1^{H} dependence on c_1^{H} , c_1^{D} , T (temperature) and B (magnetic field). Another anticipatory experiment germane to this history was an experimental investigation of relaxation time degradation under ionizing fluxes from the Brookhaven 28 GeV proton synchrotron and the Cornell 10.4 GeV electron synchrotron, to test the target’s resistance to radiation damage [11]. Numerous theoretical papers were also contributed throughout this period. These are referenced in the experimental papers we have cited, but are not explicitly listed here, primarily because the theories are thus far inadequate for explaining the results in the very low c_1^{H} regime pertinent here and also because of space limitations for this presentation. Up to this point, we have discussed only the proton. Some of the references cited also include relaxation measurements of the deuteron. It was apparent that deuteron relaxation in solid HD proceeds in a manner similar to that for H, but the relaxation times are 1 to 2 orders of magnitude slower for the same c_1^{D} , c_1^{H} conditions. Also, the proton and deuteron spin-lattice relaxation times, T_1^{H} and T_1^{D} , depend on both c_1^{H} and c_1^{D} , in a fairly complicated way [5]. T_1^{H} values of many hours, and T_1^{D} values of up to 4 days had been reached under particular conditions within the constraints of usable targets. These relaxation times were still not long enough for long duration solid target experiments, given the 50 day production time. The case of polarized D in the HD, however, presented a different opportunity. A mode of polarization similar to that of H is inadequate, because with the available fields and temperatures, the equilibrium D polarizations are too small. Secondly, analogous lowering of the starting c_1^{D} (which would provide relaxation for the D in the initial polarization production phase) even by only 2 orders of magnitude would require over 80 days, determined from the 18 day measured conversion time constant of para \rightarrow ortho D_2 in HD. The problem was solved by a dynamic polarization method for D polarization based on the intermolecular dipolar coupling between H and D nuclei on neighboring molecules. No D thermal relaxation is necessary, and thus the starting concentration of para- D_2 , c_1^{D} , can be very low, or a pre-ageing which lowers the initial c_1^{D} can be implemented. The D polarization is effected by a radio-frequency forbidden transition adiabatic rapid passage [12], whereby a maximum of $\frac{2}{3}$ of the proton polarization can be transferred to the deuterons. This process can be repeated after repolarization of the protons. In practice, this process is carried out at low magnetic field for maximum forbidden-transition probability, and thus far, only 50% efficiency has been achieved, permitting only $\frac{1}{3}$ of the proton polarization to be transferred in a single cycle. With high H polarization and two cycles, this still results in a very significant D polarization.

With this groundwork laid, the first practical application program employing polarized HD was begun in 1983 at Syracuse, where the objective was to test theoretical predictions [13] regarding nuclear fusion with spin-polarized D fuel. By the late 1980s, the protocols for achieving polarized D in HD were worked out [14], and the most interesting and manageable experiments were seen to be with inertial confinement fusion [15]. In this case, extremely long durations of the polarized state were not required. The experiments were single shot, and T_1^D of about 8 hours was adequate for maneuvering the polarized sample from its production site to the target site, which in this case included a 2 hour drive from Syracuse to Rochester's Laboratory for Laser Energetics. H polarization was irrelevant to the experiment. The shorter D polarization retention requirement and the absent H polarization requirement also entailed a relatively short polarization production time, of only 12 days. The polarization cycle for this type of D-only polarization has been reported [16], with 38% D polarization obtained on a preliminary trial, and 60% D polarization anticipated upon optimizing the procedure. The necessary cold-transport devices were invented and constructed for moving the polarized material from production site to target utilization site [17].

3. Experimental results on limiting values of relaxation times

We come now to the present effort to use these polarized targets for backscattered polarized gamma photon beams, such as in the LEGS or GRAAL experiments, where very advantageous use is made of the special properties of the HD targets already noted in the introduction section. Here, the beam does not degrade the target since the damage from pair production is quite low for the intensity and energy of the beam. We estimate that negligible beam-induced target depolarization will take place during 50 days irradiation from the less than ($10^7 \text{ s}^{-1} \text{ cm}^{-2}$) photon flux on the target. Nevertheless, for a viable target, we must assure an approximate match between polarization-production time and usage time, which means that we require a polarization retention (relaxation) time for the H and D in the HD in-beam target at 1.5 K, or possibly 0.5 K, of the order of a month. The results of a feasibility study to determine if such long T_1 's are possible are presented here.

Our interest is focused on T_1 values for H and D at 1.5 K and in various magnetic fields, since the magnitude of the field surrounding the target for different experiments can vary significantly. We had already shown that for an H and D polarized target, with c_1^D intentionally reduced to a very low initial value, c_1^H of about 3×10^{-4} resulted in a T_1^H at 10 mK and 12 T of about 1.5 days, which tentatively has been chosen as our selected starting condition. The corresponding T_1^H at 1.5 K and 0.1 T is about 20 s.

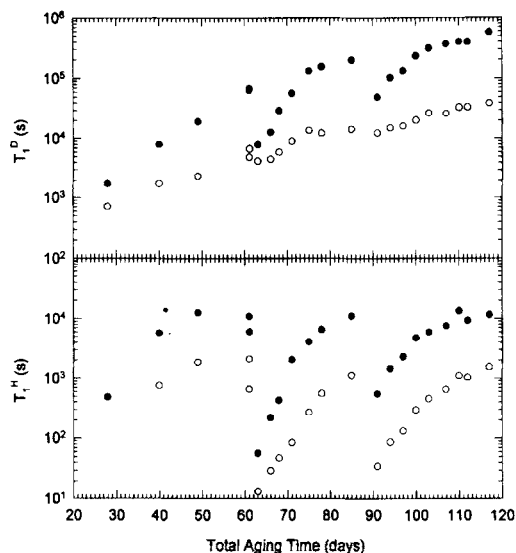


Fig. 1. Plot of increasing T_1^H and T_1^D of an HD solid sample, in a Pyrex tube container, during quasi-continuous ageing at 4.2 K. For each relaxation-time measurement, the sample spends a minimum of 5 min at room temperature in the gas phase, during which time the *o*-H₂ and *p*-D₂ impurities undergo a small amount of back-conversion towards their room temperature equilibrium values. This limits the maximum relaxation times attained. At days 60, 61, and 86, the back conversion was deliberately carried out for longer times of 1 h, 30 h, and 17 h, respectively. Solid symbols: 1.5 K. Open symbols: 4.2 K.

The sample used for most of the experiments to be reported here was HD 01, which was initially doped to an H₂ concentration of 9×10^{-4} normal-H₂ (6.8×10^{-4} *o*-H₂), and had a starting normal-D₂ concentration of about 1.8×10^{-3} (6×10^{-4} *para*-D₂). By ageing in an external liquid helium cryostat, this sample could easily be brought to the c_1^H value of 3×10^{-4} . Similarly, if it converted to a c_1^H value $< 3 \times 10^{-4}$, it could be back-converted at room temperature to the selected 3×10^{-4} value.

In Fig. 1, we illustrate these procedures while carrying out an extended ageing experiment with sample HD 01, in the quasi-continuous mode. About 0.014 mole of the HD is contained in a 0.5 l Pyrex vessel with an attached 1 m length of 6 mm o.d. Pyrex tubing. This configuration allows simple cryocondensation gas transfer among sample containers, as well as convenient insertion into our NMR probe. About 2 cm of solid HD forms at the bottom of the tube upon condensing during insertion into the NMR probes in the various cryostats. The sample remains ageing in a liquid helium storage container at 4 K, except for removal every few days for insertion into a glass cryostat for NMR measurements. During transits into and out of the NMR cryostat, the sample spends about 5 min at room temperature, during which time the *ortho*-H₂ and *para*-D₂ undergo a small amount of back conversion. Thus, the levelling-off of T_1^H near days 50, 80 and 110 is due to

back conversion just balancing the conversion in the storage cryostat during the non-measurement interval. At days 60, 61, and 86, longer back-conversions were intentionally incurred for durations noted in the figure's caption. One notes that when T_1^H is back-converted almost to its starting value, T_1^D is much less reduced. Thus, the c_1^D back conversion rate is much slower than that of c_1^H , providing a ready means of preparing initial samples of high c_1^H but very low c_1^D by judicious ageing and back converting. In the figure, the T_1^H levels off near 10^4 s, whereas T_1^D reaches values of almost a week.

We next carried out experiments with continuous ageing, using an NMR probe inside a large Janis Vari-Temp cryostat, which contains an 8 T superconducting magnet with a very homogeneous field. This apparatus was operated continuously, with relatively low liquid helium consumption, at any temperature between 1.5 K and 4.2 K, for durations exceeding 2 months. For various reasons, these continuous ageing runs would sometimes be interrupted, but the data from different ageing sequences could be combined using a simple time normalization, since the T_1^H growth evolution from any given starting value was repeatable. The ageing time axis in Fig. 2 has thus been normalized, and time $t = 0$ represents a sample at low c_1^D and c_1^H of about 3×10^{-4} . We see that T_1^H at 0.1 T reaches limiting values of about 1 day, an order of magnitude

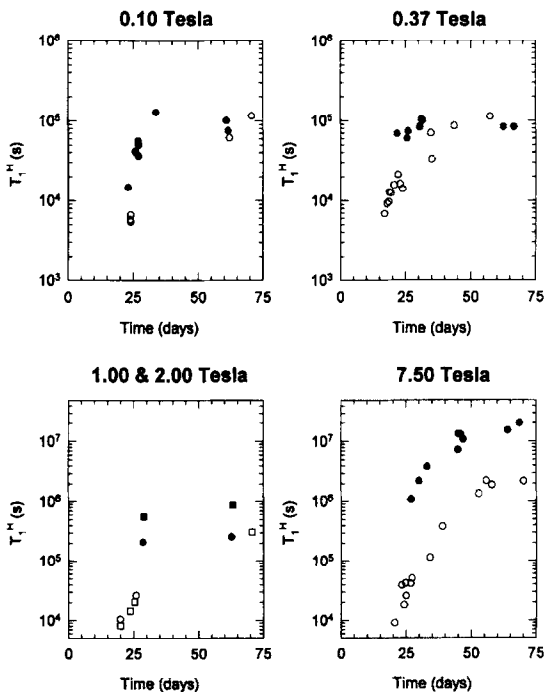


Fig. 2. Growth of T_1^H under continuous ageing in a Janis Vari-Temp Cryostat containing an NMR probe. Measurements are given at 4 values of magnetic field. Starting concentrations at day zero are $c_1^H = 3 \times 10^{-4}$, $c_1^D < 4 \times 10^{-4}$. Solid symbols: 1.5 K. Open symbols: 4.2 K. At 1.5 K and 7.5 T, T_1^H reaches 0.65 yr.

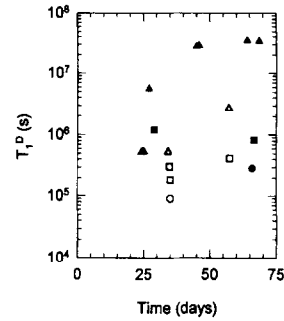


Fig. 3. Growth of T_1^D under continuous ageing in a Janis Vari-Temp Cryostat containing an NMR probe. Experimental run same as that of Fig. 2. Solid symbols: 1.5 K. Open symbols: 4.2 K. Circles: $B = 0.1$ T; Squares: $B = 0.37$ T; Triangles: $B = 7.5$ T. At 1.5 K and 7.5 T, T_1^D reaches 1.1 yr.

greater than in the quasi-continuous aging shown in Fig. 1, but still not as high as we would like. At about 1.3 T, one interpolates a 1 week T_1^H after roughly a 40 day ageing period. At 7.5 T, the levelling off doesn't occur until about day 50, and the T_1^H there exceeds a half year. Fig. 3 shows the T_1^D values during these ageings. We note that towards the end of the ageing period, at 1.5 K, T_1^D even at 0.37 T exceeds a week, and at 7.5 T, is about 1 yr. We are quite certain these are not intrinsically limited relaxation times due to a property of the host HD molecules, since the temperature and field dependence of the relaxation times do not support such an interpretation, and since we have already obtained preliminary data on longer relaxation times in other target configurations, which will be reported elsewhere [18] after being fully analysed.

Even with the T_1 's reached in the above experiments, we have a viable long duration target which can be matched to the polarization production time at applicable holding fields. For an early experiment to be undertaken at LEGS, a 1.3 T holding field is desirable. Even though T_1^H is only a week, we can envisage polarizing 4 targets in one production cycle. The first target is inserted in the in-beam target cryostat, and the others are placed in a 1.5 K storage cryostat with an 8 T magnet, similar to the one used in the experiments yielding the data in Figs. 2 and 3. Since the T_1 's are so long at 7.5 T, they don't degrade during the 1 month experimental run, and the targets are simply replaced in the in-beam cryostat once a week. There are a few complications introduced into the polarization-production cycle with multiple targets, such as requiring a longer homogeneous magnet, a more powerful dilution refrigerator to remove the heat of conversion of the extra target material, and means of effecting cold-retrieval and storage of the multiple targets. However, these are relatively minor, and we believe we have already solved them. We of course expect to have longer T_1 's with the actual large target configuration, as indicated by preliminary experiments, and we also have preliminary data indicating that

T_1^H values more than double at 0.5 K compared with their 1.5 K values. A 0.5 K target cryostat is a fairly straightforward apparatus, and is an option that is being kept open.

4. Polarization modes and projected target polarizations

It is possible to prepare targets in which only polarized H is desired, only polarized D, or both polarized H and D. The modes of polarization vary with these different objectives, with regard to starting c_1^H and c_1^D , duration of polarization-production time, and final expected polarizations. Of course, the chosen polarization-production mode also depends on the required duration of the polarization for the particular planned experiment. In Ref. [16], we already presented a polarization protocol for achieving only polarized D for a polarized fuel fusion experiment. Here, we will limit ourselves to the most demanding mode, in which high D and H polarization, of very long retention in the usage mode, are desired. This is the case for our intended experiments at LEGS.

The mode we present here is based on present capabilities and the particular chosen initial c_1^H and c_1^D discussed above. It is easy to envisage improvement in the efficiency of the forbidden transition adiabatic rapid passage, or different preferred durations of final H and D polarizations which would lead to modifications of the mode to be presented, and which could be highly advantageous with respect to final expected polarizations, and polarization production time. We now refer to Fig. 4, through which we recapitulate the polarization procedure and elucidate some interesting features of the polarization process. At the beginning of the polarization process, the target has zero polarization, the field is set at 20 T (illustrative of available technology, even though cost limits set our upper field at 17 T), the temperature is at 20 mK (owing to the high initial heat generation from c_1^H conversion and restrictions on the number of cooling wires so as not to dilute our polarized hydrogens with extraneous unpolarized nucleons), and only c_1^H at 3×10^{-4} is shown since it is presupposed that c_1^D is negligible for this mode under discussion. In about 2.5 days, the H polarization, P^H , rises to near its equilibrium polarization value, whereas P^D is shown remaining at zero, since if c_1^D were truly zero, its T_1^D would be infinite. c_1^D is indeed low, but not zero, and we return to the departure from this idealization later. At this point, the field is lowered to about 0.03 T, the 50% efficient forbidden transition adiabatic rapid passage is effected, which simultaneously polarizes D and lowers the polarization of H. The H is then repolarized until about day 6. It is apparent that the repolarization takes longer, and reaches a somewhat lower value. This is because T_1^H is constantly getting longer as c_1^H continues to decrease by conversion. T_1^H itself has an exponential dependence on time. When the time constant of its growth becomes

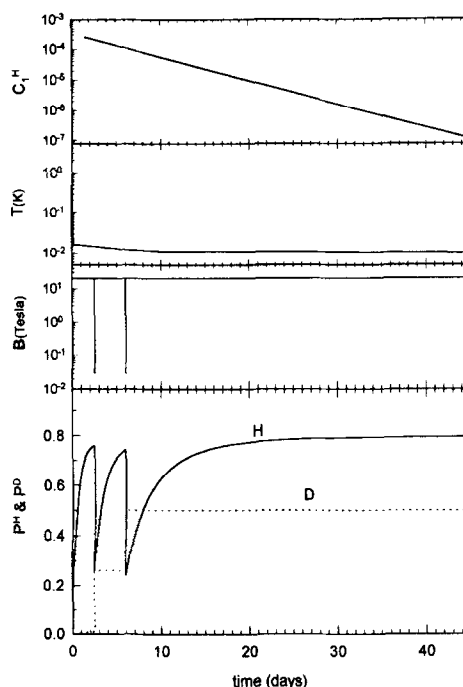


Fig. 4. Time-line of polarization process for solid HD target when both D and H polarizations are to be preserved at 1.5 K and moderate supporting fields. c_1^H is the concentration of $J = 1$ state $H_2(\text{ortho-}H_2)$. $c_1^D < 3 \times 10^{-4}$. Polarization growths are plotted using a quadratic T_1^H dependence on c_1^H up to day 6 and a linear dependence after that. At day 2.5 and day 6, polarization transfer from H to D via “forbidden” radio-frequency-induced transitions takes place. Target temperature decreases during early part of process due to decreasing heat generation from c_1^H conversion as c_1^H diminishes.

comparable with its value, one cannot ever get close to the true equilibrium polarization [6]. Because of this, one cannot start with an initial c_1^H which is too low. It is also the reason why we are somewhat restricted to only 3 cycles of H polarization. This factor is somewhat offset by the fact that the temperature is decreasing from its initial 20 mK value down towards 10 mK, as the conversion heat continually drops during the ageing process. There are several reasons why one cannot start with too high an initial c_1^H either. It would increase the conversion heat, thereby raising the target temperature, and increase the ageing time. Furthermore, little gain in polarization would occur, since the first dynamic polarization of D occurs at low field, and if c_1^H is too high, T_1^H at the low field is short and substantial H polarization is lost. In Fig. 4, at day 2.5, one descends to 0.03 T. The fast passage is effected in about 30 s, but at least 2 min is spent in the low field region before the polarization transfer. Thus, T_1^H must be at least 20 min to avoid more than a 10% loss of P^H . Thus for this mode of polarization, the window of opportunity in choice of initial c_1^H is fairly narrow. At the

end of the ageing period, the c_1^H is down more than 3 orders of magnitude from its initial value. The target is ready for cold-extraction, and the polarization retention times correspond to the results of the previous section.

In Table 1, various expected polarizations from this mode are given. The top row corresponds to Fig. 4. The row below it pertains to the same protocol but with the 17 T magnet which will be used. The other rows present plausible scenarios of improvements in the polarization process. The bottom row reflects the bonus P^D arising when the initial c_1^D is in fact not zero. With our actual sample, we did indeed attain a thermal-relaxation P^D equivalent to about 8%. One can always increase the initial c_1^D and trade away some final polarization-duration against increased P^D .

5. Target temperature during polarization production

Inherent in this polarization method is the presence of enough c_1^H at the beginning of the polarization process to assure a relaxation rate of about 1 d^{-1} at the high field, 10–20 mK polarizing conditions. This initial c_1^H value is typically about 3×10^{-4} , which generates in HD a conversion heat of about $0.8 \text{ } \mu\text{W}/\text{mole}$. This heat must ultimately be removed at the mixing chamber of the dilution refrigerator, and that is why we must have a refrigerator capable of removing $6 \text{ } \mu\text{W}$ at 10 mK, to accommodate 4 targets of about 1.5 moles each. However, the thermal conductivity of solid HD at 10 mK is very small, and to prevent large thermal gradients within the target, it is necessary to disperse wires of sufficient size and at sufficient areal density so that the generated conversion heat can be removed with as little excess temperature in the target over the base temperature of the dilution refrigerator

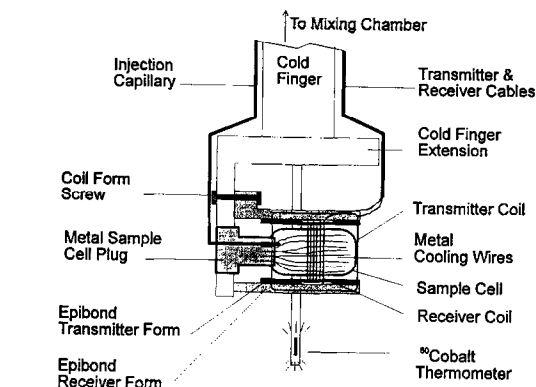


Fig. 5. Schematic of sample cell with metal cooling wires, inside dilution refrigerator. Used for polarization measurements, and Kapitza resistance measurements. Metal wires used are very pure copper, or gold-coated aluminum.

as possible. The heat must be conducted from the bulk HD to the surface of the wires, over a small enough distance so that a thermal gradient less than a few mK will arise, then through the thermal boundary (interface) resistance between the HD and the wire surface, known as the Kapitza resistance, and finally through the wires to the mixing chamber. The Kapitza resistance is the most serious of these thermal resistances, and establishes the minimum material which is necessary for the prescribed cooling. This problem was addressed previously in connection with an effort to employ HD as a thermometer at very low temperatures [19], and the results with wires were not very satisfactory. We have had a better experience, and report some early results now, although experiments are still in progress aimed at improvement. Fig. 5 shows the configuration of the wires in the target cell which we use for this

Table 1

↑D and ↑H polarizations retained (Note: Each improvement is considered to act separately in this Table. For a combination of improvements, the resultant polarization is higher, but not a simple sum of the individual polarization improvements)

B (T)	T (mK)	Forbidden transition efficiency (%)	P^D thermal (1st cycle) (%)	P^D (%)	P^H (%)	T_1^D (day) at 1.5 K			T_1^H (day) at 1.5 K			Polarization production time (day)	Comment
						0.1 T	1.0 T	8.0 T	0.1 T	1.0 T	8.0 T		
20	20–15	50	0	50	79	2.5	15	> 500	1	5	> 300	50	$c_1^D < 10^{-5}$ a
17	20–15	50	0	46	73	2.5	15	> 500	1	5	> 300	50	$c_1^D < 10^{-5}$ a
20	15–12	50	0	57	85	2.5	15	> 500	1	5	> 300	50	$c_1^D < 10^{-5}$ b
17	15–12	50	0	52	83	2.5	15	> 500	1	5	> 300	50	$c_1^D < 15^{-5}$ b
20	20–15	75	0	70	79	2.5	15	> 500	1	5	> 300	50	$c_1^D < 10^{-5}$ c
17	20–15	75	0	64	73	2.5	15	> 500	1	5	> 300	50	$c_1^D < 10^{-5}$ c
20	20–15	50	10–15	60–65	80	2.5	15	> 500	1	5	> 300	50	$c_1^D \sim 10^{-5}$ d
17	20–15	50	8–12	54–58	73	2.5	15	> 500	1	5	> 300	50	$c_1^D \sim 10^{-5}$ d

^a Under demonstrated feasibility conditions.

^b Assuming improvement in conduction wire geometry and reduced interface thermal resistance, thereby lowering target temperature.

^c Assuming increase in rf induced “forbidden” transition efficiency.

^d Assuming P^D growth via relaxation in first cycle, to between $\frac{1}{2}$ and $\frac{3}{4}$ equilibrium value.

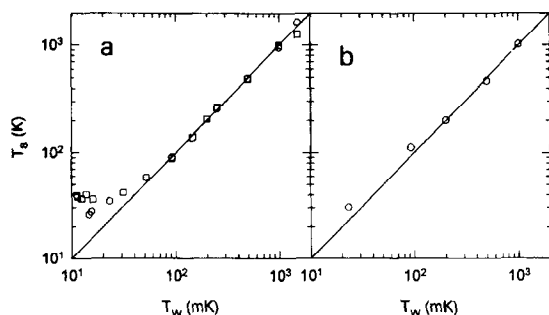


Fig. 6. (a) Plot of target temperature, T_s , versus temperature of copper wires, T_w . (b) T_s vs. T_w for gold-coated aluminum wires. At lowest temperatures, T_s is higher than T_w because of thermal boundary resistance and heat generation rate inside target.

purpose. It is advantageous to maximize the ratio of wire surface area to wire volume, since the Kapitza resistance is inversely proportional to the surface area, and the number of extraneous nucleons is proportional to the volume. Therefore, large numbers of very thin wires are desirable up to the limit where the wire cross-section becomes too small to conduct the heat out of the target cell to the mixing chamber. 12 μm wire would be best for our purposes, but for the present, we have experimented with 25 μm , and larger diameter wires, since they are easier to obtain and work with. Aluminum is superior to copper, but must be gold plated for a good soldered thermal connection to the mixing chamber. In Fig. 6a, we show the results of thermal interface resistance measurements using a cell with 120 copper wires of 25 μm diameter, and in Fig. 6b, we have 60 gold-coated aluminum wires of 50 μm diameter. Both have the same area interface with the HD. The heat generated within the target is known, since the starting c_1 's and their conversion rates are known. For Fig. 6a, sample HD 02 was employed, with initial concentrations of $c_1^H = 5.8 \times 10^{-4}$ and $c_1^D = 2.0 \times 10^{-3}$. For 0.014 moles HD in the cell, the initially generated heat is calculated as 2.8×10^{-8} W (\square), and the heat generated 12 days later is calculable from the known conversion rates (\circ). The sample used in the experiment of Fig. 6b is HD 01, with c_1^H close to 3×10^{-4} , the standard starting concentration for a polarization-production run. The Kapitza resistances, R_K , obtainable from the departure of the curves in Fig. 6 from the Curie law straight line, are almost the same for both aluminum and copper, equal to $16/T^3$ K/W. Calculation of the temperature range of our targets given in Table 1 is based on these results. The aluminum results extrapolate to a 13% contamination of extraneous unpolarized nucleons when the wire size is optimized. The technique we use for measuring Kapitza resistance is quite convenient, since we have changing heat generation rates which are calculable, the ^{60}Co nuclear orientation thermometry for the mixing chamber is reliable, the HD temperature is measured accurately through the Curie law,

and the temperatures of the copper and aluminum wires are measured from the Curie law with NMR and through the Korringa relation for the temperature dependence of the spin-lattice relaxation time of the metal.

6. Cold transport and target cells

Operating cold-transport systems have already been built and employed in connection with previous polarized fusion fuel work, and the results have been published [17]. A detailed description will thus not be given here. The basic operations, such as left-right hand thread engagement and disengagement, and the construction of the nitrogen and helium dewars, are very similar for this application. The larger diameter of the device simplifies some aspects, making translational movements more securely with bellows, as opposed to sliding o-rings used on the smaller diameter cold-transport systems. The cold-transport holding field magnets present more of a problem for the large targets since it is more difficult to obtain suitable permanent magnets which can be installed in the narrow annulus space available. We anticipate using high temperature superconducting solenoids for this, within the 77 K shroud. The paper by Rigney et al. of this conference, puts forward a working design for the HD target in-beam cryostat and cold-transport to be used for these experiments.

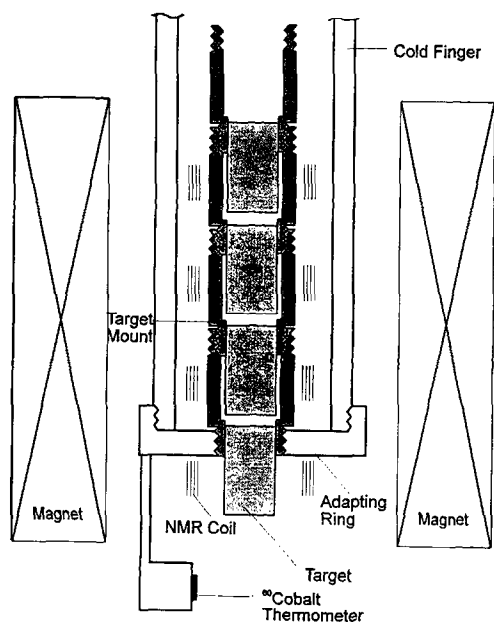


Fig. 7. Schematic of coupling of large multiple HD targets to cold finger attached to mixing chamber of dilution refrigerator. Left-right hand threaded structure allows engagement and disengagement from cold finger, and from cold transport retrieval system (not shown).

The target cells themselves are designed to be 25 mm in diameter and 60 mm long, each containing about 1.5 moles of solid HD. Fig. 7 shows a representative schematic of their mounting. Details of pins for manipulating the targets one at a time are not shown. In the cryostat in which the target cells will be filled with HD, the targets will be loaded separately, each in its own berth, from a central gas loading system which can access each target cell position. In the storage configuration, the targets will be placed in tandem, so that a strong magnetic field from a long solenoid can insure they all will have very long relaxation times.

7. Summary

Very long relaxation times for protons and deuterons in solid HD have been obtained at very accessible frozen-spin operational conditions, insuring a match between the production time of polarized targets and their usage time, in weakly ionizing beams. These include photon beams, muon beams, and even more strongly ionizing beams which can take advantage of the large targets and their high thermal conductivity at the temperatures of usage, and raster over them. The system is being assembled for experiments at the LEGS facility at BNL for operation in early 1996.

References

- [1] M. Bloom, *Physica* 23 (1957) 767.
- [2] W.N. Hardy and J.R. Gaines, *Phys. Rev. Lett.* 17 (1966) 1278.
- [3] A. Honig, *Phys. Rev. Lett.* 19 (1967) 1009.
- [4] R.S. Rubins, A. Feldman and A. Honig, *Phys. Rev.* 269 (1968) 299.
- [5] A. Honig, *Proc. Int. Conf. on Polarized Targets*, ed. G. Shapiro, Berkeley (1971) p. 99.
- [6] A. Honig, *Proc. Symp. on Experiments Using Enriched Antiproton, Polarized Proton and Polarized Antiproton Beams at Fermilab Energies*, Argonne National Laboratory Report No. ANL-HEP-CP-77-45, edn. H. Yokosawa, Argonne Natl. Lab (1977) p. 186.
- [7] H. Mano, Ph. D. thesis, Syracuse University, 1978, unpublished.
- [8] H.M. Bozler and E.H. Graf, *Proc. 2nd Int. Conf. on Polarized Targets*, ed. G. Shapiro, Berkeley (1971) p. 103.
- [9] E.H. Graf, *Brookhaven Natl. Laboratory Workshop on Physics with Polarized Targets*, BNL Report # BNL29415 (1974) p. 345.
- [10] J.A. Brown, Ph. D. thesis, State University of New York at Stony Brook, 1977, unpublished.
- [11] H. Mano and A. Honig, *Nucl. Instr. and Meth.* 124 (1975) 1.
- [12] A. Honig and H. Mano, *Phys. Rev. B* 14 (1976) 1858.
- [13] R.M. Kulsrud, H.P. Furth, E.J. Valeo and M. Goldhaber, *Phys. Rev. Lett.* 49 (1982) 1248.
- [14] A. Honig, N. Alexander and S. Yucel, *Workshop on Muon-Catalyzed Fusion, Sanibel Island, FL., May 2–6, 1988*, eds. S.E. Jones, J. Rafelski and H.J. Monkhorst, *AIP Conf. Proc. No. 181* (1989) 199.
- [15] Y.-L. Pan and S.P. Hatchett, *Nucl. Fusion* 27 (1987) 815.
- [16] A. Honig, N. Alexander, Q. Fan, X. Wei and Y.Y. Yu, *Workshop on Polarized Ion Sources and Polarized Targets*, University of Wisconsin, Madison, May 23–27, 1993, eds. L.W. Anderson and W. Haeberli, *AIP Conf. Proc. No. 213* (1994) 50.
- [17] N. Alexander, J. Barden, Q. Fan and A. Honig, *Rev. Sci. Instr.* 62 (1991) 2729.
- [18] A. Honig, Q. Fan, X. Wei, M. Rigney, A.M. Sandorfi and C.S. Whisnant, to be presented at the 11th Int. Symp. on High Energy Spin Physics and the Eighth Intl. Symp. on Polarization Phenomena in Nuclear Physics, Bloomington, Indiana, Sept. 15–22, 1994.
- [19] J.H. Constable and J.R. Gaines, *High Field NMR Thermometry Below 1 K Using HD*, 5th Symp. on Temperature, Washington, DC, June 1971.



ELSEVIER

The SMC polarized target

J. Kyyräinen

CERN, Geneva, Switzerland

On behalf of the Spin Muon Collaboration

Abstract

The Spin Muon Collaboration (SMC) at CERN uses the largest solid polarized target in operation to measure the spin-dependent structure functions of the nucleons. The target is made of butanol, doped with EHBA-Cr(V), and has a volume of $2 \times 1280 \text{ cm}^3$. The target halves are dynamically polarized to opposite directions to minimize many systematic errors, and the spin orientation can be reversed by rotating the magnetic field in the frozen spin mode without losses. Frequency modulation of the microwaves is used to increase the maximum polarization and the growth rate. The polarization is measured with 10 series Q -meters with an accuracy of 3–5%.

1. Introduction

Polarized deep inelastic lepton–nucleon scattering is used by the SMC to measure the spin-dependent structure functions g_1^p and g_1^d of the proton and the deuteron [1–3]. In the experiment longitudinally polarized 100–190 GeV muons are scattered from polarized nucleons in a solid target. The measured quantity is the asymmetry

$$A = \frac{(N^{\uparrow\downarrow} - N^{\uparrow\uparrow})}{(N^{\uparrow\downarrow} + N^{\uparrow\uparrow})} \quad (1)$$

in the counting rates $N^{\uparrow\downarrow}$ ($N^{\uparrow\uparrow}$) for antiparallel (parallel) spin orientations. The physical asymmetry follows from this, taking into account target and beam polarizations, the amount of unpolarized nucleons in the target, and corrections involving the depolarization factor, radiative effects etc. [1].

The collaboration has verified a fundamental QCD (Bjorken) sum rule

$$\int_0^1 (g_1^p - g_1^n) dx = 0.185 \pm 0.004 \quad (2)$$

to a 10% level [3] but has found deviation from the Ellis–Jaffe sum rule based on naive quark models. This can be interpreted as an unexpectedly small contribution to the nucleon spin from the valence quarks. The neutron structure function g_1^n is determined from those of the proton and the deuteron. The quantity x is the momentum fraction of the struck quark. Measurement of the transverse structure function g_2^p of the proton has also been carried out with transversely polarized target [4].

Data taking started in 1991 with the modified EMC target [5], and the new SMC target was inaugurated in 1993. The experiment will continue until 1995 to improve the statistics.

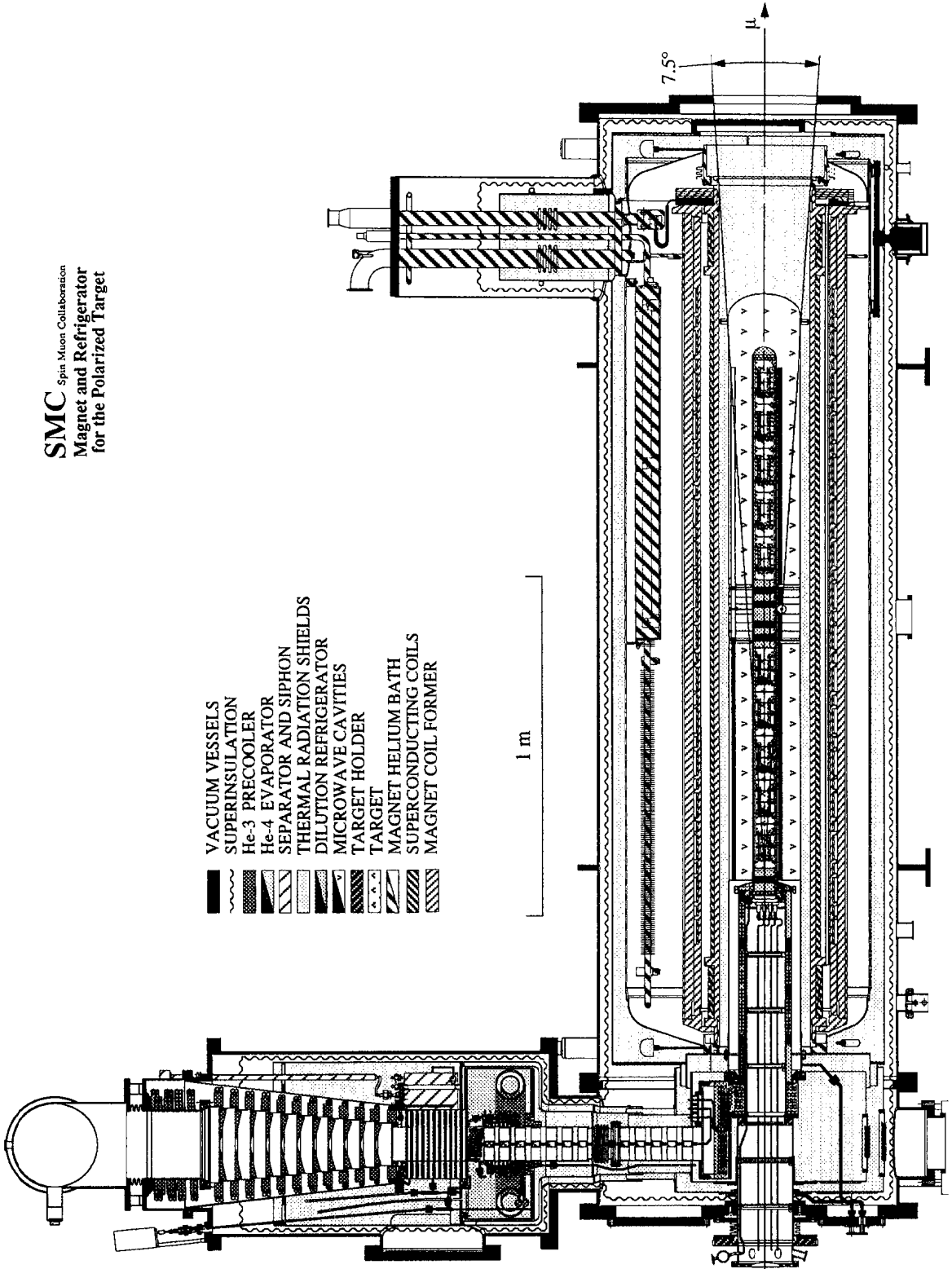
2. Target material and geometry

The asymmetry A is at most on the order of 10^{-2} and therefore it is important to eliminate sources for false asymmetries as well as possible. SMC uses a tandem target configuration in which the same beam penetrates oppositely polarized target halves. This cancels to a large extent the effect of beam flux variations. The method requires, however, that the spin directions of the halves are frequently reversed to eliminate the drift of the geometrical acceptance ratio and the effect of different amount of material in the target halves.

The material is 1-butanol containing 5 wt% of water and 4 wt% of EHBA-Cr(V) as the paramagnetic dopant [6]. All the components are either normal or perdeuterated. This material was preferred because of the absence of polarized background compared to ammonia and a higher dilution factor compared to propanediol. The material is frozen into spherical beads of 1.8 mm in diameter by dripping the room temperature liquid mixture into liquid nitrogen. Rapid freezing ensures that the material transforms into a glassy state which is required for the homogeneous distribution of the paramagnetic centres.

The target has two identical cells with a length of 650 mm (600 mm in 1993) and a diameter of 50 mm which

SMC Spin Muon Collaboration
Magnet and Refrigerator
 for the Polarized Target



- VACUUM VESSELS
- SUPERINSULATION
- He-3 PRECOOLER
- He-4 EVAPORATOR
- SEPARATOR AND SIPHON
- THERMAL RADIATION SHIELDS
- DILUTION REFRIGERATOR
- MICROWAVE CAVITIES
- TARGET HOLDER
- TARGET
- MAGNET HELIUM BATH
- SUPERCONDUCTING COILS
- MAGNET COIL FORMER

1 m

7.5°

μ

covers almost fully the muon beam with a rms spot size of $16 \times 15 \text{ mm}^2$ for 100 GeV muons. Resolution for the vertex reconstruction requires a gap of 200 mm (300 mm in 1993) between the halves. The position of the target itself is known within a few millimeters with respect to the muon spectrometer. The gross volume of the target is $2 \times 1280 \text{ cm}^3$ and the filling factor of the material is about 0.63 [6].

The target holder has two main parts, a metallic vacuum vessel to provide thermal isolation against room temperature and a plastic part confining the material itself. The vacuum chamber has two 0.1 mm stainless steel windows for the beam access and six aluminium thermal radiation shields, and provides thermal anchors for the NMR and thermometry cables. The plastic part is mostly made of Kevlar–epoxy composite for rigidity and small thermal contraction. Good convective thermal transfer is assured by making the target containers of polyester net with 60% open area. The containers weigh only 30 g each; the NMR signal from the protons in the target holder was measured to be only 1% of the size of the thermal equilibrium signal of the protons in target material at 1 K.

Loading of the material from storage dewars into the target holder is done in a special LN_2 bath to prevent the material from overheating, and then the target holder is pushed directly into the precooled mixing chamber of the dilution refrigerator. During loading helium gas is blown to the access tube of the refrigerator to prevent air and humidity condensing into it.

3. Dilution refrigerator

The large target size necessitates a high cooling power refrigerator to shorten the polarization build-up time. Due to economical constraints the pumping system from the EMC target is used, a set of eight Roots blowers in series with a nominal pumping speed of $13500 \text{ m}^3/\text{h}$ for ^3He . An internal gas purification system of the pumps and a series of two activated charcoal traps are used to filter out impurities in the ^3He return flow. Another set of pumps with a volume speed of $2000 \text{ m}^3/\text{h}$ is used to pump the evaporator and the microwave cavity cooling circuit.

The refrigerator [7] is L-shaped with vertical and horizontal vacuum chambers housing the precooling tower and the dilution refrigerator, respectively. It extends partly into the superconducting magnet, and shares the common isolation vacuum (see Fig. 1). The target holder slides into the horizontal access tube and is sealed with a cold indium seal at the still back flange. The mixing chamber is made of glass-fibre reinforced epoxy and has a length of 1500 mm and a wall thickness of 0.6 mm. The main heat exchanger is placed in a helicoidal groove around the target holder vacuum chamber and features an extended surface area made of 750 g of sintered copper powder.

The precooler has two 4-way heat exchangers to cool

the incoming ^3He gas and ^4He liquid before entering the evaporator, resulting into considerable economy in the use of liquid ^4He . The flow rate of ^4He corresponds to liquid boil-off between 15 l/h and 40 l/h depending on the ^3He flow rate which has practical minimum and maximum values of 27 and 350 mmol/s with the ^4He contamination less than 25%. A 100 l/h liquifier supplies liquid ^4He both to the dilution refrigerator and to the superconducting magnets via a 2000 l buffer dewar.

The base temperature of the refrigerator is about 30 mK, measured in the downstream end of the mixing chamber, and the cooling power is about 1 mW at 50 mK, 15 mW at 100 mK, 400 mW at 300 mK and reaches 1.3 W at 500 mK. Axial temperature uniformity in the mixing chamber is better than 30 mK at the base temperature. Temperature is measured with 4-wire AC bridges using calibrated RuO and carbon resistors, part of which are shielded against the microwave field.

4. Magnet system

The superconducting magnet system [8] has three concentric coil systems running in nonpersistent mode: A 2.5 T main solenoid with a homogeneity of better than 6×10^{-5} over the target volume, a 0.5 T dipole with a homogeneity of 0.1 and 16 correction coils for the solenoidal field. The magnet bore is 265 mm and the free angle 7.5° .

A special feature of the magnet system is the possibility to rotate the magnetic field by 180° in about 30 min. This is done by first sweeping the main field to 0.5 T and then synchronously operating the solenoidal and dipolar fields to reverse the field direction and finally sweeping the main field back to 2.5 T. Before the rotation the magnetic field is made inhomogeneous with the correction coils to prevent polarization loss of the negatively polarized protons due to superradiance. The dipolar winding was also used for producing the transverse holding field during the measurement of g_2^p .

5. Microwave system

A double microwave system is needed for simultaneous dynamic nuclear polarization (DNP) with opposite signs in the target halves. Two Extended Interaction Oscillator (EIO) tubes with a maximum output power of 20 W are used as microwave sources and the power is led through isolators, attenuators, couplers and oversized waveguides to the cryostat. The vacuum feedthroughs have FEP plastic windows, and inside the cryostat the thermal isolation is made with silvered $\varnothing 4 \text{ mm}$ CuNi tubes which are continued with K-band waveguides soldered to the microwave cavity walls. The coupling to the cavity is through tapered holes along the full length of the target, and the power

reflected back from the cavity is less than 10% of the input power. A layout of the complete microwave system is shown in Fig. 2.

The multimode copper microwave cavity has a diameter of 210 mm and is split into two halves by a microwave isolator made out of copper and graphite foils. Its measured attenuation is 20–30 dB at 69 GHz. The part of the isolator inside the mixing chamber has graphite painted honeycomb as absorbing material not to block the diffusion of ^3He and convection currents.

About 1 kHz signals are added to the cathode voltages of the EIO tubes, with amplitudes adjusted so as to produce peak modulation of about 30 MHz in the output microwave frequencies. This has been shown to increase the polarization growth rate by 20% and the maximum polarization by 10% for protons and 50% for deuterons. A more detailed discussion on the frequency modulation is given in Ref. [9].

6. Magnet and cryogenic control and safety systems

User-friendly graphic interfaces running in a Unix workstation and X terminals have been implemented to control the magnet and the dilution refrigerator. The con-

trol programs are running in VME processors [10]. More than 100 cryogenic and magnet parameters are logged and used for alarm generation. Most readout instruments are read via a GPIB bus, either directly or via a 32-channel data logger/plotter.

Magnetic field rotation is fully automated and the needle valve for evaporator filling is computer controlled. Other controls include the separator and microwave cavity flow rates and the still heater. The latter is to be controlled by the microwave power to optimize the cooling power of the dilution refrigerator.

The magnet has a separate hardware security system and the dilution refrigerator a PLC-based interlock system, powered by a 48 V uninterruptible supply to protect the target against loss of polarization and loss of ^3He .

7. NMR and polarization measurement

The polarization measurement is based on determining the area of the absorptive part of the spin susceptibility $\chi''(\omega)$:

$$P = \frac{2}{\pi \hbar \gamma^2 N I} \int_0^\infty \chi''(\omega) d\omega \cong C \int_{\omega_0 - \Delta\omega/2}^{\omega_0 + \Delta\omega/2} S(\omega) d\omega, \quad (3)$$

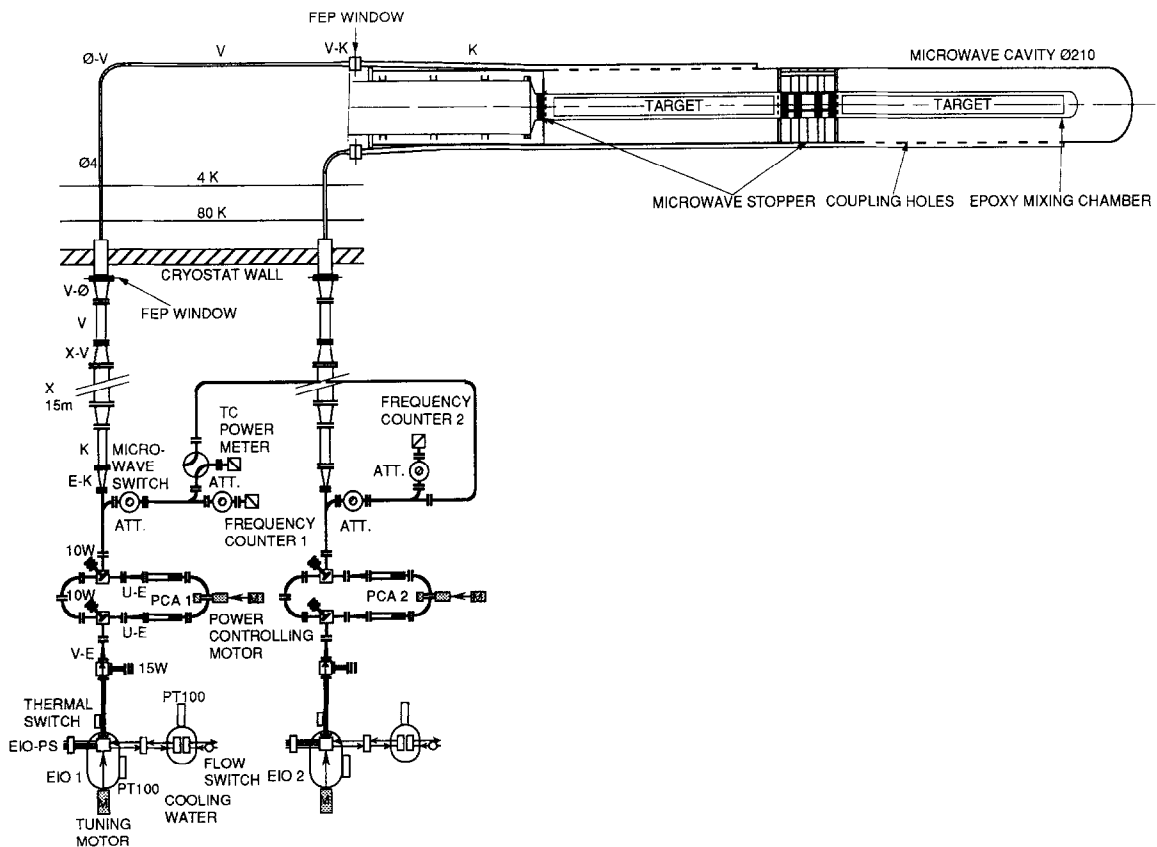


Fig. 2. The microwave system.

where S is the measured signal size, ω_0 is the Larmor frequency and $\Delta\omega$ is the width of the frequency sweep. The proportionality constant C is determined by calculating the polarization using the Curie law

$$P_{TF} = \frac{\hbar \omega_0 (I + 1)}{3kT_0} \quad (4)$$

at a known temperature T_0 at which the spin system is brought into equilibrium with the lattice.

The NMR signal is measured using 10 series Q -meters [11], with the NMR coils distributed along the target length to account for possible inhomogeneity of the polarization. We have used both buried and saddle type coils, the latter designed for a cross-coil configuration with excitation coils inside the microwave cavity. Gaps between neighbouring coils are 4–5 cm to reduce the mutual inductance. Large diameter tube as the coil material or PTFE coating around the coil decreases the rf field strength close to the coil and thereby makes the sampling more uniform. The room temperature part of the tuned cables is temperature stabilized as well as the analog part of the NMR electronics.

A CAMAC based microprocessor controls the sweep of the frequency synthesizer, the S/H-amplifiers and the D/A-converters and averages over the sweeps used for one measurement. The signal is measured at 400 points in the $\Delta\omega = 500\text{--}600$ kHz wide sweep and the numbers are then send to a minicomputer for signal integration. The parabolic baseline of the Q -meter signal is measured by shifting the field outside the resonance. The user interface for the NMR control resides also on the minicomputer [12]. A block diagram of the NMR system is shown in Fig. 3.

The calibration of the measurement system is done at 0.95–1.7 K with pure ^4He circulated in the refrigerator. This assures good temperature uniformity throughout the target volume and a short spin–lattice relaxation time, on the order of 1 min. Temperature is varied by the pumping speed or by the still heater and is measured with a ^3He vapour pressure thermometer; 2–3 days are normally needed to collect a sufficient amount of calibration data.

In the case of the deuterated target, typically 2000–10000 sweeps are required for one signal to enhance the signal-to-noise ratio where the noise is dominated by that of the synthesizer. Largest sources of error are the magne-

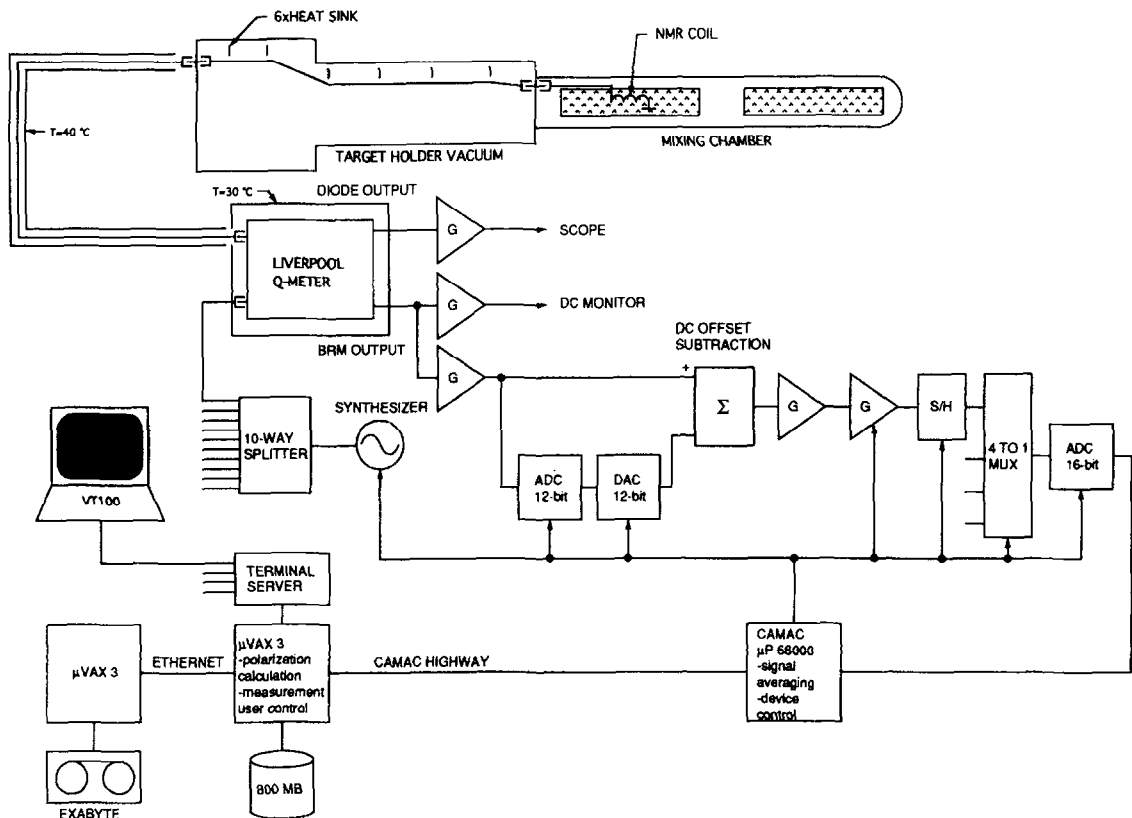


Fig. 3. Block diagram of the NMR system. Only one complete channel out of ten is shown. There are three multiplexers, 16-bit DACs and CAMAC microprocessors in the system.

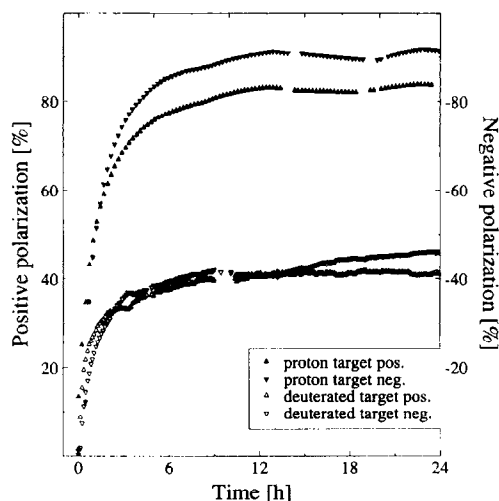


Fig. 4. Example of polarization build-up for proton and deuteron targets. The breaks in the data points correspond to magnetic field rotations.

toresistance of the NMR cables and the drift of the Q -meter circuit. In the proton target the nonlinearity of the Q -meter limits the accuracy of the measurement of the enhanced signal [13]. The overall accuracy of the polarization measurement is $\pm 3\%$ for protons [14] and $\pm 5\%$ for deuterons.

8. Performance

The cooldown of the magnet from room temperature to 4 K takes about one week, after which the dilution refrigerator can be cooled in 8 h to 77K at which the target is loaded. Final cooldown and condensing the ^4He - ^3He mixture takes less than 8 h.

The cooling power of the dilution refrigerator, limited mostly by the throughput of the pumps, sets limits to the growth rate of the polarization. A typical polarization build-up history in the beginning of DNP is shown in Fig. 4. The applied microwave power in the beginning of DNP is on the order of 2×200 mW and is gradually dropped to 2×50 mW in the end, corresponding to the ^4He - ^3He mixture temperature of 200 mK. The maximum polarizations obtained in the proton and deuteron targets are $\pm 94\%$ and $\pm 46\%$, respectively, and the average polarization for the proton target in 1993 run was $\pm 86\%$. About 95% of the maximum polarization is typically reached within 10 h of polarizing. The longitudinal homogeneity of the polarization is better than 3% and there is no evidence for radial inhomogeneity which was established by two NMR coils set at different radial distances.

In regular operation the polarization is reversed by DNP once per week and a field rotation is carried out

every 5 h. The spins are cooled down below 100 mK by turning off the microwave power 30 min before the rotation. As seen in Fig. 4, practically no loss of polarization takes place during the field rotation. Also the data taking of the main experiment stops only for about 10 min while the dipole magnet is powered.

9. Summary

In the SMC polarized target the limits of solid target technology have been extended further. A twin target configuration decreases the systematic errors considerably. The use of a dilution refrigerator and orthogonal magnetic fields enables one to manipulate the spin direction vector in the frozen spin mode without losses of polarization. We have shown that high and homogeneous polarizations can be reached and measured accurately in a target with extended dimensions. The practical limit of the target size is set by the cooling power of the dilution refrigerator, determined by the available pumping speed of ^3He .

References

- [1] B. Adeva et al. (Spin Muon Collaboration), Phys. Lett. B 302 (1993) 533.
- [2] B. Adeva et al. (Spin Muon Collaboration), Phys. Lett. B 320 (1994) 400.
- [3] D. Adams et al. (Spin Muon Collaboration), Phys. Lett. B 329 (1994) 399.
- [4] D. Adams et al. (Spin Muon Collaboration), Phys. Lett. B 336 (1994) 125.
- [5] S. Brown et al., Proc. 4th Int. Workshop on Polarized Target Materials and Techniques Bad Honnef, 1984, ed. W. Meyer, Univ. Bonn, p. 102.
- [6] S. Bültmann et al., these Proceedings (7th Workshop on Polarized Target Materials and Techniques, Bad Honnef, Germany, 1994) Nucl. Instr. and Meth. A 356 (1995) 102.
- [7] P. Berglund, J. Kynnäräinen and T.O. Niinikoski, Cryogenics 34 ICEC Suppl. (1994) 235.
- [8] A. Daël et al., IEEE Trans. Magn. 28 (1992) 560.
- [9] Y. Kisselev, these Proceedings (7th Workshop on Polarized Target Materials and Techniques, Bad Honnef, Germany, 1994) Nucl. Instr. and Meth. A 356 (1995) 99.
- [10] J.-M. Le Goff et al., *ibid.*, p. 96.
- [11] B. Adeva et al. (Spin Muon Collaboration), Nucl. Instr. and Meth. A 349 (1994) 334.
- [12] N. Hayashi et al., these Proceedings (7th Workshop on Polarized Target Materials and Techniques, Bad Honnef, Germany, 1994) Nucl. Instr. and Meth. A 356 (1995) 91.
- [13] Y. Semertzidis et al., Non-linearities in the proton NMR-signal, presented at this Workshop (7th Workshop on Polarized Target Materials and Techniques, Bad Honnef, Germany, 1994).
- [14] D. Krämer, these Proceedings (7th Workshop on Polarized Target Materials and Techniques, Bad Honnef, Germany, 1994) Nucl. Instr. and Meth. A 356 (1995) 79.



ELSEVIER

The PSI 100 cm³ frozen spin target

B. van den Brandt *, P. Hautle, J.A. Konter, S. Mango

Paul Scherrer Institut, CH-5232 Villigen PSI, Switzerland

Abstract

For measurements of the 2-spin and 3-spin transfer parameters in the n–p system in the 300–600 MeV range, a large (100 cm³) frozen spin polarized target has been built and put into operation at PSI. The holding coil system allows a virtually arbitrary polarization direction, quick polarization reversal and large opening angles.

1. The magnet system

For dynamically polarized targets a magnetic field in the range of 2.5–5 T with a homogeneity of 10⁻⁴ over the target volume is required to achieve sizeable polarizations. At the same time large opening angles from the target to the detectors are necessary. These requirements are difficult to fulfill for a large target. For this reason the so-called frozen spin target concept has been developed [1].

We have built a system in which a 100 cm³ target is dynamically polarized in a high homogeneity superconducting solenoid, housed in a room temperature bore cryostat, surrounding the target dilution refrigerator. (see Fig. 1).

In a second step the target polarization is frozen in by lowering the temperature to $T_{\min} \approx 50$ mK and subsequently the magnetic field B to 0.8 T. Then the magnetic field is taken over by a holding coil system, integrated in the target refrigerator cryostat, and the polarization solenoid is removed from its polarizing i.e. beam obstructing position (see Fig. 2).

The holding coil system consists of a split pair magnet and a saddle coil magnet, providing resp. the vertical and horizontal holding fields (see Fig. 4).

A linear combination of these fields together with the rotatability of the cryostat around the vertical axis, in dilution mode, allows virtually any quantization direction in space, only limited by the two pillars of the magnet support (see Fig. 3).

Moreover, the twofold coil system allows a quick polarization reversal by magnetic field rotation. Initial tests have shown a reversal time of 12 min.

The characteristics of the magnet system are:

- Polarizing coil: 5 T coil in room temperature bore cryostat; $B \parallel z$ -axis (vertical); $\Delta B/B \approx 1.7 \times 10^{-4}$ over 100 cm³ cube; cryostat vertically moveable.

- Vertical holding coil: 1.2 T superconducting split pair coil in target cryostat; $B \parallel z$ -axis; $\Delta B/B \approx 10\%$ over the target volume.
- Horizontal holding coil: 1.1 T superconducting saddle coil in target cryostat; $B \perp z$ -axis; $\Delta B/B \approx 7\%$.
- Opening angles of holding coil system (see Fig. 3): $2\alpha = 145^\circ$; $2\beta = 100^\circ$; $\phi = 165^\circ$.
- Dimensions of holding coil system: $r_i = 73$ mm; $r_o = 110$ mm.

2. The dilution refrigerator

The vertical dilution refrigerator (Fig. 1), constructed at PSI, has been incorporated in a cryostat in which also the twofold superconducting holding coil system has been integrated.

The main He reservoir, supplanting the magnet system, serves at the same time as a buffer volume for the two precooling loops of the dilution refrigerator insert.

Precooling of the incoming ³He is accomplished in a triple exchanger between two streams of ⁴He from the 4.2 K and sub- λ bath, with maximal recovery of the enthalpy of the outgoing ³He-gas from the inside pumping tube (Fig. 4).

Condensation of the mixture takes place in a ⁴He pot at ≈ 1.2 K.

The target loading is performed with an up-scaled version of a former PSI design [2], in which the target cell is an integral part of a central insert. This insert rod essentially consists of a cylindrical waveguide plus baffle system and a Vespel block with a 5° conical section, mating the central access hole in the supporting structure of the heat exchanger.

This loading system enables us to load a rectangular target cell into an also rectangular mixing chamber, thus minimizing the amount of background material in the target region.

At present, we have implemented a cylindrical mixing chamber and target cell. A dummy target, mounted under-

* Corresponding author.

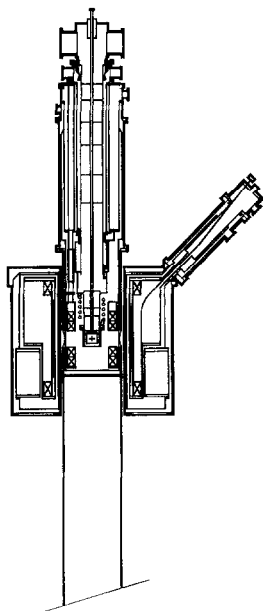


Fig. 1. Target in polarization mode.

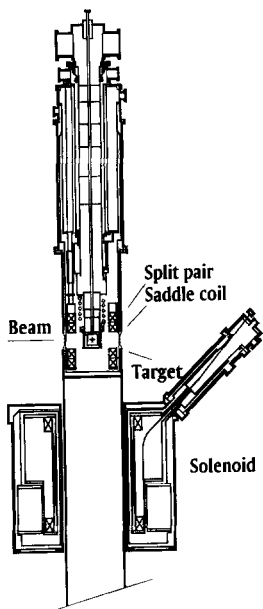


Fig. 2. Target in frozen spin mode.

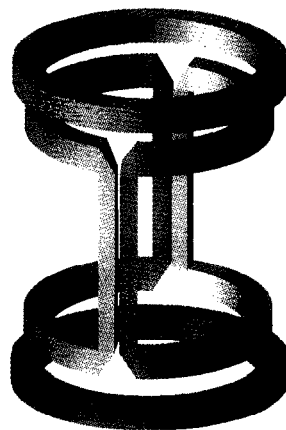


Fig. 4. Schematic drawing of the holding coils arrangement, showing the split pair for the vertical field and the saddle coil for the horizontal field.

neath the target cell in the mixing chamber, can be advanced on beam for background measurements, without interrupting the refrigerator operation (see Fig. 5).

The present version of the dilution refrigerator is equipped with a single concentric heat exchanger between still and mixing chamber. The minimum temperature which can be achieved is around 50 mK. In frozen spin mode relaxation times of about 1100 h have been reached in 0.8 T.

At high circulation rates, the cooling power is lagging behind the expectations because of a too high ^4He – ^3He ratio of the circulating mixture, contrary to measurements in the initial phases of the development. This puzzling behaviour has to be investigated further.

3. The pumping system

The pumping and gas-handling system pertaining to the dilution refrigerator, are designed for a circulation rate of $\dot{n}_3 = 30$ mmol/s.

The pumping system comprises of a series combination of Roots blowers Balzers WKP 4000, Alcatel RSV 1000, RSV 300B and ADP 80, all equipped with canned motors and compressing completely oil-free.

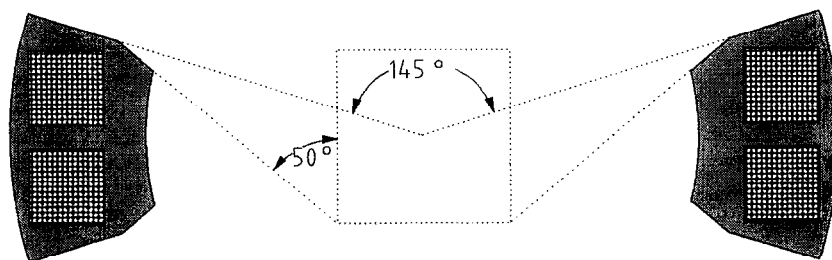


Fig. 3. Horizontal cut through pillars of the holding coil system showing the opening angles.

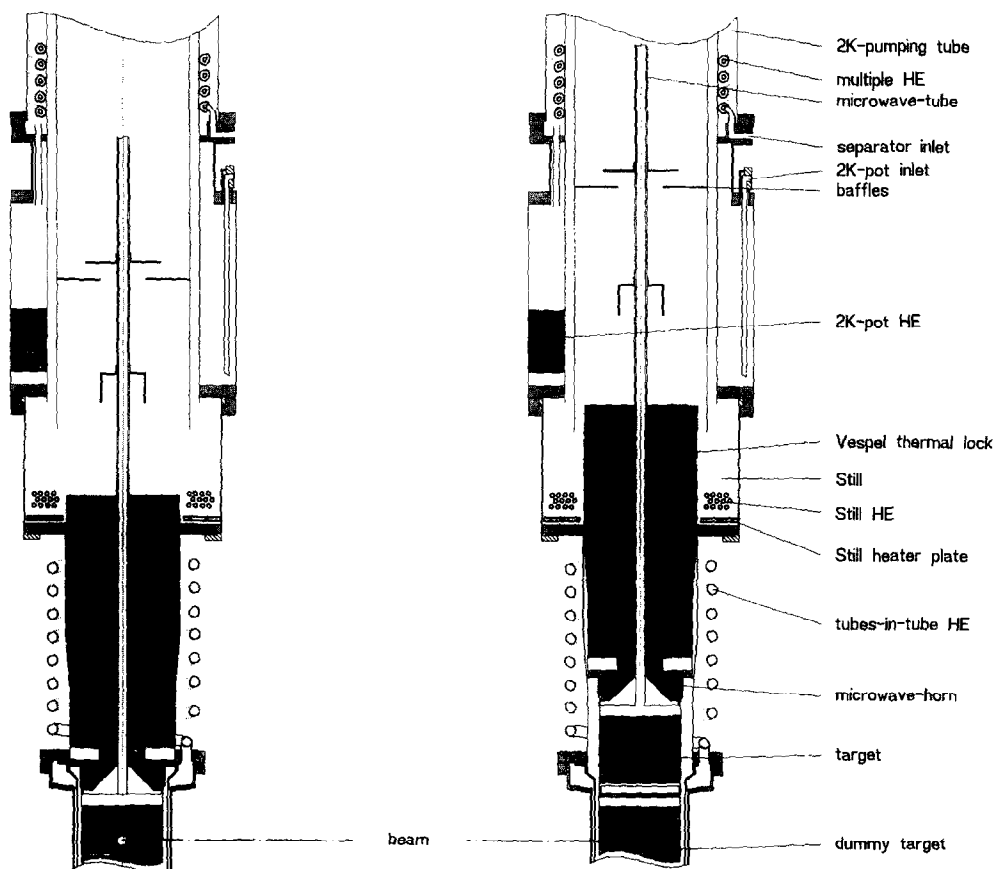


Fig. 5. Dilution refrigerator, with the central access top loading rod in the down position (target on beam, dilution mode) (left drawing) and (right drawing) in the lifted-up position (dummy target in beam height).

4. Performance

The system, installed on the NA2 polarized neutron beam line, has been in operation for several physics runs now.

Proton polarizations of up to 80% could be achieved in a 100 cm^3 target consisting of a 1-butanol/water mixture, doped with $\sim 2 \times 10^{19} \text{ EHBA-Cr}^V/\text{cm}^3$, after $\sim 5 \text{ h}$ of microwave irradiation in 2.5 T, a time-limitation imposed by the cryogenic duty cycle of the magnet.

Polarization decay times have been $\geq 1100 \text{ h}$ at $T \leq 70 \text{ mK}$ in a holding field of 0.8 T.

Rotation of the holding field had no detectable influence on the polarization decay time.

Polarization reversal by AFP on the proton system, with a HF coil geometry by far not optimized, helped in the last run to achieve the highest polarization reported.

References

- [1] T.O. Niinikoski and F. Udo, Nucl. Instr. and Meth. 134 (1976) 219.
- [2] B. van den Brandt, J.A. Konter and S. Mango, Nucl. Instr. and Meth. A 289 (1990) 526.

The CHAOS polarized proton target

P.P.J. Delheij ^{*}, I. Sekachev

TRIUMF, 4004 Wesbrook Mall, Vancouver, BC, V6T 2A3, Canada

Abstract

The CHAOS polarized proton target (CPPT) is a new dynamically polarized target for the recently commissioned Canadian High Acceptance Orbit Spectrometer at TRIUMF. The target must travel 2 m through a field-free region between the polarizing magnet and the spectrometer magnet. Therefore, a superconducting magnet, giving a field of 0.13 T on the target, is incorporated in the cryostat shell surrounding the dilution refrigerator. The magnetic field in the spectrometer will be as low as 0.5 T. These conditions require operation in frozen spin mode. Particle access and exit is by two windows spanning 320° in the horizontal plane. Vertically the opening angle is ±20°. The energy of the incident particles will be as low as 30 MeV. This requires very thin windows. A major goal is the determination of the $\pi N \sigma$ -term from low energy pion scattering. Then the strange sea quark content of the proton can be derived.

A new dynamically polarized target has been built for the CHAOS spectrometer at TRIUMF, which started operation recently. The spectrometer has a very large opening angle of 360° in the horizontal plane and ±20° in the vertical direction. The target provides an opening angle of 320° because two window support posts span each only 20° in the angular range. In the vertical directions the full 40° is supported. An important measurement is the determination of the analyzing power for elastic scattering of pions with an incident energy as low as 30 MeV. Extrapolation of the scattering amplitudes to zero energy and the application of chiral perturbation theory will set limits for the strange sea quark content of the proton.

The process of dynamic polarization is planned for the conventional magnetic field of 2.5 T with a microwave frequency of 70 GHz. However, the magnetic field in the spectrometer is only 1.4 T. Furthermore, the homogeneity is not sufficient for the process of dynamical polarization. Therefore, the polarized target must be transported over a distance of 2 m between the polarizing position in a solenoid with high homogeneity, which is located on top of the spectrometer and the scattering position in the spectrometer. To preserve the polarization, a magnetic field must be applied during the transport. Therefore, a superconducting magnet, giving a minimum magnetic field of 0.13 T on the target, is incorporated in the cryostat shell. Due to the space limitations the magnet is very thin. It is wound from multifilament NbTi wire (purchased from Supercon) with a diameter of 225 μm. The magnet con-

sists of 12 layers with 215 windings each. In a liquid helium bath the magnet could carry 34 A which exceeds the critical current specification for the superconducting

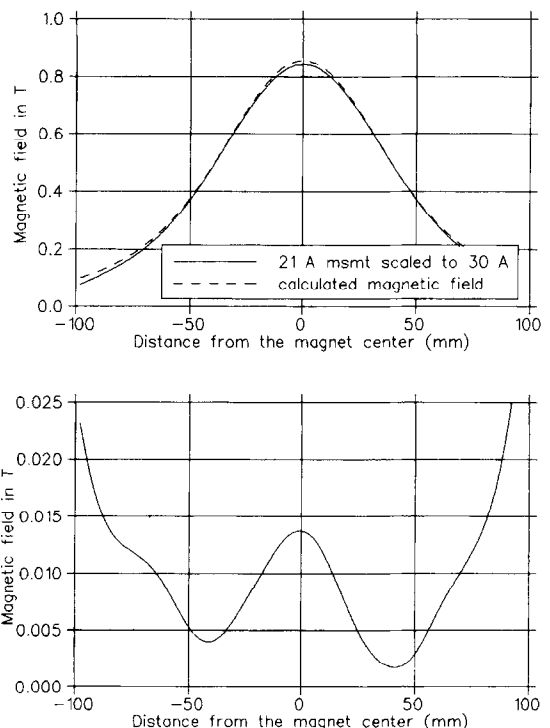


Fig. 1. Top: The measured and calculated magnetic fields on the axis of the holding magnet. Bottom: The difference of the measured and calculated values.

^{*} Corresponding author.

wire by a few percent. The calculated and measured magnetic fields are shown in Fig. 1. The measurement at 21 A is scaled to 30 A but it is not renormalized to the calculated curve. In the lower part of the figure the difference of these two curves is plotted. The agreement between the calculation and the measurement is very good with the difference being typically less than 1%. In the vacuum space of the cryostat only 19 A can be sustained. No spike from an induction voltage is observed when the magnet goes normal. A carbon glass thermometer on the magnet points to a thermal runaway. A redesign of the current leads might improve this.

The design of the ^3He - ^4He dilution refrigerator followed largely the scheme that we successfully developed previously [1]. The refrigerator consists of a tubular counter flow heat exchanger, ^4He pots at a temperature of 4.2 K and 1.3 K respectively, tubular still heat exchangers, and a dilution stage mounted on a phenolic plug. A temperature of 80 mK was reached exceeding the goal of 100 mK. The

^3He flow rate was 5 mmol/s. In comparison with the previous refrigerator the number of sintered copper heat exchangers was increased from two to six. The operation can be improved if the heat leak of approximately 1 mW can be reduced. A new pumping system has been assembled around a Balzers WKP-4000 Roots pump. Also a new control system was built based on a Motorola 68040 processor in VME. Over Ethernet any X-window terminal can control the setup. Remotely pumps can be turned on or off, solenoid valves opened or closed, settings of mass flow controllers changed, heater output modified etc. Also all sensors, like thermometers, pressure transducers, flow meters etc. are read into the computer.

References

- [1] P.P.J. Delheij, D.C. Healey and G. Wait, Nucl. Instr. and Meth. A 264 (1988) 186.



ELSEVIER

The movable polarized target as a basic equipment for high energy spin physics experiments at the JINR-Dubna accelerator complex

F. Lehar ^{a,*}, B. Adiashevich ^b, V.P. Androsov ^c, N. Angelov ^d, N. Anischenko ^e,
V. Antonenko ^b, J. Ball ^c, V.G. Baryshevsky ^g, N.A. Bazhanov ^h, A.A. Belyaev ^c,
B. Benda ^a, V. Bodyagin ⁱ, N. Borisov ^d, Yu. Borzunov ^e, F. Bradamante ^j,
E. Bunyatova ^d, V. Burinov ^d, E. Chernykh ^e, M. Combet ^f, A. Datskov ^e, G. Durand ^a,
A.P. Dzyubak ^c, J.M. Fontaine ^f, V.A. Get'man ^c, M. Giorgi ^j, L. Golovanov ^e,
V. Grebenyuk ⁱ, D. Grosnick ^k, G. Gurevich ^l, T. Hasegawa ^m, D. Hill ^k, N. Horikawa ⁿ,
G. Igo ^o, Z. Janout ^p, V.A. Kalinnikov ^d, I.M. Karnaukhov ^c, T. Kasprzyk ^k,
B.A. Khachaturov ^d, A. Kirillov ^e, Yu. Kisselev ^q, E.S. Kousmine ^d, A. Kovalenko ^e,
A.I. Kovaljov ^h, V.P. Ladygin ^e, A. Lazarev ^d, Ph. Leconte ^a, A. de Lesquen ^a,
A.A. Lukhanin ^c, S. Mango ^r, A. Martin ^j, V.N. Matafonov ^d, E. Matyushevsky ^e,
S. Mironov ^c, A.B. Neganov ^d, B.S. Neganov ^q, A. Nomofilov ^c, V. Perelygin ^q,
Yu. Plis ^d, Yu. Pilipenko ^c, I.L. Pisarev ^d, N. Piskunov ^e, Yu. Polunin ^b, Yu.P. Popkov ^c,
A.A. Propov ^c, A.N. Prokofiev ^h, M.P. Rekalo ^c, P. Rukoyatkin ^c, J.L. Sans ^f,
M.G. Sapozhnikov ^d, V. Sharov ^e, S. Shilov ^d, Yu. Shishov ^e, I.M. Sitnik ^e, P.V. Sorokin ^c,
H. Spinka ^k, E.A. Sporov ^c, L.N. Strunov ^e, A. Svetov ^c, J.J. de Swart ^j, Yu.P. Telegin ^c,
I. Tolmashov ^c, S. Trentalange ^o, A. Tsvinev ^e, Yu.A. Usov ^d, V.V. Vikhrov ^h,
C.A. Whitten ^o, S. Zaporozhets ^e, A. Zarubin ^e, A.A. Zhdanov ^h, L. Zolin ^c

^a CEA DAPNIA, CE Saclay, 91191 Gif-sur-Yvette Cedex, France

^b I.V. Kurchatov Institute of Atomic Energy, Kurchatova str. 46, 123182 Moscow, Russian Federation

^c Kharkov Institute of Physics and Technology, Akademicheskaya str.1, 310108 Kharkov, Ukraine

^d Laboratory of Nuclear Problems, JINR, Dubna, Moscow Region 141980, Russian Federation

^e Laboratory of High Energy Physics, JINR, Dubna, Moscow Region 141980, Russian Federation

^f Laboratoire National SATURNE, CNRS / IN2P3 et CEA / DSM, CE-Saclay, 91191 Gif-sur-Yvette Cedex, France

^g Institute of Physics, Belarus Academy of Sciences, 220602, Minsk, Belarus

^h Physics Department, Peterburg Nuclear Physics Institute, 188350 Gatchina, Russian Federation

ⁱ Faculty of Physics, Moscow State University, 117234 Moscow, Russian Federation

^j INFN Trieste and University of Trieste, Department of Physics, 34127 Trieste, Italy

^k ANL-HEP, 9700 South Cass Ave., Argonne, IL 60439, USA

^l Institute for the Nuclear Research of the Russian Academy of Sciences, 60th Anniversary Prospect, 7A, Moscow 117312, Russian Federation

^m Applied Physics Division, Faculty of Engineering, Miyazaki University, Kihana-dai, Miyazaki, Japan

ⁿ Nagoya University, Furo-Cho, Chikusa-Ku, Nagoya 464, Japan

^o UCLA 405 Hilgard Ave., Los Angeles, CA 90024, USA

^p Faculty of Nuclear Sciences and Physical Engineering, Czech Technical University, Břehová 7, 11519 Prague 1, Czech Republic

^q Laboratory of Particle Physics, JINR, Dubna, Moscow Region 141980, Russian Federation

^r PSI, CH-5232 Villigen, Switzerland

^s Institute for Theoretical Physics, University of Nijmegen, Toernooiveld, 6526 ED Nijmegen, The Netherlands

* Corresponding author.

Abstract

A movable polarized proton target is planned to be installed in polarized beams of the Synchrophasotron–Nuclotron complex in order to carry out a spin physics experimental program at Dubna. The project is described and the first proposed experiments are discussed.

1. Introduction

The Joint Institute for Nuclear Research (JINR) in Dubna has developed and built a new 12 GeV/*c* accelerator with superconducting magnets (the Nuclotron). The Nuclotron polarized deuteron beam reached a momentum of 3.7 GeV/*c* in March 1994, with a convenient intensity and good stability. Beam circulation has been obtained up to a deuteron momentum of 6 GeV/*c*. The Nuclotron will soon replace the old accelerator (the Synchrophasotron) and Dubna will become a unique place for providing 3–12 GeV/*c* polarized deuteron beams with high intensity and good polarization. Using a break-up of accelerated deuterons, it is possible to obtain quasi-monoenergetic polarized neutron and proton beams. A new generation of experiments can be carried out at this accelerator complex.

To get full benefit of this opportunity, the experiments with polarized beams must be performed in conjunction with polarized proton or deuteron targets. Many tests of fundamental laws, particle production as well as most of the energy dependent basic observables, depend on the spins of the beam and target nucleons.

The polarized proton target (PPT), used previously at Fermilab, has become available. Haïssinski, director of CEA-DSM-DAPNIA, CE Saclay, proposed to use this equipment in JINR-Dubna. A collaboration has been set up in order to reconstruct this PPT as a “Movable” Polarized Target (MPT), which could be easily transported from one beam line to another and to get this unit operating in Russia. This will open new possibilities for physicists from the independent states of the former Soviet Union (FSU) and for physicists from the member states of JINR and will also be attractive for scientists from the EEC and from other countries.

In 1993 the collaboration requested a support of 173 000 ECU from “The International Association for the Promotion of Cooperation with Scientists from the Independent States of the Former Soviet Union (INTAS)”. Allocation of 60 000 ECU was obtained for 1994 and the target reconstruction could start. The requested INTAS funds for 1993 and 1994 concern the reconstruction of the polarized target and its installation on the beam line only. We hope to obtain the remaining part of our request in 1995 in order to construct the polarizing magnet and the holding coils. The overall INTAS fund request represents only 15% of a totally new target. Completing the target reconstruction will involve more than 20 manyears of high technological work at Dubna, Moscow, Kharkov and Gatchina.

The Memorandum of Understanding describing the responsibilities, time schedules and budget for the movable target reconstruction, was signed on 20th January 1994 [1]. Later on, Gatchina Institute, Russia (A. Vorobyov) and PSI, Villigen, Switzerland (S. Mango) agreed with the Memorandum and decided to take part in the target reconstruction.

As the use of the polarized target involves a much larger community (19 laboratories from 9 countries), the participating institutes decided to delegate the responsibilities of its long-term management to an International Scientific Users Committee. This Committee will evaluate the relative interest of proposed measurements of physical quantities and will define priorities in order to share the use of MPT. It will include experimentalists and theorists, members of the laboratories participating in the target reconstruction as well as members of the laboratories interested in the physics programs using the movable polarized target. The Committee is foreseen to be constituted in January 1995.

2. Description of the project

The Saclay–Argonne frozen spin PPT, 20 cm long and 3 cm in diameter, was built in 1986–1988 for an experiment at Fermilab (USA). The Fermilab experiment E-704 [2] consisted of five different measurements using 200 GeV proton or antiproton polarized beams in conjunction with the PPT or a liquid hydrogen target. The following measurements were performed:

- 1) Determination of the total cross section difference with longitudinally polarized beams and targets ($\Delta\sigma_L$) in pp and $\bar{p}p$ transmission.
- 2) Elastic pp scattering in the Coulomb–nuclear interference region.
- 3) Primakoff effect used for beam polarization measurements.
- 4) Inclusive production of π^0 .
- 5) Inclusive production of Λ^0 and $\bar{\Lambda}^0$.

Experiment E-704 was closed at the end of 1992; the French owned parts have been shipped back to Saclay and then in March 1994 from Saclay to Dubna. The available ANL-HEP parts, stored in a sea-container at Argonne, were shipped to Dubna in May 1994.

Among the French parts, the superconducting polarizing magnet has been committed, before the beginning of the present project, to another collaboration with Germany.

As a result, the polarizing magnet will not be available earlier than December 1994. A new magnet has then to be built.

Experiments at Dubna will also require transverse polarization. For this purpose, transverse holding coils must be added to the set-up.

All the available parts, to which a few missing parts must be added, will constitute a unique instrument of an important value.

For the physics program in Dubna, the target must be reassembled and upgraded. It needs also to be made transportable from one experimental area to another by bonding firmly every part on separate functional decks. This is the MPT concept:

- All the elements positioned close to the beam line (target cell, magnets, power supplies, dewar, etc.) are set on two decks which can be moved as blocks to set the apparatus in and out of the beam for easy maintenance.
- The pumps will be mounted on a separate deck for easy access during beam operation.
- The control room will be installed inside a trailer. It will include remote controls for the entire operation of the target.

The collaborating laboratories propose to assemble the target at Dubna during 1994, in close co-operation with their various experts. Installation on the beam of the Synchrotron–Nuclotron complex will start in January 1995. Tests of the target will then demonstrate its operability.

The whole project is divided into five distinct parts. Each of them is well defined and will be terminated by an operating status and clear commissioning tests.

1) Obtaining a good polarization level in the target cell: This requires the assembling of all the available elements of the target on decks, provision of the missing elements and use of the existing polarizing magnet. An operating vacuum system and an operating dilution refrigerator with a ^4He and ^3He pumping system must be built. Full control of the target consists of an interlock system, a microwave system and a NMR system. This item does not require the holding coils, since no transverse polarization is needed. The final test will consist of polarization and temperature measurements.

2) Installation on the first beam line: After the polarization test, the target will be placed on the beam line and tested again. This requires power and fluid supplies, cooling and pumping capability, a magnetic field for polarization, an interlock system, a microwave system and a NMR system. The final test is the operation of the target in physics experiment conditions.

3) Building a new polarizing magnet: Drawings of the present polarizing magnet, built at Saclay, are available. The final test is field mapping.

4) Building a set of holding coils: The exact configuration was decided. The final test is field mapping.

5) Integrating the target on the beam line and managing its use for physics: Prepare the integration of the whole system together with the particle detection system at the experimental area. Provide an alignment procedure. Provide power and fluid supplies. The final test is full operation of the target, including spin rotation.

Within the 1993 INTAS allocation the participating laboratories have decided to support only task 1) in 1994. The status in June 1994 is as follows:

- a) All necessary parts of the equipment for completion of the MPT in frozen spin mode with longitudinal polarization are available in Dubna.
- b) Necessary funds and manpower for tests of the MPT in 1994 are available.
- c) A beam line is prepared for receiving the MPT.
- c) The MPT may be used starting March 1995.

3. Experimental program

An exhaustive experimental program may be determined using Dubna polarized beams and the proposed target. Three experiments have already been proposed:

– Measurements of the difference in the transmission cross sections of polarized neutrons through the PPT when the beam and target polarization directions are parallel or antiparallel. The measurements will be done at several energies up to 5 GeV, and in two different spin orientations with respect to the beam direction: transverse and longitudinal [3]. The spokesperson of the experiment is L. Strunov (LHE, JINR). Former measurements were already performed, below 1.1 GeV only, in Villigen (Switzerland), Los Alamos (USA) and Saclay (France). They showed unexpected behavior, which has to be understood by doing measurements at higher energies.

– Measurements of the spin effects in the backward elastic scattering of transversally polarized deuterons on transversally polarized protons. This experiment was proposed by JINR groups and by the groups from Kharkov Institute. The spokesperson of the experiment is I. Sitnik (LHE, JINR). The aim is to clarify the exact knowledge of the deuteron wave function which shows a disagreement with classical models [4].

– The third experiment concerns Φ meson production with polarized deuteron or proton beams and with the PPT. Recent experiments with antiprotons at LEAR show that the ratio of Φ to ω meson production is 50–100 times higher than expected from the OZI rule predictions. A strong dependence of the Φ to ω ratio on quantum numbers of the initial state (e.g. on the total spin of the nucleon–nucleon system) was found. In Ref. [5] it was suggested that this effect is connected with the polarized strange sea in the nucleon. The crucial experiments for tests of this model consist of the measurement of $pp \Rightarrow pp + \Phi$ or $dp \Rightarrow ^3\text{He} + \Phi$ reactions using polarized proton or deuteron beams and a polarized proton target. An intrinsic

nucleon strangeness will manifest itself in an asymmetry of the Φ production for parallel or antiparallel polarizations of the initial particles. This asymmetry will be independent of the space orientation of the particle spins. The spokesperson of the experiment is B. Khachaturov (LNP, JINR).

References

- [1] V. Kadyshesky (JINR-Dubna), A. Baldin (LHE, JINR-Dubna), M. Russakovich (LNP, JINR-Dubna), I. Savin (LPP, JINR-Dubna), V.A. Matveev (RAS INR, Moscow), P.V. Sorokin (KIPT, Kharkov, Ukraine), F. Bradamante (INFN, Trieste, Italy) R. Aymar (CEA, DSM, France), and Ph. Leconte (CEA/DSM/DAPNIA, France), Memorandum of Understanding (1994).
- [2] D.P. Grosnick et al., Nucl. Instr. and Meth. A 290 (1990) 269.
- [3] J. Ball et al., Proc. Int. Workshop Dubna Deuteron 91, Dubna, 11–13 June 1991, Dubna Preprint E2-92-25 (1992) p. 12.
- [4] I.M. Sitnik, V.P. Ladygin and M.P. Rekalov, Preprint JINR, E-1-94-23 (1994).
- [5] J. Ellis, M. Karliner, D. Kharzeev and M. Sapozhnikov, Preprint CERN-TH/7326-94.



ELSEVIER

Topics in NMR polarization measurement

T.O. Niinikoski

CERN, Geneva, Switzerland

Representing the Spin Muon Collaboration

Abstract

Using a precise circuit theoretical treatment of the series Q -meter, analytical expressions are derived for the relationship between the experimental NMR signal and the RF susceptibility on one hand, and their integrals and the polarization on the other. These are used for the ab initio calculation of the signal-to-noise ratio for deuteron targets, which yield a realistic ultimate calibration precision of 0.1% at 1 K. The experimental signal distortions and drift are discussed, which lead to proposed optimized tuning and design rules, improved circuits, and new applications. Among these are the measurement of ^{14}N polarization in irradiated NH_3 targets, and the improvement of the temperature scale around 1 K by one order of magnitude.

1. Introduction

In this paper we shall discuss a variety of problems related with the measurement of polarization using the continuous-wave (CW) nuclear magnetic resonance (NMR) techniques. These problems require the introduction of the exact relationship between the polarization and the RF susceptibility, which in the SI (MKSA) system of units reads [1]

$$P(I) = \frac{2}{\pi\mu_0\hbar\gamma_I^2 n_I I} \int_0^{+\infty} \chi''(\omega) \frac{\omega_0}{\omega} d\omega. \quad (1)$$

This equation holds exactly in all high-field situations, in particular for wide quadrupole broadened lines such as that of ^{14}N in ammonia at 2.5 T, and that of deuterons down to 0.1 T. It is also true in the case of high polarizations, when the absorption lineshape may become very asymmetric.

For deuterons at 2.5 T field, the difference between this expression and the more customary formula with only the absorption lineshape under the integral, remains smaller than 1% at $P_D = 0.5$, and can easily be corrected for. Such corrections, however, have never been made, because in the experimental NMR signal there are always other distortions which may cause even larger errors. These come from the measurement circuitry on one hand, and from the microscopic description of the non-saturating passage of the deuteron resonance line at very low spin temperature on the other. In this paper we shall mainly deal with measurements where neither Eq. (1) nor the signal distortions can be ignored.

The estimation of the absorption part of the RF susceptibility from the real part of the series Q -meter signal will be discussed in the next section. Because absolute signal sizes can be calculated using our equations, we can also predict the signal-to-noise ratios using the noise figure of the preamplifier and the signal-to-noise ratio of the RF source. In Section 3 we shall review the power series expansion of the Q -meter signal in the terms of the susceptibility and frequency, and use this for discussing the tuning and optimisation of the circuit elements under various circumstances. Improved NMR circuits will be proposed in Section 4, with view on some specific applications. In Section 5 we shall elaborate on the determination of polarization from very small NMR signals such as ^{14}N in ammonia, and in Section 6 improvement of the international temperature scale around 1 K will be discussed.

2. NMR polarization measurement using a series Q -meter

2.1. The series Q -meter signal

The schematic diagram of the series Q -meter circuit is shown in Fig. 1. The coupling admittance of the hybrid resonator is

$$Y = \frac{1}{R_i} + \frac{1}{R_o},$$

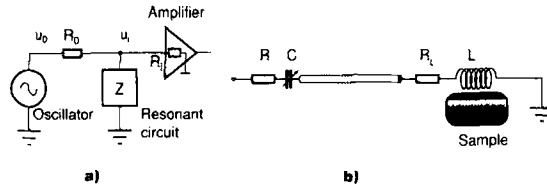


Fig. 1. Series Q -meter circuit: (a) block diagram; (b) elements of the hybrid resonator circuit.

where R_o is the oscillator feed resistance and R_i is the amplifier input impedance, both of which are assumed to be purely real parameters. The real and imaginary parts of the voltage u_i in the input of the amplifier can be written in terms of the real and imaginary parts of the resonator impedance Z as

$$\operatorname{Re}\{u_i\} = u_o \frac{\operatorname{Re}\{Z\} + Y[\operatorname{Re}^2\{Z\} + \operatorname{Im}^2\{Z\}]}{R_o[(1 + Y \operatorname{Re}\{Z\})^2 + Y^2 \operatorname{Im}^2\{Z\}]} \quad (2)$$

and

$$\operatorname{Im}\{u_i\} = u_o \frac{\operatorname{Im}\{Z\}}{R_o[(1 + Y \operatorname{Re}\{Z\})^2 + Y^2 \operatorname{Im}^2\{Z\}]} \quad (3)$$

The hybrid resonator impedance Z is

$$Z = R + \frac{1}{i\omega C} + Z_c \frac{Z_L + Z_c \tanh \gamma l}{Z_c + Z_L \tanh \gamma l}, \quad (4)$$

where the coil impedance Z_L can be expressed in terms of the RF susceptibility and effective filling factor of the spin polarized material η by

$$Z_L = R_L + i\omega L \{1 + \eta[\chi'(\omega) - i\chi''(\omega)]\}, \quad (5)$$

and the propagation constant and characteristic impedance of the coaxial line are given by

$$\gamma = \sqrt{(R_c + i\omega L_c)(G_c + i\omega C_c)} \cong i\omega \sqrt{L_c C_c} \left(1 + \frac{1}{2iQ_c}\right) \quad (6)$$

and

$$Z_c = \sqrt{\frac{(R_c + i\omega L_c)}{(G_c + i\omega C_c)}} \cong Z_0 \left(1 + \frac{1}{2iQ_c}\right). \quad (7)$$

Here the subscript c labels the distributed parameters of the coaxial transmission line, and we have furthermore defined (as usual)

$$Z_0 = \sqrt{\frac{L_c}{C_c}}, \quad \text{and} \quad Q_c = \frac{\omega L_c}{R_c}.$$

These definitions and the approximations of Eqs. (6) and (7) were first time used in Ref. [2] and it is important to note that the precise understanding of the tuning and shape distortions of wide-sweep NMR circuits should use these or even more accurate expressions rather than the usual parameters involving a real characteristic impedance and a simple or zero attenuation constant.

2.2. Series Q -meter signal expansion

The expressions (2) and (3), in principle, give accurately the output signal of the apparatus used for NMR measurements, once the gain of the amplifying and detecting circuitry is known. These or slightly less accurate expressions have been used for numeric simulation of the output signal with numerically input spectra of the RF susceptibility. Such simulations are useful for many purposes such as evaluating the distortions and non-linearity of a known circuit, but are tedious for the optimization of the circuit itself, and useless for planning the strategy of the circuit tuning procedure. To gain insight in

these, the Eq. (2) was expanded in power series of the susceptibility, with coefficients themselves expanded as power series of the frequency offset from the Larmor frequency [2].

With appropriate tuning the real part of the RF voltage Gu_i (after amplification and real-part detection with overall voltage gain of G) is

$$\begin{aligned} \operatorname{Re}\{u_i\} \frac{R_0}{u_0} = & A_0(x) \\ & + A_1(x)\eta\omega L\chi''(x) + A'_1(x)\eta\omega L\chi'(x) \\ & + A_2(x)(\eta\omega L)^2[-\chi''^2(x) + \chi'^2(x)] + A'_2(x)(\eta\omega L)^2\chi'(x)\chi''(x) \\ & + \dots, \end{aligned} \quad (8)$$

where the relative frequency offset from the Larmor precession is

$$x = \frac{\omega - \omega_0}{\omega_0}. \quad (9)$$

The term $A_0(x)$ is proportional to the experimental Q -curve $\operatorname{Re}\{Gu_i\}$ which can be measured when $\chi(\omega) = 0$. The aim of the circuit design is to make all higher order coefficients A_n, A'_n small except $A_1(x)$ which should be large and flat function of x . These features provide selectivity for the absorption lineshape, low distortions, and good linearity. The coefficients A_n, A'_n depend on the circuit parameters only, and they will be discussed in a forthcoming paper [1]. They can be approximated for narrow frequency sweep, fairly high Q_c and low Y by

$$A_0(x) = R' + \rho\omega Lx + Y\left\{-(R' + \rho\omega Lx)^2 + (\omega_0 L)^2(\delta_i + \delta + 2x)^2\right\} + \dots, \quad (10)$$

$$\begin{aligned} A_1(x) = & 1 + \frac{n\pi}{4Q_c^2} + \rho\left(\frac{1}{2Q_c} - \frac{Q}{4Q_c^2}\right) + x\left(\frac{n\pi}{2Q_c^2} - \rho Q\right) \\ & - 2Y\left\{(R' + \rho\omega Lx) + \omega_0 L(\delta_i + \delta + 2x)\left[\frac{\rho}{4Q_c^2}(2Q + 1) + \frac{(n\pi)^2}{Q_c}x\right]\right\} + \dots, \end{aligned} \quad (11)$$

$$A'_1(x) = [1 - 2Y(R' + \rho\omega Lx)]\left[\frac{\rho Q}{4Q_c^2}(2Q + 1) + \frac{(n\pi)^2}{Q_c}x\right] + 2\omega_0 L(\delta_i + \delta + 2x) + \dots, \quad (12)$$

$$A_2(x) = -\frac{n\pi}{2Z_0 Q_c} + Y\left[1 + \frac{n\pi\omega_0 L}{Z_0}(\delta_i + \delta + 2x)x\right] + \dots, \quad (13)$$

$$A'_2(x) = -\frac{2n\pi}{Z_0}x + \dots, \quad (14)$$

where $Q = \omega L/R_L$ is the Q -factor of the coil which has the equivalent series resistance R_L , and is the relative offset of the cable resonance frequency from the Larmor precession. For brevity we have used the following parameters

$$R' = R + R_L + \frac{n\pi Z_0}{2Q_c}\left\{1 + \left(\frac{R_L}{Z_0}\right)^2(Q^2 - 1)\right\} \quad (\text{effective damping resistance of } Z \text{ at } \omega_0), \quad (15)$$

$$\rho = \frac{n\pi R_L}{Z_0} \quad (\text{frequency sensitivity of effective damping}), \quad (16)$$

$$\delta \equiv \frac{n\pi R_L^2}{2Q_c Z_0^2}(Q^2 - 1) \quad (\text{tune shift due to damping in the coaxial line}), \quad (17)$$

$$\delta_i = 1 - \frac{1}{\omega_0^2 LC} \quad (\text{capacitor tune shift}), \quad (18)$$

with a physical interpretation given in the parentheses.

The above equations were derived using the following approximation for $\tanh \gamma l$:

$$\tanh \gamma l \cong n\pi \left(\frac{1+x}{2Q_c} + ix \right), \quad (19)$$

which is good for $|x| \leq 0.1$ when $n = 1$ and $Q_c \approx 30$.

2.3. Ab initio NMR signal size

One of the problems in NMR polarization measurement of the deuteron and other spin-1 systems is related with the calibration of the integrated absorption signal at a known polarization, usually at about 1 K temperature where the spin-lattice relaxation is rapid (≈ 1 min) and where the thermal equilibrium and uniformity are very easy to achieve, by immersing the target in pure superfluid ^4He . The size of the signal under these conditions is very small and requires signal averaging over extended periods of time (≈ 30 min) in order to show up above the noise. This would be relatively simple to do, if the circuit drift during averaging could be eliminated. There is, in fact, an optimum averaging time, beyond which the Q -curve drift results in errors greater than that due to the noise. Only repeated measurements and statistical analysis then will enable one to gain in the statistical accuracy, at the cost of some loss in systematics, because details of the signal such as the line center cannot be resolved with precision. In the following we shall calculate the size of the NMR signal from first principles using the circuit model parameters, and compare it with the amplifier and oscillator noise. Deuterons are used as an example, but the treatment is valid for all NMR signals of comparable size.

In the case of deuteron NMR signal the susceptibility is so small in all experimental conditions that the contribution of the second and higher order terms in Eq. (8) can be ignored. Furthermore, the frequency sweep may be limited to $\pm 1.5\%$ where the frequency dependence of the coefficients A_n, A'_n may be small if the circuit is well designed and tuned. We may then write the output signal in the form (after subtracting the Q -curve)

$$S(\omega) \equiv G[\text{Re}\{u_i(\chi)\} - \text{Re}\{u_i(0)\}] \cong \frac{Gu_0}{R_0} \eta \omega_0 (1+x) L[A_1(x)\chi''(x) + A'_1(x)\chi'(x)], \quad (20)$$

where u_0 is RF source voltage and G is the system voltage gain between the inputs of the preamplifier and the ADC.

By integrating Eq. (20) we can write the relationship between the signal integral, the polarization and the circuit parameters in the form appropriate for wide sweep:

$$\int_{\omega_{\min}}^{\omega_{\max}} S(\omega) \frac{\omega_0^2}{\omega^2} d\omega \cong \frac{Gu_0}{R_0} \eta \omega_0^2 L \int_{x_{\min}}^{x_{\max}} \frac{dx}{1+x} [A_1(x)\chi''(x) + A'_1(x)\chi'(x)]. \quad (21)$$

If $A_1(\omega)$ is a flat function and $A'_1(\omega)$ is a symmetric function about ω_0 , and if the absorption part of the susceptibility is also symmetric with cut-offs in both wings, then we can write using Eq. (1)

$$\int_{\omega_{\min}}^{\omega_{\max}} S(\omega) \frac{\omega_0^2}{\omega^2} d\omega \cong \eta \omega_0 L \frac{S_0 A_1(0)}{2 A_0(0)} \pi \mu_0 \hbar \gamma_I^2 n_I IP(I), \quad (22)$$

where the gain, oscillator voltage and feed resistance values were expressed in the terms of the signal voltage S_0 at the minimum of the Q -curve, with no NMR signal present:

$$S_0 = A_0(0) \frac{Gu_0}{R_0}. \quad (23)$$

The relationship (22) gives polarization in the terms of variables which are accurately directly measurable and/or calculable, with the exception of the effective filling factor η . If the filling factor is known from other measurements, then no calibration is required for the measurement of polarization. The approximate ratio of the coefficients $A_1(0)/A_0(0)$ from Eqs. (10), (11)

$$\frac{A_1(0)}{A_0(0)} \cong \frac{(1-2YR')(1-\rho Q/Q_c^2)}{R'(1-YR')} \quad (24)$$

is obtained using the circuit parameters, the values of which can be verified with precision by fitting the Q -curve with the theoretical expression of Eq. (2). The spin density is obtained from the density of the material and from the chemical formulae of its components. We shall discuss several applications of Eq. (22) below.

2.4. Signal-to-noise ratio

In the following we shall assume narrow NMR absorption lines, which is the usual case in high field, such as protons and deuterons at 2.5 T. Within the frequency range of interest we may then put $(\omega_0/\omega)^2 \approx 1$, which allows us to define the absolute effective signal strength S_{eff} from Eq. (22) once we know the effective width of the NMR signal $\Delta\omega_{\text{eff}}$, defined as

$$\int_0^{+\infty} S(\omega) d\omega \cong S_{\text{eff}} \Delta\omega_{\text{eff}}. \quad (25)$$

As an example let us estimate the deuteron NMR signal height in frozen butanol-water, with $\Delta\omega_{\text{eff}} = 2\pi \cdot 280$ kHz, at 2.5 T field. With circuit parameters $R' = 15 \Omega$, $L = 450$ nH, $n = 1$, $Q = 10$, $Q_c = 80$, and $Y \cong 1/(50 \Omega)$, and filling factor $\eta = 0.2$ usual with embedded probe coils, we find from Eqs. (22)–(25)

$$\frac{S_{\text{eff}}(P = 0.5)}{S_0} = 2.7 \times 10^{-3} \quad (26)$$

and

$$\frac{S_{\text{eff}}(P = 5 \times 10^{-4})}{S_0} = 2.7 \times 10^{-6}, \quad (27)$$

the first case corresponding to maximum deuteron polarization and the second to the calibration signal measured in thermal equilibrium around 1 K temperature. With about 0.3 mA current into the resonant circuit we have $S_0 = 4.5$ mV; this corresponds to respective 12 μV and 12 nV changes in the signal amplitudes at the input of the preamplifier. These have to be compared with the amplifier noise floor of 40 nV (with 30 kHz single-sideband bandwidth) and the oscillator noise of 100 nV (using the RF source signal-to-noise ratio of 93 dB). The theoretical TE signal-to-noise ratio is therefore

$$\frac{S_{\text{eff}}^{\text{TE}}}{V_n} = \frac{2.7 \times 10^{-6} \times 4.5 \text{ mV}}{\sqrt{1.16} \times 100 \text{ nV}} \cong \frac{1}{8.9}, \quad (28)$$

which indicates that the TE signal is always completely invisible without signal averaging. The fully polarized signal, however, is about hundred times higher than the RMS noise, but even this is only about one third of the depth of the Q -curve (with 500 kHz sweep width).

Above we have calculated the signal-to-noise ratio from the first principles, applicable for a raw experimental spectrum obtained by one frequency scan. A large reduction of noise is obtained by the appropriate processing of many such signals. The processing consists of averaging a number of spectra, subtracting the Q -curve obtained by averaging over same number of spectra without NMR signal, correcting for the Q -curve drift and field effect by subtracting a function (usually a polynomial of order 2) obtained by fitting the sides of the spectrum to an expected residual Q -curve, and integrating the resulting spectrum. This procedure is repeated a number of times to reach the desired statistical accuracy and to examine systematic effects in the equipment used for the measurements.

In the CERN deuteron NMR equipment [3] the deuteron NMR signals are digitised and averaged at N_p points of the frequency scan with about 500 kHz width. The scan is made by stepping from the minimum to the maximum frequency and then stepping back to the minimum frequency; a scan thus has 2 measurements of the spectrum. Averaging N_s such scans reduces the noise by $[2N_s]^{-1/2}$; subtraction of a Q -curve obtained with equal number of scans increases the noise by $2^{1/2}$. N_e points on each end of the scan fall out of the absorption spectrum and are used to determine the residual Q -curve under the signal. Integration of the signal then improves the signal-to-noise ratio by a factor f

$$f = \sqrt{N_s} / \sqrt{\frac{1}{N_p - 2N_e} + \frac{1}{2N_e}}. \quad (29)$$

With $N_s = 10^4$, $N_p = 400$ and $N_e = 70$, the above equation gives $f = 954$; applying this to Eq. (28) yields a statistical accuracy of about 1% for determining the integrated absorption spectrum from one set of averaged signals and Q -curves. This was confirmed by determining the RMS noise in the experimental signal outside the edges of the DMR absorption lineshape [4].

By repeating the measurement N_n times a further theoretical improvement by a factor of $[N_n]^{1/2}$ will be obtained in the statistical accuracy of the integrated calibration signal. With $N_n = 100$ the theoretical statistical accuracy is 0.1%. This can be achieved in about 2 days of data taking. The result is interesting because it has been previously thought that precise TE calibration for deuterons is impossible without substantial saturation. This result also calls for improved control of systematics if a comparable systematic accuracy is desired.

3. Optimisation of the series Q-meter

3.1. Design criteria

With the analytical expressions (8)–(18) the optimisation of the series Q-meter circuit can be performed for each particular case. These equations give the distortion and non-linearity of the transfer function of the complex RF susceptibility, allowing their optimisation. The signal-to-noise ratio can also be maximized using these equations. Furthermore, criteria for the stability for each component can be easily obtained, with requirements imposed by the TE calibration signal size which is calculable.

The Eqs. (8)–(18) also show how the circuit should be tuned for best performance. This will be discussed in Section 3.2. The criteria of the tuning follow from the requirements of the signal symmetry and absence of dispersion contribution, and from the shape of the Q-curve which sets requirements for the dynamic range.

In the circuit design two major parameter specifications emerge: maximum signal size and required scan width. For large narrow signals, such as that of highly polarized protons, the circuit design problem involves mainly the control of the linearity of the response function. For very small signals the signal-to-noise ratio is to be maximized, while ensuring a reasonable flatness of the functions A_n , A'_n .

The case of very wide signals can also be dealt with the Eqs. (8)–(18), although more precise description of the coaxial line resonator will be required then. The practical limit of sweep width is determined by the nearest quarter wavelength resonances of the coaxial line below and above the half wavelength resonance near the Larmor frequency; for $n = 1$ the sweep width is thus limited to less than $\pm 50\%$ relative to the Larmor frequency.

The most important component of the circuit is the probe coil, the design of which is discussed in Section 3.4.

3.2. Tuning

The Eq. (19) for the coaxial transmission line is valid if the cable length is adjusted by minimizing the impedance

$$Z_l = Z_c \tanh \gamma l \quad (30)$$

of a shorted line at frequency ω_0 . This procedure results in a length of

$$l \approx \frac{n\pi}{\omega_0 \sqrt{L_c C_c}} \left(1 + \frac{1}{8Q_c} \right) = \frac{n\pi c}{\omega_0 \sqrt{\epsilon_r}} \left(1 + \frac{1}{8Q_c} \right), \quad (31)$$

which can be shown [1] to give good symmetry properties for the transfer function of the resonant circuit.

If the cable tune is not correct or if the cable length is used for obtaining particular characteristics of the tuned circuit, we may replace x in the Eq. (19) by $x - x_c$ where x_c is the relative offset of the cable resonance from the Larmor precession

$$x_c = \frac{\omega_c - \omega_0}{\omega_0}. \quad (32)$$

In Ref. [2] the assumption was made that the transmission line is tuned to resonate at the frequency ω_c which has a relative deviation of

$$x_c = \frac{Q}{2Q_c}. \quad (33)$$

This tuning which was derived for a special case of proton NMR circuit at 106.5 MHz, results in the cancellation of the coefficient of the first-order dispersion term at the centre of the NMR line which, in turn, ensures that the first-order contribution of the dispersion part of the RF susceptibility in the experimental Q-meter signal becomes rather symmetric about the centre frequency, if the absorption part is a symmetric function. This holds only for low values of Q/Q_c . Low-frequency and wide-sweep systems require a more precise expression for estimating the required cable mistune, and the Eq. (22) cannot then be used.

The tune shift δ due to damping in the coaxial line influences the flatness of all parameters A_n , A'_n . The tune shift can be reduced by designing the coaxial line so that a high effective quality factor results. This is strongly influenced by the cryogenic part of the line, where high-resistivity materials are used for reducing the heat input to the target refrigerator. Outer conductor material made of alloys such as BeCu, CuNi and brass are excellent, because of their low heat conductivity. If the centre conductor is silvered, the quality factor is mainly determined by the skin depth of the outer conductor, and Q_c becomes nearly temperature-independent because these materials have a small temperature coefficient of the resistivity.

In copper jacketed semi-rigid coaxial lines with high Q_c the center conductor surface resistivity determines the quality factor. Because this is a strong function of temperature, thermal drift of the line results in a tune shift of the circuit. Thus the temperature of such a line must be stabilised for ultimate stability of the Q -curve and transfer function.

Small diameter of the center conductor and low ϵ_r result in high Z_0 which is beneficial for low circuit distortions. Low ϵ_r is also desirable because lower n can be achieved in high-frequency applications. Although presently 50 Ω solid PTFE-isolated lines are used almost exclusively, it would be interesting to develop foam-isolated semi-rigid 75 Ω lines for NMR polarization measurement applications.

Finally, the part of the coaxial line which runs in the magnetic field must be made of non-magnetic materials so that the Q -curve will not change when the magnetic field is shifted for the measurement of the curve. The BeCu lines with silvered center conductors have turned out to be excellent in this respect.

The value of the tuning capacitor is adjusted first to obtain a fairly symmetric Q -curve. This value is usually corrected with highly polarized spins by making the NMR signal as symmetric as possible. The Eq. (11) explicitly shows how the capacitor tune shift δ influences the symmetry of $A_1(x)$, while mainly influencing only the magnitude of $A_1'(x)$. The coefficients A_2 are also changed by the capacitor tune, but all the functions cannot be made symmetric with the same value of the capacitor.

3.3. Circuit design

In discussing the design of the series Q -meter circuit we shall use the Eqs. (8)–(19). The Eq. (10) shows explicitly the frequency dependence of the Q -curve. We note that the Q -curve can be made symmetric by a suitable capacitor tune shift δ , although this is perhaps not the main aim, as was discussed above. The depth of the Q -curve is mainly determined by the inductance L of the probe coil, which should be made as small as is practical. The depth is also strongly influenced by the coupling admittance Y which should also be made as low as possible, while maintaining the imaginary component in the coupling negligible. In high frequency systems this is difficult and a compromise is often necessary.

The flatness of the function $A_1(x)$ is improved by high Q_c , low Y , low L and low Q . The latter cannot be made arbitrarily small by a choice of a high-resistivity material, because these are often magnetic. The probe coil design will be discussed in greater detail in Section 3.4.

The same parameters reduce and flatten the coefficient of the dispersion term in the same way; there is thus no conflict in pushing these parameters to their practical limits. The same is true with the second-order coefficients of Eqs. (13) and (14).

Specific problems in the circuit design at 106.5 MHz for protons and at 16.35 MHz for deuterons will be addressed below.

3.3.1. Design of the proton series Q -meter

Based on the Eqs. (10)–(14), the following rules apply for the series Q -meter optimized for the measurement of proton polarization:

- 1) The cable should have a loss-factor as low as possible, to yield a high effective Q_c ;
- 2) The cable should be as short as possible, preferably $n \leq 3$;
- 3) The coil should have a low inductance, preferably $\omega L < Z_0$;
- 4) The feed resistance and the amplifier input impedance should be as high as possible, while maintaining both real. This requires placing a resistor of about 70 Ω in series with the input of the preamplifier, and using several low-inductance resistors in series to build the feed resistance.
- 5) The Q -factor of the coil should be low (≈ 3), and its series resistance should therefore be high; it is preferable to place the additional damping resistor $R \approx 15 \Omega$ between the coil and the cable rather than between the cable and the tuning capacitor.

6) One must have maximum $\eta \chi''(\omega) \omega L < 0.3 R'$ to preserve good linearity of the integrated absorption signal with respect to the polarization, and to avoid superradiant oscillations at large negative polarization. With embedded coils this requires special precautions for obtaining a low enough effective filling factor (to be discussed below).

7) One must satisfy maximum $\eta | \chi(\omega) | \omega LY \ll 1$ to avoid non-linear distortions of the lineshape; this condition is difficult to achieve in sizeable polarized proton targets, and satisfactory results can be obtained with the less stringent condition 6). The less strict condition is often sufficient because the non-linear signal distortions tend to integrate to zero.

8) To avoid linear distortions of the lineshape, one must have $2Qx \ll 1$, $2Y\omega Lx \ll 1$, $2n\pi(R_L/Z_0)Y\omega Lx \ll 1$, and $Q^2 n\pi YZ_0 x \ll 1$. One or more of these conditions limit the maximum practical sweep width in high-frequency systems.

3.3.2. Design of the deuteron series Q -meter

The deuteron has the spin $I = 1$ and a sizeable quadrupole moment, which broadens the high field NMR spectrum to about 280 kHz in butanol and other glassy hydrocarbons, with a characteristic shape featuring two resolved peaks and broad

minimum in between, and relatively flat pedestals outside. The peaks are associated with the two magnetic transitions; the intensity ratio of these transitions, in principle, gives the spin temperature and therefore polarization, if the thermal distribution of level populations is valid, and if the polarization is homogeneous. Because of its large width and because of the small magnetic moment of the deuteron, the accurate measurement of the DMR absorption spectrum shape, however, is difficult.

At 2.5 T field the deuterons in glassy butanol thus have a total line breadth of about 2×10^{-2} relative to the center frequency of 16.35 MHz; this can be contrasted with protons in the undeuterated butanol, where dipolar interactions give a FWHM of about 4×10^{-4} at 106.5 MHz.

As a consequence, the frequency dependence of the coefficient of the term $A_1(x)$ cannot be ignored, and the real part of the experimental signal becomes distorted. On the other hand, the RF susceptibility of highly polarized deuterons remains very small, so that the terms, which are of second or higher order in the RF susceptibility, will remain negligible. We may therefore focus the discussion only on the Eqs. (11) and (12).

The linear distortion in a practical circuit can be so large that it is not recommendable to use the experimental NMR line peak asymmetry as a way of determining the polarization, because the heights and shapes of the two superimposed signals do not accurately reflect the transition intensities. The distortion also makes it unreliable to fit the Q -curve drift during recording of the dynamic nuclear polarization, because the admixture of the distorted dispersion signal extends far beyond the edges of the absorption signal.

Provided that the distortions are small or can be sufficiently well corrected, however, the asymmetry of the DMR signal in a large target gives a unique means of estimating the polarization variation in the target volume, if the average polarization is known accurately on the basis of the integrated signal calibrated in TE at 1 K, for example. The inhomogeneity of the polarization in a large target leads to a systematically higher asymmetry than that determined from the measured average polarization; this difference, although not highly sensitive to the polarization variation, gives a reasonable estimate of the RMS variation of polarization in the volume sampled by the probe coil.

As an example, if the average polarization $P^*(D) = 0.4$ can be determined to 3% relative accuracy and asymmetry within 5%, the variation of polarization

$$P(x) = P^* \pm \delta P(x), \quad (34)$$

is limited to $|\delta P| \leq 0.15$ in the volume sampled by the probe. This limit can be made substantially lower with better accuracy in the polarization measurement, distortion control and asymmetry determination.

As the deuteron signal is very small, the Q -meter design should aim at a good sensitivity which implies high filling factor, high inductance L , and a relatively high overall Q of the circuit. A low admittance Y is desirable for optimum signal-to-noise performance. The control of the linear distortion on the other hand requires that Q_c be as high as possible and L be low, $\rho Qx \ll 1$, $2Y\omega Lx \ll 1$ and $2\rho Y\omega Lx \ll 1$. These clearly set the limit for a maximum Q , and indicate that the coupling admittance Y should be as small as is practically possible from the noise performance point of view. Practical design values are $L = 0.4 \mu\text{H}$, $Y = 0.01 \Omega^{-1}$ and $R' = 15 \Omega$, with damping resistor placed between the coil and the coaxial line.

3.4. Probe coil design

Above it was found repeatedly that low L and Q are desirable for the probe coil. The inductance is controlled by the length and diameter of the wire used for the coil; it is therefore preferable to use a short and thick wire of high resistivity material. Practical coils are made of thin-walled CuNi tubes of 1 to 4 mm diameter and 10 to 40 cm length, bent to a suitable shape around or inside the target.

For proton probe coils the filling factor should be minimized, which can be achieved by placing the coil outside the target, or by surrounding the wire by a PTFE tube which excludes the material from the area of the highest RF field near the wire. Another way of reducing the effective filling factor is to orient the coil (usually one loop) so that the uniform part of the RF field is parallel to the main field; this is made by keeping the wire always perpendicular to the main field. This design concentrates the sampling to the vicinity of the wire, which can be sometimes interesting if localized measurements are desired. A dipole loop made of a tube with length of 15 cm and diameter of 4 mm gives an inductance of about 100 nH. Such a loop, made of CuNi, gives a high Q -factor, which can be reduced by placing a suitable series resistor between the coil and the coaxial line.

In the case of deuteron probe coils one wishes to maximize the effective filling factor by using a bare large-diameter embedded wire, predominantly aligned along the main field. A 50 cm tube of 2 mm diameter gives an inductance of about 450 nH, which can be easily reduced by selecting a shorter length and a larger diameter. The filling factor can be varied between 0.2 and 0.3 by varying the diameter of a possible PTFE tube around the wire.

An alternative for lowering the Q of the coil is to make the probe conductor out of a thin film of high-resistivity non-magnetic material deposited on a suitable flexible substrate. If a series resistor is used at low temperature, it is very important that its resistance value has low temperature and field coefficients.

4. Improved NMR circuits

4.1. Series Q -meter improvements

The receiver selectivity can be greatly enhanced by changing from the present homodyne receiver technique [5] into a heterodyne or superheterodyne technology. These enable good control of the noise sidebands by the appropriate design of filters and frequency management. As the final amplifier stages operate at constant frequency, the filter design can be focused on off-band rejection ratio and time response rather than on flatness in the frequency domain.

The main benefit of heterodyne receiver technique lies in the better elimination of off-band and low-frequency parasitic signals. This, however, can be also accomplished by improved control of electromagnetic interferences in all parts of the circuitry, and therefore the use of a highly selective receiver is not necessary. This is due to the fact that the leading source of noise is the oscillator, whose output noise power spectrum is concentrated close to the carrier frequency and cannot therefore be eliminated if a reasonable frequency scan speed is desired.

The damping resistor of the Q -meter circuit is best placed between the coil and the coaxial line, if minimum circuit distortions are desired. This removes the Johnson noise of the resistor, and improves the linearity and flatness of the circuit [2].

More fundamental improvements involve changes in the circuit which necessitate different circuit theoretical treatment; some of these are briefly discussed below.

4.2. Capacitively coupled series Q -meter

In high-frequency systems a major problem is to obtain a low real value of the coupling admittance Y . By examining the circuit of Fig. 1 we note that the absorption part of the RF susceptibility can be detected also if purely capacitive coupling is used. The expression for the signal is then

$$\operatorname{Re}\{u_i\} = u_o \omega C_o \frac{\operatorname{Im}\{Z\} - \omega C [\operatorname{Re}^2\{Z\} + \operatorname{Im}^2\{Z\}]}{(1 - \omega C \operatorname{Im}\{Z\})^2 + \omega^2 C^2 \operatorname{Re}^2\{Z\}} \quad (35)$$

and

$$\operatorname{Im}\{u_i\} = u_o \omega C_o \frac{\operatorname{Re}\{Z\}}{(1 - \omega C \operatorname{Im}\{Z\})^2 + \omega^2 C^2 \operatorname{Re}^2\{Z\}} \quad (36)$$

where $C = C_o + C_i$ with C_o and C_i replacing the oscillator feed and amplifier input resistors R_o and R_i , respectively. The absorption thus appears predominantly in the imaginary part of the output signal, which necessitates a 90° hybrid in the reference arm of the RF circuit.

With the low values of $|Y|$ available using small capacitors an excellent linearity entails, and low distortions could become possible in wide-sweep systems. A possible problem is the stability of the capacitors, which certainly requires temperature stabilisation of the circuitry.

The coupling capacitors also eliminate the Johnson (thermal) noise present in the coupling resistors. The preamplifier should be specially optimized for best noise performance in the resulting circuit.

4.3. Crossed-coil NMR circuit

One way of reducing the oscillator noise is to use the crossed-coil principle for NMR. Although there exist no adequate circuit-theoretical model for such a system, it is easy to show that the NMR signal is no more distorted by the crossed-coil circuit than by the series Q -meter circuit. However, the benefit of measuring the oscillator strength simultaneously is lost. Furthermore, as the orthogonality of the coils enables rarely better than 30 dB rejection of the fundamental oscillator signal in the pickup coil, the wide-band noise rejection may be much less good than might seem at first. However, as the two coils can be designed and optimized individually, important system benefits might entail from the new degrees of freedom in the optimization process.

In discussing the crossed-coil NMR circuit we shall call the primary coil connected to the oscillator (RF source) the transmitter coil, and the one connected to the preamplifier the receiver coil. These coils are mounted so that their axes are perpendicular and the capacitive coupling of the wires of the coils is also minimized. Fine adjustment at room temperature helps in reducing the coupling between the transmitter and receiver coils.

One of the obvious benefits is that the transmitter coil can be designed so that the RF field is rather uniform in the volume probed by the receiver coil. This requires a transmitter coil which is substantially larger than the receiver coil, a feature which also facilitates in reducing the (capacitive) coupling between the coils.

Because H_1 is almost constant in the volume probed by the receiver coil, the signal size will be much larger compared with the series Q -meter with the same value of saturation and embedded or tightly enclosing coil.

If the transmitter coil is outside the target, its filling factor can be made small. This reduces the influence of the RF susceptibility on the transmitter coil current and results in improved linearity of the circuit. In the first approximation the RF field H_1 in the target can then be assumed independent of the susceptibility at resonance, which facilitates the circuit-theoretical analysis. This is not, however, a strict requirement for the best measurement of small signals.

The crossed-coil NMR circuit requires one additional coaxial line for feeding the transmitter coil. Because all receiver probes can share a common transmitter coil, multicoil systems will not require doubling the number of coaxial lines.

The tuning of the crossed-coil circuit is more difficult than that of the series Q -meter, because there are now two hybrid resonant circuits with a loose mutual coupling. The series or parallel capacitor of the transmitter circuit is tuned first using a vector voltmeter or a Q -meter amplifier connected to the transmitter resonant impedance Z_t . The series or parallel capacitor of the receiver circuit is tuned either using the residual RF signal coupled via the coil pair, or the NMR signal itself. Alternatively, the receiver circuit can be tuned using a small signal injected to the receiver resonant impedance Z_r . A further alternative consists of matched rather than tuned receiver circuit; this might provide the best wideband performance, with some cost in noise performance.

A large transmitter coil requires a larger amount of RF power for getting the oscillating transverse field H_1 equal to that of the embedded probe of a series Q -meter.

If the transmitter coil covers the entire target volume, it might be interesting to use it also for the manipulation of the spin systems in the target. The reversal of polarization by adiabatic passage might thus be performed using the transmitter part of the crossed-coil circuit, with much increased RF power. The cooling of the transmitter coil then needs to be separated from the refrigeration circuit of the target material.

Because the Q -curve is eliminated in first order, a wider dynamic range becomes available and a higher RF gain can be used. Furthermore, this circuit may be designed so that it is well adopted to the measurement of very wide NMR signals, such as that of ^{14}N spins in solid ammonia.

4.4. Measurement of complex RF susceptibility using quadrature mixer

Quadrature mixer detector will allow to measure simultaneously the real and imaginary parts of the RF signal Gu_i , enabling the reconstruction of the real and imaginary parts of the RF susceptibility without theoretical modelling and fitting of the NMR signal, from Ref. [6]:

$$\chi(\omega) = \frac{R_o F^2(\omega)}{\eta G i \omega L} \left\{ u_i(\omega, \chi) - u_i(\omega, 0) \right\} / \left\{ 1 - \frac{R_o F(\omega)}{Z_0} \cosh \gamma l \left[Y Z_0 + \left[1 + Y \left(R + \frac{1}{i \omega C} \right) \tanh \gamma l \right] \right] \right\} \times \left[u_i(\omega, \chi) - u_i(\omega, 0) \right] \quad (37)$$

where

$$F(\omega) = \frac{1 + YZ}{Z_0} \left[Z_0 + (R_L + i \omega L) \tanh \gamma l \right] \cosh \gamma l \quad (38)$$

is a complex function involving the circuit parameters only.

This procedure avoids any complications resulting from circuit distortions and non-linearity, and thus enables one to focus on the noise performance in the Q -meter. The tuning of the input circuit will also be greatly facilitated by quadrature detection, because the system operates effectively as a vector network analyser.

Reconstruction of the NMR susceptibility from the Q -meter output signal, however, requires the precise knowledge of the circuit parameters. These are best obtained by a fit of the complex Q -curve to the theoretical description of Eqs. (2) and (3) [6].

5. Measurement of polarization from very small NMR signals

Assuming that the NMR signal is small and that the ratio

$$\frac{A'_1(x)}{A_1(x)} \quad (39)$$

is a symmetric function about $x = 0$, the Eq. (22) can be rewritten in the form

$$P(I) \cong \frac{2}{\pi\mu_0\hbar\gamma_I^2 n_I I} \frac{A_0(\omega_0)}{\eta\omega_0 L} \int_{\omega_{\min}}^{\omega_{\max}} \frac{S(\omega)}{A_1(\omega)} \frac{\omega_0^2}{\omega^2} d\omega, \quad (40)$$

which takes into account the frequency response of the Q -meter circuit. The neglect of the correction due to the dispersion signal can be easily justified for relatively narrow signals even if the ratio (37) has a small deviation from exact symmetry, provided that A'_1 is made small by circuit design and tuning.

The polarization $P(N)$ of the spin species N can then be obtained from its NMR signal by comparing with the signal of another nucleus H with known polarization $P(H)$, measured at the same center frequency and with the same circuit:

$$P(N) \cong P(H) \frac{\gamma_H^2 n_H I_H \int_{\omega_{N,\min}}^{\omega_{N,\max}} \frac{S_N(\omega)}{A_1(\omega)} \frac{\omega_0^2}{\omega^2} d\omega}{\gamma_N^2 n_N I_N \int_{\omega_{H,\min}}^{\omega_{H,\max}} \frac{S_H(\omega)}{A_1(\omega)} \frac{\omega_0^2}{\omega^2} d\omega}. \quad (41)$$

This provides a convenient and accurate calibration for the measurement of the polarization of rare spin species and with such a wide NMR lines that TE calibration becomes impossible. The method requires that the spin density ratio be known from chemistry or from other measurements, for example those made in liquid state so that all NMR lines are narrow.

A special application of the method is in the measurement and monitoring of the ^{14}N polarization in NH_3 and ND_3 targets at 2.5 T field. The Larmor frequency of ^{14}N is 7.694 MHz and the spectrum features a peak separation of 2.37 MHz and total width of 4.74 MHz, requiring a minimum of 5.3 MHz frequency scan from 5 to 10.3 MHz. Although the tuned coaxial line of the series Q -meter becomes a major problem with such a wide sweep, the use of a quadrature mixer and extraction of the absorption part of the RF susceptibility would enable one to overcome the problem related with the dispersion part in Eq. (41). Inserting the numeric values for the ratios of the gyromagnetic factors (2.79268/0.40347), of the spin densities (3/1) and of the spins (1/2), yields

$$P(^{14}\text{N}) \cong 71.86 P(^1\text{H}) \frac{\int_{\omega_{N,\min}}^{\omega_{N,\max}} \chi_N''(\omega) \frac{d\omega}{\omega}}{\int_{\omega_{H,\min}}^{\omega_{H,\max}} \chi_H''(\omega) \frac{d\omega}{\omega}}, \quad (42)$$

where the absorption parts of the RF susceptibilities are obtained from the complex experimental signals using the Eq. (37).

The measurement of ^{14}N NMR signal requires the measurement of the Q -curve at the nominal field value, which is best performed at zero polarization before DNP. It is clear that the stability of the Q -curve is a major concern here.

The Eq. (41) can also be used for finding the ratio of spin densities if the polarizations are known from other measurements or arguments such as that based on equal spin temperatures. The special case of TE polarizations at equal lattice temperatures gives

$$\frac{n_1}{n_2} \cong \frac{\gamma_2^2 I_2 (I_2 + 1) \int_{\omega_{1,\min}}^{\omega_{1,\max}} S_1(\omega) \frac{\omega_0^2}{\omega^2} d\omega}{\gamma_1^2 I_1 (I_1 + 1) \int_{\omega_{2,\min}}^{\omega_{2,\max}} S_2(\omega) \frac{\omega_0^2}{\omega^2} d\omega}, \quad (43)$$

where the signal gain was assumed flat in the narrow frequency scan range where TE signal measurement is possible, and where the integrated signals are the TE signals measured at constant temperature and same center frequency.

In a deuterated target usually the degree of deuteration and the chemical sites and composition are known to a relatively high accuracy. The exact amount of residual protons can then be obtained using the Eqs. (41) or (43).

6. Improvement of the international temperature scale

The TE calibration accuracy depends mainly on the accuracy of the determination of the target temperature during NMR signal measurement. If the calibration of the polarization measurement could be obtained more accurately from another method, the measurement of the integrated NMR signal around 1 K temperature would provide determination of the temperature with similar accuracy, which we shall evaluate below.

As an example we may take partly deuterated propanediol $C_3D_6(OH)_2$ with reacted Cr(V) compounds which yields very high DNP and excellent agreement with the equal spin temperature hypothesis between all nuclear spin species [7]. A statistical accuracy of 0.1% was above shown to be possible for the deuteron TE calibration; this is roughly equal to the precision $\delta T \approx 1$ mK of the temperature scale ITS90 [8] around $T = 1$ K. Assuming that in a dedicated apparatus the systematic accuracy can be even better, deuteron polarization after DNP can hence be measured to the precision in the range of 0.1%.

A value of $P(D) = 0.5$ can be reached in a dilution refrigerator at 2.5 T homogeneous field using microwave frequency modulation. This corresponds to a spin temperature around 1 mK, which can be now determined also to about 0.1% accuracy. Because the proton polarization is nearly complete and is known from the spin temperature, its precision is roughly given by

$$\delta P_p \cong \frac{\omega_p}{\omega_d} \frac{2 \log R}{R^{\omega_p/\omega_d}} \frac{\delta T_S}{T_S}, \quad (44)$$

where R is

$$R = \exp \frac{\hbar \omega_d}{k_B T_S} = \frac{P_d + \sqrt{4 - 3P_d^2}}{2(1 - P_d)}. \quad (45)$$

The calibration of the proton polarization measurement is thus improved by a numeric factor over that of the deuteron calibration accuracy and the ITS90. Using the proton NMR signal now as a thermometer, the temperature scale can be improved over ITS90 by a similar factor, which is 8 or 20 for deuteron polarizations of 0.4 or 0.5, respectively.

The improved temperature scale can be now used for the improvement of the calibration of the deuteron polarization measurement, and the same factor of improvement in the temperature scale will result after repeating the above procedure. The practical limitations for the precision which can be obtained will arise from the statistical accuracy to which the integrated NMR signals can be determined at 1 K, and from the homogeneity of the spin temperature and validity of the assumption that the two spin systems are in good thermal equilibrium with unique temperature after DNP.

Estimates based on the ab initio calculation of the NMR signal-to-noise ratio indicate that the integrated proton TE signal can be measured to a relative accuracy of 10^{-5} in partly deuterated propanediol. A relative accuracy 10^{-4} of the temperature scale at 1 K would therefore seem possible. Many systematic errors can be controlled by performing the transfer of the calibration at both positive and negative ultimate spin temperatures.

7. Summary

We conclude that although the series Q -meter technique has reached the status of mature technology, it can still be improved and developed for specific applications. Some new applications, however, may require improved circuits. The measurement of the polarization of ^{14}N in ammonia might be one of these.

References

- [1] To be published in a full paper (in preparation).
- [2] T.O. Niinikoski, Proc. 2nd Workshop on Polarized Target Materials, 1979, eds. G.R. Court, S.F.J. Cox, D.A. Cragg and T.O. Niinikoski Report RL-80-080 (SRC, Rutherford Laboratory, 1980) p. 80.
- [3] T.O. Niinikoski and A. Rijllart, Nucl. Instr. and Meth. 199 (1982) 485.
- [4] Spin Muon Collaboration (SMC), B. Adeva et al., to be published in Nucl. Instr. and Meth. A (1994) (Preprint CERN-PPE/94-54).
- [5] G.R. Court, D.W. Gifford, P. Harrison, W.G. Heyes and M.A. Houlden, Nucl. Instr. and Meth. A 324 (1993) 433.
- [6] Y.F. Kisselev, C.M. Dulya and T.O. Niinikoski, to be published in Nucl. Instr. and Meth. A (1994) (Preprint CERN-PPE/94-118).
- [7] T.O. Niinikoski, Polarized Targets at CERN, in: High Energy Physics with Polarized Beams and Targets, Int. Symp. on High Energy Physics with Polarized Beams and Targets 1976, ed. M.L. Marshak, AIP Conf. Proc. 35 (1976) 458.
- [8] H. Preston-Thomas, Metrologia 27 (1990) 3.



ELSEVIER

The Bonn polarized target NMR-system [☆]

G. Reicherz ^{*}, C. Bradtke, H. Dutz, R.M. Gehring, S. Goertz, D. Krämer ¹, W. Meyer,
M. Plückerthun, A. Thomas

Physikalisches Institut der Universität Bonn, Nussallee 12, 53115 Bonn, Germany

Abstract

The Bonn frozen spin target is used for meson photoproduction experiments in combination with the facility PHOENICS at ELSA. The maximum polarization field of 7 T is provided by a superconducting solenoid. For electron scattering experiments a target apparatus which uses a superconducting 4 T magnet in a Helmholtz configuration is employed. For dynamic nuclear polarization of protons or deuterons various microwaves sources with frequencies of 70 GHz, 98 GHz or 140 GHz are available. Ammonia, butanol and lithium hydrides are used as target materials.

The main part of the polarization detection system is the so-called Liverpool nuclear magnetic resonance module, which ensures a high flexibility for the polarization measurements of different nuclear species, e.g. ¹⁵N at 2.5 T ($f_L = 10.8$ MHz) and protons at 50 T ($f_L = 213$ MHz).

1. Introduction

Intermediate energy physics experiments with polarized targets have reached a state where more precise measurements of polarization observables can be performed. The first target asymmetry measurements of the pion photoproduction have been done at the new continuous wave electron stretcher accelerator ELSA in Bonn [1]. At high energies new experiments with polarized beams and polarized targets have been performed to study the spin structure of the nucleons [2–5].

Improvements in the polarized target technology over many years have led to highly polarized protons and deuteron targets. Using butanol or ammonia, proton polarization values of 90% to 100% and for deuterons more than 50% polarization have been measured. In particular, the latest results of the experiments mentioned above have indicated that the systematic error due to the present accuracy of the polarization measurement is a limiting factor. Currently most of the polarized target systems use the so-called Liverpool nuclear magnetic resonance (NMR) module. Nevertheless, each experiment has its own specific requirements, e.g. the size of the target volume, geometry of the inductance coil, magnetic field etc. which requires an appropriate design of all NMR parameters to

minimize error sources. On the other hand a high flexibility of the NMR-system is desirable for the studies of the polarization behaviour of different target materials e.g. lithium hydrides or -deuterides.

In this article first the Bonn NMR-system is described. Then its operation to detect thermal equilibrium (TE) signals is outlined. Finally the main error sources for the polarization measurements are discussed.

2. NMR-system

The degree of the nuclear polarization is measured with the continuous wave nuclear magnetic resonance (NMR) technique. The polarized nucleons or nuclei give the target material a complex susceptibility $\chi(\omega)$ where

$$\chi(\omega) = \chi'(\omega) - i\chi''(\omega). \quad (1)$$

$\chi(\omega)$ is a function of the applied angular frequency ω . The polarization P is connected to $\chi(\omega)$ by the relation

$$P = K \int_0^\infty \chi''(\omega) d\omega, \quad (2)$$

where K is a constant involving the properties of the nucleus concerned. For polarized protons and neutrons $\chi(\omega)$ is zero for all frequencies except for a small band close to the Larmor frequency ω_0 .

The system works with the Q -meter technique. A coil with an inductance L_0 , which is in or around the target material, is a part of a series LC -circuit. The material modifies the inductance of the coil by the relation

$$L(\omega) = L_0(1 + 4\pi\eta\chi(\omega)), \quad (3)$$

[☆] Supported by the Bundesministerium für Forschung und Technologie.

^{*} Corresponding author.

¹ Now at Universität Bielefeld, Fakultät für Physik, 33501 Bielefeld, Germany.

Table 1
Variable parameters in the RF-circuit for the proton and deuteron NMR-system

	Proton	Deuteron
R_{cc} / Ω	600	600
R_d / Ω	10	5
U_{RF}	95 mV	90 mV
$\nu_{2.5T}$	106.5 MHz	16.35 MHz
$n_{\lambda/2}^2$	6.96 m	6.48 m
V_{LF}	100	≤ 10000
Sweeps	200	8000
Coil windings	3	10

where η is the filling factor of the coil. The coil and the capacitor C are connected by a coax cable with a length of $n\lambda/2$. Changes in $\chi(\omega)$ cause changes in the Q of this resonant system which may be measured as a change in the impedance. The main part of the NMR-system is the Liverpool NMR module [6]. This module consists of RF amplifiers and a phase sensitive detector (BRM²). The frequency bandwidth is variable between 5 and 250 MHz which covers the Larmor frequencies of all used materials at magnetic fields between 2.5 and 5.0 T. A disadvantage is the built-in, wide banded amplifiers, which cause a smaller signal to noise ratio compared to the narrow banded amplifiers. Two different RF-synthesizer (U_{RF}) are used. One is digitally coupled via a GPIB 488 board and the second one is DC-coupled. The frequency of the DC-coupled generator is scanned by a sawtooth voltage output by a DAC. The DC-coupled can be modulated for the "lock in" technique [7]. A comparison of the variable parameters in the RF-circuit for the proton and deuteron NMR-system operating at 2.5 T is listed in Table 1. These variable parameters of the NMR-circuit are shown schematically in Fig. 1. The output voltage of the Liverpool NMR-box is a parabola with a height ≤ 100 mV and has an offset of about -3 V. The first LF (low frequency)-card is a DC-compensation board which subtracts the measured DC-offset after every sweep, and is triggered by a TTL signal. The amplification factor V_{DC} is 1, 10 or 100. After the DC-compensation there is a following second LF-card for the parabola compensation. This board has a further amplification factor V_{pa} of 1, 10 or 100. One sweep is divided into a maximum of 500 channels and the sweep duration is 50–60 ms. The first step before the parabola compensation is the detection of the parabola voltage outside the NMR-resonance and the storage of the voltage array in the memory. During the sweep procedure the appropriate parabola voltage will be output by a DAC. This voltage is subtracted from the signal. After the parabola compensation a second LF-amplifica-

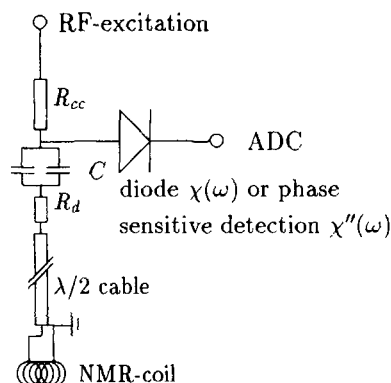


Fig. 1. The variable parameters of the NMR-circuit: amplitude of the RF-excitation, constant current resistor R_{cc} , capacitor C , dumping resistor R_d , $\lambda/2$ -cable and the inductance L of the NMR-coil.

tion is possible. This causes a better utilization of the ADC resolution. The $\lambda/2$ -cable outside the refrigerator is an UT85 type with a propagation delay of 4.72×10^{-9} s/m. The $\lambda/2$ -cable and the RF-part is temperature stabilized by water, to minimize electronic shifts.

The result of this procedure explained above is demonstrated in Fig. 2, where the thermal equilibrium (TE) signal for deuterons in ${}^6\text{LiD}$ is plotted.

Two different control systems are available. One is based on a VME-bus system with MC68000 processor and the GEM shell. The second system is based on a PC with National Instrument boards and the Turbo Vision shell from Borland C++. Both systems are connected via MIDI or RS232 with the target control system. The target control system is a second VME bus system with different I/O boards for control of the target periphery like pump-

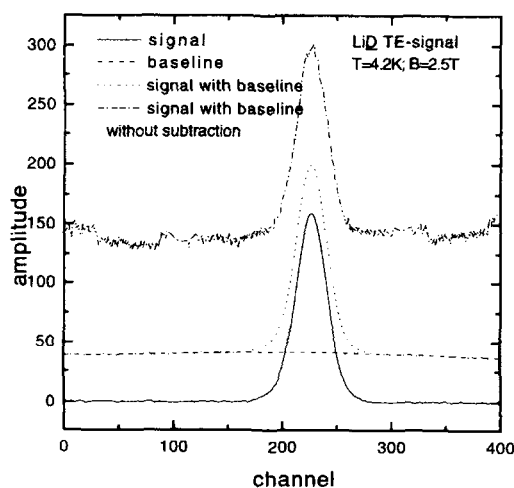


Fig. 2. The deuteron TE-signal ($T = 4.2$ K, $B = 2.5$ T) of ${}^6\text{LiD}$ before "subtraction" (upper), after "subtraction" and inclusive baseline fit (middle) and subtracted baseline (lower) is presented.

² Balanced ring modulator.

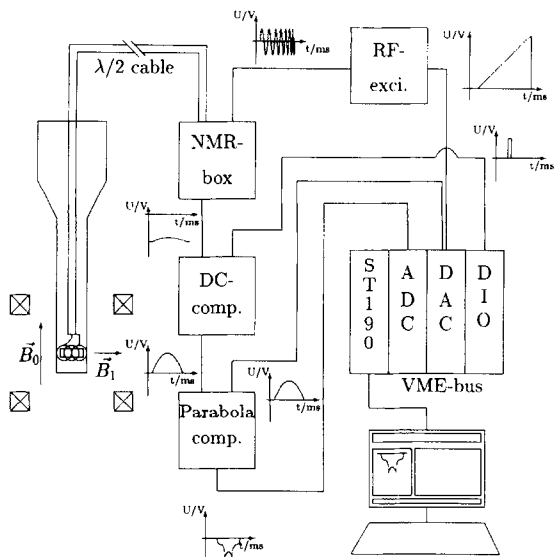


Fig. 3. Overview of the NMR system.

ing system, microwaves, refrigerator, (resistance bridge AVS), magnet power supplies and others. The experiments slow control software is the same for both VME systems. By switching the menu between “NMR” and “DAQ” only the systems are exchangeable. An overview of the Bonn NMR-system is shown in Fig. 3.

3. Thermal equilibrium signals

The correct way to calibrate the polarization value is to measure the proportionality factor K given in Eq. (2) during the thermal equilibrium. TE-signals for ammonia and butanol are taken at 1 K and for lithium hydrides at 2 and 4.2 K. For big TE-signals like protons we reduce the quality factor Q of the circuit to minimize the modulation and the non-linearities. The TE-signal and highly polarized signals for protons in butanol taken at 1 K and 5 T are shown in Fig. 4. An explanation for the signal shifts depending on the polarization values is given in Ref. [1].

In Fig. 5a TE deuteron signal from ${}^6\text{LiD}$ and ${}^{14}\text{ND}_3$ is plotted. The NMR-parameters for both measurements are nearly the same. As can be seen the line shape of these signals is completely different. The more complicated deuteron line shape in ${}^{14}\text{ND}_3$ has its origin in the interaction of the deuteron quadrupole moment with the electric field gradient. Such an electric field gradient does not exist in the face-centered cubic lattice structure of the lithium hydrides. As a result of this the deuteron line shape in ${}^6\text{LiD}$ is approximately Gaussian. Thus the TE-signal with a width of 3 kHz (FWHM) is easy to detect, even at a temperature of 4.2 K (see Fig. 5).

This NMR-technique is not suitable for signals with a line width of greater than 1 MHz. In particular the signal

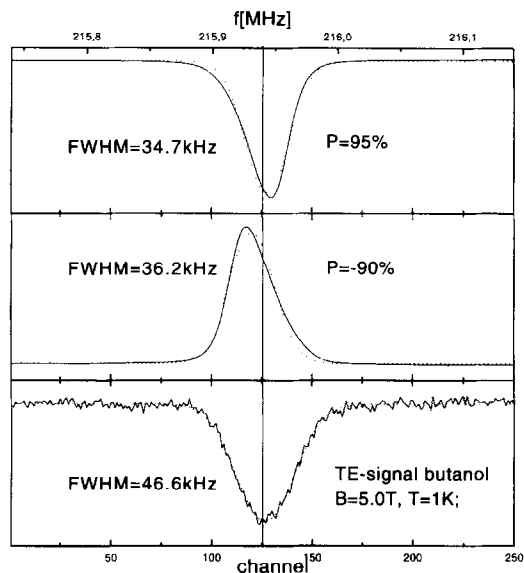
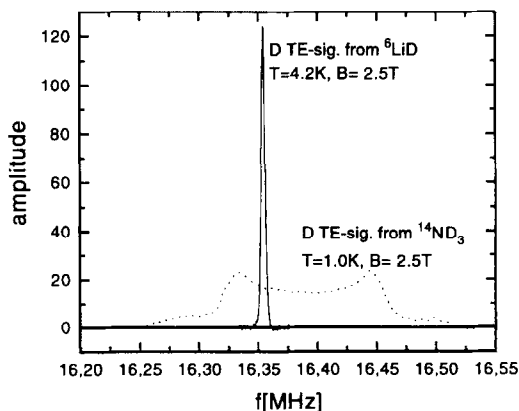


Fig. 4. Negative, positive and TE polarized proton signals at 5 T. The dashed lines are fitted by Gaussians.

for the spin 1 particle ${}^{14}\text{N}$, where the peak distance is 2.4 MHz, is extremely difficult to detect.

One method of obtaining such signals is the “lock in”-technique. The voltage U_s which has measured will be modulated with a parameter p . This parameter p is periodically varied by a reference frequency ω_r around a value p_0 . In the case of NMR there are two methods with which the signal voltage can be modulated, the RF-frequency and the magnetic field. In most cases, the magnetic field modulation is complicated, because there is no room for a modulation coil inside the refrigerator and the polarization magnet is normally not designed for a fast modulation ($\omega_r > 50$ Hz). It is much easier to modulate the RF-excitation by using a DC-coupled synthesizer. By sweeping the

Fig. 5. For comparison a TE deuteron signal from ${}^6\text{LiD}$ and ${}^{14}\text{ND}_3$ is plotted. The NMR circuit-parameters are nearly the same. Note the temperature difference.

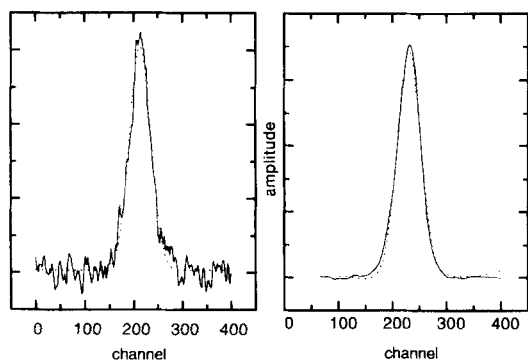


Fig. 6. TE-signals ($T = 4.2$ K, $B = 2.5$ T) of deuterons in ${}^6\text{LiD}$, obtained with the “normal” detection method (left) and with the “lock in”-technique (right). The sweep times are approximately equal. The dashed lines are the Gaussian fits of the lineshapes.

RF over the NMR resonance, one can detect only signals with a small bandwidth ($\Delta\nu \leq 10$ kHz) (6), because the resolution of the “lock in”-amplifiers is too small in the wings of the circuit parabola. However, if one sweeps the magnetic field over the resonance, the measurement of the signals with very large bandwidth (${}^{14}\text{N}$) is possible. By this method the RF-frequency can always be kept in the center of the parabola, where there is no unwanted contribution of the dispersive part of the susceptibility. It is obvious that during the sweeping of the magnetic field the DNP is not recommendable. It has also been taken into account that the TE polarization changes during the sweeping procedure of the magnet field. In addition, the differential signal, taken by the “lock in”-technique must be integrated to evaluate the degree of the polarization.

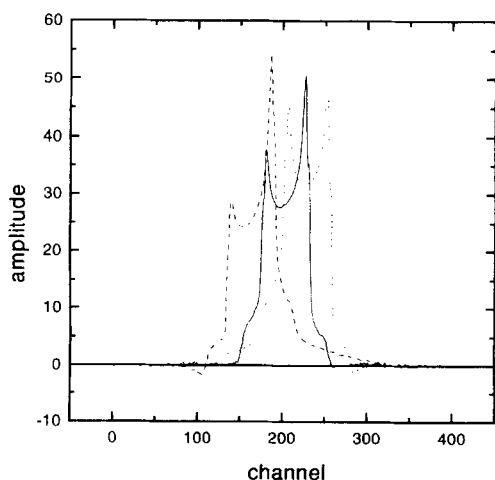


Fig. 7. Three dynamic deuteron signals with equal polarization, but with different positions on the circuit parabola (1000 kHz scan). For explanation see text.

Table 2

The errors in the measurement of the polarization for protons and deuterons in ammonia and butanol, as well as $\Delta P/P$ of ${}^6\text{Li}$ and deuterons in ${}^6\text{LiD}$

	$\Delta P/P$		
	Ammonia, butanol		${}^6\text{LiD}$
	proton	deuteron	deuteron, ${}^6\text{Li}$
ΔT	1.5%	1.5%	1.5%
ΔFE_{TE}	1.0%	4.0%	2.0%
ΔV_{HF}	1.0%	1.0%	1.0%
ΔV_{LF}	0.5%	0.5%	0.5%
$\Delta l_{\lambda/2}$	0.5%	0.5%	0.5%
Sum	2.2%	4.5%	2.8%

4. Determination of the deuteron polarization

The most accurate determination of the deuteron polarization involves measuring the factor K in Eq. (2) by the TE-method (“area method”). To minimize the errors a temperature stabilization of the $\lambda/2$ -cable and the RF-part as well as a very stable and reproduceable magnetic field is required. A polarization measurement accuracy of better than 4.5% has been obtained (see Section 5).

It is not recommended to determine the polarization degree of the deuterons in D-butanol or ND_3 by the so-called “asymmetry method” ($P = (R^2 - 1)/(R^2 + R + 1)$) [8]. For NMR-signals detected with a series circuit Q -meter, the dispersive part of the susceptibility can result in errors. It is extremely important to center the deuteron signal exactly on the NMR-circuit parabola, where wrong contributions to the signal area i.e. parts at the edges of the pedestals are negligible (see Fig. 7). The signals, outlined by dotted and dashed lines, were off-centered by shifting the magnetic field slightly. As can be seen clearly, the asymmetric signal shape varies strongly. Consequently, the deuteron polarization measured by the “asymmetry method”, also varies e.g. 6% and 60% for the dotted and dashed signals, respectively.

5. Polarization errors

The principal contributions to the error in the evaluation of the polarization are the uncertainty in the temperature ΔT of the material while taking the TE-signal, the determination of the TE-signal area ΔFE_{TE} , the non-linearities of RF-amplifiers ΔV_{RF} and the LF-amplifiers ΔV_{LF} and the changes in the electronic length of the $\lambda/2$ -cable due to the shifts in the temperature $\Delta l_{\lambda/2}$. The errors are listed in Table 2.

6. Summary

The Bonn polarized target NMR-System is based on the Liverpool NMR-module. Presently there are two control systems. One is based on the VME bus with a MC68000 processor and the second is based on PC with National Instrument boards. The NMR-system consists of three NMR modules, which can be controlled in parallel with different frequencies for different nuclear spin species. The LF-part exists of two compensation cards, one for the DC-offset and an other for the parabola compensation. The system has been used in several particle experiments: a measurement of the target asymmetry of the single pion photoproduction [1], a measurement of the polarization behaviour of ammonia in an intense electron beam [9] and the measurement of the polarization behaviour of LiH(D) at low temperature irradiation [10]. The polarization measurement error for protons and deuterons in ammonia and butanol is 2.2% and 4.5%, respectively. Proton polariza-

tion in ${}^7\text{LiH}$ is determined to a precision of 2.2%, whereas the polarization measurement error of ${}^6\text{Li}$ and deuterons in ${}^6\text{LiD}$ is 2.8%.

References

- [1] H. Dutz et al., Nucl. Instr. and Meth. A 340 (1993) 272.
- [2] B. Adeva et al., Phys. Lett. B 302 (1993) 533.
- [3] D. Adams et al., Phys. Lett. B 329 (1994) 399.
- [4] P.L. Anthony et al., Phys. Rev. Lett. 71 (1993) 959.
- [5] R. Arnold et al., Conf. on the Intersections of Particle and Nuclear Physics St. Petersburg, Florida, 1994.
- [6] G. Court et al., Nucl. Instr. and Meth. A 324 (1993) 433.
- [7] G. Reicherz, Dissertation BONN-IR-94-16.
- [8] G. Guckelsberger and F. Udo, Nucl. Instr. and Meth. 137 (1976) 415.
- [9] A. Thomas et al., these Proceedings (7th Workshop on Polarized Target Materials and Techniques, Bad Honnef, Germany, 1994) Nucl. Instr. and Meth. A 356 (1995) 5.
- [10] S. Goertz et al., *ibid.*, p. 20.



ELSEVIER

High precision measurement of the polarization in a large target

Dirk Krämer

Universität Bielefeld, Fakultät für Physik, D-33615 Bielefeld, Germany

On behalf of the Spin Muon Collaboration

Abstract

The individual error sources of the proton polarization measurement during the SMC '93 run were carefully analyzed. Main error groups were the calibration temperature, the NMR signals in thermal equilibrium and those of the enhanced polarization, and the LF gain ratio. After corrections to the raw polarization values, the overall error amounts to $\Delta P/P = 2.1\%$. The averaging of the polarization values, the correlations between the errors and the polarization homogeneity throughout the large target were also considered, resulting in a final relative accuracy of 3%.

1. Introduction

The SMC experiment aims at measuring the spin dependent structure functions by deep inelastic scattering of longitudinally polarized muons off polarized proton and deuteron targets [1,2]. A general description of the SMC polarized solid state target can be found in the references above and in Ref. [3]; Ref. [4] gives an overview of the NMR system used to measure the nucleon polarization. The target consists of two separated cells of 60 cm length and 5 cm diameter, which are polarized in opposite directions via the dynamic nuclear polarization process. The exceptional size of the target has made it more susceptible to possible radial or longitudinal polarization inhomogeneities, and thus requires a multi-channel Q -meter circuit, in our case consisting of eight large and two small NMR probes embedded in the target material, to determine the proton polarization throughout the target.

In principle the dynamic polarization value is derived by comparing the enhanced signal area $\int S_{\text{enh}}(\omega) d\omega$ with that of the thermal equilibrium (TE) signal:

$$P = G_{\text{LF}} \frac{\int S_{\text{enh}}(\omega) d\omega}{\int S_{\text{TE}}(\omega) d\omega} P_{\text{TE}}, \quad (1)$$

with the ratio G_{LF} of the LF-amplifier gain factors and the natural polarization for a spin- $\frac{1}{2}$ particle $P_{\text{TE}} = \tanh(\hbar\omega_0/2kT)$ (Curie law), where k is the Boltzmann constant, and ω_0 is the Larmor frequency of the proton. Besides the already mentioned polarization inhomogeneity, Eq. (1) indicates the main groups of uncertainties we have to face: calibration temperature errors; TE signal errors; enhanced signal errors; and gain ratio errors.

2. The temperature calibration errors

Ref. [5] gives a general description of the dilution refrigerator including the thermometry system. The TE-signal is derived at temperatures around 1 K in order to get fast polarization build-up times and temperature values which are easy to measure accurately. The most exact temperature determination around 1 K we would have extracted from the ^3He vapour pressure measurement. Unfortunately the ^3He -bulb was blocked soon after target loading. So alternative methods have been used during several TE-calibrations: Speer carbon resistors with four-wire AC bridge measurement for the first calibration and ^4He vapour pressure inside the still and RuO resistors for all other calibrations.

To improve the Curie-law method, the still heater has been used to change the calibration temperature in small steps around 1 K. Table 1 gives an overview of the main error sources. A leading error, ΔT_{noise} , originates from the readout noise of the MKS Baratron used for the vapour pressure measurement, especially for the low pressures around 1 K. Other errors linked to this device are the scale offset, ΔT_{off} , due to the reference vacuum and an observed bias of the amplifier, ΔT_{range} , when switching to different ranges. In addition, substantial errors arise due to the necessary extrapolation of the ITS 90 temperature scale below 1.25 K, ΔT_{ITS} , and due to the uncertainty in thermomolecular corrections of the pressure reading. The stability in time during the TE signal averaging (~ 4 min) was found to contribute with $\Delta T_{\text{stab}} = \pm 3$ mK. Minor influences were estimated for the ADC resolution of the pressure reading, the film creep of superfluid ^4He inside the manometer tube, and the contamination of the ^4He with ^3He . Other possible items, like pressure differences

Table 1
Main error sources for the temperature estimation as a function of T

Origin	Temperature			
	1.0 K	1.2 K	1.4 K	1.6 K
ΔT_{range} (mK)	3.0	3.0	3.0	3.0
ΔT_{offset} (mK)	3.0	1.0	0.3	0.1
ΔT_{ITS} (mK)	5.0	2.5	1.0	1.0
ΔT_{therm} (mK)	3.0	1.0	0.2	0.1
ΔT_{ADC} (mK)	1.0	0.5	0.2	0.1
ΔT_{creep} (mK)	0.4	0.2	0.1	0.1
ΔT_{cont} (mK)	0.3	0.3	0.3	0.3
ΔT_{stab} (mK)	3.0	3.0	3.0	3.0
ΔT_{noise} (mK)	8.0	4.0	2.0	2.0
ΔT_{tot} (mK)	11	7	5	6
$\Delta T/T$ (%)	1.1	0.6	0.4	0.4

due to the still pumping, field dependences, or intrinsic heating of the resistance sensors, have been evaluated to be negligible. These temperature errors result in an overall polarization error of $\Delta P_{\text{temp}} = 0.8\%$ for the calibrations 2–4. The first TE calibration has to be treated in a different way as already mentioned; the main error source is here the calibration of the Speer resistor: $\Delta P_{\text{temp}} = 2.1\%$ for calibration 1, as the first calibration has been done exclusively around 1 K.

3. The TE signal errors

As the thermal equilibrium polarization of protons at 1 K is around 0.25%, the appropriate NMR signal areas are 400 times smaller than those of the enhanced signals, thus making detection more difficult. For that reason the noise reduction is extended by $10 \times$ longer signal averaging (number of sweeps $n = 2000$), which reduces the statistical noise like $\sim \sqrt{n}$, but which on the other hand increases the influence of thermal drifts in the Q -meter parameters. In Table 2 we list the main uncertainties of the TE signal, resulting in a total error of the TE signal area of $\pm 1.1\%$.

Table 2
Main error sources of the TE signal (“background” and “polarity” are residual errors after correction)

Origin	Value
Polarity	0.60%
Magnetoresistance	0.50%
Background	0.40%
Long term drift	0.40%
Q -curve jumps	0.30%
Noise	0.30%
Relaxation	0.20%
Short term drift	0.10%
$\Delta P_{\text{TE}}/P$	1.1%

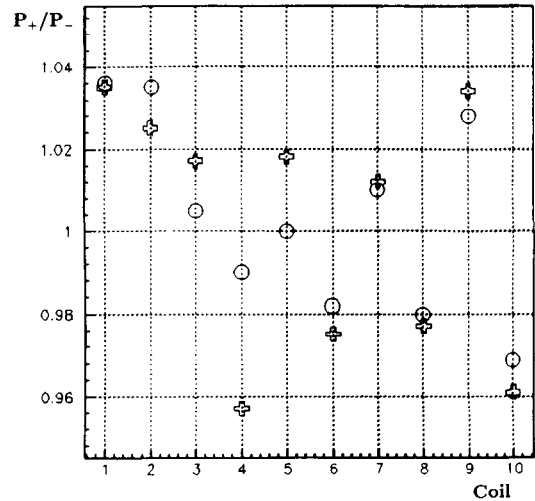


Fig. 1. The influence of the field polarity shown by the ratios of enhanced polarization before and after a field reversal (O) and for the ratios of the polarity dependent TE signal areas (+) for each NMR channel.

Note that the noise is the only statistic error source, while all others are systematic ones. For two of the main error sources, namely for the proton background signal of the empty target containers and for a field polarity effect on the calibration coefficients, corrections were applied. The container's NMR signal was found to be on the order of 1% of the TE signal size, but with a relatively large uncertainty. The influence of the field polarity on the signal areas, most probably caused by the stray field on the RF 10-way splitter used to feed the individual NMR probes from a single synthesizer, is illustrated in Fig. 1. Other main sources of uncertainty in the TE signal are slight tuning changes at the 1.5% higher baseline field due to magnetoresistance of the coils and cables inside the cryostat, drifts of the Q -meter circuits in time, noise, and observed small irregular jumps in the Q -curves, for which no satisfactory explanation could be given so far. There is also a small contribution due to the change in the TE polarization caused by the baseline taking at a different field together with the finite relaxation time on the order of minutes.

4. The enhanced signal errors

As the enhanced signals are much larger than those of the TE, some of the so far discussed error sources are of minor interest, namely the noise, the background, and the magnetoresistance. But there are also additional error sources for the enhanced signals: Some of the biggest problems of the polarization measurement arise from the large modulation depth of the highly enhanced signals, that is the signal height relative to the RF-level outside the

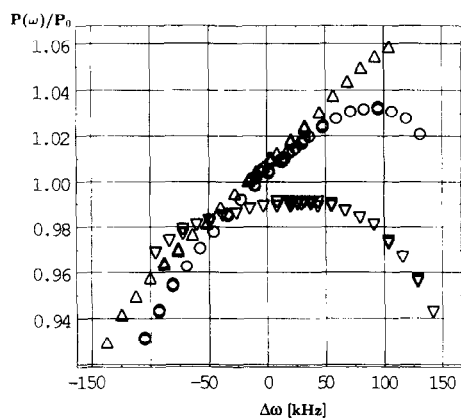


Fig. 2. Relative polarization change as a function of the off-centering frequency $\Delta\omega$ for the coils #2 (○), #3 (▽) and #6 (△) at 600 kHz sweep width.

resonance. This modulation can exceed 60% for the negative signal, which leads to a non-linear distortion of the line shapes and thus to a wrong estimation of the signal area. Please refer to Ref. [6] for a more detailed analysis. The correction to be made on the polarizations due to our simulation of the Q -meter circuit is on the order of 5% with a residual uncertainty of up to 0.9%.

Another correction was necessary for the observed signal shifts caused by the internal magnetization of the aligned magnetic moments. Fig. 2 shows the measured changes in the signal areas due to the frequency dependence of the Q -meter response function and due to the signal cut-off.

Other items are the linearity of the Balanced Ring Modulator (BRM) used in the Liverpool Q -meters to receive the real part of the output voltage, some observed sudden tuning changes, and a possible contribution from the hyperfine-broadened protons in the EHBA-chromium (V) complex, which could not be measured. In Table 3 the leading error sources of the enhanced signals are summarized for the two sweep widths used through the 1993 run, adding to an overall error of 1.2 and 1.0%, respectively.

The LF amplifier gain ratio between TE and enhanced signal turns out to be an additional source of error on the order of 0.5%.

Table 3

Remaining systematic error sources of the enhanced signal after corrections for 400 and 600 kHz sweep width, respectively

Source	400 kHz	600 kHz
Nonlinearity	0.90%	0.60%
BRM linearity	0.60%	0.60%
Offcentering	0.50%	0.40%
EHBA-signal	0.15%	0.15%
System drifts	0.30%	0.15%
Tuning jumps	0.50%	0.50%
$\Delta P_{\text{enh}} / P$	1.2%	1.0%

5. Polarization homogeneity and averaging

The polarization values given by the individual coils were averaged for each target cell and over the time of one data run (typically 0.5 h) considering the following points:

- The coils do not sample the whole target volume and it is different for the small and the big coils.
- Correlations between the polarization errors have to be taken into account not only for the coils of one half regarding the averaged value, but also for the difference of upstream and downstream cells (which is the relevant parameter for the measured observable). At last the correlation in time for a given error has to be considered.
- Only the entirely uncorrelated part of the error will shrink like $1/\sqrt{n}$ of the the number of used coils, n .

In addition, it has to be analyzed, whether the different readings of the individual coils reflect a substantial inhomogeneity throughout the target cells. While the longitudinal homogeneity has less impact due to the “averaging” by the beam, a large radial dependence of the polarization would cause serious systematic problems. There are several physical reasons which might affect the polarization homogeneity in the target volume:

- Magnetic field flatness: Small deviations from the main field of 2.5 T can lead to differences in polarization build-up time and final values in parts of the target. This deviation should not exceed a few gauss, as shifts of the microwave center frequency of 10 MHz result in a slight depolarization for values of P beyond 90%. However, the superconducting solenoid provides a magnetic field flatness of $\Delta B/B < 10^{-4}$, so that this influence is largely diminished.

- Microwave distribution: The absorption of the microwaves by the paramagnetic centers of the target may lead to an attenuation of the microwave strength towards the center of the target. This would cause a troublesome radial inhomogeneity. Fortunately the optimal microwave frequencies for positive and negative DNP are situated slightly beneath the ESR line, e.g. our target is highly transparent.

- Microwave leakage: A microwave leakage through the microwave stopper between the two target cells might cause a drop of the polarization towards the inner ends because of the opposite spin directions in the two halves. This effect has been investigated, showing no significant microwave leakage.

- NMR saturation: The RF field of the proton larmor frequency used for the NMR system destroys a small part of the polarization. Feeding high RF power directly inside the coils results in a strong depolarization within a few seconds. However, the appropriate choice of the circuit parameters leads to a negligible depolarization: The relaxation time caused by the NMR system is on the order of several hundred hours.

- Superradiance: The superradiance [7,8] has destroyed the negative polarization substantially during every field

Table 4
Summary of the applied polarization corrections and the residual error

Correction	Magnitude	Residual
Background	1.0%	0.4%
Polarity	2.0%	0.6%
Gain	2.0%	0.5%
Off-centering	0.6%	0.5%
Non-linearity	4.0%	0.8%

reversal used to change the spin direction every 5 h before it was discovered, how to prevent this effect by means of an inhomogeneous field created by the solenoid's trim coils during the ramp down of the field. Moreover, the superradiance takes place at particular NMR coils, destroying thus the polarization very locally and creating inhomogeneities in excess of 40%.

After corrections the largest differences inside a given cell are below 3%. To probe a possible radial inhomogeneity, two small coils have been installed in the upstream target, one centered and the other perpendicular ~ 1 cm off center. The readings from these coils also do not differ

Table 5
Final error of the averaged coils for upstream and downstream targets during the 1993 proton run

Period	σ_{tot} (up)	σ_{tot} (down)
May–Jun.	2.8%	2.7%
Jun.–Sep.	2.1%	1.8%
Sep.–Nov.	2.2%	1.7%
Nov.–Dec.	1.9%	1.7%

significantly, either from the averaged value nor from each other.

6. Summary

Table 4 gives an overview of the applied corrections to the polarization values, the number of magnitude and the residual error. Not included are special treatments of the temperature measurements themselves, like the thermomolecular correction. Summarizing the contributions of all investigated error sources, the final error of the averaged polarization for upstream and downstream cells is given in Table 5. If we include the small inhomogeneity observed by the different probes, the overall error of both target halves averaged over the whole run turns out to be:

$$\Delta P_{\text{tot}}/P = 3.0\%,$$

where the mean polarization value throughout the data taking was $\bar{P} = 86\%$.

References

- [1] SMC, B. Adeva et al., Phys. Lett. B 302 (1993) 533.
- [2] SMC, B. Adams et al., Phys. Lett. B 329 (1994) 399.
- [3] J. Kyyräinen, these Proceedings (7th Workshop on Polarized Target Materials and Techniques, Bad Honnef, Germany, 1994) Nucl. Instr. and Meth. A 356 (1995) 47.
- [4] N. Hayashi et al., *ibid.*, p. 91.
- [5] P. Berglund et al., A large dilution refrigerator for polarized target experiments, to be submitted to Cryogenics.
- [6] Y. Semertzidis et al., Ref. [3], p. 83.
- [7] Y.F. Kisselev et al., Zh. Eksp. Teor. Fiz. 94 (2) (1988) 344; Sov. Phys. JETP 67 (1988) 413.
- [8] L.A. Reichertz et al., Nucl. Instr. and Meth. A 340 (1994) 278.



ELSEVIER

Estimation of non-linearity in NMR polarization measurement

Yannis K. Semertzidis

PPE Division, CERN, CH-1211 Geneva 23, Switzerland

On behalf of the Spin Muon Collaboration

Abstract

The non-linearity of the proton NMR signal of the SMC target during the 1993 run is considered here. It is estimated that the highest negative (positive) polarizations were systematically overestimated (underestimated) by about 5% when the total scan width used was 400 kHz, and by about 3% when the total scan width was 600 kHz.

1. Introduction

The polarization measurement of the NA47 (SMC) experiment at CERN [1], which measures the spin dependent structure functions of the proton and neutron, is done by the continuous wave nuclear magnetic resonance (NMR) [2,3] method. There are two target halves which are polarized in opposite directions in order to reduce the systematic errors in the NA47 experiment. The polarization of the protons is measured by 10 coils embedded in the target material and read by 10 series *Q*-meters.

The absolute polarization is proportional to the integral of the absorption part of the susceptibility [4]:

$$P = \frac{2}{\mu_0 \pi \hbar \gamma^2 N I} \int_0^\infty \chi''(\omega) d\omega, \quad (1)$$

where γ is the nuclear gyromagnetic ratio, I the spin of the species in question and N the spin density of the material. The complex susceptibility is $\chi(\omega) = \chi'(\omega) - i\chi''(\omega)$ in the SI units that are used throughout this text. $\chi'(\omega)$ is the dispersion and $\chi''(\omega)$ the absorption part of the susceptibility. The enhanced proton polarization signal is compared to the proton NMR integral at a thermal equilibrium (TE) with the lattice temperature at about 1 K:

$$P = \frac{\int_0^\infty S(\omega) d\omega}{\int_0^\infty S_{TE}(\omega) d\omega} P_{TE}, \quad (2)$$

where $S(\omega) = V_{out}(\chi(\omega)) - V_{out}(\chi(\omega) \equiv 0)$ and V_{out} is the series *Q*-meter signal.

For Eq. (2) to hold true the *Q*-meter circuit must respond linearly in a wide range since the ratio of the largest signal to the TE signal is more than 400.

There are more works [5,6] on computer based analysis of the NMR *Q*-meters but here we will show explicitly why to first order the non-linearity cancels and how to find the remaining error and correct for it. A more complete version of this work can be found in Ref. [7].

2. Circuit analysis

The equivalent circuit [8,9] used for NMR is shown in Fig. 1. The real and imaginary parts of the voltage output are [9]:

$$\begin{aligned} \text{Re}(V_{out}) &= \frac{GV_0}{R_0} \frac{\text{Re}(Z) + X[\text{Re}^2(Z) + \text{Im}^2(Z)]}{[(1 + X \text{Re}(Z))^2 + X^2 \text{Im}^2(Z)]}, \\ \text{Im}(V_{out}) &= \frac{GV_0}{R_0} \frac{\text{Im}(Z)}{[(1 + X \text{Re}(Z))^2 + X^2 \text{Im}^2(Z)]}, \end{aligned} \quad (3)$$

where $X = 1/R_i + 1/R_0$, with R_i the amplifier input impedance, R_0 the current limiting resistor, G the amplifier gain, and V_0 the synthesizer voltage output.

The impedance of the coil in the target material is

$$Z_L = R_L + i\omega L(1 + \phi(\omega)), \quad (4)$$

where R_L is the coil resistance, L the coil inductance and $\phi(\omega) = \phi'(\omega) - i\phi''(\omega) = \eta(\chi'(\omega) - i\chi''(\omega))$ with η the coil filling factor. The proton polarization can be detected by integrating the change of the coil RF impedance when scanning over the proton Larmor frequency. In practice it is the $\text{Re}(V_{out})$ that is integrated. Unfortunately, there is always a need for a cable that transports the signal to the detector and tuning system, which distorts it some-

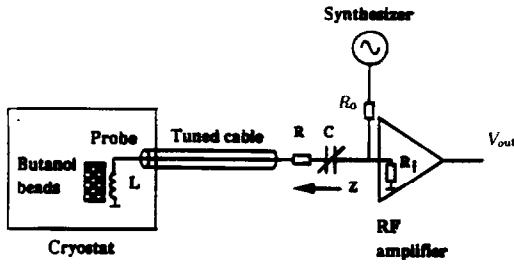


Fig. 1. Series Q -meter NMR circuit.

what. The total impedance $Z(\omega)$ including the cable and the tuning electronics is then

$$Z(\omega) = R + \frac{1}{i\omega C} + Z'_L, \quad (5)$$

with

$$Z'_L = Z_c \frac{Z_L + Z_c \tanh \gamma_c l_c}{Z_c + Z_L \tanh \gamma_c l_c}, \quad (6)$$

where Z'_L is the image impedance of the coil impedance which is also responsible for introducing the non-linearity in the final signal, C the value of the tuning capacitor, and R the damping resistance. Z_c is the cable impedance and is equal to [9]:

$$Z_c \approx Z_0 \sqrt{1 + \frac{R_c}{i\omega L_c}} \approx Z_0 \left\{ 1 + \frac{1}{i2Q_c} \right\}, \quad (7)$$

with $Z_0 = (L_c/C_c)^{1/2}$ the cable characteristic impedance (equal to 50 Ω for the cables used in our case). R_c , L_c , C_c are the cable resistance, inductance and capacitance per unit length respectively. $Q_c = \omega L_c/R_c$ is the cable ‘‘quality’’ factor, and l_c the cable length. The propagation constant γ_c can be approximated to

$$\gamma_c = \sqrt{(R_c + i\omega L_c)i\omega C_c} \approx \frac{\omega\sqrt{L_c C_c}}{2Q_c} + i\omega\sqrt{L_c C_c}, \quad (8)$$

which can be identified with the expression

$$\gamma_c = \alpha + i\beta, \quad (9)$$

where α is the attenuation constant and β the phase constant of the cable ($\beta = D\omega$, and D is the propagation delay).

The cable length is chosen so that on resonance (the Larmor frequency) $\tanh(\gamma_c l_c)$ is purely real, i.e.

$$l_c = \frac{n\pi}{\omega_c \sqrt{L_c C_c}}, \quad (10)$$

where ω_c is the cable resonance angular frequency, which here we will assume is the same as the Larmor angular frequency ω_0 , and n is the number of half wavelengths of the Larmor frequency in the cable. Then

$$\gamma_c l_c = in\pi \frac{\omega}{\omega_0} \sqrt{1 + \frac{1}{iQ_c}} \approx in\pi \frac{\omega}{\omega_0} \left(1 + \frac{1}{i2Q_c} \right). \quad (11)$$

At $\omega = \omega_0$, $\tanh(\gamma_c l_c) = \tanh(n\pi/(2Q_c))$ and the length of the cable is $l_c = n\lambda/2$ with λ the wavelength of the ω_0 in the cable.

In principle, the circuit is analysed and once knowing the various parameters one can reproduce the observed Q -curves and NMR signals. In practice, only some of the parameters are measured with very high accuracy, and therefore we will fit the Q -curves in order to obtain more precise values of them.

It is clear that the voltage output of the Q -meter is highly non-linear in view of Eqs. (3), (6) and (11), and it is the size of the signal itself that determines the amount of error made when applying Eq. (2). In other words the non-linear contributions depend on the relative height (or else the modulation depth M) which is the ratio of the absolute height of the signal divided by the minimum value of the RF-level:

$$M = \frac{S(\omega_0)}{V_{\text{out}}^{\text{min}}(\chi(\omega) \equiv 0)}. \quad (12)$$

3. Kramers–Kronig relations

With the help of the Mathematica [10] software package we developed the real part of the V_{out} of Eq. (3) (we give it here in units of volts after setting the term $GV_0/R_0 \approx 0.1$ A):

$$\begin{aligned} \text{Re}(V_{\text{out}}) = & 3.5 - 17.0\Delta + 1200\Delta^2 \\ & + (3.0 + 110\Delta - 550\Delta^2)\phi' \\ & + (0.3 + 58\Delta + 2900\Delta^2)\phi'' \\ & + (1.5 + 70\Delta + 1900\Delta^2)(\phi'^2 - \phi''^2) \\ & - (0.5 + 5.0\Delta + 4900\Delta^2)\phi'\phi'', \end{aligned} \quad (13)$$

with $\Delta = (\omega - \omega_0)/\omega_0$, from where we can see that the coefficient of the non-linear term is only 50% less than that of the linear term and is potentially very damaging. Of course the non-linear term would be negligible if ϕ was very small but we have observed modulations (M) as much as 65% for the negative and 40% for the positive polarization and therefore this is not the case here.

Fortunately the non-linear terms ϕ'^2 and ϕ''^2 enter in Eq. (13) with the same coefficient and opposite sign so that their contributions are in competition with each other. It turns out that because the dispersion and absorption parts of the susceptibility are related through the Kramers–Kronig relations [11]:

$$\begin{aligned} \phi'(\omega_0) &= \frac{2}{\pi} P \int_0^\infty \frac{\omega \phi''(\omega)}{\omega^2 - \omega_0^2} d\omega, \\ \phi''(\omega_0) &= -\frac{2\omega_0}{\pi} P \int_0^\infty \frac{\phi'(\omega)}{\omega^2 - \omega_0^2} d\omega \end{aligned} \quad (14)$$

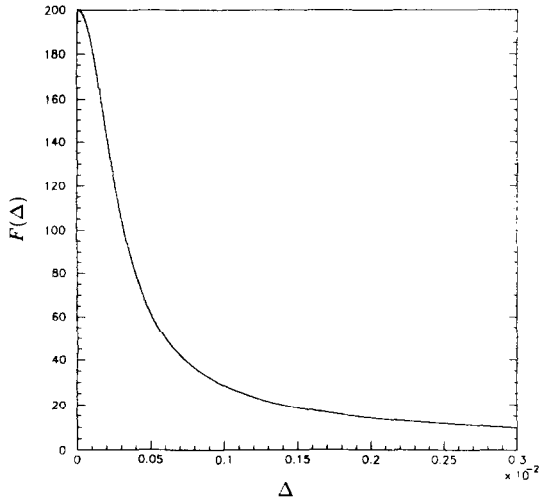


Fig. 2. Function $F(\Delta)$ versus Δ (see Eq. (17)) with FWHM = 53.2 kHz. The right end corresponds to $f - f_0 = 319.5$ KHz.

(where P denotes the principal value of the integral), the following is also true [12]:

$$\int_0^\infty \phi'^2(\omega) d\omega = \int_0^\infty \phi''^2(\omega) d\omega. \quad (15)$$

Even though the two integrals are the same, the frequency dependence of $\phi'^2(\omega)$ and $\phi''^2(\omega)$ is very different and the two do not quite cancel when integrating the NMR signal in a finite frequency range. The remnant $\int_{\omega_0 - \omega_B}^{\omega_0 + \omega_B} (\phi'^2 - \phi''^2) d\omega$ depends on the ratio of the signal (ϕ'') width over the total scan width ($2\omega_B$). Therefore the signal width is a very important parameter in this analysis and special care should be taken to determine it. The term $\phi'\phi''$ is antisymmetric and does not contribute to the signal integral.

The shape of the absorption part of the susceptibility is calculated using the modified Lorentzian function¹

$$\phi''(\omega) = \frac{1}{1 + \left| \frac{\Delta}{\Delta_H} \right|^{2.5}}, \quad (16)$$

where Δ_H is half the full width at half maximum (FWHM). The FWHM is taken from the experimental TE signals, where the contribution of $\phi'(\omega)$ to the line width can be neglected. The higher order contributions to the width of the TE signals are totally negligible. Fig. 2 shows the function

$$F(\Delta) = - \frac{\int_0^\Delta (\phi'^2 - \phi''^2) d\omega}{\int_0^\Delta (\phi'^2 + \phi''^2) d\omega} \times 200, \quad (17)$$

¹The final result will not be different for a Gaussian, or Lorentzian Function.

versus Δ for FWHM = 53.2 kHz, which goes asymptotically to zero as the angular frequency goes to infinity. The non-cancellation of the integrals of ϕ'^2 and ϕ''^2 is 15% for 400 kHz scan and 10.5% for 600 kHz.

4. Q-curve fitting, correction formulas

In order to simulate the response function of the detector, the non-linearity, the signal shape change etc., there is a need to know the circuit parameters. Those we have obtained by a fit to the Q -curve and restricting their values to be around the measured ones. For the fit we used the exact formulas from Section 2, and the subroutine HFITH from the HBOOK which in turn is based on the Minuit package [13].

As is apparent from Eq. (3) the factor GV_0/R_0 would also be needed to fit the real data. In order to avoid this we have normalized the data and the fitting function by their minimum values, making the knowledge of that parameter unnecessary [14]. After we have obtained the rest of the parameters (5) from the fit, we used those to fit GV_0/R_0 to the original data, with the result given here for reference ($GV_0/R_0 = 0.10$ A).

The width of the TE NMR signals is FWHM = 66 kHz, i.e. 6.2×10^{-4} relative. This is more than 6 times than that which can be due to the magnet inhomogeneity. This width is assigned to be due to the dipolar broadening which becomes less important at high polarizations. Fig. 3 shows how a positive (dashed) and an inverted negative signal, using the same input signal with the above width, would look like at the output of the Q -meter circuit. The

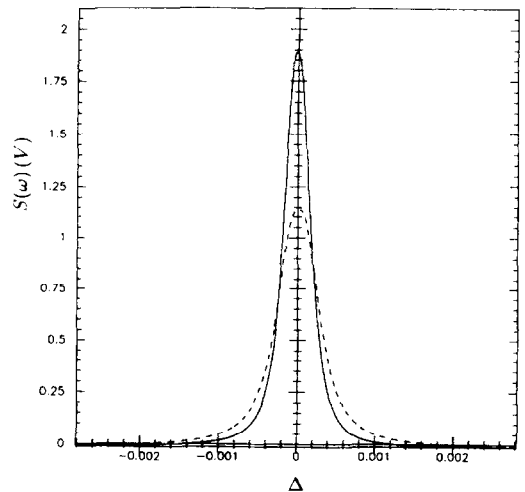


Fig. 3. Simulated positive (dashed) and inverted negative signals at the output of the Q -meter. The FWHM for the input absorption function is 66 kHz. The output signals have FWHM of 75 kHz and 51 kHz for the positive and negative polarities respectively. The positive modulation is 0.34 and the negative 0.57.

definite conclusion is that the positive signal becomes wider, and the negative narrower, the reason being that the non-linearity contributes to the signal shape in different ways (see Eq. (13)). The width of the simulated negative signal becomes $\text{FWHM} = 51$ kHz (i.e. a reduction of 22%) and that of the positive $\text{FWHM} = 75$ kHz (i.e. an increase of 15%). Assuming about (20%) reduction in the dipolar broadening effect, at high polarizations, we would get a net slow reduction of the positive signal widths and a much faster reduction of the negative ones as the polarization increases, consistent with the experimental data. Taking this into account we have simulated the final signals with a $\text{FWHM} = 53.2$ kHz which is about 20% less than that of the TE signals. This 20% reduction in the signal

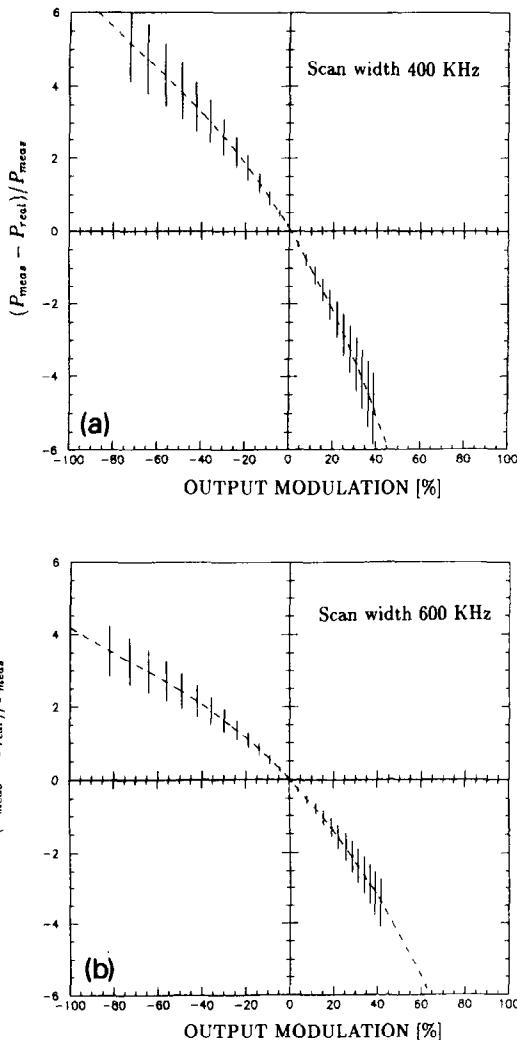


Fig. 4. (a) Non-linear contributions to the integrated series Q -meter signal for negative and positive polarizations, as a function of the output voltage modulation M . The total scan width is 400 kHz. (b) Same as (a), but here the total scan width is 600 kHz.

Table 1

Estimated parameters a , b , c , d for the different scan widths

Total Scan	a	b	c	d
400 kHz	6.5×10^{-2}	-10×10^{-2}	-5.9×10^{-4}	-2.6×10^{-6}
600 kHz	4.5×10^{-3}	-6.3×10^{-2}	-3.7×10^{-4}	-1.6×10^{-6}

width results in the reduction of the corrections by about 10% which we will treat as a source of error.

Another important feature of the non-linear terms is that the positive and negative (inverted) signals cross the zero line and become negative doing this at different points. Because the determination of the real zero point is in practice difficult, we take, after the baseline subtraction, the average of 20 points from the left end, and the same from the right end of the signals, and assume that those are the real zero points.

Using the simulated signals we show in Figs. 4a and 4b how much the relative polarization is overestimated (negative polarization) or underestimated (positive polarization) as a function of the signal output modulation, when using scan width of 400 and 600 kHz respectively. We have fitted the function

$$\frac{P_{\text{real}} - P_{\text{meas}}}{P_{\text{meas}}} [\%] = a + bM [\%] + c(M [\%])^2 + d(M [\%])^3, \quad (18)$$

and used the χ^2 minimization to determine the parameters. Figs. 4a and 4b show the corresponding estimations for 400 kHz and 600 kHz total scan width, and the parameters are given in Table 1. Even though the modulations of the positive and negative signals, for the same absolute polarization values, are very different, the non-linearity is roughly the same in magnitude for the same polarization.

The total error of about 20% is the total estimated error due to uncertainties in the circuit simplifications, the dipolar broadening change with polarization, and the fact that each coil is tuned slightly different from every other one (i.e. the circuit parameters are not the same for every coil).

5. Conclusions

The maximum experimentally observed modulation of the negative signals was 65% and that of the positive 40%. From Fig. 4a we then see that the polarizations were overestimated (underestimated) by a maximum of about 5% for the negative (positive) signals when 400 kHz total scan width was used. The same numbers go down to 3% when 600 kHz total scan width is used. These corrections have been already applied to the data [15], and it turns out

that the positive and negative polarization values are much closer than before.

The impact of this result on the SMC experiment is small because the overestimation of the negative polarization and underestimation of the positive polarization are largely cancelled when the two target halves have the same absolute polarization and in the limit that the acceptance for both target halves is the same. This is so, because for the spin asymmetry analysis the difference between the two polarizations is relevant. However, experiments which only use a single target could benefit more from this analysis. This analysis helps the polarized target group to give more accurate absolute polarization values, since the non-linearity was the source of the highest single error in the polarization measurement.

Appendix

Various circuit and signal parameters are given here for reference. Some of the values are measured directly, and some are taken from the fit of the Q -curve (baseline).

$P_{TE} = 0.00255$	Proton TE polarization at 1 K and 2.5 T.
$f_0 = 106.5$ MHz	Proton Larmor frequency at 2.5 T.
$\omega_0 = 2\pi f_0$	Proton Larmor angular frequency at 2.5 T.
$\Delta = (\omega - \omega_0)/\omega_0$	Fractional angular frequency. For a 600 kHz total scan $\Delta \approx 2.82 \times 10^{-3}$ at the right end of the scan.
$\Delta_H = 2.5 \times 10^{-4}$	Is the half width at half maximum of $\phi''(\omega)$ equal to 26.6 kHz which is used for the signal simulation.
$n = 5$	The length of the cables was $5\lambda/2$.
$C = 20$ pF	Tuning capacitor.
$R = 34$ Ω	Damping resistor.
$L = 90$ nH	Coil inductance.
$R_L = 0.35$ Ω	Coil resistance.
$X = 1/R_i + 1/R_0$ $= 9.5 \times 10^{-3} \Omega^{-1}$	$R_i = 118$ Ω is the sum of the amplifier input impedance of 50 Ω and the external series resistor of 68 Ω . $R_0 = 940$ Ω is the current limiting resistor.
$Q = \omega L/R \approx 170$	Coil quality factor.
$Q_c = \omega L_c/R_c \approx 65$	Combined cable quality factor.
$Z_0 = 50$ Ω	Cable characteristic impedance.
$\alpha = 0.0242$ Np/m	Cable attenuation constant.

$\beta = D_\omega \approx 3.16$ rad/m	Phase constant of the cable.
$D = 4.72 \times 10^{-9}$ s/m	Cable propagation delay.
$\beta = \omega\sqrt{\epsilon}/c$	$\epsilon \approx 2.0$ is the dielectric constant of the cable, and c the speed of light in vacuum.

References

- [1] SMC, B. Adeva et al., Phys. Lett. B 302 (1993) 533; SMC, G. Baum et al., Proposal CERN/SPSCS 88-47 (SPSC/P242) (1988).
- [2] EMC, J. Ashman et al., Nucl. Phys. B 328 (1989) 1.
- [3] S.C. Brown et al., Proc. 4th Int. Workshop on Polarized Target Materials and Techniques, ed. W. Meyer, University of Bonn (1984) p. 102.
- [4] M. Goldman, J. Magn. Res. 17 (1975) 393.
- [5] J.J. Hill and D.A. Hill, Nucl. Instr. and Meth. 116 (1974) 269.
- [6] F. Spericen, Nucl. Instr. and Meth. A 260 (1987) 455.
- [7] Y. Semertzidis and T. Niinikoski, Correction of Non-Linearity in NMR Polarization Measurement SMC/94/8; Y. Kisselev, C. Dulya and T. Niinikoski, SMC/94/10, submitted to Nucl. Instr. and Meth. A.
- [8] G. Court, D.W. Gifford, P. Harrison, W.G. Heyes and M.A. Houlden, Nucl. Instr. and Meth. A 32 (1993) 433.
- [9] T.O. Niinikoski, Proc. 2nd Workshop on Polarized Target Materials, eds. G.R. Court, S.F.J. Cox, D.A. Cragg and T.O. Niinikoski, Report RL-80-080, SRC, Rutherford Laboratory (1980) p. 80.
- [10] Mathematica version 2.2 from Wolfram Research Inc.
- [11] J.D. Jackson, Classical Electrodynamics, 2nd ed. (Wiley, 1975) p. 311.
- [12] G. Arfken, Mathematical Methods for Physicists, 3rd ed. (Academic Press, 1985) p. 425.
- [13] F. James and M. Roos. MINUIT-Users Guide, Program Library D506. CERN, (1981).
- [14] However, in the Q -meter circuit there is also a DC offset card whose functionality is to provide a better dynamic range for the readout system. It works by detecting the voltage of the left most data point (at the beginning of the baseline scan) with an A/D converter and then applying a DC voltage offset of the same value and opposite polarity with a D/A converter. Afterwards there is a card with software selectable nominal gains of 1, 227 and 315. During the SMC proton data run of 1993 the nominal gain of 1 was used throughout, which was determined by D. Krämer to be equal to 0.90, the value that was used in this paper.
- [15] Error Analysis for the NMR Polarization Measurement, SMC Polarized Target Group, SMC/94/7.



ELSEVIER

Analysis of deuteron NMR signals

C.M. Dulya

University of California, Department of Physics, Los Angeles, CA 90024, USA

Abstract

A method of extracting the Q -curve from deuteron NMR signals has been developed in order to treat signals which are highly distorted because of Q -curve instabilities. The extracted Q -curve can then be used to calculate the subtracted signals, thus leading to the determination of the polarization.

1. Introduction

The polarization of the deuterons in dynamically polarized target materials of high energy physics experiments is usually measured using a nuclear magnetic resonance (NMR) technique. The polarization of the target material is given by [1]

$$P \sim \int_0^\infty d\omega \chi''(\omega), \quad (1)$$

where $\omega = 2\pi\nu$ is the angular frequency of the applied rf field and $\chi''(\omega)$ is the absorptive part of the nuclear susceptibility $\chi(\omega) = \chi'(\omega) - i\chi''(\omega)$, which is non-zero only in a small range of frequencies around the Larmor frequency, ω_d , of the deuteron. A deuteron of magnetic moment μ in a field H_0 has a Larmor frequency of $\hbar\omega_d = \mu H_0$.

By embedding a coil of inductance L_c in the target material, the absorption $\chi''(\omega)$ can be measured through the inductive coupling between the nuclear spins and the coil. The inductance will vary as [2]

$$L = L_c(1 + \eta\chi(\omega)), \quad (2)$$

where η is the filling factor of the coil. The change in inductance is detected by a series Q -meter [3] connected to the coil via a coaxial transmission cable. The Q -meter scans the rf frequency over a small range $\omega_u - \omega_l$ and provides a real voltage $V = V(\omega, \chi)$. The Q -curve, $V_Q = V(\omega, \chi = 0)$, is measured by changing H_0 such that $\chi''(\omega) = 0$ for the entire frequency scan. Then, the NMR signal, $V = V(\omega, \chi)$, is detected on resonance by scanning the frequency at the nominal field H_0 , where $\omega_l < \omega_d = \omega H_0/\hbar < \omega_u$. The two signals are then subtracted and the result is that $\dot{S}(\omega) \approx \chi''(\omega)$. In this case, the polarization is approximated by

$$P = \mathcal{N} \int_{\omega_l}^{\omega_u} d\omega S(\omega) \quad (3)$$

where \mathcal{N} is a constant determined by making a thermal equilibrium (TE) calibration of the system [4].

2. The series Q -meter

The constant current series Q -meter of Fig. 1 is used to detect the NMR signal. It consists of a coil of inductance L_c , resistance r_c and stray capacitance C_c connected by a coaxial cable of length l to a room temperature tuning capacitor C and damping resistance R . It is driven by an rf source of voltage V_0 through a feed resistance R_0 . An amplifier of gain A and input impedance R_a amplifies the signal and then its real part is detected by comparing its phase to the rf phase with a phase sensitive detector (PSD).

The new method developed for extracting the Q -curve is based on the following idealized description of the series Q -meter circuit. From Eq. (2), the impedance of the coil changes as

$$Z_c = \{r_c + i\omega L_c(1 + \eta\chi(\omega))\}^{-1} + i\omega C_c. \quad (4a)$$

Consider a cable of impedance Z_0 , length l and complex wave number $\gamma = \alpha + i\beta$ with the load from Eq. (4a) connected to one side. The coil impedance is seen as

$$Z_t = Z_0 \frac{Z_0 \tanh(\gamma l) + Z_c}{Z_0 + Z_c \tanh(\gamma l)} \quad (4b)$$

at the other end of the cable. The circuit impedance $Z(\omega, \chi)$ of the cable, coil, C and R is

$$Z(\omega, \chi) = R + 1/i\omega C + Z_t. \quad (4c)$$

Thus, the complex voltage V_a at the output of the rf amplifier in terms of ω and χ is

$$V_a(\omega, \chi) = \frac{AV_0}{R_0} \frac{Z(\omega, \chi)}{1 + xZ(\omega, \chi)}, \quad (4d)$$

where $x = 1/R_0 + 1/R_a$ is the admittance.

3. Background subtraction

Normally, a Q -curve is taken and subtracted from the deuteron NMR signals for many hours to follow. However,

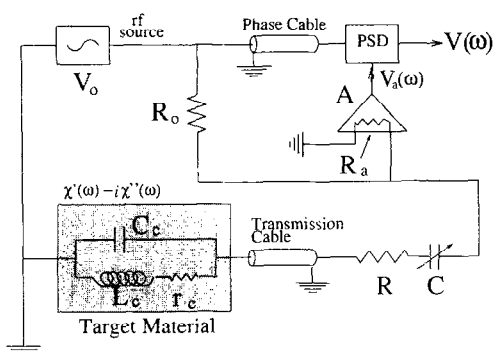


Fig. 1. The constant current series Q -meter.

the subtracted signal $S(\omega)$ may still contain a residual Q -curve caused by changes in the circuit parameters between the times when the Q -curve and the NMR signal are taken. Because the wings of χ'' for the deuteron are flat, an additional background subtraction is facilitated. The difference in two Q -curves measured at different times is parabolic if either the Q -curve itself is parabolic or if the drift of the Q -curve is small. In this case, a background subtraction by fitting the wings of $S(\omega)$ to a parabola is justified; this is demonstrated in Fig. 2.

4. Highly distorted signals

In cases like Fig. 3, the drift of the Q -meter circuit is so great that the parabolic background subtraction is no longer applicable. Thus, a more adaptable and reliable background subtraction method has been developed. The principal idea of the new method is to work with the NMR signal $V(\omega)$, not the subtracted signal $S(\omega)$, in order to avoid fluctuations that may occur in the time between the Q -curve and NMR signal measurements. The goal is to

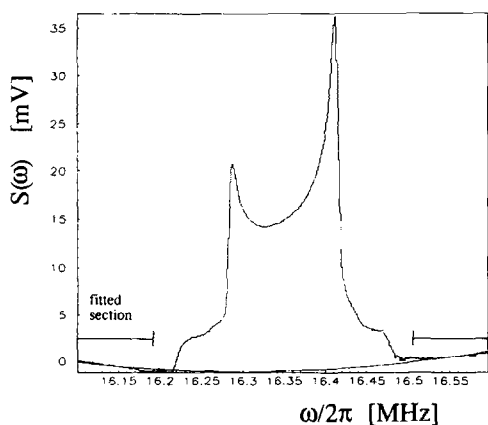


Fig. 2. A subtracted signal as a function of frequency. The smooth curve near the bottom is a parabolic background fit to 85 kHz on each wing.

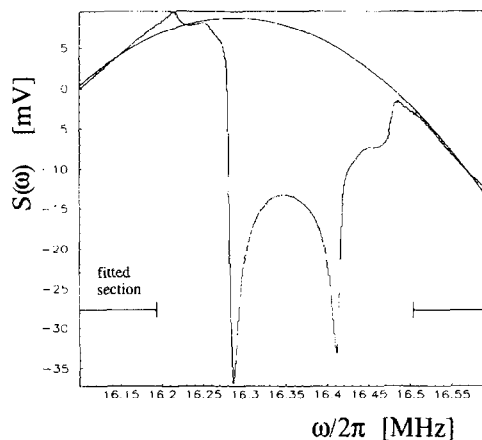


Fig. 3. A parabolic background fit to a highly distorted subtracted signal where the parabolic fit no longer works. The subtracted signal is shown in Fig. 5.

find the average Q -curve that applies during the NMR signal taking, which can be done by fitting Eq. (4) to the wings of the NMR signal. Then, this fitted Q -curve can be subtracted from the NMR signal to give $S(\omega)$ from which the polarization is to be calculated.

For a total scan width of 500 kHz, the real part of Eq. (4d), $V(\omega, \chi)$, is typically fit to 85 kHz segments of the spectrum on each side of the NMR signal. The independent parameters of the fit are the circuit gain AV_0/R_0 , the admittance x , the circuit parameters R and C , the coil parameters L_c , C_c , and r_c , and the cable parameters α , β and l . As an example, Fig. 4 shows a Q -curve extraction from an NMR signal by this fitting method. The signal used in Fig. 4 is the same signal as in Fig. 3, only the Q -curve has been added again to the subtracted signal. Fig. 5 shows the resultant subtracted signal $S(\omega)$ obtained after subtracting the fitted Q -curve from the NMR signal. For

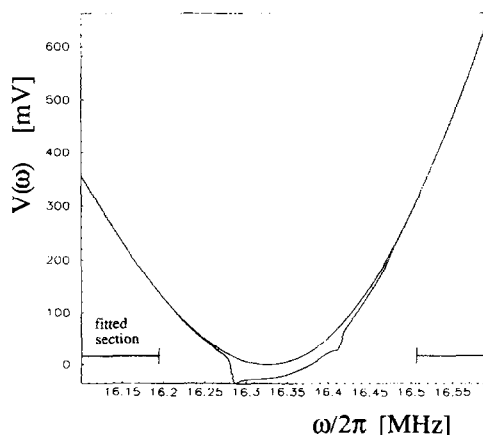


Fig. 4. Q -curve (upper curve) extraction from a deuteron NMR signal (lower curve). The subtracted signal is shown in Fig. 5.

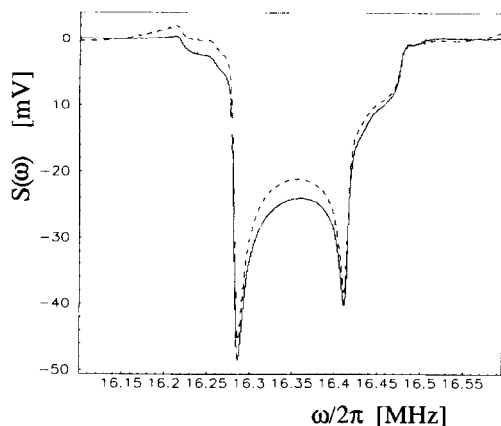


Fig. 5. Comparison of the subtracted signal from the parabolic background fit (dotted line) to the one from the Q -curve extraction method.

the sake of comparison, Fig. 5 also shows $S(\omega)$ after the parabolic background given in Fig. 3 is subtracted. Because it is more flexible than the parabolic background fit, the new method yields a much better signal for cases where the Q -meter tuning changes and the Q -curve drifts are large. Due to these facts, the polarization values calculated from the new method are more stable than those calculated with the parabolic background fitting, even in cases where the drift is small. This fact is demonstrated in Fig. 6, which shows a 14 h history of polarization values. The Q -curve was measured at 0 h, and then subtracted from the NMR signal for the next 12 h. However, starting

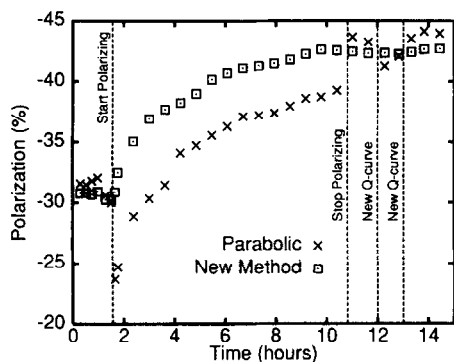


Fig. 6. A 14 h deuteron polarization history.

from about 1.6 h until about 11 h, the deuteron target material was dynamically polarized with 70 GHz microwaves at 300 mW of power. The change in temperature of the target material causes the circuit characteristics to change and, thus, the Q -curve drifts. This causes the large background evident in Fig. 3, which is a subtracted signal from this period of dynamic polarization. The parabolic background subtraction immediately shows a 5% drop in polarization when the microwave power is applied, and a 5% increase when the microwave pumping stops. After 12 h and again after 13 h, new Q -curves were measured and show up as kinks in the graph of the parabolic background fit method in Fig. 6. However, the new method of background subtraction shows a smooth polarization increase during the entire 14 h period.

5. Conclusions

A new method of calculating the deuteron polarization from signals measured with a series Q -meter has been developed. This new method is mainly concerned with treating subtracted signals with a large residual background. It produces equally good results as the standard parabolic background subtraction method when the Q -curves have small drifts. However, it works much better when treating the highly distorted signals caused by large Q -curve drifts.

Acknowledgements

This work was supported by the US Department of Energy and done for the SMC collaboration.

I wish to thank Yannis Semertzidis for helpful discussions, many of which led to corrections of the calculations made in this work.

References

- [1] M. Goldman, *J. Magn. Res.* 17 (1975) 393.
- [2] A. Abragam, *Principles of Nuclear Magnetism* (Clarendon, Oxford, 1961) p. 75
- [3] G.R. Court et al., *Nucl. Instr. and Meth. A* 324 (1993) 433.
- [4] G.D. Wait, P.P. Delheij and D.C. Healey, *Nucl. Instr. and Meth. A* 274 (1989) 516.



ELSEVIER

On-line system for NMR polarization measurement

N. Hayashi ^{e,*},¹, M. Boutemur ^{i,2}, S. Bültmann ^a, D. Crabb ^h, D. Day ^h, S. Dhawan ⁱ,
C. Dulya ^c, E. Gülmez ^b, T. Hasegawa ^{e,3}, N. Horikawa ^e, S. Ishimoto ^{e,4}, T. Iwata ^e,
A. Kishi ^e, L. Klostermann ^f, D. Krämer ^a, J.M. Le Goff ^g, A. Magnon ^{g,d},
T.O. Niinikoski ^d, A. Rijllart ^d, W. Thiel ^{a,5}, S. Trentalange ^c

^a University of Bielefeld, Physics Department, 33501 Bielefeld, Germany ⁶

^b Boğaziçi University, Istanbul, Turkey ⁷

^c University of California, Department of Physics, Los Angeles, 90024 CA, USA ⁸

^d CERN, 1211 Geneva 23, Switzerland

^e Nagoya University, Department of Physics, Furo-Cho, Chikusa-Ku, 464 Nagoya, Japan ⁹

^f NIKHEF, Delft University of Technology, FOM and Free University, 1009 AJ Amsterdam, Netherlands ¹⁰

^g DAPNIA, C.E. Saclay, 91191 Gif-sur-Yvette, France

^h University of Virginia, Department of Physics, Charlottesville, 22901 VA, USA ¹¹

ⁱ Yale University, Department of Physics, New Haven, 06511 CT, USA ⁸

Abstract

The on-line system of the SMC polarized target with emphasis on the NMR polarization measurement system is presented. Target subsystems are controlled or monitored by local processors and a host μ -VAX computer which collects all data and provides the user interface. The Global Section scheme is used as a common data block and achieves the synchronization between subsystems. The communication between the μ -VAX and a newly added SUN-VME based system is made by the Remote Procedure Call.

1. Introduction

The Spin Muon Collaboration (SMC) is an experiment to measure the spin dependent structure functions of the proton and the deuteron by using a polarized target and a polarized high energy muon beam and aims to examine the Bjorken sum rule which is a rigorous QCD prediction.

Its recent results are described elsewhere [1,2]. The experimentally measured counting asymmetry is very small, on the order of 10^{-3} . In order to obtain a good statistical accuracy, quite a long data taking period over several years is required with a very large target. This requires reliable on-line programs to operate the target easily by many shift crews.

The target is divided into two sections and each half is polarized longitudinally with respect to the muon beam, but in opposite directions. This feature and frequent reversals of the orientation of the spin by the magnetic field reduce the systematic uncertainty of the asymmetry measurement. We have used two different target systems, the EMC and the SMC target, but both targets have a similar structure explained above.

The polarization is measured by ten NMR coils to monitor possible inhomogeneity and to provide redundancy.

* Corresponding author.

¹ Research Fellow of the Japanese Society for the Promotion of Sciences.

² Now at University of Montreal, PQ, H3C 3J7, Montreal, Canada.

³ Permanent address: Miyazaki University, 88921 Miyazaki-Shi, Japan.

⁴ Permanent address: KEK, 305 Ibaraki-Ken, Japan.

⁵ Now at Philips Kommunikations-Industrie AG, Nürnberg 10, Germany.

⁶ Supported by Bundesministerium für Forschung und Technologie.

⁷ Partially supported by TUBITAK and Centre for Turkish-Balkan Physics Research and Applications (Boğaziçi University).

⁸ Supported by the Department of Energy.

⁹ Supported by Ishida Foundation, Mitsubishi Foundation and Monbusho International Science Research Program.

¹⁰ Supported by the National Science Foundation (NWO) of the Netherlands.

¹¹ Supported by the National Science Foundation.

In this paper, we describe the on-line system which is used in the SMC polarized target focusing on the NMR polarization measurement system.

2. Hardware

2.1. Overview

Our polarized target consists of four major subsystems, the dilution refrigerator, the superconducting magnet system, the microwave system and the NMR polarization measurement system. Each subsystem has a local CPU, a CAMAC or PC for control or monitoring. A host computer, a μ -VAX III called TX, collects the information through an RS-232C line or CAMAC bus. The TX is a part of the SMC on-line VAX cluster so that it is easy to transfer data or messages to other machines (see Fig. 1).

When the new dilution refrigerator and magnet were introduced, the magnet control system was updated as well. The cryogenic monitoring and control system was also replaced by a system similar to the magnet control in later.

The local CPU for cryogenic instruments is an ICC (independent crate controller), which uses a CAMAC crate and module but is independent of a host computer.

2.2. NMR hardware

A schematic diagram of the NMR instrumentation is shown in Fig. 2. The heart of the polarization measurement system is a standard continuous wave NMR set-up, consisting of a Liverpool Q -meter box [3], a Yale offset card, a set of CERN STAC/NMR-interfaces [4,5] and a frequency synthesizer¹².

There are ten NMR coils embedded in or wrapped around the material, five for each half, and operated simultaneously. These coils are placed so that their predominant fields are perpendicular to the solenoid field axis and also to the field of the neighboring coils to reduce the mutual inductance. Even in this configuration, the mutual inductance is not negligible. If one coil is retuned, the neighbor coils may need to be retuned, too.

The NMR signal picked up by the coil inside the cryostat is brought to the Q -meter box through a semi-rigid cable, whose length is one half (for deuteron) or five halves (for proton) of the wavelength at the nuclear Larmor frequency. The synthesizer feeds the RF to all ten Q -meter boxes after the RF-splitter.

¹² PTS250, Programmed Test Sources, Inc., Beaver Brook Road, Littleton, Massachusetts 01460, USA.

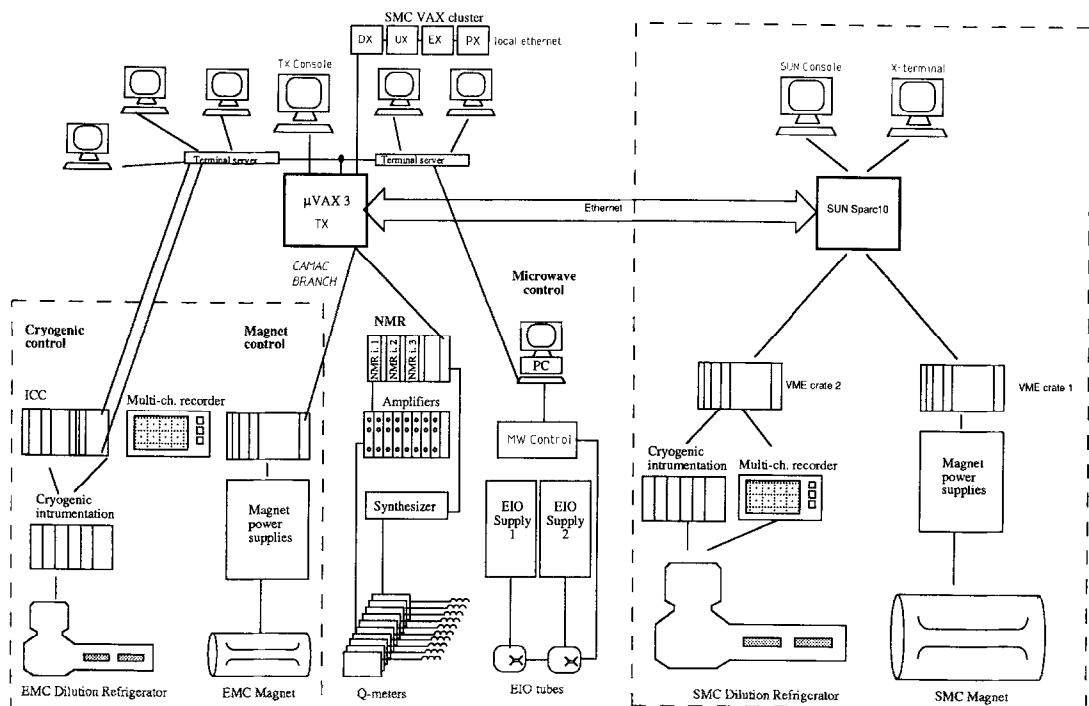


Fig. 1. The on-line hardware of the SMC target. Dashed box indicates new part added (right) and old part removed (left) in later.

The RF-signal is decomposed into a LF-signal inside the Q -meter box and the real part of the signal goes to the offset card. The NMR signal on the Q -curve has a 3–4 V DC offset which is subtracted before further signal amplification. In addition, coarse amplification ($\times 1$, $\times 207$ or $\times 335$) is possible on the offset card. A CERN-built NIM module amplifier is used to adjust the signal size to match with the input range (from -5 to 5 V) of the 16 bit ADC in the “NMR interface”.

Finally, the NMR signal is digitized and averaged by the two CAMAC modules developed at CERN. The “NMR interface” can read up to four channels by multiplexing with sample-and-hold amplifiers and has an interface for the synthesizer control. It is controlled by the STAC (stand-alone CAMAC processor) which has a Motorola 68000 CPU that averages data over a number of sweeps. The NMR frequency is swept from lower to upper edge and swept back from upper to lower. This one cycle is called “one double sweep”. The STAC module can be used for other purposes by exchanging its EPROM (erasable programmable ROM).

In the current EPROM program, the total memory space of the STAC is 1820 long words¹³. This means that up to 455 steps are available for 4 channel inputs, however we normally use 400 steps.

Even though there are ten sets of the Q -meters, offset cards and NIM amplifiers, we need only three sets of STACs with their NMR interfaces, because they have four input channels. All three are operated by means of a multi-STAC synchronization mechanism [6]. The data acquisition parameters, center frequency etc. are downloaded from TX, when required.

Our rough estimation of the sweeping speed is about $160 \mu\text{s}$ for a 4 channel input configuration. It would be shorter for fewer channels, because the ADC conversion and multiplexing time would be reduced. The data transfer from STAC to TX for 5460 long words ($= 1820 \times 3$) takes several seconds by single CAMAC read function (not block data transfer). Typical sweeping times are about 30 s, 4 min and 20 min for 200, 2000 and 10000 double sweeps, respectively.

2.3. New items

A new SMC magnet and SMC dilution refrigerator were introduced in 1993 and some parts of the on-line system have been replaced by a VME-Sun based control system. (The magnet part since 1993 and the cryogenic part since 1994.) The VME modules are controlled by the VME processor of each VME crate, and the graphical user interface, the data storage and the source program code for the VME processor are on the Sun workstation. For the communication between TX and Sun, Remote Procedure Call (RPC) is used through an Ethernet connection.

A detailed description is given in another contribution to this workshop [7].

3. Software

On the host computer TX four independent (detached) processes were made to communicate with the local CPUs. The TX also provides the user interface to control or monitor the subsystems.

In order to share the information or communicate among processes, we set a common data block in memory, a so-called global section. Its size is 16 384 long words. The

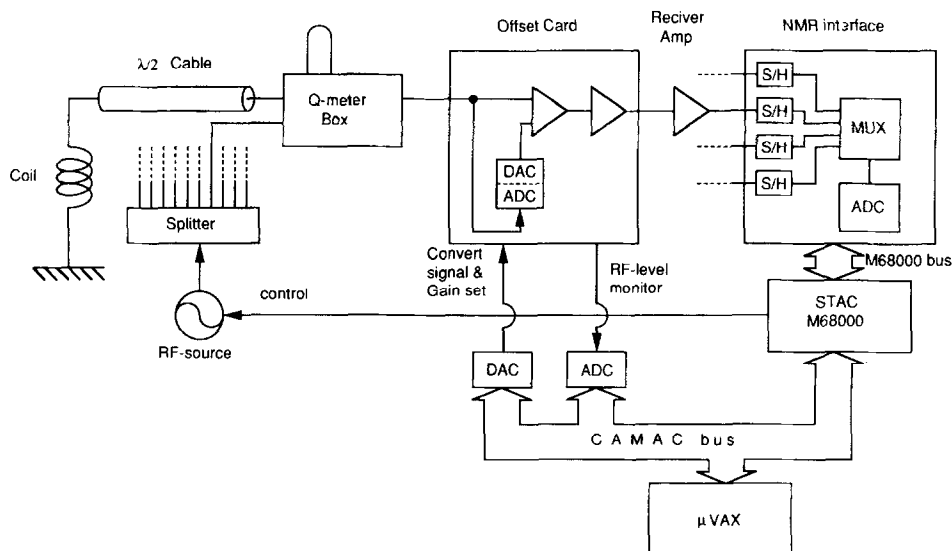


Fig. 2. The schematic diagram of NMR hardware.

¹³ one long word = 4 bytes.

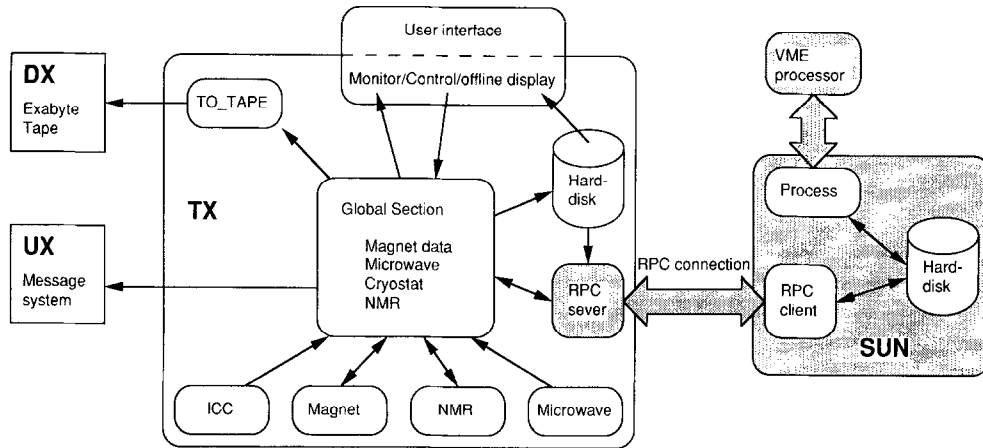


Fig. 3. The on-line software diagram of the target. Shaded area indicates new part added in later, when SUN-VME system was introduced.

first three 512 long words fields are assigned for the magnet system, the microwave system and the cryogenic system. In each field a place for the solenoid current, some thermometer readings, command status or other data is assigned. The rest of the region is used for the NMR system, data acquisition parameters and the 10 channels of signal and baseline raw data and some on-line analysed parameters, like polarization values and centers of the signals. To avoid collisions in accessing to the global section by the various processes at the same time, an event flag is used as a busy indicator. Some event flags are also used for other purposes, e.g. the availability of new data.

TX sends relevant information to DX, which is responsible for writing all apparatus data onto the Exabyte tape. TX can send messages or alarms to UX which manages the message system for all the equipment.

The software related to the new items is discussed separately. Here, only the communication part is described. The remote procedure call (RPC) is used to establish this communication. The RPC "allows a program on one machine to call a subroutine on another machine without knowing that it is remote" [8]. In our system a client program is on SUN and a server program is running on TX and there are three permanent connections. One is a magnet data transfer program which transfers a command (field shift) only for the calibration run mode. The second one is similar to the first one but transfers the cryogenic data. The last one carries out the automatic NMR data transfer to the SUN disks. Because a complicated off-line analysis needs some CPU power, which cannot be available on the on-line μ -VAX.

The schematic diagram from the software point of view is shown in Fig. 3, which is a similar structure to the hardware scheme.

4. Examples

Here are some examples of the on-line programs.

4.1. POLCON

This is a control interface for the NMR and the (EMC) magnet. NMR data acquisition parameters, the NMR center frequency, sweep width frequency, number of steps and sweeps and the solenoid or dipole current values can be modified through this interface.

4.2. PTMONITOR

PTMONITOR is a standard status display of the target. It shows the polarization and center values for all NMR coils, NMR data acquisition parameters, magnet current, microwave parameters and Speer thermometer values for each half of the target. From this screen, one can see the target status immediately.

If there is any missing process which should be running, or magnet, cryogenic data is not updated within a certain time, PTMONITOR complains with an error and an instruction how to fix the problem on the screen. Otherwise, it quietly indicates the remaining time until the end of physics run.

Fig. 4 shows an example of the PTMONITOR screen.

```

***** Polarized Target Status *****                17-JUN-1994 10:41:00

      Polar  NSUM  Center  MW-P [mW]  Freq. [GHz]  Speer [Ohm]
Upstream: -48.44 -49.13  202.02    0      0.000    566.0
Downstream: 36.73  43.18  201.63    0      0.000    565.5
Delta:    85.17  92.31

-- Frozen Solid --
Magnet: Current = 416.194 A
Dipole: Current = -0.317 A Last Magnet Reading: 17-JUN-1994 10:38:31
NMR: Normal run remaining time: -6 sec
Center: 16.35 MHz Width: 500 kHz Sweeps = 1000

Software: ok; all tasks running

COUNTDOWN : until the end of run ...
              119 days 13:19: 0 total 10329540sec

Coil:  #1  #2  #3  #4  #5  #6  #7  #8  #9  #10
Pol:  -47.41 -50.32 -48.66 -49.09 -46.71 35.49 34.98 37.77 39.89 38.87
NSUM: -58.40 -44.50 -43.39 -46.67 -52.66 41.96 43.00 40.06 42.56 47.71
Center: 201.96 202.44 202.01 202.10 201.59 202.05 201.47 201.51 201.54 201.49
Last Signal: 17-JUN-1994 10:38:56 Baseline: 17-JUN-1994 07:58:35
CTRL-Y to stop TE from 10-MAY-1994 Options: uf=0 pf=1 cp=0 cd=1 qc=0

```

Fig. 4. An example of PTMONITOR screen.

4.3. NMRDISPLAY

This shows the last measured signal or baseline data. It is updated for every new measurement. If a trim coil has a problem, one would see the signal badly distorted due to the inhomogeneous magnetic field.

4.4. DERIV & TIME

In order to optimize dynamic nuclear polarization, i.e. to maximize the polarization growth rate dP/dt , by changing microwave frequency, power or modulation parameters, a time history plot and data table of the growth rate is required. TIME displays the average polarization and growth rate together with the signal center for up- and downstream. To display dP/dt , it uses a filter to reduce measurement noise, which is especially critical for small dP/dt at high polarization.

DERIV gives the event-by-event differences and averaged values of an arbitrary number (typically the last 5 measurements) for each coil.

4.5. Calibration run

An NMR system has to be calibrated by measuring the thermal equilibrium (TE) signals at around 1 K to determine the absolute polarization. The TE signal is very small, especially the deuteron one, and it needs a large number of sweeps to improve the signal-to-noise ratio. In the 1992 set-up, the Q -curve depth was on the order of 1 V and the peak height of the deuteron TE signal was about 0.5 mV after times 10 amplification at the Receiver amplifier.

However, increasing the number of sweeps makes the drift of the circuit more significant for an accurate measurement. It was shown that the maximum deviation of the circuit drift may be as big as the size of the TE signal [9]. To suppress this effect, the baseline data and the signal data should be taken frequently and alternatively.

One sub-menu of POLCON provides such an option and performs the following procedure over different subsystems and repeats it automatically.

- (1) Shift field for baseline.
- (2) Wait for a certain delay, usually 5 min.
- (3) Take baseline data with a defined number of sweeps.
- (4) Shift field back to nominal value.
- (5) Wait for a certain delay before signal taking.
- (6) Take signal.
- (7) Check whether the data file is written.

The measurement of the target temperature during the calibration run is quite important to obtain a natural polarization. For that, ^3He vapor pressure in a bulb inside the mixing chamber is measured by an MKS Baratron pressure gauge. The ^3He vapor pressure value is stored into the global section and written into the NMR data file, which is used for the off-line analysis.

5. Summary

The on-line system of the SMC polarized target was presented. The concept of a random accessible file system on a μ -VAX computer, called global section, was described which allows an easy way of storing data and establishing communication among the different subsystems present. Several programs were described, like PT-MONITOR providing a status display of the target and calibration run mode allowing the easy control of the TE calibration process which is different subsystems involved. This shows the versatility of the conceptual design. An extension in its usage across different hardware platforms was demonstrated by adopting a Sun-VME based cryogenic and magnet control system via the RPC facility.

Acknowledgement

The authors thank the colleagues of the SMC for technical suggestions and advice.

References

- [1] SMC, B. Adeva et al., Phys. Lett. B 302 (1993) 533.
- [2] SMC, D. Adams et al., Phys. Lett. B 329 (1994) 399.
- [3] G.R. Court et al., Nucl. Instr. and Meth. A 324 (1993) 433.
- [4] T.O. Niinikoski and A. Rijllart, Nucl. Instr. and Meth. 199 (1982) 485.
- [5] A. Rijllart, Proc. 4th Int. Workshop on Polarized Target Materials and Techniques, Bonn (1984) p. 155.
- [6] A. Rijllart et al., Proc. 9th Int. Symp. on High Energy Spin Physics, Vol. 2, eds. W. Meyer, E. Steffens and W. Thiel Bonn (1990) p. 272.
- [7] J.M. Le Goff, these Proceedings (7th Workshop on Polarized Target Materials and Techniques, Bad Honnef, Germany, 1994) Nucl. Instr. and Meth. A 356 (1995) 96.
- [8] T.J. Berners-Lee, Introduction to Remote Procedure Call, CERN-DD (1988).
- [9] SMC, B. Adeva et al., CERN-PPE/94/54, to be published in Nucl. Instr. and Meth. (1994).



ELSEVIER

Computer control of the SMC polarized target

J.-M. Le Goff^{a,b,*}, R. Azoulay^c, P. Berglund^d, C. Dulya^c, J.F. Gournay^c, N. Hayashi^f,
J. Kyyrääinen^b, A. Magnon^a, G. Matichard^c, T.O. Niinikoski^b, S. Trentalange^e

^a CEA, DAPNIA / SPHn, CE Saclay, 91191 Gif-sur-Yvette, France

^b CERN, CH-1211 Genève 23, Switzerland

^c CEA, DAPNIA / SIG, CE Saclay, 91191 Gif-sur-Yvette, France

^d Low Temperature Laboratory, Helsinki University of Technology, SF-02150 Espoo, Finland

^e University of California, Department of Physics, Los Angeles, 90024 CA, USA

^f Nagoya University, Department of Physics, Furo-Cho, Chikusa-Ku, 464 Nagoya, Japan

Abstract

The SMC polarized target is controlled through VME crates driven by CPUs working under the VxWorks operating system. The CPUs are connected to a SUN workstation which provides the user interface due to a graphical package named SL-GMS. This results in user friendliness, high modularity and flexibility.

The system allows the control of: (1) the superconductive solenoid and the transverse dipole: control of the power supplies; automatic reversal of the spin direction by field rotation; acquisition, display and storage of the electric and cryogenic parameters; generation of alarms; and (2) the dilution refrigerator: evaporator level control; acquisition, display and storage of ≈ 100 cryogenic parameters; and generation of alarms.

1. Introduction

The SMC target [1] includes two cells, polarized in opposite direction, the direction of the spins being reversed from time to time. The extraction of the asymmetry requires the assumption that the ratio of the acceptance for the two cells is a constant at the time scale of a polarization reversal. The fluctuation of this ratio then represents a major source of systematic errors in the experiment.

In the original EMC experiment [2] the polarization was reversed once a week by repolarizing with microwaves. The situation was improved for the first run of SMC in 1992 [3] when we achieved three reversals of the spins per day by rotating the magnetic field. This rotation was performed due to the combination of a main 2.5 T solenoid and a transverse 0.2 T dipole. However, this transverse field was a bit low and the procedure was partially manual, quite delicate and led to a polarization loss of at least 2% at each reversal.

A new target was built for the 1993 run [4] with new magnets [5] including a 0.5 T transverse dipole. Also a modern control system was developed in Saclay with the technical support of DAPNIA/SIG engineers. It allows an automatic rotation procedure which is now performed five times per day with only ten minutes without data taking. For the 1994 run this system was extended to the dilution refrigerator control.

2. General description of the system

The control is done through a SUN workstation and two VME crates. One controls the magnet supplies and the other controls the dilution refrigerator. The control of the NMR system [6] is described elsewhere.

Each VME crates is driven by a CPU (Matrix MD-CPU334) which includes a Motorola 68030 processor running at 25 MHz, a floating point unit and 4 Mb of RAM. The interfaces with the instruments are made with 8/16 channels 12-bit DACs boards (ADAS ICV712), 12-bit ADC boards with multiplexers for 64 channels (ADAS ICV150) and a digital input/output board for 96 channels (ADAS ICV196). Most channels are optically isolated in a signal conditioner. Finally, several devices are read through GPIB by a VME GPIB controller (National Instrument 1014P).

The VME crates are then connected to a SUN Sparc10 workstation through a private Ethernet network. The SUN provides development capabilities and a graphical interface.

3. The graphical interface package: SL-GMS

The Sherrill-Lubinski Graphical Modeling System (SL-GMS) provides a very powerful graphical interface. The developer can design his own graphical objects without any coding due to drawing software. One is not limited to a set of predefined graphical objects, since it is possible to

* Corresponding author.

draw with a mouse any kind of geometrical items and give them some dynamical properties. The appearance of the object will change depending on a (set of) real world parameter(s).

One can design passive objects to represent any real world variable. This can be, for instance, just a numerical display, some histograms versus time, some LED-like objects that change color with the status of some parameter(s), some analog-like meters, a valve that will appear open or closed. Interaction objects (buttons, sliders etc.) can also be designed and connected to C-functions through a “callback” mechanism. This allows both graphical actions, like opening of a new window, and real world actions.

The C-code is organized in well identified modules which are automatically activated by the SL-GMS main loop. Basically, an “activate method” is used for initialization, an “update method” is activated periodically by a timer in order to read the probes and to refresh the control screens and a “deactivate method” is used when a screen is closed. The event handling (mouse, keyboard, windows) is done by SL-GMS which in turn calls the user defined callback function. This results in a very clear organization of the code which is moreover common to all SL-GMS programs.

4. The VME operating system: VxWorks

The VME CPUs use the real-time operating system VxWorks from Wind River System. The VxWorks package is resident in the SUN workstation and is loaded into the CPU at booting. Only a few booting parameters are permanently stored inside the CPU; the code is written in ANSI-C and compiled in the SUN by a cross compiler. The object files are then loaded into the CPU and the corresponding tasks can be activated. This system allows multitasking and definition of priority levels.

The software is organized in several layers. (1) The upper layer (application layer) where one can find the alarm generation task, the data logging tasks and specialized tasks like the rotation procedure (see next section). (2) The intermediate layer which provides the Application Programming Interface (API) to access the real world devices and parameters. This API offers transparent access to the equipment independently of the calling program location (local or remote VME, SUN workstation). This feature allows a great flexibility for the software: no change needs to be done if one program is moved from one system to another. (3) The lower layer which consists of the drivers used to access the VME interfaces and of a protocol (UDP on Ethernet) to achieve the communications between the intermediate layer and remote devices.

Our philosophy has been to design one task per controlled device, together with the drivers themselves and the storage and alarm generation tasks.

5. Magnet control

The solenoid supply is directly read and controlled by the CPU through a RS232 line. A high precision measurement of the current inside the solenoid is also available due to a current transducer (Danphysiks ULTRASTAB 860R), read through GPIB. The dipole and trim coils supplies are controlled by a DAC and read by an ADC. The ADC is also used to read magnet cryogenics parameters. A hardware magnet security system can force the supplies slowly to zero (slow trip) or even open the magnet contactors (fast trip). The status of this system is read through a logic/logic board.

An automatic rotation procedure has been developed which is started just by clicking one button: the solenoid is ramped down to 0.5 T; the dipole is ramped up to 0.5 T while the solenoid is ramped down to zero; the trim coils and the solenoid polarity is reversed; the solenoid is ramped up to min -0.5 T while the dipole is ramped down to zero; the solenoid is ramped up to the baseline field and the rotation procedure is paused for baseline taking [6]. Finally the solenoid is ramped up to -2.5 T. The rotation is performed five times per day; it requires about 35 minutes; however, data taking must only stop for 10 minutes while the dipole is on.

At the beginning of the 1993 proton data taking, there was some loss of the negative polarization during rotation due to the so-called super-radiance effect. To get rid of it, we had to make the field inhomogeneous during the rotation by intentionally setting the trim coils polarity to the opposite value. This meant reversing this polarity three times, at the beginning, at zero solenoid field and at the end. This modification in the standard procedure could be included and tested in a few hours, which demonstrates the flexibility of the system.

6. Dilution refrigerator control

The dilution refrigerator system includes about one hundred channels. There are 26 Pt100 platinum resistors for normal temperature reading (pumps, NMR system, etc.). They are read through a bridge to an ADC; the bridge is actually a VME board itself (VMIC 3413). A DAC is used to control the still and the mixing chamber heater together with some valves. All the other devices are read through GPIB: two Schlumberger 7061 9-channel multimeters read cryogenic diode thermometers. Three AVS-46 bridges with 7-channel multiplexer read temperature resistors. A datalogger/plotter (Siemens multireg C1732) provides 32 analogous inputs; they are used for pressure and level probes, for flow-meters and for an oxygen monitor located in the ^4He recovery line.

The graphical interface can be seen in Fig. 1. It provides a histogrammation of the most relevant parameters (top right). Some pull-down menus are available (top left).

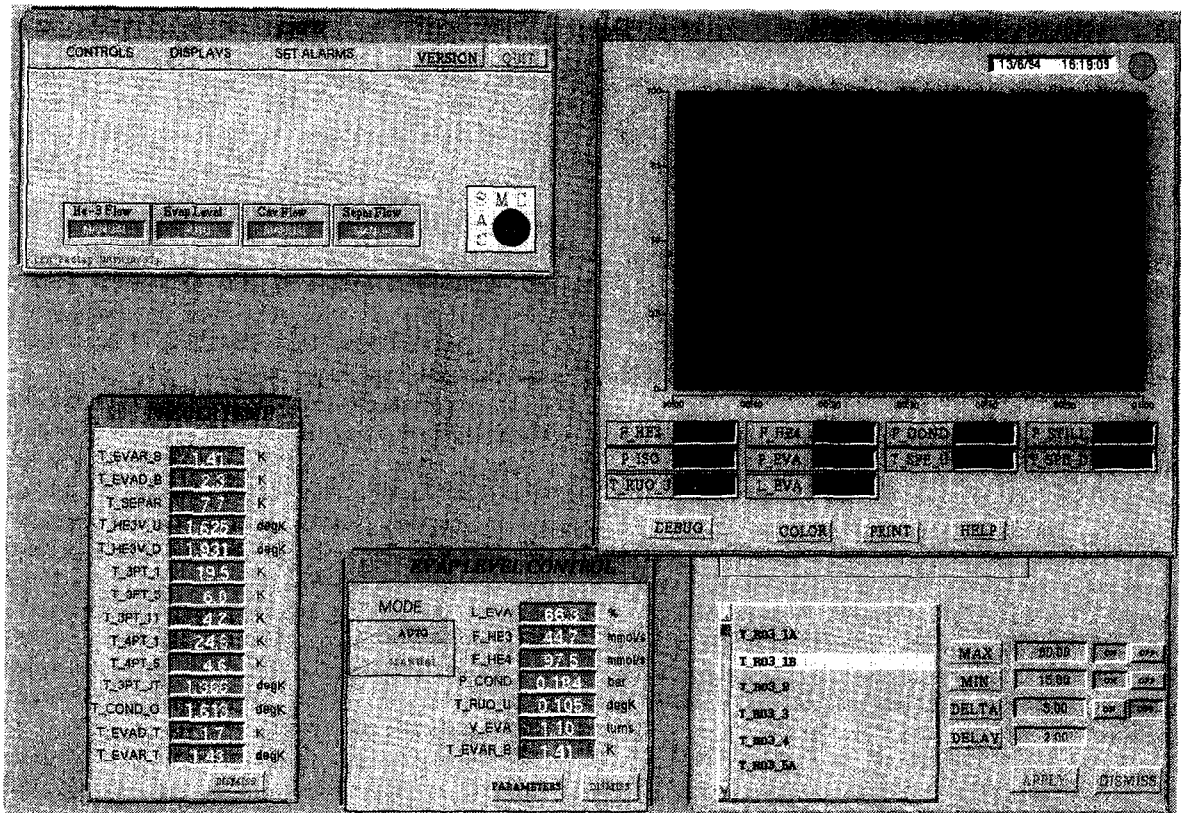


Fig. 1. Graphical interface for the dilution refrigerator (see text for explanations).

The “display” menu allows one to open windows for the numerical display of all the parameters (The pre-cooler temperature window is open on the bottom right.) The evaporator level is controlled and the control parameters can be modified in the “evaplevel” window (bottom middle) which can be opened with the “control” menu.

There are alarm thresholds on all the parameters for minimum and maximum values and for maximum time variation. The “set alarms” menu provides the possibility to set threshold values and enable or disable alarm for each channel individually (see partially covered window on the bottom right). When an alarm occurs, a horn starts and a window appears indicating which alarm occurred at what time.

7. Off-line capabilities

The parameters of the magnets and the dilution refrigerator are stored every minute in a file and a new file is started every week. This file can be read by another SL-GMS application. Up to ten channels can be plotted

together versus time and one can also plot correlations between two channels.

8. Conclusion

We have developed a control system for the magnets and the dilution refrigerator of the SMC polarized target with a very user-friendly graphical interface. It has proven to be very efficient and reliable and at the same time quite flexible. There are now plans to extend this system to the control of the microwaves as well.

References

- [1] J. Kyyräinen, these Proceedings (7th Workshop on Polarized Target Materials and Techniques, Bad Honnef, Germany, 1994) Nucl. Instr. and Meth. A 356 (1995) 47.
- [2] EMC J. Ashman et al., Phys. Lett. B (1988) 364.
- [3] SMC, B. Adeva et al., Phys. Lett. B 302 (1993) 533.
- [4] SMC, D. Adams et al., Phys. Lett. B 329 (1994) 399.
- [5] A. Daël et al., Proc. 12th Magnet Technology Conf., Cryomag 91-05, 1991.
- [6] N. Hayashi et al., Ref. [1], p. 91.



ELSEVIER

The modulation effect on the dynamic polarization of nuclear spins

Yu.F. Kisselev

JINR, Laboratory for Super High Energy Physics, Dubna, Russian Federation

On behalf of the Spin Muon Collaboration ¹

Abstract

We report on the discovery of a large gain in the dynamic nuclear polarization (DNP) of the 1.5 l target of SMC after application of microwave (MW) frequency modulation (FM). In the glassy deuterated butanol material doped with a paramagnetic EDDBA-chromium (V) complex the maximum polarization increases by 65% with FM while in the case of proton material the increase was found to be 10%. Also, the polarization build-up time decreased for the deuterated material by a factor of almost two. The effect appears at temperatures around 0.3 K with a modulation frequency 10–10³ Hz and an amplitude of about 30 MHz. Bolometric measurements of the MW energy inside the cavity show that FM gives rise to additional absorption of MW energy which depends on the modulation amplitude and frequency and which is more pronounced in the edges of the EPR absorption line.

1. Introduction

A strong increase in deuteron polarization due to Frequency Modulation (FM) was discovered in 1992 in the butanol-D10 material of the large 1.5 l polarized target of the Spin Muon Collaboration (SMC) [1]. In 1993 a 10% relative increase due to FM was observed in the undeuterated 1-butanol target of SMC. The modulation effect was reproduced in 1994 in the new SMC polarized target [2] with a larger volume of 2.5 l. The material of the target is glassy 1-butanol with about 5% of water and EHBA-Cr(V) complex as a paramagnetic dopant [3]. In such materials only small enhancements were found [4] previously.

After our initial discovery of the large FM effect in the deuterated material, several other laboratories have reported similar results in materials doped with the stable Cr(V) complexes and in other materials.

2. DNP results in the large targets

In 1989, the SMC stimulated investigation of glassy butanol-D10 doped with a paramagnetic EDDBA Cr(V)-complex in different institutes. The results are presented in Table 1 together with those obtained in our large targets. The small sample data were obtained at about the same

temperature (0.3 K) of the ³He–⁴He mixture but with higher MW power per unit volume compared with the large targets. According to Table 1, high polarization can also be reached without FM; the –47% PSI result is similar to the SMC 1992 result of –49% with FM.

The deuteron polarization in the large targets was measured once each 0.5–2 min using 10 series Q-meters [5] calibrated against the known polarization in thermal equilibrium at 1 K. The relative reproducibility of the measurement was better than 0.5% and the calibration accuracy was 4% in 1992 mainly due to the neglect of the effect of the magnetic field shift on the Q-curve. The precision of the 1994 result is preliminary and will improve after offline corrections.

By adjusting the MW power and frequency in order to get the best value and build-up time for the nuclear polarization, we obtained the data shown in Fig. 1 for the time dependence of deuteron polarization with and without FM at 2.5 T field. These data demonstrate the increase of both the ultimate polarization and growth rate due to FM. The maximum polarization increases by 65% in deuterated butanol, while the increase for proton material was found to be 10%. For deuterons, a given polarization is obtained in a time shorter by roughly a factor of two when FM is used. We also observe that if the modulation is switched off when the highest polarization is attained, the polarization drops down rapidly to its steady state value without FM.

The maximum FM effect appears at the lowest optimised power of about 0.05–0.2 mW/g which can be

¹ For the complete list of authors and institutions, see Ref. [1].

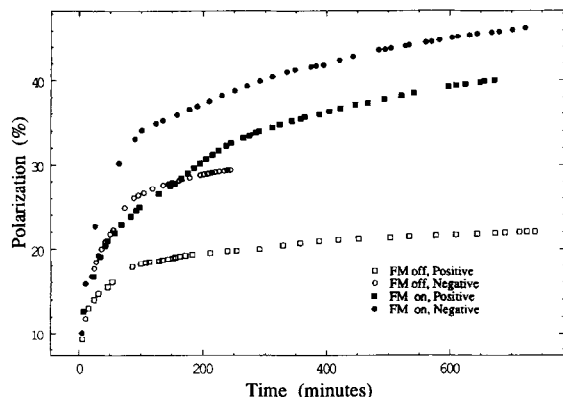


Fig. 1. The time dependence of the deuteron polarization in butanol-D10 with and without FM.

absorbed at a helium temperatures below 0.3 K, with a modulation frequency in the range of $10\text{--}10^3$ Hz and an amplitude in the range of 15–30 MHz about the mean frequencies around 69.040 GHz for positive and 69.535 GHz for negative polarizations. With same MW power and frequency, the effect of FM becomes negligible or even disappears around 1 K.

We also find consistently that, if FM is turned on after steady DNP was reached with no external FM, the deuteron line asymmetry agrees better with the value deduced from the average polarization measured by each probe coil using the TE method, indicating a better homogeneity.

In the latest run, deuteron polarizations of about -53% and $+44\%$ have been reached at CERN with FM.

3. The bolometric measurements of microwave energy in the cavity

The SMC target is contained in a 60 l closed copper cylinder with a microwave stopper in the middle. Both sides of this stopper can act as independent cavities for the slightly different MW frequencies necessary to polarize the halves of the target in opposite directions. They are fed

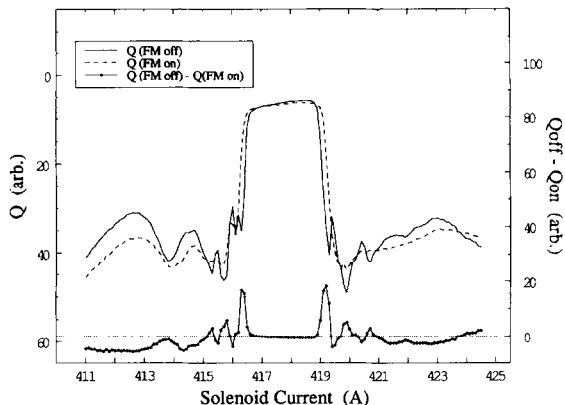


Fig. 2. The energy spectra of a cavity with and without frequency modulation at a MW frequency of 69540 MHz, taken with a Speer 220 Ω resistor a high level of MW power. The bottom curve shows the spectrum of an additional steady state absorption, due to FM. The bandwidth of this spectrum is about 60–80 MHz.

from two independent Extended Interaction Oscillator (EIO) klystrons. Fig. 2 shows energy spectra for one of the cavities while the applied magnetic field is stepped through the EPR line during 3–4 h. These spectra were obtained using a 220 Ω Speer carbon composite resistance thermometer as a bolometer, located in the dilute phase of the mixing chamber outside the target material. At low temperature, the power dissipated in this resistor is [6]

$$Q_{\text{mw}} = \text{const.} \times (T_{\text{Sp}}^4 - T_{\text{mix}}^4), \quad (1)$$

where T_{Sp} is the temperature of the carbon composite and T_{mix} that of the mixture. As the power absorbed by the resistor is proportional to the energy in the cavity, Eq. (1) allows one to deduce the microwave power dissipated in the cavity from the temperatures of the bolometer and the helium. As the input power is roughly constant and is equal to the sum of the resonant power losses in the target material and of the non-resonant ones elsewhere in the cavity, the power dissipated in the resistor Q_{mw} is in linear relationship with the power absorbed in material.

Table 1
Comparison of polarization data for deuterated butanol obtained in several institutes

Institute	Team	B (T)	Volume (cm^3)	FM	P_{max}^+	P_{max}^-	σ
Bonn	Krämer	3.5	6	off	+27%	–	$\pm 5\%$
Bonn	Bültmann	3.5	2	off	–	–33%	$\pm 5\%$
Triumf	Wait	2.5	2.4	off	–	–29%	$\pm 3.4\%$
GKSS	Stuhrmann	2.5	1	off	+30%	–32%	–
Dubna	Kisselev	2.5	1	off	+27%	–32%	$\pm 3\%$
CERN	Niinikoski	2.5	5	off	–	–40%	$\pm 5\%$
PSI	Trentalange	2.5	1	off	+42%	–47%	$\pm 5\%$
CERN 1992	SMC	2.5	1500	off	+27%	–35%	$\pm 4\%$
CERN 1992	SMC	2.5	1500	on	+43.4%	–49.0%	$\pm 4\%$
CERN 1994	SMC (preliminary)	2.5	2500	on	+44%	–53%	$\pm 5\%$

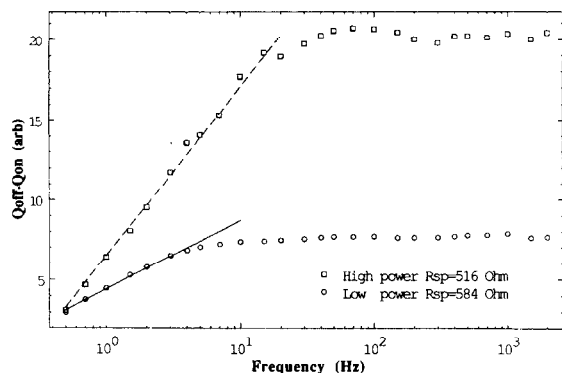


Fig. 3. FM absorption versus the frequency of modulation at two microwave power levels. The linear fit shows an exponential dependence of the effect vs. the modulation frequency.

The top spectra in Fig. 2 were taken at a high level of applied power using two levels of frequency modulation; one with the emission bandwidth of the EIO tube corresponding to a modulation of about 0.1 MHz, and that other with external modulation of 30 MHz width. The bottom plot in Fig. 2 shows the differential spectrum of the additional MW absorption.

We found experimentally that the FM enhancement of nuclear polarization disappears at low enough frequencies of modulation, as does the additional MW absorption due to FM. To show this, we measured the dependence of the additional paramagnetic MW absorption versus the frequency of modulation. Both of the curves in Fig. 3 were taken at an amplitude of modulation equal to 30 MHz, but at two different levels of applied MW power. The curves are well fit by the exponential functions shown. On the basis of these data, we may argue that the FM effect in DNP is intimately related with the additional absorption of MW energy.

4. Conclusions

We summarize that the FM of the microwaves was essential to get high polarization in the large targets of SMC, yielding results even beyond those of any of the small samples without FM.

After analysing EPR data similar to those displayed in Figs. 2 and 3, we can draw the following conclusions:

- 1) At the edges of the EPR line, the FM gives increased MW absorption. The spectrum of this additional absorption resembles qualitatively the derivative of the absorption spectrum with no FM.
- 2) Due to FM, the EPR spectrum is broadened as can be seen in Fig. 2. The MW frequencies that excite the maximum positive and negative nuclear polarization are shifted by about 20 MHz outwards from the EPR line. The shift thus goes in the direction of a more transparent zone for MW irradiation and amounts to slightly more than half the modulation amplitude.

References

- [1] Spin Muon Collaboration, B. Adeva et al., Phys. Lett. B 302 (1993) 533.
- [2] J. Kynnäräinen, these Proceedings (7th Workshop on Polarized Target Materials and Techniques, Bad Honnef, Germany, 1994) Nucl. Instr. and Meth. A 356 (1995) 47.
- [3] S. Bültmann et al., *ibid.*, p. 102.
- [4] Sh. Ishimoto, Sh. Hiramatsu, Sh. Isagawa, A. Masaike and K. Morimoto, Jpn. J. Appl. Phys. 28 (1989) 1963.
- [5] Spin Muon Collaboration, B. Adeva et al., Nucl. Instr. and Meth. A 349 (1994) 334.
- [6] O.V. Lounasmaa, Experimental Principles and Methods Below 1 K (Academic Press, London 1974) p. 265.



ELSEVIER

Properties of the deuterated target material used by the SMC

S. Bültmann^{a,*}, G. Baum^a, P. Hautle^c, L. Klostermann^d, J. Kyynäräinen^c,
T. Niinikoski^c, S. Takala^c, W. Thiel^{a,4}, S. Trentalange^b

^a Universität Bielefeld, Fakultät für Physik, D-33615 Bielefeld, Germany¹

^b University of California, Department of Physics, Los Angeles, 90024 CA, USA²

^c CERN, CH-1211 Genève 23, Switzerland

^d NIKHEF, Delft University of Technology, FOM and Free University, 1009 AJ Amsterdam, Netherlands³

^e Paul Scherrer Institut, 5232 Villigen, Switzerland

Abstract

The target material used in the SMC experiment NA47 at the CERN SPS is described. The arguments for selecting the material are given and the problems of the production and their solutions are presented. Relevant properties with respect to the scattering experiment are discussed and parameters like polarization build-up rate and relaxation times are highlighted.

1. Overview

The Spin Muon Collaboration (SMC) is studying the spin dependent structure functions of the proton and the neutron. The chosen approach is the measurement of the counting rate asymmetries in the deep-inelastic scattering of polarized muons off polarized protons [1] and deuterons [2]. The experiment is carried out at the polarized muon beam line of the CERN SPS with an energy of 100 and 190 GeV. The intensity of the beam used is $4 \times 10^7 \mu^+/\text{spill}$ and its polarization was measured to be about $P_{\text{beam}} = -0.80$.

The muons are scattered off a polarized solid target and detected with the upgraded EMC/NMC spectrometer. In order to cancel variations in the beam flux and different amounts of target material the target was built in a twin configuration with oppositely polarized target halves. The polarizations of both halves are reversed every 4 to 5 h to account for their different acceptances. A detailed description of the target set-up is given elsewhere [8].

The asymmetry in the measured counting rates $N^{\uparrow\uparrow}$ ($N^{\uparrow\downarrow}$) for parallel (antiparallel) muon and nucleon spins can be written as

$$\frac{N^{\uparrow\downarrow} - N^{\uparrow\uparrow}}{N^{\uparrow\downarrow} + N^{\uparrow\uparrow}} \approx P_{\text{beam}} P f D A_1,$$

where P denotes the target polarization, f the dilution factor, D the depolarization factor and A_1 the virtual-photon nucleon cross section asymmetry to be determined. In this report we will focus on the quantities directly related to the target material, P and f . We will also constrain the discussion to the case of deuterated target material.

2. Target material

The target material chosen consists of 91.4% 1-butanol- d_{10} , 4.6% deuterium oxide and 4.0% EHBA-Cr(V)- d_{22} (referred to as EDDBA) as the paramagnetic dopant, necessary for dynamical nuclear polarization (DNP). All percentages are with respect to the weights.

A suitable solid state target material has to fulfil several criteria. Among them are a high dilution factor, a high density, a high polarization with a fast build-up and long relaxation time, and the feasibility of a fast production of large quantities. With the low intensity muon beam, a high radiation resistance was of minor importance. For the SMC target we needed a quantity of around half a million homogeneous glassy beads (~ 1.8 kg).

The dilution factor f is defined as the fraction of scattering events from (polarized) deuterium. To first approximation it is equal to the fraction of deuterium nuclei

* Corresponding author.

¹ Supported by Bundesministerium für Forschung und Technologie.

² Supported by the Department of Energy.

³ Supported by National Science Foundation (NWO) of the Netherlands.

⁴ Now at Philips Kommunikations-Industrie AG, Nürnberg, Germany.

in the target material. This number is substantially higher for deuterated ammonia (0.333) than for deuterated butanol (0.238). However, to reach sizeable polarizations comparable to EDDBA doped deuterated butanol, the paramagnetic centers in deuterated ammonia have to be produced by in-situ irradiation at liquid helium temperatures with a charged particle beam of high intensity, which was not possible at CERN. Doped ammonia did not show high polarization values in previous experiments [4]. When using ammonia the polarization of the nitrogen nuclei has to be taken into account. The polarization of the ^{14}N -nuclei is difficult to measure because of a large width of the signal, on the order of 2.4 MHz (peak-to-peak width). Normally the NMR technique used is scanning in a range of less than 1 MHz. More details on ammonia can be found elsewhere (see Refs. [3,11]).

In prior tests at CERN and at PSI, several small samples of deuterated alcohol/water mixtures with radicals added were studied at different magnetic fields [12]. Besides the $\sim 15\%$ higher density, propanediol showed slightly higher polarizations at all fields compared to butanol. This advantage is nearly compensated by its lower dilution factor. Finally, butanol was chosen as the target material because with propanediol one has a more complicated production of the free radicals. They have to be produced by a chemical reaction in the liquid instead of simple mixing like in the case of butanol.

3. Production of target beads

The actual target material has to be in the form of small pieces, preferably of equal size, to provide good and uniform cooling of the material. In addition, a homogeneous polarization requires that the paramagnetic centers are distributed uniformly. The latter is fulfilled in a glassy state. Deuterium oxide was added to the liquid butanol to increase the viscosity of the solution at low temperatures. A high viscosity and a fast cool-down during the production are of major importance for the glass formation in the beads.

The production of the target material was made in a glove box. This provided a water vapour free atmosphere, needed, because the deuterated materials are hygroscopic. At first, the 1-butanol- d_{10} and the deuterium oxide were mixed together at room temperature. The degree of deuteration of the butanol, as given by the supplier and confirmed by (liquid) NMR measurements, was 99.4 at%, while the D_2O was fully deuterated.

Into this mixture the EDDBA-crystals, providing one free electron spin per molecule, were dissolved. Recently, this material had been available in deuterated form (Krupolc, University of Illinois at Chicago, see also Ref. [7] and references therein). The molecular weight is 391.46 g/mol and the chemical formula reads $[\text{C}_{12}\text{D}_{20}\text{O}_7\text{Cr} \cdot \text{D}_2\text{O}]^- \text{Na}^+$.

The concentration of the paramagnetic centers is 6.35×10^{19} spins/g.

At room temperature the chromium complex in a watery solution decays at a rate of about 2% per hour [6], whereas it is stable in a glass or solid. Therefore the liquid solution was frozen into beads as fast as possible.

The beads were formed by dropping the liquid solution at 20°C through two needles, operating in parallel, onto the surface of a LN_2 bath. The droplets ($3 \mu\text{l}$) froze within 4 to 5 s and then sank in the liquid nitrogen as beads of 1.8 mm in diameter. The fast sinking down of the droplets was achieved by blowing helium gas on the LN_2 surface, which prevents the liquid nitrogen from boiling and so suppressed the formation of bubbles effectively. The temperature of the liquid solution in their containers was stabilized by foam isolation and by circulating water from a thermostat to prevent freezing of the liquid, especially inside the needles. The drip rate was adjustable by controlling the pressure inside the container over the liquid solution.

To allow the fast production of a large number of beads, the liquid nitrogen bath was constructed with separate compartments, which turned at controlled speed in succession under the needles, thereby avoiding sticking together of the freezing droplets. Each compartment contained on average one bead at a time. A sketch of this apparatus is shown in Fig. 1.

The drip rate was typically 2 s^{-1} and the production was done in batches of 60 ml of liquid solution, lasting nearly 90 min for each batch.

4. Measurement of target material properties

The density of the deuterated target material was determined using the method of weighing samples in two media with different densities, in our case liquid nitrogen and very cold nitrogen gas. The temperatures of the liquid and the gas were measured to be 77.3 K and 77.5 K, respectively. At these temperatures, the density of the nitrogen is $\rho(\text{LN}_2) = 0.8086 \text{ g/cm}^3$ for the liquid and $\rho(\text{N}_2) = 0.0046 \text{ g/cm}^3$ for the gas [9]. The density of the target material is calculated from the measured values as follows:

$$\rho = \frac{(W_{s+m}(\text{N}_2) - W_s(\text{N}_2))(\rho(\text{LN}_2) - \rho(\text{N}_2))}{(W_{s+m}(\text{N}_2) - W_{s+m}(\text{LN}_2)) - (W_s(\text{N}_2) - W_s(\text{LN}_2))} + \rho(\text{N}_2),$$

where $W_{s+m}(\text{LN}_2)$ and $W_{s+m}(\text{N}_2)$ are the weights of a sample of the target material (m) contained in a sock (s) in liquid nitrogen and in the cold nitrogen gas, respectively. Additionally, one needs the weight of the sock without material in these two phases ($W_s(\text{LN}_2)$ and $W_s(\text{N}_2)$, respectively).

The weights are measured by suspending the sample from the hook of an underfloor balance into a dewar which

has a stainless steel cylinder inside. The cylinder is closed at the bottom and is half filled with liquid nitrogen. The gap between the dewar and the cylinder wall is filled up to the top with liquid nitrogen (see Fig. 2). To measure the weight in the liquid, the target material is submerged completely in LN₂, while for obtaining the value in the gas phase, the material is lifted up just above the meniscus of the liquid. The cold wall of the stainless steel cylinder protects the sample from changing its temperature significantly. We observed a change of less than 0.3 K.

The measurement of the weight of the material in the gas phase is problematic, as the balance reading is continuously decreasing. This is caused by the slow evaporation of liquid nitrogen accumulated between the beads, when they were immersed in liquid nitrogen.

The density of the deuterated target material was found to be $1.106 \pm 0.012 \text{ g/cm}^3$ at 77 K. A stable asymptotic value is obtained only after about 5 h.

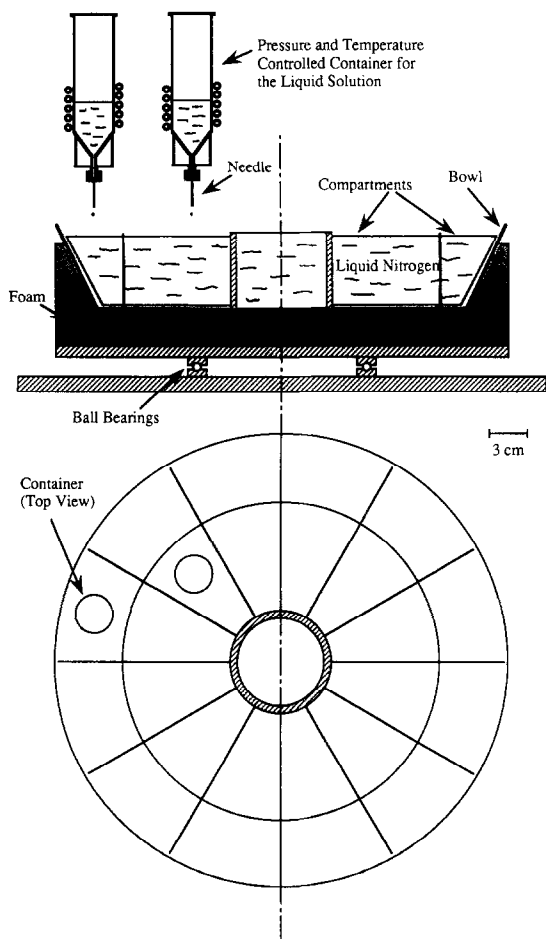


Fig. 1. The rotatable liquid nitrogen bath with compartments. The two containers for the liquid solution are shown at their positions above the bath.

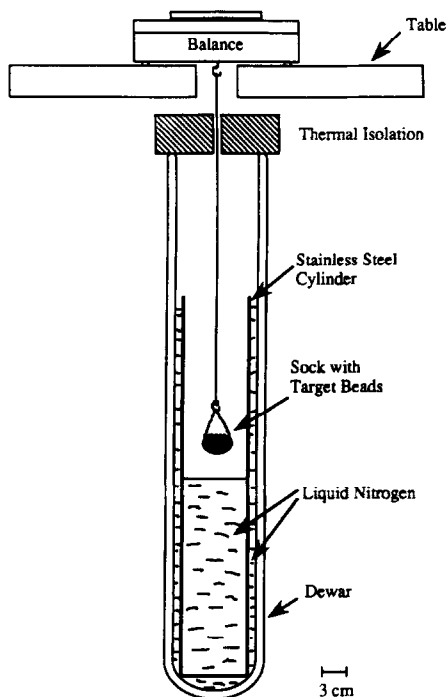


Fig. 2. Setup for density and weight measurements. The target material is contained in the polyamid sock hanging underfloor the balance on a thin copper wire.

The packing factor F of the target material inside the target cartridges was determined by measuring the weight of the material of each cartridge separately in the above described way. By combining these values with the measured density and the known volume of the cartridges one obtains $F = 0.63 \pm 0.04$, this has to be compared with the maximum possible packing factor of $F = 0.74$ for hexagonally close-packed beads.

The above given value of the dilution factor f does not take into account the presence of other materials than the butanol in the target. In reality, one has to account for the additives as well as for the coolant (mixture of helium isotopes) and the NMR coils embedded in the target material. These coils consist of a Cu₇₀Ni₃₀ alloy and are partially covered by a thin layer of PTFE tape. Also, the scattering cross-sections σ of the individual elements has to be taken into account. One can write the dilution factor as follows

$$f = \frac{n_d \sigma_d}{n_d \sigma_d + \sum n_x \sigma_x},$$

where x stands for the different contributing elements. In Table 1 these elements are given together with their amounts n_x and their relative cross-sections in comparison to the one of deuterium. The dependence of the cross-sections on the kinematics and on the difference between a bound and an unbound nucleus, known as the ‘‘EMC-ef-

Table 1
Contributions to the dilution factor

Element	n_x (moles)	σ_x / σ_0
^2H	118.4	1.0
^3He	2.2	1.5
^4He	16.7	2.0
C	46.7	6.0
O	14.4	8.0
F	1.0	9.5
Na	0.1	11.5
Cr	0.1	26.0
Ni	0.2	29.3
Cu	0.5	31.7

fect'', has been accounted for [2], but is for simplicity not regarded here.

The influence of the deuterium oxide, the EDDB and the helium mixture lowers the average dilution factor from $f=0.238$ to $f=0.214$ and the NMR coils lead to an additional decrease to a value of about $f=0.202$.

To obtain information of the glass properties of the target material, differential microcalorimetric studies as described by Hill and Hill [5] were undertaken. The principle of these measurements is to observe the temperature difference between a bead and a reference point during warm-up.

In Fig. 3 the results from two measurements are shown. The beads were warmed up with a speed of 5 K/min. The peaks can be interpreted as exothermic or endothermic processes occurring during the temperature change. Similar measurements were done earlier by Takala et al. [10]. The lower curve was taken with a bead made as a test sample without using the above described production apparatus.

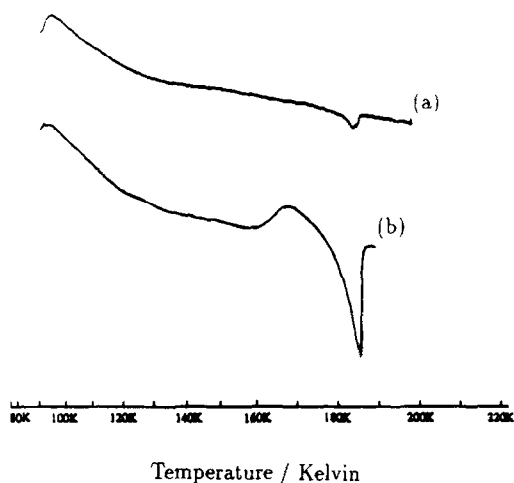


Fig. 3. Melting curves of deuterated target material of the same chemical composition as given in the text. (a) SMC target material and (b) material of a test sample. Positive (negative) peaks indicate exothermic (endothermic) processes. The overall slope is due to the adjustment of the set-up.

One can clearly see the exothermic peak of devitrification (maximum), which occurs above 160 K and is due to the crystallization in the material. The endothermic peak (minimum) starting at 180 K is due to the melting of the bead. In comparison, the actual target material produced for the SMC experiment (upper curve) does not show the devitrification peak. This leads to the conclusion that no microcrystals or other impurities were present inside the glassy bead, which could act as seeds for crystallization. This emphasizes the importance of a fast and controlled cooling-down of the liquid droplets to obtain a perfect glass. A warm-up of the target material to a temperature close to 140 K did not lead to any deterioration in its properties.

Indeed, the polarization build-up is rather fast and values of $P=0.30$ (0.40) are obtained within 1.5 (7) h with no significant difference for the two signs of polarization. The maximum polarization reached so far is above $P=0.50$. The relaxation of the polarization was measured at a temperature of 40 mK and 2.5 T over a time of nearly 3 days under stable conditions (frozen spin mode). The relaxation time constant was found to be of the order of $\tau \approx 2300$ h.

5. Conclusions

The deuterated material used in the SMC target is showing good characteristics regarding all relevant polarization parameters. Furthermore, it was found that an increase in temperature presumably close to 140 K did not alter these properties.

References

- [1] SMC, D. Adams et al., Phys. Lett. B 329 (1994) 399.
- [2] SMC, B. Adeva et al., Phys. Lett. B 302 (1993) 533.
- [3] D. Crabb and D.B. Day, these Proceedings (7th Workshop on Polarized Target Materials and Techniques, Bad Honnef, Germany, 1994) Nucl. Instr. and Meth. A 356 (1995) 9.
- [4] D.A. Hill, Proc. 2nd Workshop on Polarized Target Materials, Oxford 1979 RL-80-080 (Rutherford Laboratory 1980) p. 67.
- [5] D.A. Hill and J.J. Hill, ANL-HEP-PR-81-05, Argonne National Laboratory, 1981.
- [6] M. Krumpolc, private communication, 1990.
- [7] M. Krumpolc et al., Proc. 9th Int. Symposium on High Energy Spin Physics, Bonn 1990, Vol. 2 (Berlin, 1991) p. 340.
- [8] J. Kyyr arainen, Ref. [3], p. 47.
- [9] L'air Liquide, Encyclopedie De Gaz.
- [10] S. Takala and T. Niinikoski, Proc. 9th Int. Symposium on High Energy Spin Physics, Bonn 1990, Vol. 2 (Berlin, 1991) p. 347.
- [11] A. Thomas et al., Ref. [3], p. 5.
- [12] S. Trentalange et al., Proc. 9th Int. Symposium on High Energy Spin Physics, Bonn 1990, Vol. 2 (Berlin, 1991) p. 325.

Cross-relaxation between protons and ^{13}C nuclei

S. Bültmann ^{a,*}, G. Baum ^a, C.M. Dulya ^b, N. Hayashi ^f, A. Kishi ^f, Y. Kisselev ^e,
D. Krämer ^a, J. Kyynäräinen ^c, J.-M. Le Goff ^d, A. Magnon ^d, T. Niinikoski ^c,
Y.K. Semertzidis ^c

^a Universität Bielefeld, Fakultät für Physik, D-33615 Bielefeld, Germany ¹

^b University of California, Department of Physics, Los Angeles, 90024 CA, USA ²

^c CERN, CH-1211 Genève 23, Switzerland

^d DAPNIA, C.E. Saclay, F-91191 Gif-sur-Yvette, France

^e JINR, Laboratory of Super High Energy, Dubna, Russian Federation

^f Nagoya University, Department of Physics, Furo-Cho, Chikusa-Ku, 464 Nagoya, Japan ³

Abstract

In an applied microwave field, the free electron spin–spin interaction reservoir in polarized target material couples strongly to the Zeeman interaction reservoirs of different nuclei. This leads to an effective cross-relaxation between different nuclei, which was studied at different levels of microwave power between protons and ^{13}C nuclei in the large SMC target using butanol as material.

1. Introduction

The measurements to be described were performed on proton target material made out of 90.5% butanol, 5.0% water and 4.5% EHBA-Cr(V). The target material contained 93 moles of ^1H -nuclei and 36 moles of carbon-nuclei. The natural abundance of ^{13}C nuclei in carbon is 1.1%, which gives an amount of 0.4 moles of ^{13}C in the target. The Larmor frequency of the proton is roughly four times larger than the one of the ^{13}C nuclei. At a magnetic field of 2.5 T the values are $\nu(^1\text{H}) = 106.5$ MHz and $\nu(^{13}\text{C}) = 26.78$ MHz.

One half of the large SMC target with a volume of 1170 cm^3 was used. Five NMR coils, embedded in the material, are longitudinally aligned in the target half. Four of them were tuned for the measurement of the proton polarization during asymmetry data taking of the SMC, while one of the five coils was used for the measurement of the ^{13}C signals. No calibration of this coil by measuring the natural ^{13}C thermal equilibrium signal was done.

The measurement of the polarization was done by NMR, using series Q -meters (see Refs. [1,2] and the references mentioned therein). The integral of the reso-

nance signal obtained by this NMR circuit is proportional to the polarization of the probed spin species. One can write

$$P \propto \frac{1}{\pi \hbar \gamma^2 N I} F,$$

where γ denotes the gyromagnetic ratio, N the spin density, I the spin and F the integral of the absorption line

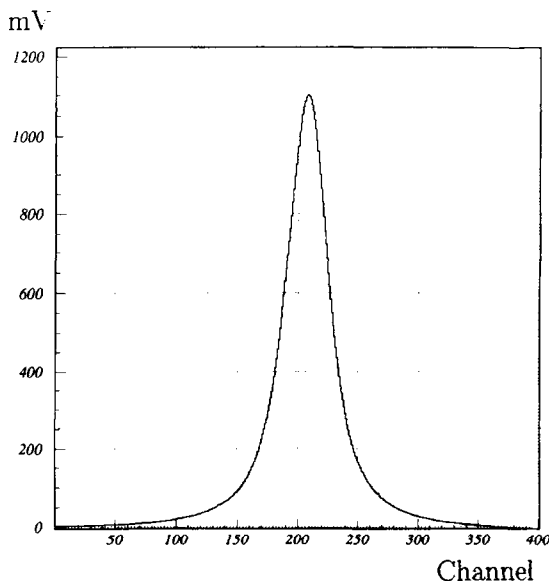


Fig. 1. Proton resonance signal (400 channels = 600 kHz).

* Corresponding author.

¹ Supported by Bundesministerium für Forschung und Technologie.

² Supported by the Department of Energy.

³ Supported by Ishida Foundation, Mitsubishi Foundation and Monbusho International Science Research Program.

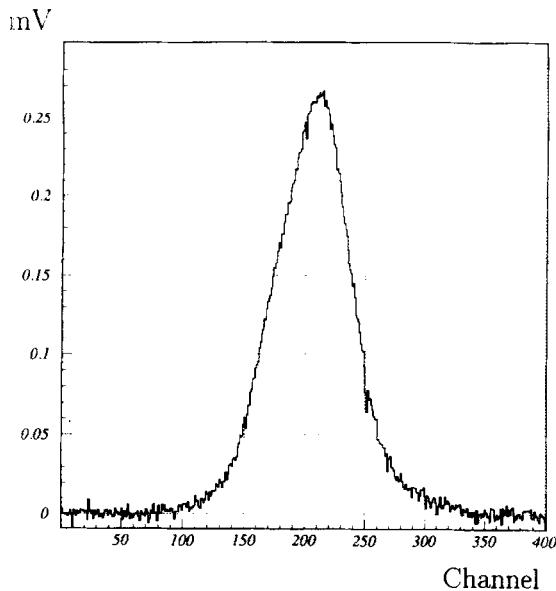


Fig. 2. Carbon-13 resonance signal (400 channels \equiv 160 kHz).

shape over the frequency range (sweep width) $\Delta\omega$, centered around the Larmor frequency.

2. Measurements

The target was polarized by dynamical nuclear polarization (DNP) [3], at microwave frequencies around 69 GHz in a magnetic field of 2.5 T. After DNP and cooldown to the frozen spin mode at a temperature below 100 mK, the polarizations of the protons and the carbon-13 nuclei were measured with their respective coils. For the protons a polarization of $P = 0.81$ was obtained from the measured $\Gamma(^1\text{H}) = 82.5 \text{ V kHz}$ ($\Delta\omega = 600 \text{ kHz}$, see Fig. 1). For the carbon-13 we measured $\Gamma(^{13}\text{C}) = 8 \text{ mV kHz}$ at $\Delta\omega = 160 \text{ kHz}$ (see Fig. 2).

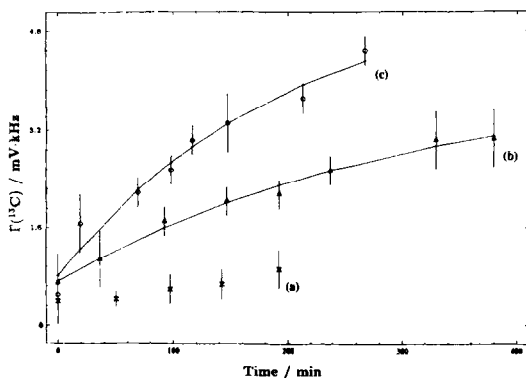


Fig. 3. The integral $\Gamma(^{13}\text{C})$ versus time for different levels of microwave power. (a) No microwave power applied, (b) low power (3 mW) and (c) high power (22 mW). The results of the fits are given in the text.

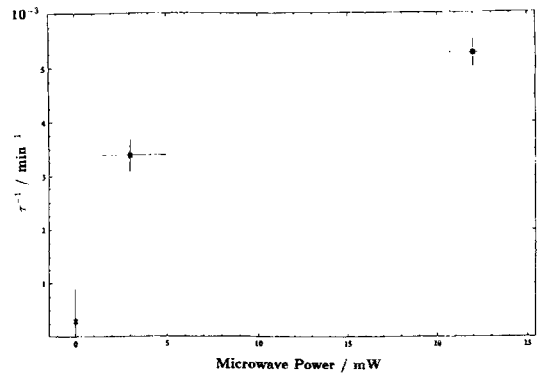


Fig. 4. The reciprocal of the time constant τ versus the applied microwave power.

In the following step, the ^{13}C polarization was destroyed by saturating their spins using a RF signal at Larmor frequency, which was fed directly into the NMR coils from the RF output of a frequency synthesizer. However, as the available power was limited to 13 dB m, the polarization could not be destroyed completely (see the first data points in Fig. 3). After that, the slow increase of the ^{13}C polarization with time was measured. The time constant of this process is in the order of 3000 min. By turning on the microwaves for the DNP, a drop in the polarization build-up time of the ^{13}C nuclei was observed. This polarization build-up was measured at two different levels of microwave power, 3 mW and 22 mW. The resulting curves are given in Fig. 3. An exponential fit gives values of $\tau(3 \text{ mW}) = 295 \text{ min}$ and $\tau(22 \text{ mW}) = 190 \text{ min}$ for the build-up time constants, respectively. The reciprocal values of the three time constants are shown in Fig. 4. A clear increase in the relaxation speed can be seen with the microwave power, demonstrating that it can promote the cross-relaxation between the two spin species. A decrease of the proton polarization was not observable as expected from the small relative number of the ^{13}C spins.

3. Conclusions

A decrease of the polarization build-up time of the ^{13}C nuclei with applied microwave power was observed, due to the cross-relaxation mechanism between the two spin species. The results of this preliminary experiment support further feasibility studies of axion detection via nuclear cross-relaxation in a large polarized target [4].

References

- [1] G.R. Court et al., Nucl. Instr. and Meth. A 324 (1993) 433.
- [2] N. Hayashi et al., these Proceedings (7th Workshop on Polarized Target Materials and Techniques, Bad Honnef, Germany, 1994) Nucl. Instr. and Meth. A 356 (1995) 91.
- [3] J. Kynnäräinen et al., *ibid.*, p. 47.
- [4] Y.K. Semertzidis et al., *ibid.*, p. 122.



ELSEVIER

Polarization reversal by adiabatic fast passage in various polarized target materials

P. Hautle ^{*}, B. van den Brandt, J.A. Konter, S. Mango*Paul Scherrer Institut, CH-5232 Villigen PSI, Switzerland*

Abstract

Spin-polarization reversal by the use of the adiabatic fast passage mechanism has been investigated in a variety of polarized target materials. The high efficiencies achieved open the way to the application of the AFP method in operational polarized solid targets.

1. Introduction

Many particle physics experiments studying spin effects with polarized solid targets suffer from large systematic uncertainties due to the infrequent reversal of the target polarization, practically imposed by the time consuming process (dynamic nuclear polarization at low temperature, DNP [1]) normally exploited to perform the reversal.

A most elegant solution to the problem is in principle given by the adiabatic fast passage (AFP) method already suggested in 1946 by Bloch [2]. In fact, such a method by which the polarization of a system of nuclear spins can be reversed in the order of a second has been tried in the past in polarized proton targets. However, the deceiving polarization reversal efficiencies achieved ($\delta P = -0.5$) have prevented any practical application and discouraged further work in the field since 1984 [3]. Recently, the method has been revisited in our laboratory and the encouraging results obtained [4] have suggested additional work, which we are going to report on.

2. Principles of the AFP method

A nuclear spin system situated in a strong magnetic field B_0 is irradiated with a rf field B_1 linearly polarized in a plane perpendicular to B_0 , of frequency close to the Larmor frequency $\omega = -\gamma_0 B_0$. A passage through the nuclear magnetic resonance line, performed by either varying the frequency ω of the rf field or by changing the strength of the field B_0 at a fixed ω , can result in a reversal of the magnetization direction with little loss of its

magnitude. Classical NMR theory [5] gives for the feasibility of polarization reversal the very general adiabatic condition

$$A = \frac{\gamma B_1^2}{dB/dt} \gg 1, \quad (1)$$

where dB/dt is the sweep rate. A lower limit to the sweep rate is set by the condition that the entire sweep has to take place in a time τ much shorter than the spin–lattice relaxation time $T_1\rho$ in the field B_{eff} in the frame rotating at the frequency ω of the rf field about the field B_0 :

$$\tau \ll T_1\rho. \quad (2)$$

There is therefore an optimum sweep rate for given values of B_1 and $T_1\rho$ for which the polarization loss is smallest.

Goldman et al. [6] gave an extensive description of the AFP mechanism in a spin- $\frac{1}{2}$ system in the frame of the spin temperature concept on the basis of the Provotorov equations [7]. Their theory, which is in good qualitative agreement with experiments [3], describes the polarization reversal as a transfer of order from the Zeeman to the dipole–dipole subsystem and back to the Zeeman subsystem with reversed orientation.

3. Experiments

All measurements were performed in a field of $B_0 = 2.5$ T at a temperature of $T \sim 80$ mK in a dilution cryostat [8]. Most of the samples of about 1 cm^3 volume were contained in a brass cavity 18 mm high, 18 mm wide and 5 mm thick. A single vertical wire grounded to the cavity bottom was used as rf coil for both NMR measurements and AFP irradiation. Tests showed that this simple geometry produces a sufficient rf field homogeneity over the sample volume. The somewhat different setup employed in the deuteron AFP experiments is described in Ref. [4].

^{*} Corresponding author.

We have investigated the reversible fraction of the polarization $\delta P = P_{\text{fin}}/P_{\text{ini}}$ as a function of $B_1^{-2}dB/dt$, where P_{ini} and P_{fin} are the intensities of the NMR signals before and after the sweep, for a series of substances in which sizeable nuclear polarization can be achieved by DNP processes.

3.1. Spin systems without quadrupole interactions

The short relaxation time $T_{1\rho}$, which is essentially the spin–lattice relaxation time of the dipolar subsystem, and the relatively weak coupling of the subsystems (Zeeman–dipolar) set the practical limits to the achievable reversal efficiency. The paramagnetic centers added to the dielectric solid to perform dynamic nuclear polarization are also the main source of nuclear spin relaxation and have a great influence on $T_{1\rho}$. Too high a dopant concentration can make the application of the AFP mechanism impossible. Therefore AFP polarization reversal might be of special interest for slowly polarizing materials.

1-butanol: The proton spin system of ordinary alcohols is the most widely employed polarized target in particle physics experiments. Up to now, the polarization reversal has been accomplished by DNP and or rotation of the holding field B_0 , as the AFP method did not seem to be practicable [3]. A fresh investigation has shown that the situation is not so hopeless as one believed. In fact, the achieved efficiency $\delta P = -0.76$ in a weakly doped sample shows that in some cases (under certain conditions) AFP polarization reversal could help to optimize the duty cycle of polarization experiments.

There is even a possibility for improvement of δP by starting the AFP reversal with a higher initial polarization (we were limited to a maximum polarization of about $\pm 70\%$). This, because the efficiency was observed to be clearly depending on the magnitude of the initial polarization, is plausible, as the linewidth and thus the strength of the local fields are decreasing with increasing degree of polarization of the spin system.

Octofluoro-1-pentanol: In this fluorinated alcohol both nuclei ^{19}F and ^1H possess spin- $\frac{1}{2}$ with a comparable magnetic moment. One therefore expects a response on rf irradiation similar to ordinary alcohols. This we actually found in our AFP experiments. The low efficiency achieved, most likely due to the very high concentration of paramagnetic centers in the sample investigated, could probably be improved to the high values obtained in the moderately doped n-butanol.

^7LiH : This material has a symmetric fcc crystalline structure so that the electric field gradient is vanishing and no quadrupole shifts exist in the ^7Li system. Possibly due to a low concentration of paramagnetic centers, polarization and relaxation times of the sample at our disposal are very long, in particular a full polarization reversal by DNP takes about 2 days [9]. The AFP method looked attractive for it and the low concentration of paramagnetic centers

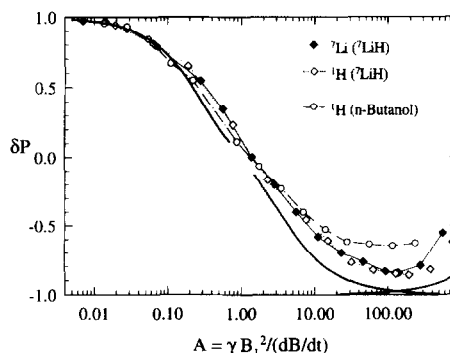


Fig. 1. Dependence of the efficiency δP on the adiabatic parameter A for the AFP spin orientation reversal in ^7LiH and 1-butanol. The solid curve indicates the theoretical prediction.

allowed one to expect a high efficiency of the AFP reversal.

The obtained efficiencies are plotted in Fig. 1 as a function of the adiabatic parameter for both spin species together with the results from 1-butanol. The data points correspond to measurements with an initial polarization of about two thirds of the maximum polarization. Similar to 1-butanol, the efficiency rises with the initial polarization and maximum values of $\delta P = -0.90$ have been achieved for both spin species for maximum initial polarizations (^7Li : $+0.46$, -0.37 ; ^1H : $+0.64$, -0.53). We illustrate the result by the practical example shown in Fig. 2. Starting from $+0.46$ ^7Li polarization, one can achieve by AFP reversal in seconds -0.40 , which is more than one can obtain in 2 days by DNP. This means that a full DNP build-up has to be executed only once; data taking can then go on without interruption with a very high polarization of either sign, kept near maximum by eventually topping it up by microwave irradiation after the AFP reversals.

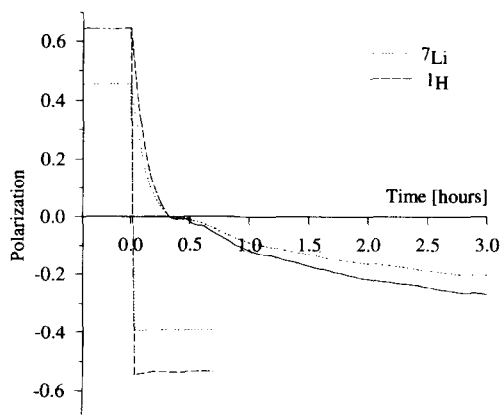


Fig. 2. Comparison between DNP and AFP polarization reversal in ^7LiH .

3.2. Spin systems with quadrupole interactions

Due to the presence of a strong quadrupole interaction, the response of the spin-1 system in deuterated alcohols to rf irradiation is different from that of a spin- $\frac{1}{2}$ system.

1-butanol-d₁₀: We actually found a peculiar behaviour in the deuterated alcohol: One full sweep through the resonance as practiced in spin- $\frac{1}{2}$ systems was not enough to reverse the polarization. An additional half-sweep with the same direction to the center of the deuteron magnetic resonance line had to be performed. Also unexpected high reversal efficiencies ($\delta P > -0.90$) could be achieved under conditions where adiabaticity in the classical sense (Eq. (1)) is not fulfilled [10], i.e. irradiating with low rf power only during a short time. The key point to understand the behaviour of this deuteron spin system seems to be the fact, that the reversal takes place consecutively within spin packets in spin- $\frac{1}{2}$ transitions. The narrow width of the packets assures a very fast transfer of order

Table 1
Results from AFP experiments with various nuclei in different target materials

Nuclei	Substance dopant	e ⁻ conc. (spins/g)	δP^{\max}
¹ H	1-butanol EHBA-Cr(V)	2.0×10^{19}	-0.76
⁷ Li	⁷ LiH	low	-0.90
¹ H	(irradiated)		-0.90
¹⁹ F	8-fluoro-1-pentanol	1×10^{20}	-0.37
¹ H	TEMPO		-0.40
² H	1-butanol-d ₁₀ EHBA-Cr(V)-d ₂₂	2.36×10^{19} 6.35×10^{19}	-0.92 -0.90

from the Zeeman to the quadrupole subsystem and back to the Zeeman subsystem [11].

4. Conclusions

The main results of our investigations are compiled in Table 1. Noticeable is the very high efficiency for the spin- $\frac{1}{2}$ systems with low concentrations of paramagnetic centers and for the spin-1 system in a deuterated alcohol. Therefore the main focus for an application lies on slowly polarizing materials and on systems with large inhomogeneous quadrupole broadenings. There the improvement of the duty cycle of a scattering experiment and thus of the systematic and statistical accuracy of its result can be tremendous.

References

- [1] A. Abragam and M. Goldman, Rep. Prog. Phys. 41 (1978) 395.
- [2] F. Bloch, Phys. Rev. 46 (1946) 460.
- [3] L.B. Parfenov and A.F. Prudkoglyad, Sov. Phys. JETP 60 (1984) 123.
- [4] P. Hautle et al., Phys. Rev. B 70 (1992) 6596.
- [5] A. Abragam, The Principles of Nuclear Magnetism (Oxford University Press, London, 1961).
- [6] M. Goldman, M. Chapellier and Vu Hoang Chau, Phys. Rev. 168 (1968) 301.
- [7] B.N. Provotorov, Sov. Phys. JETP 14 (1962) 1126.
- [8] B. van den Brandt et al., Proc. 8th Int. Symp. on High Energy Spin Physics, Minneapolis 1988, AIP Conf. Proc. 187 (1989) 1251.
- [9] B. van den Brandt et al., Proc. 10th Int. Symp. on High Energy Spin Physics, Nagoya, 1992, (Universal Academy Press, Tokyo, 1993) p. 369.
- [10] P. Hautle et al., *ibid.*, p. 371.
- [11] P. Hautle, Thesis, ETH Zürich (1993).



ELSEVIER

An internal superconducting “holding-coil” for frozen spin targets

H. Dutz^{*}, R. Gehring, S. Goertz, D. Krämer[†], W. Meyer, G. Reicherz, A. Thomas*Physikalisches Institut der Universität Bonn, Nussallee 12, 53115 Bonn, Germany*

Abstract

A new concept of a small superconducting holding magnet, placed inside a polarizing refrigerator, has been developed for frozen spin targets. The superconducting wire has been wound on the inner cooling shield of the vertical dilution refrigerator of the Bonn frozen spin target. The maximum field of the magnet is 0.35 T. The total thickness of the superconducting coil consisting of the wire and the copper carrier is of the order of 500 μm . Based on this concept, a frozen spin target is under construction for the measurement of the Gerasimov–Drell–Hearn sum rule with polarized real photons at the Mainz microtron MAMI and the Bonn electron stretcher accelerator ELSA.

1. Introduction

One powerful tool to study spin dependent reactions in low intensity particle beams – i.e. tagged photons, pions, muons or protons – are frozen spin polarized solid state targets.

One advantage of frozen spin targets is the possibility to prepare the polarization direction of the nucleon for a spin dependent experiment in any arbitrary direction. This is done with different types of so called “holding magnets”. Existing targets are operating with external superconducting magnets providing a “holding field” of the order of 0.5 T in the target area. These magnets are large and have a strong fringe field. Therefore such frozen spin targets cannot be operated in combination with 4π -detectors, where detector components are placed close around the target refrigerator.

To overcome this problem, a new type of small superconducting “holding coil” has been built. The coil has been wound on the inner cooling shield of the refrigerator in the target area. This scheme allows a substantial reduction of the magnetic field affecting the detector components.

Here we will describe in detail the first test of an internal superconducting “holding coil” which has been located in the isolation vacuum of the vertical $^3\text{He}/^4\text{He}$ dilution refrigerator of the Bonn frozen spin target. The characteristics of the wire and the coil as well as the field measurements are discussed briefly.

2. The frozen spin target

High nucleon polarization in a solid state sample can be achieved by means of the so-called DNP (dynamic nuclear polarization) process by which the high electron polarization of some paramagnetic impurities is transferred via microwave induced transitions to the nucleon spin system. The proton equilibrium (TE) spin polarization is represented in terms of the magnetic field B and the temperature T as follows

$$P = \tanh\left(\frac{\mu B}{2kT}\right), \quad (1)$$

with μ the magnetic moment and k the Boltzmann constant. This basic equation implies which components are necessary for a polarized target apparatus:

- a continuous working cryogenic system,
- a high field magnet with excellent homogeneity throughout the target area,
- a microwave source for the DNP process,
- a NMR circuit to measure the nucleon polarization value,
- a suitable, specially prepared target sample.

A further criterion is that both primary beam and final-state particles be affected as little as possible. A suitable technical solution for this demand is to use a frozen spin target.

The operation of the frozen spin target is based on the experimental fact that the nucleon relaxation time T_1 is a very steep function of the temperature. T_1 characterizes the polarization decay after the DNP mechanism (microwaves) is switched off. Typical values for T_1 are minutes at a temperature of 1 K and days below 100 mK. The principle of the frozen spin target operation is to polarize the target material at a high field (e.g. 5 T) and around 300 mK. Once the target material is optimally polarized, the mi-

^{*} Corresponding author.

[†] Now at Universität Bielefeld, Fakultät für Physik, 33501 Bielefeld, Germany.

crowaves are switched off and the polarization is frozen at temperatures around 50 mK (“frozen spin mode”). Due to the long proton relaxation time T_1 at these temperatures, it is possible to maintain the polarization at a substantially lower field (“holding field”). In a scattering experiment this will be provided by the “holding magnet” of about 0.35–0.5 T, allowing an open geometry for the outgoing particles. In practice the spin orientation will be reversed once per day, as the polarization build up time τ_p is in the order of hours, to minimize systematic effects on the asymmetry measurement. Detailed information about frozen spin targets are given in Refs. [1,2].

3. Design and construction of the internal “holding magnet”

The existing components of the Bonn frozen spin target have been used to test an internal “holding coil”. They include a vertical superconducting 7 T polarizing solenoid and a vertical $^3\text{He}/^4\text{He}$ dilution refrigerator with a base temperature of 49 mK. The homogeneity $\Delta B/B$ of the polarizing magnet is better than 5×10^{-5} over a target volume of 30 cm^3 . The maximum cooling power was measured at 280 mK to be 80 mK with a mass flow rate of 14 mmol/s [3]. The zero point temperature of the refrigerator corresponds to a ^3He circulation speed of 3.5 mmol/s. Fig. 1 shows a cutaway view of the refrigerator. The lower part of the figure represents the dilution unit of the system, consisting of the still, the sintered heat exchanger and the mixing chamber where the target is placed. The refrigerator is enclosed by two cooling shields to reduce the heat load on the cryostat. Both shields are built into the insulation vacuum vessel of the refrigerator. The inner cooling shield is a copper tube with a length of 46 cm, a diameter of 6.6 cm and a wall thickness of 2.3 mm. The upper part of the tube is connected to the still of the refrigerator. The lower part of the shield is machined down to a thickness of $300 \mu\text{m}$ on a length of $\pm 8 \text{ cm}$ symmetrical around the target to support the wire of the coil. The temperature of the inner shield is determined by the temperature of the still ($T_s \approx 1 \text{ K}$) and that of the outer cooling shield. Taking into account the material parameters of the used copper tube, a temperature of $T_c \approx 1.2 \text{ K}$ at the end of the tube can be achieved.

With the present geometric inputs the magnetic field and the parameters of the coil were computed by a summation of the field of single current loops, which can be expressed with elliptical integrals [4]. Due to a center field of 0.35 T and a number of windings of $N = 2500$ a current of $I_n = 19.36 \text{ A}$ is needed. These values lead to a current density of $J_c = 2466 \text{ A/mm}^2$ by using a wire with an outer diameter of $D_o = 100 \mu\text{m}$. Such a thin wire was chosen to fulfill the condition of a low mass density and a low wall thickness of the magnet for scattering experiments using a compact detector. Thereby it is wound as a 2

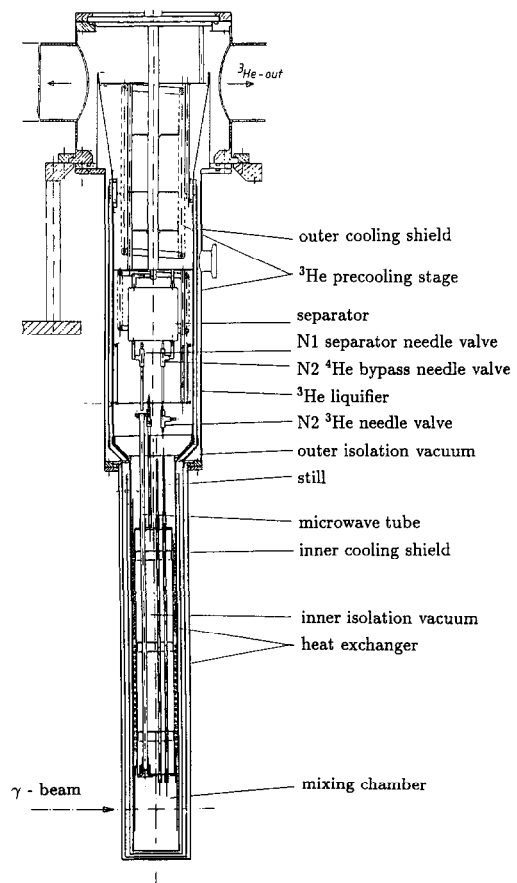


Fig. 1. Cut view of the vertical dilution refrigerator of the Bonn frozen spin target.

layer solenoid, each of 1250 windings. The complete layer consisting of the copper carrier, the windings and the glue has a thickness of about $500 \mu\text{m}$. The coil has a length of 160 mm. Computed field maps of the configuration are shown in Figs. 2 and 3 [5]. Note that the fringe field is extremely small so that tracking of charged particles becomes much easier.

A multifilament NbTi wire² with a diameter of $D_o = 100 \mu\text{m}$ was chosen as superconductor for the magnet. It is isolated with a $10 \mu\text{m}$ varnish insulation. The characteristic parameters of the wire, specified by the manufacturer are a critical current of $I_c \leq 8 \text{ A}$ ($J_c \leq 1000 \text{ A/mm}^2$) at $T = 4.2 \text{ K}$ and $B_c = 0.5 \text{ T}$.

A safe operation of a superconducting magnet is given if the operation temperature of the magnet T_o is less than the current-sharing-temperature T_{cs} when the coil quenches. To estimate T_{cs} of a superconducting coil as a function of the critical current I_c , the critical temperature at a fixed field value $T_c(B)$, the actual current I and the operation

² Vacryflux 5001 F54/0.1, VAC Hanau.

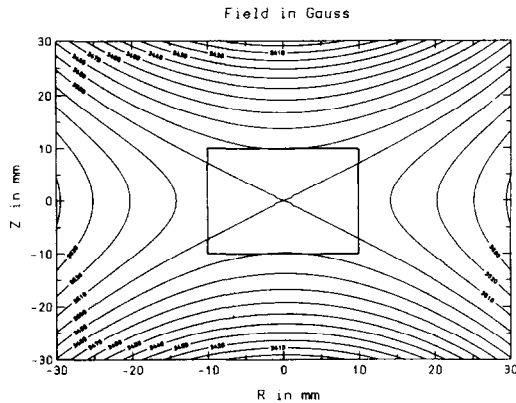


Fig. 2. Computed field of the internal solenoid. The plot shows the inner field of the magnet. The field values are given in G and the values of the x and y axis are the distances from the center of the coil in mm. The rectangle in the center of the magnet shows the target area.

temperature T_0 of the coil, the following linear expression can be used [6]:

$$T_{cs}(I) = T_0 + (T_c(B) - T_0) \left(1 - \frac{I}{I_c}\right). \quad (2)$$

Assuming the operation temperature T_0 of about 1.4 K and a ratio of $(I/I_c) \approx 0.95$, the approximation leads to a current-sharing temperature of $T_{cs} = 1.78$ K. The parameters of the coil are summarized in Table 1.

The coil was built in the workshop of the Bonn institute. The gluing was done by “wet winding”, applying the glue directly to the copper tube and winding the wire into the glue. The glue was standard epoxy-resin³ which was put into a small vacuum vessel (50 mbar) for about 2 min to remove the bubbles from mixing the components.

The normal conducting current leads were made of three copper wires with 0.75 diameter each. They were wound around the inner stainless steel tube of the cryostat vessel. The superconducting wires were connected to the current leads close to the still area and soldered across a range of 10 cm to provide a good contact with low resistance. The soldered parts were isolated with a thin teflon foil and attached to the inner cooling shield.

4. Test of the magnet

The isolation vacuum vessel and the refrigerator is precooled with liquid nitrogen. After inserting the refrigerator into the vessel the cool-down of the system including the shields and the coil from 77 K down to 1 K takes 1 h. When the inner cooling shield has reached a temperature

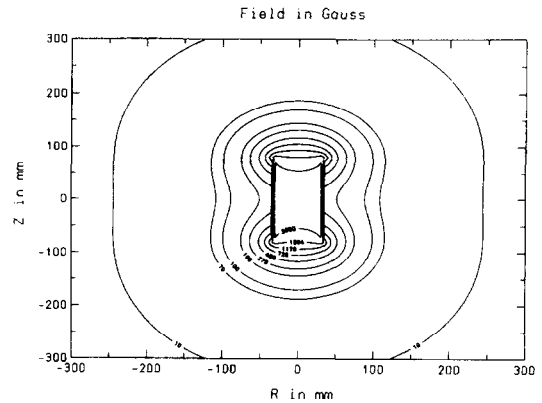


Fig. 3. Calculated field of the internal solenoid. Shown is the outer fringe field of the magnet. The field values are given in G and the values of the x and y axis the distance from the center of the coil in mm.

of 1.4 K the current can be increased to the maximum current of $I_{\max} = 19.7$ A. The ramping time up to the maximum current was of the order of 5 min. The inductance voltage across the coil was about 100 mV.

During operation the voltage drop across the current leads increased slightly from 110 mV up to 170 mV because the resistance of the current leads increased from 5.6 m Ω to 8.7 m Ω . This self-heating effect is caused by a insufficient cooling of the current leads and the fact that the heat load of the refrigerator in the area of the still is directly proportional to the length of the wire at a given current. The maximum heat load is in the order of $Q_{\max} = 6.6$ W. By increasing the helium consumption of the refrigerator by about 20% the self heating effect was compensated. No temperature rise was observed during a long term operation of the system.

Some tests were performed to investigate the characteristics of the coil, e.g. the quench behaviour. The critical current I_c was achieved at a value of $I_c = 19.8$ A. As a consequence the coil quenched within the calculated specification, causing no damage to the magnet.

Table 1
List of the coil parameters

Coil length	16 cm
Inside diameter	6.6 cm
Layers	2
Windings	1250 per layer
Total length of shield	46 cm
Coil thickness (with copper carrier)	500 μ m
Maximum field	0.35 T
Wire diameter	100 μ m
Wire diameter (with isolation)	120 μ m
Current density at 0.35 T	2466 A/mm ² (= 19.36 A)
dB/B in target area	$\leq 0.5\%$
Inductance	0.168 H
Operating temperature	≤ 1.7 K

³ Ciba Geigy Araldit CY221, Hardener HY2967.

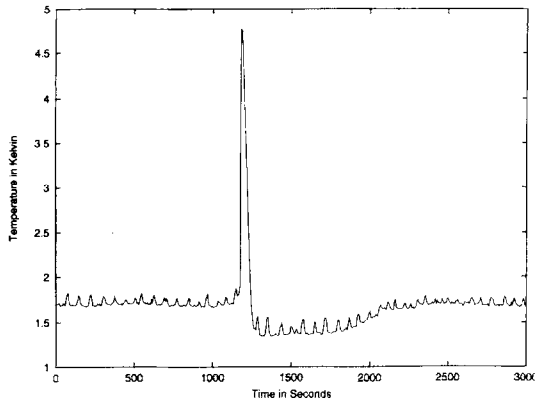


Fig. 4. Time variation of the temperature of the inner cooling shield during a quench.

Previous simulations with a computer program [7] showed that the maximum temperature of the coil after a quench would rise to approximately 70 K. However, the measured temperature was much lower, since the program did not take into account the heat capacity of the copper shield. We measured a temperature increase of 5–6 K only. Fig. 4 shows the temperature rise after a quench. The low inductance of the coil (168 mH) leads to a short characteristic decay time of the current of the order of some milliseconds. Thus there is no necessity for a special quench detection system. This allows fast operation and easy handling of the magnet. After a large number of stimulated quenches, no training behaviour of the coil as a function of the current was observed. The magnet has proved to be very reliable during a long term run at $(I/I_c) \approx 0.95$.

5. Field measurement

To verify the computed magnetic field distribution, the field in the target area and outside of the refrigerator was measured. The outer fringe field was determined with a hall magnetometer. The field in the refrigerator at the target area was achieved by means of the standard nuclear magnetic resonance (NMR)-technique, deriving an absorption signal proportional to the nucleon polarization at the nuclear Larmor frequency.

A schematic layout of the NMR system is shown in Fig. 5. The target material with a volume of 6.5 cm^3 was surrounded by an induction coil which covered the total length of the target. It was placed inside a cylindrical microwave cavity of 90 cm^3 volume. The NMR coil was connected to a Q -meter by a $\lambda/2$ cable. The polarization of the target nucleons was measured using a phase sensitive Liverpool-NMR system [8] tuned to the Larmor frequency of the nucleons at a given polarizing field.

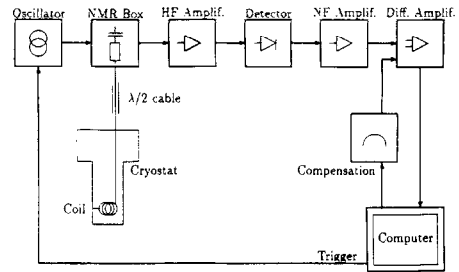


Fig. 5. Schematic layout of the nuclear magnetic resonance (NMR) system to detect the polarization of the deuteron spin system.

Using the 7 T magnet we dynamically polarized a target sample of D-butanol ($\text{C}_4\text{D}_9(\text{OD})$) at a polarizing field of 3.564 T corresponding to a NMR-frequency of 23.1 MHz. After polarizing the sample we increased the current in the holding coil in small steps up to 2 A, superimposing both fields. The shift of the NMR-frequency of the peaks related to the deuteron signal are used to calculate the field produced in the holding coil via the equation:

$$B = \nu \frac{2\pi\hbar}{\gamma}, \quad (3)$$

B is the field in T, ν the frequency in Hz and the constant \hbar/γ is given by the magnetic moment and the g -factor of the deuteron. In Fig. 6 both the signal at the polarizing field of 3.564 T and the shifted NMR signal with the additional field are shown. The error on the frequency shift is $\pm 2 \text{ kHz}$ at an absolute frequency of 23.3 MHz. This calibration results in a maximum field of $B_{\text{max}} = 0.34672 \text{ T}$ at a current of $I_{\text{max}} = 19.7 \text{ A}$, to be compared to a calculated field of 0.35 T at $I = 19.36 \text{ A}$.

In addition we measured the polarization of a proton target material (butanol $\text{C}_4\text{H}_9\text{OH}$) in the "holding coil" at a field of 0.32 T during the frozen spin mode of the target.

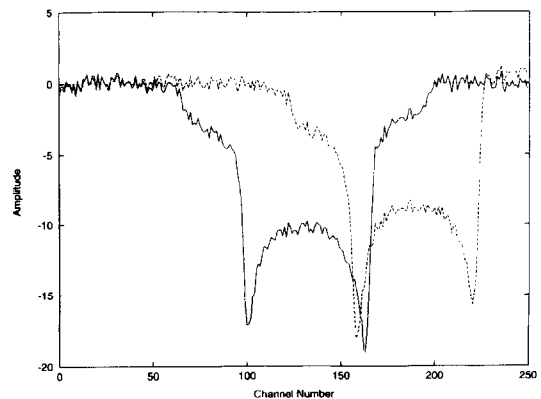


Fig. 6. Deuteron NMR signals at a polarizing field of 3.564 T (solid line) and at the superposition of the polarizing and "holding" field at 3.916 T (dotted line).

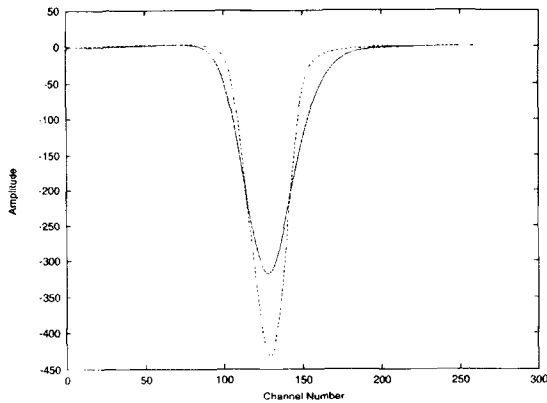


Fig. 7. Proton NMR signals, dotted line: polarization magnet, solid line: "holding magnet" at a field of 0.32 T.

The signal determined in the "holding field" was slightly broadened due to the inhomogeneity of the "holding magnet" compared to the one measured with the polarization magnet at the same field value. In Fig. 7 both signals are shown. The dotted curve was measured in the polarizing magnet at a field of 0.32 T the solid curve represents the polarization at the low field of the "holding coil". Note that the areas of each signal are the same and that therefore the concept of the internal "holding coil" allows the measurement of the polarization in the frozen spin mode, which has hitherto been impossible in operational frozen spin targets, e.g. the Bonn frozen spin target [9].

6. Conclusions

With the technique of an internal superconducting "holding coil" the use of frozen spin targets will be extended. Especially scattering experiments requiring detectors with a large solid angular acceptance can be performed in the future. In combination with the circularly polarized tagged photons measurements of the Gerasimov–Drell–Hearn sum rule [10] can be started now [11]. During initial tests in the Bonn frozen spin target the technique has proved to be very reliable. A magnetic field of 0.35 T has been achieved by operating the superconducting coil in a safe range of 95% of the critical parameters. The required low temperatures of about 1.4 K are available in dilution refrigerators and the additional heat

load can be compensated by a slight increase of the helium consumption of the system. The detector components are influenced only slightly due to the small dimensions of the magnet: at a distance of 20 cm axial and radial from the center of the coil the field diminishes to a value of about 10 G. The compact size of the magnet leads to a very homogeneous central field. This allows for the first time to measure the polarization of the nucleons during the frozen spin mode of the target with the standard NMR-technique. As a next step, an internal "holding coil" providing a "vertical" holding field of 0.4 T for the Bonn frozen spin target is planned. This coil will be wound in a split pair configuration on the inner cooling shield of the refrigerator. It will replace the outer superconducting "vertical holding coil" used in pion photoproduction experiments. The technique of the internal superconducting coils turns out to be a cheap and convenient alternative to existing external outer superconducting "holding magnets" and features improvements concerning the in-situ monitoring of the polarization and the field influence on the detector components.

Acknowledgement

We gratefully acknowledge Mr. H. Peschel who has done excellent work on the manufacture of the coil and of the dilution refrigerator. This work was supported by the BMFT.

References

- [1] T.O. Niinikoski and F. Udo, Nucl. Instr. and Meth. 134 (1976) 219.
- [2] H. Dutz et al., Nucl. Instr. and Meth. A 340 (1994) 272.
- [3] H. Dutz, Ph.D. Thesis BONN-IR-93-49 (1993).
- [4] M.W. Garret, J. Appl. Phys. 34(9) (1963) 2567.
- [5] R.M. Gehring, Diploma Thesis BONN-IR-93-35 (1993).
- [6] P. Schmüser et al., CERN Accelerator School (1988) 87.
- [7] C. Lesmond, private communication.
- [8] G. Reicherz, Ph.D. Thesis BONN-IR-94-16 (1994).
- [9] D. Krämer, Ph.D. Thesis BONN-IR-93-48 (1993).
- [10] S.B. Gerasimov, Yad. Fiz. 2 (1965) 598; Sov. J. Nucl. Phys. 2 (1966) 430; S.D. Drell and A.C. Hearn, Phys. Rev. Lett. 16 (1966) 908.
- [11] J. Ahrends et al., Proposal to the PAC MAMI Mainz (1992); G. Anton et al., Proposal to the PAC ELSA Bonn (1992).



ELSEVIER

Solid HD polarized target: conceptual design of transport and in-beam cryostat[☆]

M. Rigney^{a,*}, M. Breuer^a, S. Buhler^a, C. Commeaux^a, J.-P. Didelez^a,
P. Hoffman-Rothe^a, A. Honig^b, A. Sandorfi^c, C. Schaerf^c, R. Skowron^a, N. Vellard^a,
S. Whisnant^d

^a Institut de Physiques Nucléaire, 91406 Orsay, France

^b Syracuse University, Physics Dept., Syracuse, NY 13210-4441, USA

^c Università de Roma Tor Vergata and INFN Sezione di Roma 2, Rome, Italy

^d University of South Carolina, Physics Dept., Columbia, SC 29208, USA

^e Brookhaven National Laboratory, Upton, NY 11973, USA

Abstract

A description of a cold transport/retrieval Dewar for the removal and insertion of a polarized solid HD target is given. The procedure for removing such a target from the production dilution refrigerator, storing the target for long periods of time until needed, inserting it into the in-beam cryostat, and finally disengaging it will be discussed. This apparatus considerably reduces the complexity of the in-beam cryostat at both the LEGS and GRAAL Compton Laser Backscattering facilities, where the new HD polarized target will have its first use.

1. Introduction

More than 25 years ago, it was first suggested that solid HD could be used as a polarized target [1]. Since then, many of the technical problems have been solved enabling highly polarized hydrogen and deuterium frozen spin targets to be realized for investigations in intermediate energy electro- and photonuclear physics.

The solid hydrogen and deuterium targets presented here have many interesting properties. For example, it is possible to polarize either the H or the D, or both. Furthermore, the spin orientations are independent and thus the polarization directions of H and D can be independently reversed. All of the “free” protons in solid HD are polarized and these represent half of all protons, while all the deuterons (and thus all the neutrons) are polarized. Furthermore, these targets have other applications and physical properties, which are discussed in another paper in these proceedings [2].

Equilibrium proton vector polarizations with the proposed setup ($B = 17$ T, $T < 15$ mK) exceeds 80% and could reach higher than 95% with present technology. Measured deuteron polarizations of 38% have been achieved [3], and deuteron polarizations above 60% are

expected. The deuteron final polarization is not obtained by equilibrium polarization, which would give only about 20% with the proposed setup, but instead is obtained by polarization transfer from the hydrogen using a forbidden-transition adiabatic fast passage technique [4].

The spin–lattice relaxation time for pure HD is essentially infinite. Although this long relaxation time is useful for carrying out nuclear physics scattering experiments, it also implies that polarization production time is exceedingly long. However, by condensing the HD gas molecules with small concentrations ($\approx 10^{-4}$) of the $J = 1$ species of ortho- H_2 and para- D_2 , the H and D spins in HD are coupled to the lattice via these $J = 1$ impurities. This decreases the initial relaxation time to the order of a day, and permits one to obtain the equilibrium polarization of the H and D in the HD molecule in a reasonable time. These $J = 1$ impurities at low temperatures (< 4.2 K) convert to the magnetically inert para- H_2 and ortho- D_2 ($J = 0$ species) with time constants of 6.5 days and 18.2 days, respectively. Therefore, by aging the targets at low temperatures and at high fields for the order of a month, the relaxation times increase sufficiently for use as a practical target as the $J = 1$ dopants convert to the $J = 0$ state. Once polarized, these solid targets retain their polarization at a temperature of 1.5 K with a field of 0.4 T for the order of a week. This polarization retention time increases rapidly with increasing magnetic field.

[☆] Supported in part by HC&M, Brussels and the NSF, USA.

* Corresponding author.

2. Cold transfer / retrieval tube

The target production apparatus consists of a fairly large power dilution refrigerator ($6 \mu\text{W}$ at 10 mK) as well as an extended length (320 mm) 17 T superconducting magnet. This apparatus, if situated within the beam, would place large constraints on the detector system surrounding the target, such as the minimal distance between the detectors and the target. Also, the amount of non-target material within the beam, as well as in the path of recoil particles, is harder to minimize with such an apparatus. Finally, the manipulations necessary to insert and remove the polarizing and holding magnets also increase the complexity of the detector system and corresponding support structures. In order to eliminate the complexity of the in-beam cryostat due to the reasons mentioned above, an attempt is being made to decouple the target production apparatus and the in-beam usage apparatus. This mandates the use of a cold-transport Dewar that is able to engage the target from the dilution refrigerator, transport to the in-beam cryostat, and finally disengage the target into the in-beam cryostat, while maintaining a temperature below 4.2 K and a modest field of greater than 0.02 T . The cold transfer system described here is based on Syracuse University systems invented for inertial confinement fusion experiments with polarized D [5].

The intended operation of the cold transfer/retrieval cryostat is the transfer to and from a dilution refrigerator equipped with a 17 T , large bore magnet, a storage cryostat which operates with an 8 T magnet, and the in-beam cryostat that has a holding magnet of a few tenths of a tesla. The dilution refrigerator is the polarization production apparatus. Once the target is fully polarized and aged it can be transferred to the storage cryostat. The storage cryostat is used for keeping the fully polarized target for periods of up to a year, since the spin-lattice relaxation times exceed one year at the storage cryostat conditions of 8 T and 1.5 K . Once the target is needed for experiments, it is transferred to the in-beam cryostat for use with the intended photon beam.

This cold transfer cryostat, shown in Fig. 1, consists of concentric stainless steel tubes containing liquid nitrogen (LN_2) and liquid helium (LHe), separated by vacuum. For purposes of description, the lower part of the cold transfer

and retrieval tube is considered to be at the position of the sample holder which is the case during all operations with the tube except when placing it within the beam cryostat. In this case the transfer system is horizontal and necessitates the use of asymmetric liquid nitrogen and helium reservoirs. The lowest portion of the system consists of a vacuum lock assembly. The sample, approximately 1.5 mol of solid HD (cylinder with diameter 25 mm and length of 60 mm) is cocooned by the two radiation insulating shrouds, the outer one thermally grounded to the liquid nitrogen reservoir, while the inner one is in thermal contact with the liquid helium reservoir. The outer-most stainless steel can of the cryostat consists mainly of three separate sections of exterior bellows that permit contractions of 850 , 1200 , and 740 mm respectively. The first contraction consists of sliding both the LN_2 and LHe tubes together through the vacuum lock assembly while the lower bellows is correspondingly compressed.

The 77 K radiation shield consists of two reservoirs of liquid nitrogen. The lower one permits the liquid nitrogen to flow between two concentric tubes down to the level of the target where the nitrogen shroud is attached. This lower LN_2 reservoir is asymmetric to maintain the liquid within the tubes down to the shroud even during engagements within the in-beam cryostat. Between the upper and lower LN_2 reservoirs are telescoping concentric 77 K radiation shields that are thermally linked to both of these LN_2 reservoirs. These telescoping tubes, along with the middle outer bellows permit the displacement of the entire LHe Dewar and the lower portion of the LN_2 Dewar by 1200 mm .

The liquid helium Dewar also consists of two concentric stainless steel tubes with an asymmetric reservoir (also for horizontal use) at the top. The LHe may be within the tubes all the way down to the level of the He radiation shroud. The innermost target positioning rod is made of pure copper on the lower part where it is in thermal contact with the liquid helium, while the upper stainless part is thermally decoupled from the LHe by use of a small vacuum space between the rod and the LHe stainless steel tubes. This positioning rod has both a translational degree of freedom, as well as a rotational degree of freedom with respect to the rest of the transfer system. The former degree of freedom of 740 mm enables the telescoping of

Transfert cryostat - Schematic view



Fig. 1. The completely "closed" cold transport/retrieval cryostat showing the position of the target within the small coil and the two radiation shrouds. The three displacement lengths correspond to the contracting lengths of the three sets of bellows at these positions.

Transfert Cryostat Target introduction position

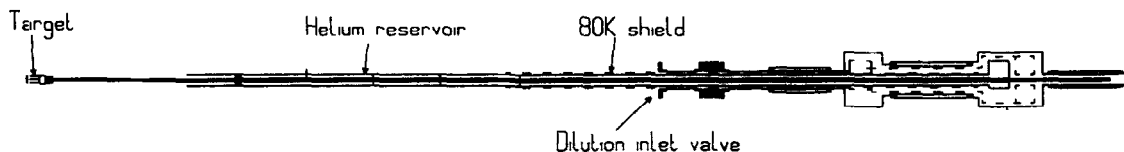


Fig. 2. The completely “open” cold transport/retrieval cryostat. In this position the target would be at the engaging/disengaging position of either the dilution refrigerator, the storage cryostat, or the in-beam cryostat and the target positioning rod would then be continually turned in one direction making use of the left-hand and right-hand screw system.

the rod within the LN₂ and LHe tubes in order to position the target holder. The rotational degree of freedom permits the engaging/disengaging of the target in the various apparatuses using a left-hand and right-hand screw system. The completely telescoped retrieval tube is shown in Fig. 2

3. The in-beam cryostat

The in-beam cryostat is used to maintain the polarized target in the center of a 4π detector, while liberating the space for the passage of the beam. Fig. 3 shows an example of this cryostat with two concentric liquid nitrogen and liquid helium Dewars. The liquid helium part can be a prolonged cylinder around the target in order to support an internal superconducting coil used to supply a magnetic field of the order of 0.4 T. It is here advantageous to reduce the temperature of the target within the beam cryostat in order to increase the relaxation time further. This is simply accomplished by pumping on the liquid helium bath to reduce the temperature to about 1.5 K. Further reduction would require the use of a closed cycle ³He cryostat. Additional small coils necessary to

measure the polarization of the target by crossed coil NMR while within the beam are not shown in Fig. 3.

The intended first nuclear physics uses of this polarized target are to measure spin observables in photonuclear reactions. The LEGS Compton Laser Backscattering facility at the Brookhaven National Laboratory is a unique photon beam with the intrinsic property of having 100% polarization at the maximum energy of the Compton edge, 471 MeV. A new detector system based on large blocks of NaI detectors, wire chambers, and a forward angle shower counter is being installed on the LEGS beam line in order to measure the helicity-dependent photo-reaction amplitudes for both the proton and the neutron from pion-threshold to 470 MeV. [6]. In this detector system, ample space exists to place two pairs of modified Helmholtz coils between the target and the NaI detectors. One pair is used as a longitudinal holding coil and the second pair as a transverse holding coil. Both pairs would produce a magnetic field of the order of 1 T at the target and would also aid in identifying the charge of the outgoing particles.

Similarly, at the ESRF in Grenoble, France, the GRAAL Compton Laser Backscattering facility is being installed [7]. Due to the higher electron energy of the storage ring,

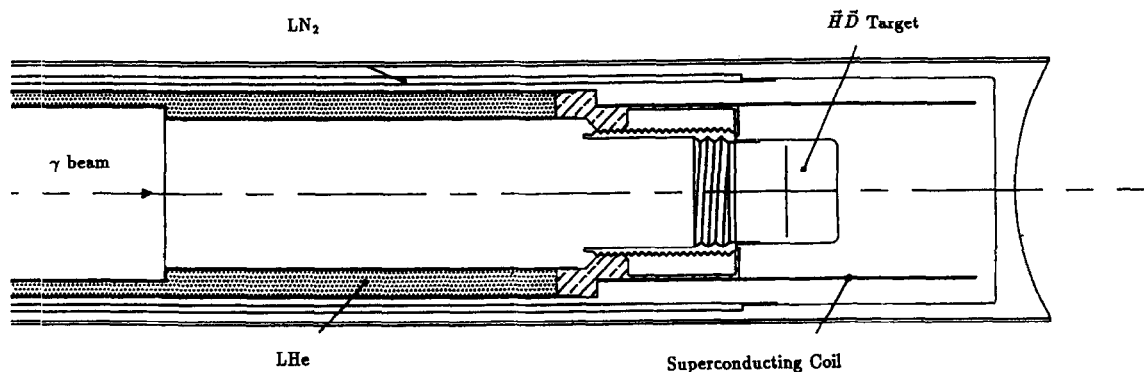


Fig. 3. A cross sectional view of the in-beam cryostat. Surrounding the target and thermally linked to the liquid He bath is the internal superconducting holding coil.

this photon beam will produce an energy of 1.5 GeV at the Compton edge, also with 100% photon beam polarization. The GRAAL detector system is also of the 4π type consisting of a large array of BGO crystals, wire chambers, as well as a forward detector system. However, unlike the LEGS detector system, space constraints preclude the use of external holding coils. Work has been done on the internal superconducting holding coil by the polarized target group at Bonn [8].

Acknowledgements

The authors would like to express their appreciation for many enlightening talks with the senior graduate students Q. Fan and X. Wei of Syracuse University.

References

- [1] A. Honig, Phys. Rev. Lett. 19 (1967) 1009.
- [2] A. Honig, these Proceedings (7th Workshop on Polarized Target Materials and Techniques, Bad Honnef, Germany, 1994) Nucl. Instr. and Meth. A 356 (1995) 39.
- [3] A. Honig, N. Alexander, Q. Fan, X. Wei and Y.Y. Yu, Workshop on Polarized Ion Sources and Polarized Gas Targets, Madison, WI, 1993, AIP Conf. Proc. 293 (1993) 50.
- [4] A. Honig and H. Mano, Phys. Rev. B 14 (1976) 1858.
- [5] N. Alexander, J. Barden, Q. Fan and A. Honig, Rev. Sci. Instr. 62 (1991) 2729.
- [6] The LEGS Spin Collaboration, Measurements of the Spin Structure of the Nucleon, BNL internal report.
- [7] J.P. Bocquet et al., Proc. 13th Int. Conf. on Particles and Nuclei Perugia, Italy, 28 June–2 July 1993, p. 835.
- [8] R. Gehring, presented at this Workshop; see also R. Gehring, Diplomarbeit, Bonn-IR-93-53 (1993) unpublished.



ELSEVIER

The TRIPLE spin filter

P.P.J. Delheij ^{a,*}, J.D. Bowman ^b, C.M. Frankle ^b, D.G. Haase ^c, T. Langston ^b,
R. Mortensen ^b, S. Penttila ^b, H. Postma ^d, S.J. Seestrom ^b, Yi-Fen Yen ^b

^a *Triumf, University of British Columbia, 4004 Wesbrook Mall, Vancouver, BC, V6T 2A3, Canada*

^b *LANL, Los Alamos, USA*

^c *North Carolina State University, USA*

^d *University of Technology Delft, Delft, Netherlands*

Abstract

A new dynamically polarized proton target at LANL polarizes an epithermal neutron beam in the energy range from 0.1 eV to 50 keV. In a ⁴He bath at a temperature of 1.1 K, irradiation doped ammonia is polarized longitudinally in a magnetic field of 5 T. The sample has a diameter of 80 mm and is 13 mm thick. The typical proton polarization is 0.85 giving a neutron polarization of 0.75. With the polarized neutron beam parity violation has been studied in many samples with a high degree of sensitivity.

A new longitudinally-polarized proton-spin filter has been installed on the beam line 2 of the high-intensity spallation source at the Los Alamos Neutron Scattering center (LANSCE). The filter produces a polarized neutron beam in the energy range from 0.1 eV to 50 keV on a 60-m long flight path. Parity violation (PV) effects have been measured in transmission and capture experiments. The following samples were studied: ²³⁸U, ²³²Th, ¹³⁹La, ¹²⁷I, ^{113,115}In, ¹¹³Cd, ^{107,109}Ag and ⁹³Nb.

With polarized protons a neutron beam can be polarized because the singlet scattering dominates the cross section [1]. At present, the most efficient filtering material for this process is ammonia. It has a high proton polarization when dynamically polarized at 1 K and 5 T. It has also a high free proton density and unpolarized nuclei have a small contribution to the cross section. The paramagnetic polarizing centers are introduced by electron irradiation at 30 MeV. When the sample is cooled to a temperature of 1.1 K in a magnetic field of 5 T (the homogeneity on the beam line over the target volume is 1.4×10^{-4}), a microwave power of 2 W at a frequency of 140 GHz polarizes the sample in about 40 min. The filter has a diameter of 80 mm and a thickness of 13 mm.

The proton polarization is measured with a constant current, series resonant cw-NMR setup. During the experiments the NMR measurements typically gave a proton

polarization of 0.85. The proton polarization can also be derived from the neutron transmission through the ammonia sample. The beam intensity increases from I_{unpol} to

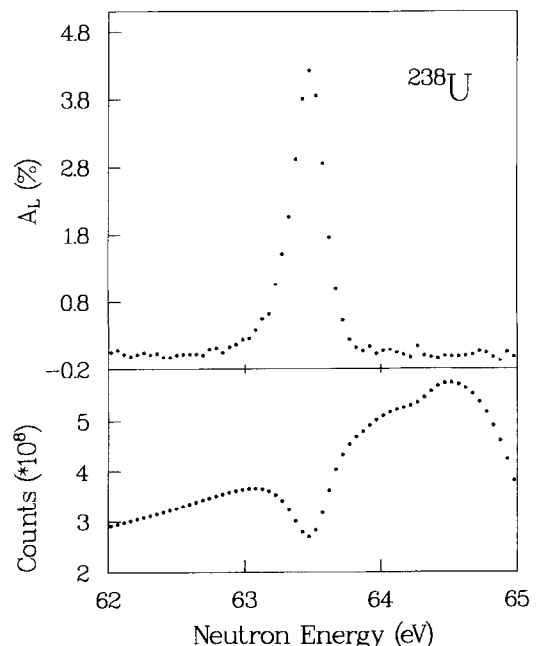


Fig. 1. The transmitted neutron intensity is shown in the lower part near the p-wave resonance at 63 eV in ²³⁸U. In the upper part the longitudinal analysing power is plotted.

* Corresponding author.

I_{pol} when the free protons become polarized,

$$I_{\text{pol}}/I_{\text{unpol}} = \cosh(P_p n \sigma_{\text{pol}} t),$$

where P_p is the proton polarization, n is the proton density, $\sigma_{\text{pol}} = 16.7$ b [1] is the polarization cross section and $t = 0.8$ cm is the effective sample thickness. Then, the neutron beam polarization P_n is obtained with P_p from

$$P_n = \tanh(P_p n \sigma_{\text{pol}} t) = \sqrt{1 - (I_{\text{unpol}}/I_{\text{pol}})^2}.$$

The third method to determine the neutron polarization is based on the well-known PV analysing power of the 0.7-eV p-wave resonance in ^{139}La . This analysing power was determined absolutely in a symmetric experiment where the polarizer and analyser were identical samples separated by a spin flipper to reverse the neutron polarization [2]. The result for the neutron polarization from these

measurements was 0.70. The three methods for determining the neutron beam polarization have completely different systematic errors. The agreement between the three results is very good.

An example of the PV asymmetry is shown in Fig. 1 for the neutron resonance in ^{238}U at 63 eV. The statistical significance of the PV effect is 135 standard deviations. From data on resonances in ^{238}U and ^{232}Th the mean PV matrix elements are derived near the 4p peak of the p-wave strength function.

References

- [1] V.I. Lushchikov, Yu.V. Taran and F.L. Shapiro, *Yad. Fiz.* 10 (1969) 1178.
- [2] V.W. Yuan et al., *Phys. Rev. C* 44 (1991) 2187.



ELSEVIER

Polarized targets as dark matter detectors

Y.K. Semertzidis ^{c,*}, G. Baum ^a, P. Berglund ^f, S. Bültmann ^a, C.M. Dulya ^b, P. Hautle ^e,
N. Hayashi ^h, S. Ishimoto ^h, A. Kishi ^f, Y. Kisselev ^g, D. Krämer ^a, J. Kyynäräinen ^c,
J.-M. Le Goff ^d, A. Magnon ^d, T. Niinikoski ^c

^a Universität Bielefeld, Fakultät für Physik, D-33615 Bielefeld, Germany

^b University of California, Department of Physics, Los Angeles, 90024 CA, USA

^c CERN, PPE Division, CH-1211 Genève 23, Switzerland

^d DAPNIA, C.E. Saclay, 91191 Gif-sur-Yvette, France

^e ETH, 8093 Zürich, Switzerland

^f Helsinki University of Technology, Low Temperature Laboratory, Otakaari 3A, 02150 Finland

^g JINR, Laboratory of Super High Energy, Dubna, Russian Federation

^h Nagoya University, Department of Physics, Furo-Cho, Chikusa-Ku, 464 Nagoya, Japan

Abstract

The strong electron paramagnetic resonance (EPR) of polarized targets can be used to search for axions as dark matter candidates in the range of (1–100) GHz. Once the axions are absorbed they can provide the communications gate for spin thermal contact between different nuclei that were kept artificially at different temperatures.

The axions appeared first as a solution to the strong CP problem, the fact that the QCD Lagrangian was violating the charge parity (CP) symmetry whereas the experimental limit for the electric dipole of the neutron did not support it. Peccei and Quinn [1] first introduced a symmetry (named after them) and Weinberg and Wilczek [2] showed that from the breakdown of this symmetry appears a particle, the axion.

The microlensing events reported by EROS, MACHO, and OGLE [3] stimulated a lot of discussion as to whether different kinds of cold dark matter (CDM) are worth seeking for in our galaxy. Gates and Turner [4] claim that microlensing is not a sensitive probe for local dark matter (LDM) and that the best motivated CDM candidates are the axion with a mass around 10^{-5} eV and neutralinos (a superposition of photino, zino and two higgsinos) with mass between 10 GeV and 1 TeV.

There are several experiments which searched for axions that couple to two photons as LDM as well as making attempts for a direct production in a limited mass region [5–9]. The coupling constant versus mass exclusion regions from them are given in Fig. 1 (from Ref. [7]) where some astrophysical bounds are also given.

Axions can also couple directly to fermions and to the spin of the electrons [10–14] a feature we will try to exploit in this paper. Polarized target materials contain a

large amount of paramagnetic centers [15] which help in the nucleon polarization buildup. Those centers are essentially semi-free electron spins which exhibit strong EPR lines in high magnetic fields and low enough temperatures. The axions are pseudoscalars (0^-) and behave effectively very similarly to M1 photons; they can induce an electron spin flip when their mass coincides with the EPR frequency. Their de Broglie wavelength is (10–100) m and their kinetic energy very small (since they are bosons their energy can all be in the same energy state) making their energy fractional width Γ_a very small ($Q_a = m_a/\Gamma_a = 10^6$). In order to provide the closure of the universe their local density must be around $\rho_a = 0.3$ GeV/cm³.

The axion absorption rate can be inferred from Eq. (12) of Ref. [14] and is:

$$N_a = (4/q^2) \rho_a V (m_e g_e / F)^2 Q_f \chi_0 u_{\perp}^2, \quad (1)$$

where q is the electron charge, $V = 2340$ cm³ the volume of the polarized target, m_e the electron mass, g_e model dependent dimensionless constant of order one, Q_f the quality factor of the EPR resonance (which here we will assume to be limited by the magnetic field inhomogeneity i.e. about 10^4), χ_0 the static susceptibility, $u_{\perp}^2 = 10^{-6} c^2$ the axion velocity orthogonal to the direction of the electron spins (which is equal to the virial velocity of the galaxy), and F the breaking scale of the Peccei–Quinn symmetry, and related to the axion mass by:

$$m_a = 6 \times 10^{-6} \text{ eV} (10^{12} \text{ GeV} / F). \quad (2)$$

* Corresponding author.

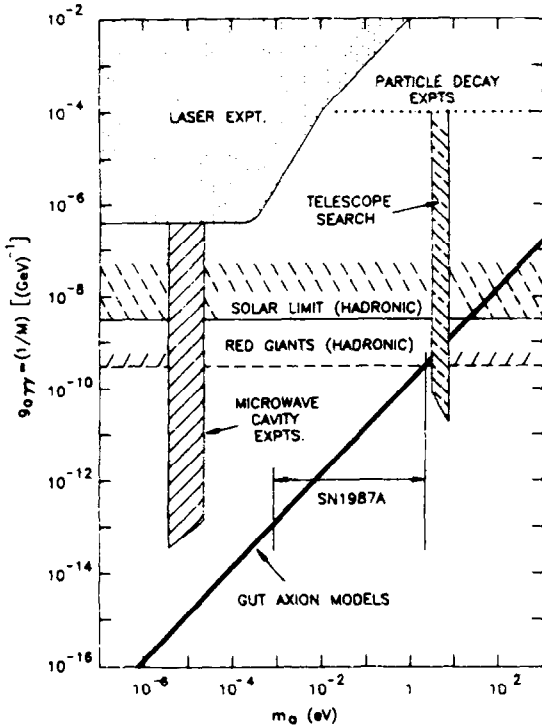


Fig. 1. Axion coupling to two photons versus axion mass limits from past experiments and star models. Axions with mass in the ($5 \times 10^{-6} - 5 \times 10^{-4}$) eV range are excellent candidates for LDM.

We can now calculate the axion absorption rate at say $B = 2.5$ T and $T = 50$ mK which are routinely attainable during the physics run of the spin muon collaboration (SMC) [16]. First we need to calculate χ_0 :

$$\chi_0 = \mu_0 \frac{N \hbar^2 \gamma^2 I(I+1)}{3kT} \approx 10^{-2}, \quad (3)$$

where $\mu_0 = 4\pi \times 10^{-7}$ Vs/Am, $N = 7 \times 10^{25}$ spins/m³ the electron spin density, $\gamma = 2\pi f/B$ with f the EPR frequency, I the electron spin, and k the Boltzmann's constant. From Eq. (1) we have that $N_a \approx 0.35 \times 10^{-2}$ axions/s. The estimated background at 50 mK from the thermal photons of the copper microwave cavity (emissivity $\approx 10^{-3}$), surrounding the polarized target, is less than 10^{-4} photons/s with frequency which peaks around 1 GHz and therefore is totally negligible. In reality the polarized target is kept at 50 mK whereas the cavity is at 3 K with vacuum between the two systems. However, in principle, the cavity temperature can be kept very close to that of the target.

Since axions behave like microwave photons we can calibrate the system by turning on the microwaves in the polarized target and setting their frequency to be close to the EPR line. In our polarized target there are different nuclear species that are not in thermal contact when the microwaves are off. However, when the microwaves are switched on, the various spin species establish thermal contacts and tend towards the same final spin temperature. Last year this prospect motivated the work on the cross relaxation between protons and ¹³C-nuclei [17] where we had saturated the ¹³C polarization by RF and observed the polarization buildup with and without microwaves. There is certainly an enhancement of the thermal spin contact with the microwaves present. This year the material is deuterated [15] with the contents of the protons being much more than that of the ¹³C, and the proton signal being much stronger, we might assume that we can observe 1 nJ of microwave energy. Assuming a total run of 10^6 s for scanning the EPR frequency between 1–70 GHz by moving the magnetic field, the experiment could approach the solar limit shown in Fig. 1.

References

- [1] R.D. Peccei and H.R. Quinn, Phys. Rev. Lett. 38 (1977) 1440; Phys. Rev. D 16 (1977) 1791.
- [2] S. Weinberg, Phys. Rev. Lett. 40 (1978) 223; F. Wilczek, Phys. Rev. Lett. 40 (1978) 279.
- [3] E. Aubourg et al., Nature 365 (1993) 623; C. Alcock et al., Nature 365 (1993) 621; A. Udalski et al., Acta Astron. 43 (1993) 289.
- [4] E. Gates and M.S. Turner, Phys. Rev. Lett. 72 (1994) 2520.
- [5] W. Wuensch et al., Phys. Rev. D 40 (1989) 3153.
- [6] Y. Semertzidis et al., Phys. Rev. Lett. 64 (1990) 2988.
- [7] R. Cameron et al., Phys. Rev. D 47 (1993) 3707.
- [8] C. Hagmann et al., Phys. Rev. D 42 (1990) 1297.
- [9] M.A. Bershadsky et al., Phys. Rev. Lett. 66 (1991) 1398.
- [10] F.T. Avignone III et al., Phys. Rev. D 35 (1987) 2752.
- [11] G.G. Raffelt and D.S.P. Dearborn, Phys. Rev. D 36 (1987) 2211.
- [12] F. Caspers and Y. Semertzidis, CERN report CERN/PS 89-40 (1989).
- [13] P.V. Vorobyev et al., Particle World 1 (1990) 163.
- [14] R. Barbieri et al., Phys. Lett. B 226 (1989) 357.
- [15] S. Bültmann et al., these Proceedings (7th Workshop on Polarized Target Materials and Techniques, Bad Honnef, Germany, 1994) Nucl. Instr. and Meth. A 356 (1995) 102.
- [16] D. Adams et al., Phys. Lett. B 329 (1994) 399.
- [17] S. Bültmann et al., Ref. [15], p. 106.



ELSEVIER

Proton- and deuteron spin targets in biological structure research

H.B. Stuhmann^{a,*}, N. Burkhardt^b, G. Dietrich^b, R. Jünemann^b, W. Meerwinck^a,
M. Schmitt^a, J. Wadzack^b, R. Willumeit^a, J. Zhao^a, K.H. Nierhaus^b

^a GKSS Forschungszentrum, D-21502 Geesthacht, Germany

^b MPI für Molekulare Genetik, D-14195 Berlin, Germany

Abstract

Polarized neutron scattering from polarized nuclear spin targets has been used to study the in situ structure of ribosomal components in solutions. The progress of this technique is substantiated by first results obtained from protonated tRNA and mRNA labels in a deuterated ribosome. The site of the tRNA could be determined uniquely, whereas there are several orientations of the [tRNA]₂-mRNA complex which are compatible with the neutron scattering data. Similarly, a small, protonated mRNA fragment was studied. Its size favours a complicated path of the mRNA chain through the ribosome. The role of deuteron spin targets is discussed.

1. Introduction

Polarized targets were used in structure research for the first time at the Institute Laue–Langevin (ILL) [1]. The target material was a single crystal of lanthanum magnesium nitrate ($\text{La}_2\text{Mg}_3(\text{NO}_3)_{12} \cdot 24\text{H}_2\text{O}$) doped with $^{142}\text{Nd}^{3+}$. The proton spins of the crystal water were dynamically polarized [2] and studied by polarized neutron diffraction [1]. The intensity of the diffracted neutrons not unexpectedly turned out to be most sensitive to the structure and polarization of the hydrogens of the crystal water [3]. It was concluded that the use of nuclear polarization as a method of labeling protons in a complicated unit cell might have advantages for determining the proton structure, e.g. the proton configuration around the active site in an enzyme [3]. Although this method did not find a continuation at the ILL, it must be regarded as a highlight in neutron physics of the seventies which initiated further experiments of polarized neutron scattering by polarized targets elsewhere in the mid-eighties.

The renaissance of this technique was due to a new class of polarized target materials in high energy scattering experiments. Using a dilution refrigerator ($T < 0.5$ K) and a 2.5 T magnetic field proton spin polarizations up to 98% were obtained in Cr(V) doped alcohols, like butanol or 1,2 propanediol) [4,5]. Contrary to the crystalline LMN, these target materials were frozen liquids and, moreover, well-

known solvents in cryobiochemistry [6]. It is therefore not surprising that the proton spins in frozen solutions of macromolecules were polarized and studied by polarized neutron small-angle scattering. In 1986, first results from contrast variation of protonated particles in deuterated solvents by proton spin polarization were obtained at the GKSS Research Centre, Geesthacht in collaboration with CERN, Geneva [7]. In 1987, frozen solutions of protonated crown ethers were studied at KENS, Tsukuba [8]. Proton spin polarization dependent neutron small-angle scattering from block copolymers has been started at the Orphée reactor, Saclay [9].

The impact for the construction of the polarized target facility at GKSS came from molecular biology, more precisely from the structural studies on ribosomes. Ribosomes are the site of protein biosynthesis in each living cell. The fairly compact structure of this organelle ($M = 2.3 \times 10^6$ dalton) called 70S ribosome may dissociate into two unequal subunits, called 50S and 30S subunit, respectively. Each of these subunits consists of ribonucleic acid by $\frac{2}{3}$ of its mass and numerous different proteins. There are 21 proteins (S1 to S21) of the small subunit and 33 proteins (L1 to L36, where L7 = N-acetylated L12, L8 = (L7/L2)₄ and L26 = S20) of the large subunit in the case of ribosomes from E.coli bacteria. Most important for the purpose of specific isotopic substitution of ^1H (= H) by ^2H (= D) is the controlled dissociation of the ribosome into its 3 ribosomal RNAs (rRNA) and 54 different proteins and their recombination to a functional complex capable of protein synthesis in vitro [10,11]. During protein synthesis the ribosome is bound to a messenger RNA (mRNA) which provides the genetic information for the sequence of

* Corresponding author.

the amino acid chain. The transfer RNAs (tRNAs) solve the logistic problem of making the required amino acid available for incorporation into the nascent peptide chain. There are always two tRNAs bound in the functional elongation complex of the ribosome [12].

Although various steps of the binding process of an amino acid to the nascent protein chain can be defined, the underlying structural mechanism is less known. Attempts are made to correlate the stereochemistry of the tRNA–mRNA interaction with constraints imposed by the ribosomal topography [13]. So far, neither electron microscopy nor diffraction methods could single out the correct model among the conflicting ones. Considering the complexity of the ribosomal structure the analysis of a selected region of the structure as it is provided by neutron scattering from specific deuterated substances can be helpful. Polarized neutron scattering from nuclear spin polarized targets is introduced as an ultimate choice of a powerful, non destructive labelling method. This paper will present first results of polarized neutron scattering from polarized proton spins of tRNA and mRNA labels in deuterated ribosomes.

2. Materials and methods

2.1. Specific deuteration of the ribosome

Specifically deuterated ribosomes are prepared by reconstitution from appropriately selected protonated and deuterated components [11,14]. The average deuteration of the ribosome reaches about 0.94. The 70S functional complexes containing 1) two protonated tRNA and a protonated mRNA fragment (46 nucleotides), 2) a protonated mRNA fragment in protonated form (tRNAs deuterated), were prepared by specific binding of the respective RNA ligands to fully deuterated, native ribosomes. The length of the mRNA chain is equal to that section of a long mRNA shown to be covered by the ribosome [15]. The mRNA fragments were identical in both samples and the sequence of their nucleotides was arranged in such a way that the ribosome could be fixed in the middle of the mRNA chain by binding tRNA^{Met} to the ribosomal P-site and N-acetyl-Phe-tRNA^{Phe} to the ribosomal A-site. At this point the ribosomes are in the pretranslocational state. In a further step of the elongation cycle (during translocation) the deacylated tRNA^{Met} moves from the P-site to the E-site and the N-acetylated Phe-tRNA^{Phe} (peptidyl-tRNA-analog) moves from the A-site to the P-site [12]. The functional complex then is in the posttranslocational state. Samples (1) and (2) were prepared in the pretranslocational and in the posttranslocational state. The respective functional state of each sample was confirmed and quantified by the relative puromycin sensitivity of the bound N-acetyl Phe-tRNA^{Phe} [12]. This paper presents data from the functional complex in the pretranslocational state.

2.2. Polarized target material

The target material is a dilute solution of ribosomes. It is prepared as follows: 0.5 ml of the aqueous ribosome solution (2 wt.%) is dialyzed against a buffer (100 mM imidazol C₃H₄N₂, 10 mM MgCl₂, 100 mM KCl in D₂O). 13 mg of sodium bis(2-ethyl-2-hydroxybutyrate)-oxochromate(V) monohydrate, Na[Cr(C₆H₁₀O₃)₂O] · H₂O, were dissolved in 0.15 ml D₂O. This radical is synthesized from dry sodium dichromate and 2-ethyl-2-hydroxybutyric acid (EHBA) in acetone [16] 60 mg of the concentrated solution of KCl (1.6 M) and MgCl₂ (0.16 M) in D₂O are added to 820 mg deuterated glycerol, C₃D₈O₃ (98.6% D). The average deuteration of the solvent is 0.97.

The components are mixed in the following way. The ribosome solution in the deuterated buffer is added to the deuterated glycerol and stirred for 5 min. Then the concentrated solution of EHBA–Cr(V) is rapidly diluted in the ribosome solution and frozen immediately in a liquid nitrogen cooled copper mold, as the EHBA–Cr(V) decomposes at pH 7 with a half-time of about 10 min. Therefore the time between the addition of EHBA–Cr(V) to the ribosome solution and freezing of the sample is kept short, typically to less than 1 min.

2.3. Polarization of the target material

The frozen sample (3 × 17 × 17 mm³) was introduced into the cavity of the dilution refrigerator [17,18]. Dynamic nuclear spin polarization (DNP) was obtained in a magnetic field of 2.5 T by applying microwave power into the multimode cavity. The microwave frequency was 69.0 GHz for positive and 69.3 GHz for negative polarization. The proton spin polarization was determined by comparing the enhanced nuclear magnetic resonance (NMR) signal with the thermal equilibrium signal. The deuteron spin polarization was calculated from the asymmetry of the resonance profile [18].

All non-spinless nuclei are affected by DNP. In the target material described above only the nuclear spins of the hydrogen isotopes ¹H and ²H need to be considered. Pure proton spin targets were obtained by selective depolarization of the deuteron spins [18]. The selective depolarization of the proton spin system yielded a pure deuteron spin target. At temperatures below 150 mK the relaxation time of the polarized targets is of the order of several weeks. Thus, the nuclear spin polarization is almost constant during a two days neutron scattering experiment. In a run of one week, the same sample was studied as a proton target, as a deuteron target and as a dynamic polarized target without selective nuclear spin depolarization.

2.4. Polarized neutron small-angle scattering

The experiments were done at the small-angle scattering instrument SANS1 at the research reactor FRG1 of

GKSS [18]. Polarized neutrons as obtained by total reflection from magnetized surfaces [19] were monochromatized by a mechanical velocity selector [20]. The wavelength distribution centred at 8.5 Å had a fwh of 0.1. The range of momentum transfer from 0.009 to 0.28 Å⁻¹ was large enough to observe both the characteristic dimensions of the ribosome with its average diameter of 250 Å and those of its labels which are an order of magnitude smaller. The polarization direction of the neutron beam was changed after each measurement of 1000 s by a flat coil spin flipper [21]. The scattering intensity was recorded by an area counter [22].

2.5. Data reduction and analysis

The aim of data reduction is to separate coherent neutron scattering from incoherent scattering and to analyse the coherent scattering in terms of the basic scattering functions. The analysis of the basic scattering functions provides information about the spatial correlation between the scatterers and eventually these correlations will yield a three-dimensional model.

Hydrogenous substances give rise to strong, mainly incoherent neutron scattering intensity, the spin dependence of which is exploited by polarized proton spin filters for neutron spin polarization [23]. The cross section of incoherent scattering is much lower for the heavier isotope of hydrogen. For structural studies, incoherent scattering is minimized by massive deuteration. This explains the isotopic composition of the polarized target material. Incoherent scattering is eliminated by subtraction of a constant level of background scattering which is assumed to be dominant at large transfer Q [24].

For a particle consisting of M nuclei (N out of them are non-spinless) one defines

$$U(\mathbf{Q}) = \sum_{j=1}^M b_j e^{i\mathbf{Q} \cdot \mathbf{r}_j},$$

$$V(\mathbf{Q}) = \sum_{j=1}^N P_j I_j B_j e^{i\mathbf{Q} \cdot \mathbf{r}_j} = P_H V_H(\mathbf{Q}) + P_D V_D(\mathbf{Q}),$$
(1)

where $U(\mathbf{Q})$ is the amplitude of the unpolarized sample and $V(\mathbf{Q})$ the increase of the amplitude due to nuclear polarization P . \mathbf{r}_j is the position of the nucleus j with the spin I_j and the scattering lengths b_j and B_j . The indices H and D refer to the proton spin target and deuteron spin target respectively. According to Abragam and Goldman [25] the intensity of coherent polarized neutron scattering is

$$S(\mathbf{Q}) = |U(\mathbf{Q})|^2 + 2p \operatorname{Re}[U(\mathbf{Q})V^*(\mathbf{Q})] + |V(\mathbf{Q})|^2,$$
(2)

where p denotes the neutron spin polarization. A dilute solution of identical particles gives rise to small-angle

scattering which can be described in a way analogous to Eq. (2). Averaging Eq. (2) with respect to the solid angle yields the intensity $I(Q)$

$$I(Q) = 2\pi^2 \sum_{j=0}^{\infty} \sum_{m=-1}^{+1} |U_{lm}(Q)|^2 + 2p \operatorname{Re}[U_{lm}(Q)V_{lm}^*(Q)] + |V_{lm}(Q)|^2,$$
(3)

where a multipole expansion of the amplitude has been used. For $U_{lm}(Q)$ for instance, we have

$$U_{lm}(Q) = \sqrt{\frac{2}{\pi}} i^l \sum_{j=1}^M b_j j_l(Qr_j) Y_{lm}^*(\theta_j, \phi_j),$$
(4)

where $Q = |\mathbf{Q}| = 4\pi/\lambda \sin \theta$. j_l is the spherical Bessel function of l th order and the Y_{lm} are the spherical harmonics. The site of the j th nucleus is given by its radial distance r_j and the polar angles θ_j and ϕ_j . For dilute solutions of identical particles, $I(Q)$ is proportional to the scattering from one particle. This equation is quite handy for the calculation of scattering profiles from complex particles.

There are many features common to Eqs. (2) and (3). They contain three functions differing in their dependence on nuclear and neutron spin polarization. When there is no nuclear polarization only $|U(\mathbf{Q})|^2$ is observed. Nuclear spin polarization adds $|V(\mathbf{Q})|^2$, even if unpolarized neutrons are used [8,9]. With polarized neutrons the cross term $2 \operatorname{Re}[U(\mathbf{Q})V^*(\mathbf{Q})]$ is observed from polarized samples. The basic scattering functions mentioned above are obtained from measurements of neutron scattering using different polarizations of both the neutron beam and the target nuclei.

The analysis of the data starts from a model which consists of two parts,

- the low resolution model of the ribosome known from electron microscopy [26] and
- the label, the in situ structure of which needs to be determined.

As the number of structural parameters which can be derived from small-angle scattering of randomly oriented particles is limited to the order of 10 the information obtainable will include hardly more than the location and orientation of the label with respect to the ribosome. The amplitude of the ribosome $M(\mathbf{Q})$ and of the label $L(\mathbf{Q})$ are developed as a series of harmonics. Both are normalized to the volume of their structures at $Q=0$. After multiplication of M and L with the contrast c (or k for the spin dependent part) the amplitudes U and V are obtained in units of a scattering length

$$U(\mathbf{Q}) = c_M M(\mathbf{Q}) + c_L L(\mathbf{Q}),$$

$$V(\mathbf{Q}) = k_M M(\mathbf{Q}) + k_L L(\mathbf{Q}).$$
(5)

As the volume of the ribosome is two orders of magnitude larger than that of the label the amplitude of the ribosome will dominate. The intensity of $|V|^2$ would be

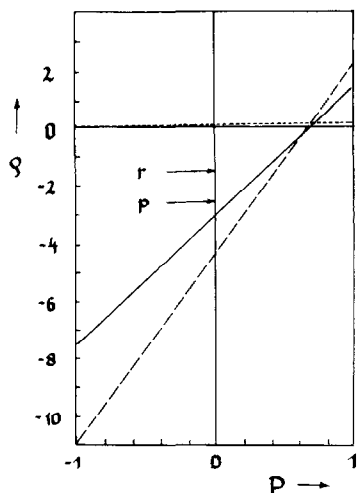


Fig. 1. Polarization dependent contrast ρ of protonated labels and of the deuterated ribosome in a mixture of deuterated glycerol and in heavy water as described in the text, full line: protonated tRNA, dashed line: protonated proteins, dotted line: deuterated ribosome (mean deuteration = 0.94). For comparison the contrast of proteins (p) and tRNA (r) in a $\text{H}_2\text{O}/\text{D}_2\text{O}$ mixture containing 92% D_2O is shown. The scattering density of this solvent matches that of appropriately deuterated rRNA and ribosomal proteins [11,14].

lower to that of $|U|^2$ by 4 orders of magnitude and hence escape to the observation by neutron scattering. The choice of deuterated ribosomes in a deuterated glycerol/water mixture avoids this situation as the contrast c_M of the

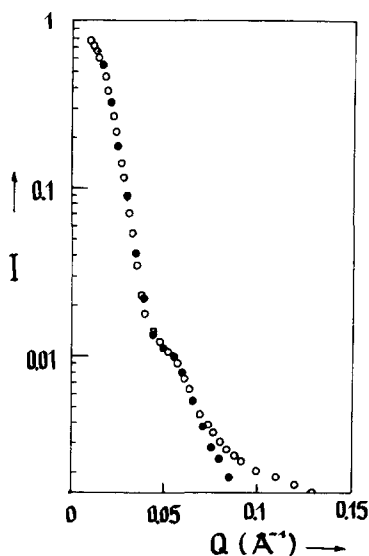


Fig. 2. Comparison of neutron small-angle scattering of the frozen solution of protonated ribosomes in a deuterated solvent (O) with the shape scattering function derived from neutron scattering in $\text{H}_2\text{O}/\text{D}_2\text{O}$ mixtures at room temperature (●). The shoulder in the intensity profile is present in both samples.

ribosome with respect to the solvent and the polarization dependent contrast k_M turn out to be very small (Fig. 1). The contrasts c_M and k_M are determined from polarized neutron small-angle scattering of the deuterated, unlabelled ribosome [27].

The contrast c_L of the protonated label in the unpolarized state and its polarization added contrast k_L are calculated from the chemical composition using the spin dependence of the scattering lengths of the hydrogen isotopes:

$$b_H = (-0.374 + 1.456pP_H)10^{-12} \text{ cm},$$

$$b_D = (+0.667 + 0.27pP_D)10^{-12} \text{ cm}. \quad (6)$$

The spin dependent contrast of the protonated labels and the deuterated rRNA is shown in Fig. 1. The polarization added contrast exceeds considerably the contrast of the label in the unpolarized state. We also note that the contrast of a protonated label in a mixture of deuterated glycerol and heavy water (1/1) is higher than it is in heavy water.

3. Results and discussion

3.1. The unlabelled, protonated ribosome

Polarized neutron scattering was measured from the frozen spin target of protonated ribosomes in mixture of deuterated glycerol and heavy water. The basic scattering functions obtained from the proton spin target are very similar, except for the sign. The similarity is due to the fact that the ratio between the contrast of rRNA and that of the ribosomal proteins in the unpolarized state is rather close to the corresponding value of the polarization added contrasts. (Fig. 1). The negative sign of the cross term $2 \text{Re}[UV_H^*]$ tells us that the sign of U is different from that of V_H . As the proton concentration of the solute is much higher than that of the solvent the proton spin polarization added contrast (or proton spin contrast) is positive and so is $V_H(0)$. Hence, $U(0)$ must be negative, as is easily seen from Eq. (6).

The profile of neutron scattering from the frozen target shown in Fig. 2 is in good agreement with data obtained at room temperature [28]. The radius of gyration of this particle is $R = 95 \text{ \AA}$.

A positive cross term $2 \text{Re}[UV_D^*]$ is observed when the deuterium spin target is studied by polarized neutron scattering (Fig. 3). As the amplitude U is negative, the polarization added amplitude V_D must be negative as well. This is expected as the density of deuterons inside the volume of the ribosome is much smaller than in the solvent. The deuterium spin contrast of the protonated ribosome in the deuterated solvent is negative. It remains negative even in highly deuterated ribosomes as the density of deuterons in nucleic acids and proteins is lower than that in deuterated solvents.

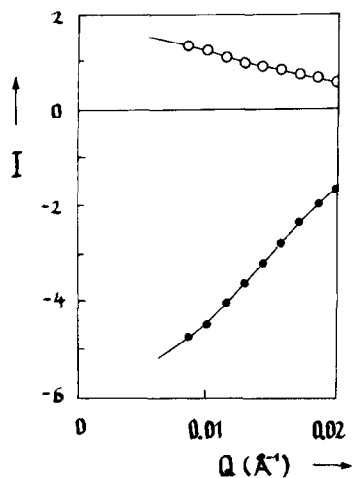


Fig. 3. The cross terms $2\text{Re}[UV]$ of the proton spin target ($-\bullet-$) and the deuteron spin target ($-\circ-$) of protonated ribosomes in a deuterated solvent. The intensity is given in units of 10^5 neutrons/1000 s/pixel. Pixel size of the area detector: 9×9 mm², irradiated sample area: 15×15 mm², collimation length: 2 m. Neutron scattering intensities taken at other collimation lengths of the small-angle instrument are merged with the data taken at 2 m collimation. The background scattering at $Q = 0.2 \text{ \AA}^{-1}$ amounts to about 1 n/s/pixel.

Both the ribosomal proteins and the rRNA contain only a small amount of deuterons. Their deuteron spin contrasts are nearly equal, i.e. the amplitude V_D is close to that of the shape of the ribosome, whereas the contrast of proteins contributing to U is higher than that of rRNA. The radius of gyration deduced from the cross term of neutron scattering from the deuteron spin target is 91 \AA .

Shape scattering of the ribosome could be obtained from $|V_D|^2$ of the deuteron target. Due to the low values of deuteron spin polarization ($|P_D| < 0.3$) and that of the deuteron spin contrast the accuracy of this basic scattering function is so poor that it does not allow any detailed analysis.

We note in passing that a relatively uniform contrast of the ribosomal particle is achieved when the deuterated ribosome is dissolved in a protonated solvent. The radius of gyration of the shape of the frozen ribosomal particle is 89 \AA .

3.2. Protonated ribosomal RNA in a deuterated ribosome

A strong internal contrast is created by deuterating all the ribosomal proteins and leaving rRNA protonated. The radius of gyration as derived from a Guinier plot ($\ln(I(Q))$ versus Q^2) drops to $R = 81 \text{ \AA}$. As the contrast is mainly due to the protonated part of the ribosome, it is concluded that the rRNA is preferably occupying the core of the particle. This is in agreement with earlier experiments of neutron scattering in $\text{H}_2\text{O}/\text{D}_2\text{O}$ mixtures [28]. The radii

of gyration observed at room temperature are slightly smaller than those of the rRNA in the frozen sample (Fig. 4). This may be due to small amounts of the dissociation products of the ribosome, which may be different in both samples. As the change of the radius of gyration with the contrast is the same in both samples it may be assumed that the internal structure of the ribosome is hardly changed, when being frozen in a glycerol–water mixture.

3.3. Protonated tRNAs and mRNA in a deuterated ribosome

The protonated complex of two tRNAs ($M = 2 \times 28000$) and mRNA ($M = 15000$) in the deuterated ribosome gives rise to a contribution to neutron scattering shown in Fig. 5, which is small compared to that of protonated proteins in the large subunit of the ribosome (Stuhmann 1993). There are two reasons for this:

- 1) The contrast of RNA in a deuterated solvent is lower by a factor 1.5 due to the lower hydrogen concentration (Fig. 1). The same holds for the proton spin polarization added contrast.
- 2) The occupation density of the ribosomal binding sites by tRNAs does not exceed 40%.

This results in a decrease of the scattering intensity from the tRNA/mRNA label by an order of magnitude with respect to protonated protein labels in ribosomal subunits (Fig. 5). Nevertheless, polarized neutron scattering from the proton spin target of the functional complex labelled in its two tRNAs and the mRNA fragment clearly revealed the basic scattering functions of proton spin contrast variation shown in Fig. 6.

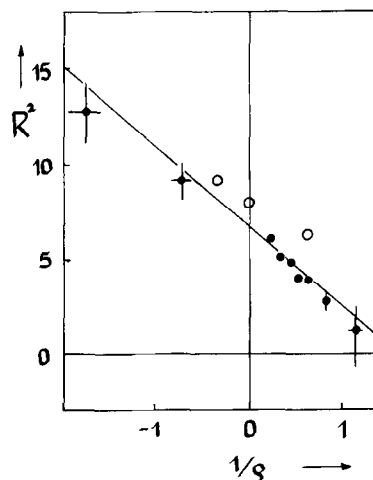


Fig. 4. The square of the radius of gyration R^2 of the 70S ribosome in units of 10^3 \AA^2 versus the reciprocal value of the contrast $1/\rho$ in units of 10^{10} cm^2 . (\bullet) data obtained in $\text{H}_2\text{O}/\text{D}_2\text{O}$ mixtures at room temperature, (\circ) data from frozen solutions of ribosomes in a mixture of glycerol and heavy water.

In a first step the center of mass of the $(\text{tRNA})_2\text{-mRNA}$ complex was determined. The model of the complex is that of a sphere. Its radius of gyration of 33 \AA has been determined from the neutron scattering data. The coordinates of the center of mass of the protonated label were varied stepwise all over the volume and the near neighbourhood of the ribosome particle and the root mean square deviation Δ of the calculated basic scattering functions from those determined by the experiment was calculated. The lowest Δ is achieved at the interface between the ribosomal subunits (Fig. 7). There is another not so deep minimum of Δ which is also located at the interface. The variation of Δ with the distance r along the line connecting the position of the minimum of Δ with the origin of the ribosome is shown in Fig. 8. The distance between the centre of the label and the origin of the ribosome is close to 50 \AA .

In a further step we try to determine the orientation the tRNAs with respect to the ribosome. To achieve this task two facts are helpful: 1) the structure of tRNA is known to atomic resolution [29], and 2) the extremes of the structure of tRNA must be rather close to each other (Fig. 9). There

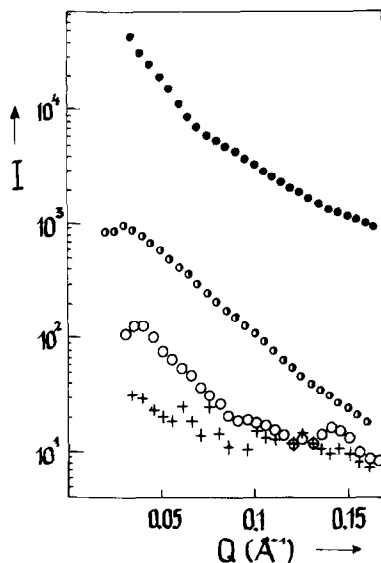


Fig. 5. Neutron spin polarization dependent scattering intensity, $I = -2 \text{ Re}[UV^*]$, from proton spin polarized ribosome samples. Various protonated labels have been introduced into the deuterated ribosome: full circle: protonated ribosomal RNA ($\frac{2}{3}$ of the ribosomal volume is labelled), half-full circle: protonated L3-protein (0.02 of the volume of the large subunit is labelled), open circle: protonated complex of two tRNAs and a mRNA fragment (0.03 of the ribosome volume is labeled, only 40% of the particles contain the complex), full line: protonated mRNA fragment (0.006 of the ribosome volume is labelled, only 40% of the particles contain the complex, tRNAs being deuterated). The positive values of the cross terms of the tRNA and mRNA labelled samples at low Q have been omitted.

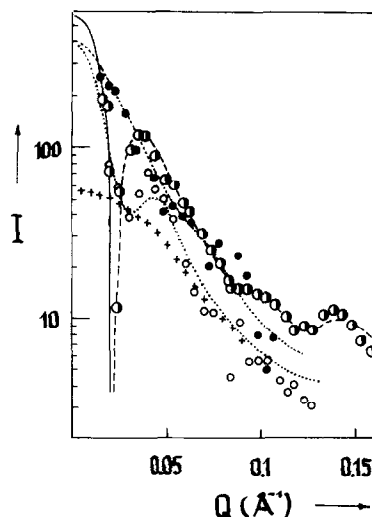


Fig. 6. The basic scattering functions of the deuterated functional complex of the ribosome with protonated tRNAs and protonated mRNA fragment. open circle, dotted line: $|U|^2$, half-full circle, full line: $2 \text{ Re}[UV^*]$ positive, half-full circle, broken line $2 \text{ Re}[UV^*]$ negative, full circle, dotted line: $|V|^2$. The full, dotted and broken lines are calculated values from the model of the functional complex. The crosses represent the scattering from the tRNAs in $|U|^2$ in the absence of any neutron scattering from the ribosome. The intensity scale of neutron scattering is the same as Fig. 3.

is also an estimation of the angle between the planes of the tRNAs, which is supposed to be close to 90° [30].

At low resolution the structure of the L-shaped tRNA will be described by four points (Fig. 9). There is no significant difference between the scattering curve of the full set of about 1600 atoms of tRNA and that of the 4 spheres at $Q > 0.2 \text{ \AA}^{-1}$. The mRNA fragment (20% of the mass of the $(\text{tRNA})_2\text{-mRNA}$ complex) has been omitted. The orientation of the tRNA-complex is varied over the whole range of the Eulerian angles while the center of the label is kept at $(r = 60 \text{ \AA}, \theta = 2.35, \phi = -0.92)$ of Frank's model. The reason for the slightly increased radial distance r is due to the different structure factor of the label. The values of Δ vary between 4.18 and 4.8. Considering Δ values not greater than 4.3 six different orientations are compatible with the neutron scattering data. Two of them are favoured in the biochemical literature [13] (Fig. 10). The anticodons (as in Fig. 10) of the tRNAs are close to the neck of the small ribosomal subunit, whereas these two models suggest different sites of the aminoacyl group (aa in Fig. 10). The two orientations of the complex to some extent resemble the R- and S-configurations respectively [13]. If this were true, then it would be difficult to distinguish between the R- and the S-state of the functional complex of the ribosome on the basis of neutron scattering alone. A detailed discussion of this point will be given elsewhere.

3.4. Protonated mRNA in a deuterated ribosome

Polarized neutron scattering the deuterated functional complex of the ribosome with two deuterated tRNAs and a protonated mRNA fragment ($M = 15\,000$, or 0.6% of the

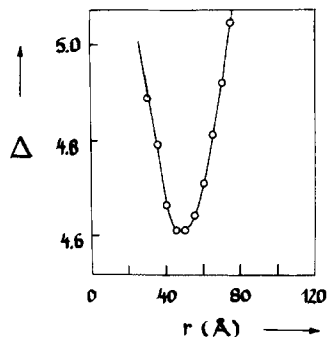
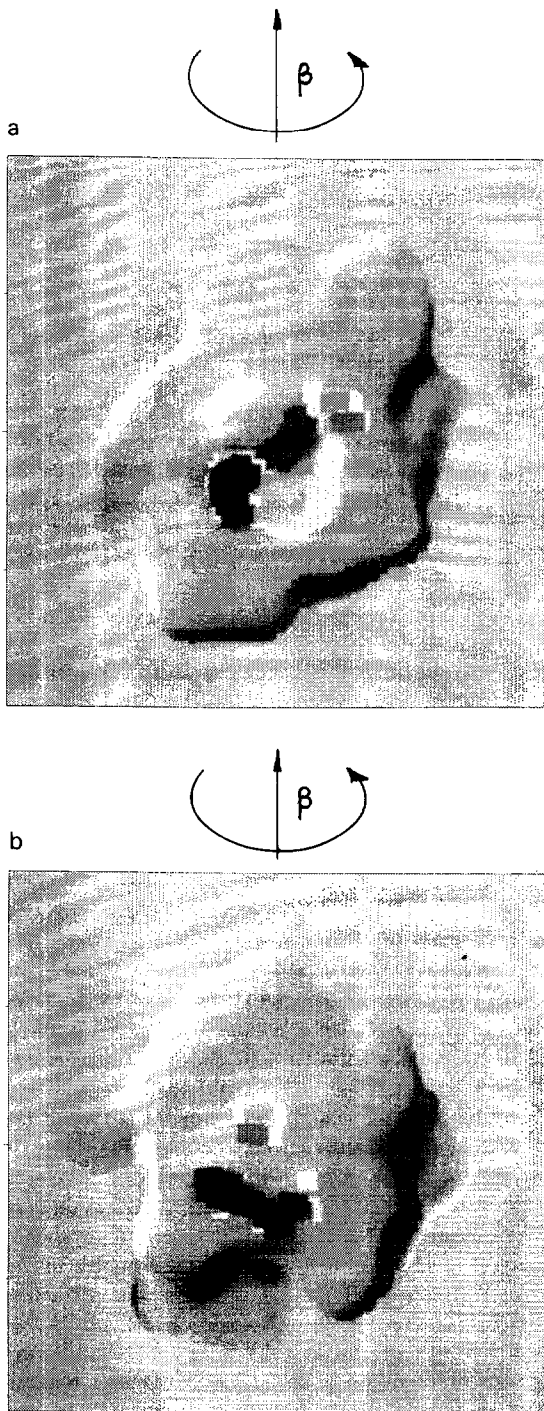


Fig. 8. The deviation Δ as defined in the text along the line connecting the position of the minimum of Δ with the origin of the ribosome.

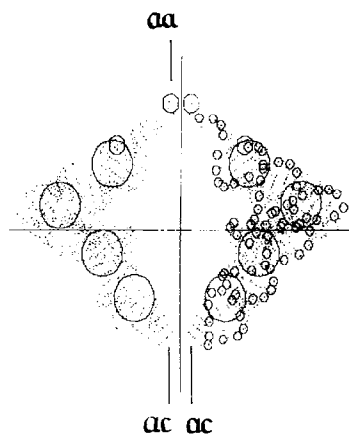


Fig. 9. The anticodons (ac) of the two tRNAs and the aminoacyl group (aa) of the tRNA at the extremes of the structure must be rather close as the former bind to adjacent codons on the mRNA and the latter is near the peptidyltransferase center of the ribosome. The planar mutual orientation of the two tRNAs shown in the figure folds to an almost orthogonal orientation. Points denote atoms, small circles in one of the tRNAs represent phosphorus atoms, medium circles denote the ends of the chain molecules. The large circles present a low resolution description of the tRNAs by 8 spheres.

Fig. 7. The deviation Δ of the calculated basic scattering functions scattering of the model from the basic scattering functions determined by polarized neutron scattering. Only the lowest Δ are shown: dark squares indicating the minimum of Δ are concentrated at the large hole between the two ribosomal subunits. The ribosome model has been obtained by electron microscopy [26]. Two orthogonal views of the ribosome are presented. (a) Frank's model is rotated by the Eulerian angles $\alpha = 0$, $\beta = 2.30$, $\gamma = 0$ in order to show the open interface between the two subunits more clearly. The lower part is the small ribosomal subunit. (b) The model is rotated by $\beta = 0.8$.

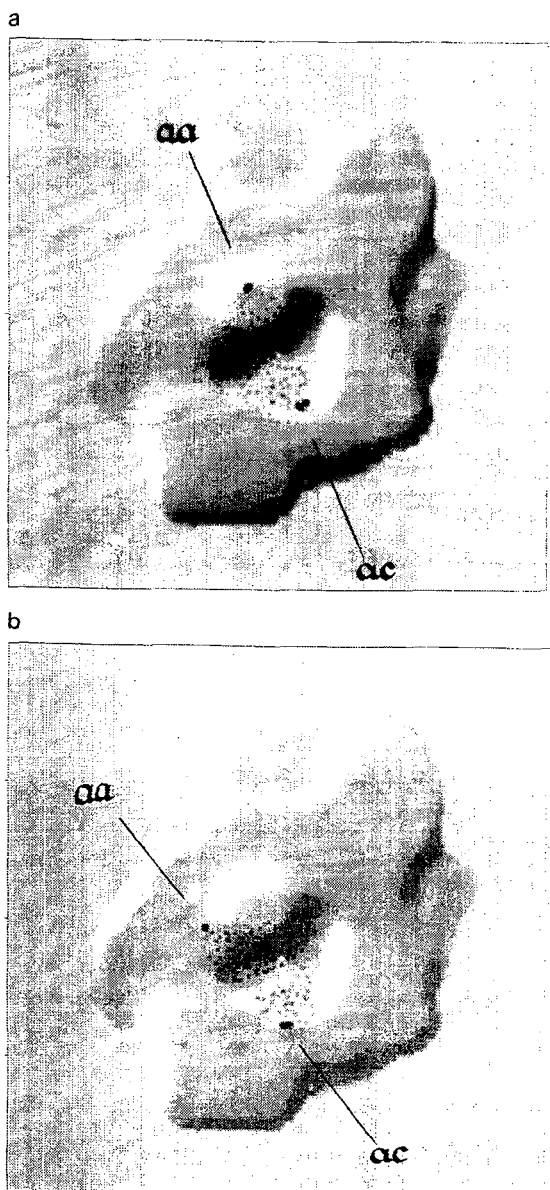


Fig. 10. Two out of the six orientations of the tRNAs with respect to the ribosome which are compatible with the basic scattering functions of the proton spin target. The anticodons (ac) are close to the neck of the small ribosomal subunit in both models. The models (a) and (b) differ in the position of the aminoacyl group (aa) of the tRNA. View across the interface (as in Fig. 7a).

ribosome mass) has been measured for 8 weeks. We discuss data which were taken in a period of two weeks. The crossterm $2 \text{Re}[UV^*]$ of proton spin contrast variation is shown in Fig. 5. The analysis of the basic scattering functions yields a radius of gyration $R = (15 \pm 2) \text{ \AA}$. This preliminary value excludes an extended conformation of the mRNA chain.

4. Conclusions

Polarized neutron scattering from polarized nuclear spin targets of biological origin extends the possibilities of the methods of isotopic substitution widely used macromolecular structure research. The increase in contrast by proton spin polarization is very helpful in those cases where the relatively low hydrogen content (like in tRNA) and the relative small size (like that of mRNA) exclude the use of conventional methods of neutron scattering.

The method of nuclear spin contrast variation is a nondestructive labelling method. Using good glass formers as a solvent (like mixtures of glycerol and water, with a glycerol content above 0.5) and rapid freezing is a good way to preserve the properties of biomolecules. Performance of neutron scattering at temperatures below 1 K and storing the samples in liquid nitrogen minimizes the damage to the sensitive biological material.

Hence, neutron scattering data can be accumulated over a long period of time in order to increase their accuracy. The results from neutron scattering of a small label like protonated mRNA would greatly improve at a more powerful neutron source. The latter is also a necessary prerequisite for polarized neutron diffraction from polarized nuclei in protein crystals.

Acknowledgements

It is evident that the construction and running of the complicated instrument needed the co-operation of many people. We thank everyone who contributed to this project. We wish to enumerate some of them: T. Niinikoski, A. Rijllart, M. Rieubland and Ch. Pollicella from CERN helped us to install a polarized target station of CERN at the reactor of the GKSS Research Centre. The dilution refrigerator has been modified at CERN to meet the requirements of neutron scattering. The neutron spin polarizer is that of O. Schärpf from the institut Laue–Langevin, Grenoble. The small-angle instrument with its area detector was constructed at the technical workshop of GKSS. The skill of W. Müller and M. Marmotti is traceable in more recently built parts of the system. The project has been supported in its initial stage by the Bundesministerium für Forschung und Technologie.

References

- [1] J.B. Hayter, G.T. Jenkin and J.W. White, *Phys. Rev. Lett.* 33 (1974) 696.
- [2] A. Abragam and M. Goldman, *Rep. Prog. Phys.* 41 (1978) 395.
- [3] M. Leslie, G.T. Jenkin, J.B. Hayter, J.W. White, S. Cox and G. Warner, *Phil. Trans. R. Soc. London B* 290 (1980) 497.
- [4] A. Masaike, H. Glättli, J. Ezratty and A. Malinovski, *Phys. Lett. A* 30 (1969) 63.

- [5] W. de Boer and T.O. Niinikoski, Nucl. Instr. and Meth. 114 (1973) 495.
- [6] P. Douzou, Cryobiochemistry, An Introduction (Academic Press, London, 1977).
- [7] W. Knop, K.H. Nierhaus, V. Nowotny, T.O. Niinikoski, M. Krumpolc, M. Rieubland, A. Rijllart, O. Schärpf, H.-J. Schink, H.B. Stuhmann and R. Wagner, Helv. Phys. Acta 50 (1986) 741.
- [8] M. Koghi, M. Ishida, Y. Ishikawa, S. Ishimoto, Y. Kanno, A. Masaïke, Y. Masuda and K. Morimoto, J. Phys. Soc. Jpn 56 (1987) 2681.
- [9] H. Glättli, C. Fermon and M. Eisenkremer, J. Phys. (Paris) 50 (1989) 2375.
- [10] J.A. Langer, D.M. Engelman and P.B. Moore, J. Mol. Biol. 119 (1978) 463.
- [11] K.H. Nierhaus, R. Lietzke, R.P. May, V. Nowotny, H. Schulze, K. Simpson, P. Wurmbach and H.B. Stuhmann, Proc. Nat. Acad. Sci. USA 80 (1983) 2889.
- [12] H.J. Rheinberger, U. Geigenmüller, A. Gnirke, T.-P. Hausner, J. Remme, H. Sauyama and K.-H. Nierhaus, in: The Ribosome: Structure, Function and Evolution, eds. W.E. Hill, A. Dahlberg, R.A. Garret, P.B. Moore, D. Schlessinger and J.R. Warner (American Society for Microbiology, Washington D.C., 1990) p. 318.
- [13] V. Lim, C. Venclovas, A. Spirin, R. Brimacombe, P. Mitchell and F. Müller, Nucleic Acids Research 20 (1992) 2627.
- [14] K. Vanatalu, T. Paalme, R. Vilu, N. Burkhardt, R. Jünemann, R. May, M. Rühl, J. Wadzack, K.H. Nierhaus, Eur. J. Biochem. 216 (1993) 315.
- [15] D. Beyer, E. Skripkin, J. Wadzack, K.H. Nierhaus, J. Biol. Chem. (1994), in press.
- [16] M. Krumpolc, B.G. de Boer and J. Rocek, J. Am. Chem. Soc. 100 (1978) 145.
- [17] T.O. Niinikoski and F. Udo, Nucl. Instr. and Meth. 134 (1976) 219.
- [18] J. Zhao, W. Meerwinck, T. Niinikoski, A. Rijllart, M. Schmitt, R. Willumeit and H.B. Stuhmann, submitted to Nucl. Instr. and Meth. (1994).
- [19] O. Schärpf, in: Neutron Spin Echo, ed. F. Mezei, Proc. ILL Workshop, Oct. 15–16, 1979; Lecture Notes in Physics no. 128 (Springer, 1980) p. 27.
- [20] Friedrich H., V. Wagner and P. Wille, Physica B 156 & 157 (1989) 547.
- [21] O. Schärpf, Physica B 174 (1981) 514.
- [22] R. Dose, M. Pauls, H.-J. Tauffenbach and R. Wagner, GKSS Jahresbericht ISSN 0174-4933, (1986) p. 24.
- [23] Y. Masuda, S. Ishimoto, M. Ishida, Y. Ishikawa, M. Koghi and A. Masaïke, Nucl. Instr. and Meth. A 264 (1988) 169.
- [24] J. des Cloizeaux and G. Jannink, Les Polymères en Solution: leur Modélisation et leur Structure, les édition de physique (Les Ulis, 1987) p. 221.
- [25] A. Abragam and M. Goldman, Nuclear Magnetism: Order and Disorder, International Series of Monographs in Physics, edn. J.A. Krumhansl, W. Marshal and D.H. Wilkinson (Clarendon Press, Oxford, 1982).
- [26] J. Frank, P. Penczek, R. Grasucci and S. Srivastava, J. Cell Biology 115 (1991) 597.
- [27] H.B. Stuhmann, Phys. Scripta T 49 (1993) 644.
- [28] H.B. Stuhmann, M.H.J. Koch, J. Haas, K. Ibel and R.R. Crichton, J. Mol. Biol. 119 (1978) 203.
- [29] J. Sussman, S.R. Holbrook, R.W. Warrant, G.M. Church and S.-H. Kim, J. Mol. Biol. 123 (1978) 607.
- [30] A.S. Spirin and V.I. Lim, in: Structure, Function, and Genetics of Ribosomes, eds. B. Hardesty and G. Kramer, Springer Series in Molecular Biology, Series Editor A. Reich (Springer, Heidelberg, 1985) p. 556.



ELSEVIER

The polarized target station at GKSS

J. Zhao ^{a,*}, W. Meerwinck ^a, T. Niinikoski ^b, A. Rijllart ^b, M. Schmitt ^a, R. Willumeit ^a,
H. Stuhmann ^a

^a Institute of material research, GKSS-Research Center, 21052 Geesthacht, FRG

^b CERN, CH-1211, Geneva, Switzerland

Abstract

In cooperation with CERN, a dynamic polarized nuclear target station was built at GKSS-Research Center on SANS-1, aimed at investigation of biomolecule structure. The target consists of a 20 mmol/min dilution refrigerator, which has a basic temperature of 50 mK, a 2.5 T electromagnet, and a carcinotron which delivers the 4 mm microwave at a power up to 5 W. A NMR-system based on the Liverpool *Q*-meter and the CERN 68K-STAC fulfills the task of polarization measurement, and especially selective nuclear depolarization.

1. Introduction

The knowledge of biomolecule structure is inevitable for the understanding of living matter on molecular level. This knowledge of many molecules, however, is still a challenge in the field of molecular biology. There are many ways to acquire this knowledge. Crystallography, electronmicroscopy and NMR-spectroscopy are some excellent examples among all. From the time on when the DNA double helix was revealed crystallography gained firm ground in this field. The electronmicroscopy visualizes the micro-world. The newcomer in this field (though old itself), the NMR-spectroscopy is gaining its importance not only in structure resolving, but also in kinetics.

Yet there are cases in which other methods are needed. An example is the ribosome [1]. It is the place where the genetic codes are translated into proteins. The ribosome has a molecular weight of about 2.6 million and a diameter of 250 Å. Till now there is still no breakthrough in crystallography to determine its structure. The electronmicroscopy delivers mainly its surface structure. For the NMR-spectroscopy, the ribosome is still too big to study. A promising answer here is the small angle neutron scattering (SANS). Using hydrogen/deuterium exchange, SANS has successfully resolved the structure of the small subunit (30S) of ribosome [2]. But for its large subunit (50S) and the ribosome as whole (70S), this method is also hitting its limits. In the later cases, the ribosomal proteins and RNAs are too small compared to the 50S and 70S to be seen by the neutrons with enough resolution. However,

the ability of (not only) SANS can be increased by the new technique spin contrast variation (SCV) which is based on spin dependent neutron scattering. We know that the neutron scattering length can be expressed as spin dependent and spin independent parts:

$$b = b_0 + b_1 \mathbf{I} \cdot \mathbf{s}. \quad (1)$$

\mathbf{I} and \mathbf{s} represent the spins of nuclear and of neutron. A closer look at the scattering amplitude of hydrogen (^1H) ($b_0 = -0.37 \times 10^{-12}$ cm, $b_1 = 5.84 \times 10^{-12}$ cm) which is the richest element in living matter, shows already the potential of this new technique. The effect of spin-dependent scattering of its heavier isotope deuterium (^2H , D) is much less profound ($b_0 = 0.667 \times 10^{-12}$ cm, $b_1 = 0.56 \times 10^{-12}$ cm). The influence from other elements with non-zero spin in biological matters like ^{13}C and ^{14}N is negligible.

The coherent and incoherent neutron scattering amplitude from an assembly of nuclei can be expressed as [3].

$$I_{\text{coh}} = S_0 + P_n P_1 S_{\text{op}} + P_1^2 S_p, \quad (2)$$

$$I_{\text{incoh}} = X_0 - P_n P_1 X_{\text{op}} - P_1^2 X_p. \quad (3)$$

The three terms S_0 , S_p and S_{op} , called basic scattering functions, come from spin-independent, spin-dependent scattering and the interference of these two. P_n , P_1 are neutron and nuclear polarization. By changing P_n and P_1 , the three functions can then be separated. The three terms in I_{incoh} originate actually all from the spin dependent part of the scattering length b_1 . They are written so for comparison.

In order to examine the information content of the basic scattering functions, we take again the ribosome as an example. Biologically one can exchange the hydrogen in the ribosome with its heavier isotope deuterium while

* Corresponding author.

keeping a specified part of ribosome protonated. This protonated part, called a label, can be one or more ribosomal proteins, RNAs or some molecules bounded on the ribosome like the transfer-RNA and messenger-RNA. The structure of the label information is often the point of interest. Assume we have only the protons in the ribosome polarized (a proton target in term of SCV), the meaning of the three basic functions is then obvious: they are the scattering from the ribosome (S_o), from the label (S_p) and the interference of them (S_{op}).

The technical challenges on the spin contrast variation are then the polarization of the neutrons and of the nuclei. The polarization of slow neutrons can be achieved by reflection on magnetized surface. To polarize the nuclei in organic material, the only effective way is the dynamic nuclear polarization.

2. The GKSS-polarized target station

The station is consisted of an electromagnet, a dilution refrigerator and a microwave synthesizer. A NMR system is used to carry out the polarization measurement and the selective depolarization (Fig. 1).

2.1. The magnet

The 2.5 T magnetic field is supplied by an electromagnet. It has a homogeneity of 10^{-4} T cm $^{-1}$ and an opening angle of 21° in the vertical direction for the scattering. The two poles are separated by 62 mm.

2.2. The $^3\text{He}/^4\text{He}$ dilution refrigerator

The dilution refrigerator was originally designed and built at CERN [4] for use in high energy physics. It is a 20

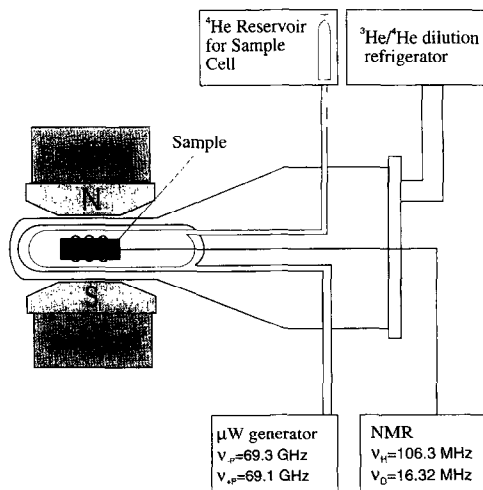


Fig. 1. Schematic overview of the polarized target station at GKSS.

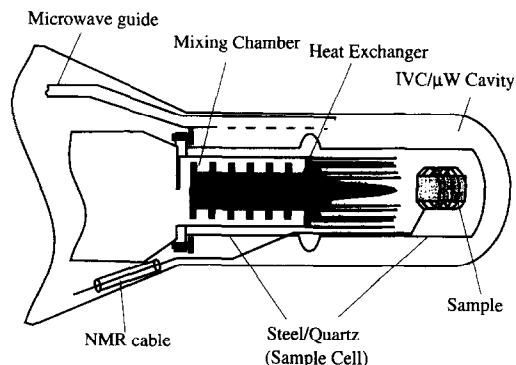


Fig. 2. The sample and heat exchanger.

mmol/min horizontal fast loading cryostat. Its screen and ^3He precooling are pumped by membrane pumps. For the evaporator and ^3He -lines two sets of vacuum- and roots pump system are used. The evaporator level is controlled by a feed back analog circuit and proved to be very stable. The inner vacuum chamber (IVC) is used as microwave cavity. At its normal running conditions the refrigerator consumes about 2 l helium an hour. The loading procedure has been optimized and it takes normally less than four hours to cool down the cryostat to its basic temperature (50 mK) starting from mounting the sample.

To use the cryostat in neutron scattering, a separate sample cell is needed (Fig. 2). ^3He is a strong neutron absorber, therefore we can not put the sample in the mixing chamber. The sample cell is built of 3-mm thick quartz and stainless steel jointed together with a glass-metal transition. It has a diameter of 30 mm and length of about 200 mm. Quartz is chosen here to ensure the microwave to reach the sample. The sample cell is filled with pure ^4He and coupled with the mixing chamber by a special designed heat exchanger (see Fig. 2). The heat exchanger has to have the ability to bring away the heat produced by the microwave while the target is polarizing.

2.3. The microwave generator

A carcinotron is used as microwave generator. Its covers a frequency range from 68 GHz to 72 GHz. The maximal output is about 5 W.

2.4. The NMR system

The continuous wave NMR system is based on the Liverpool Q -meter [5]. A CERN 68K-STAC [6] is used for data acquisition (Fig. 3). The sweep bandwidth is set to 200 kHz centered at 16.42 MHz for deuteron and 106.3 MHz for proton signal. Each sweep step covers 1 kHz and takes 20 μs to settle. 400 double sweeps are averaged for each run.

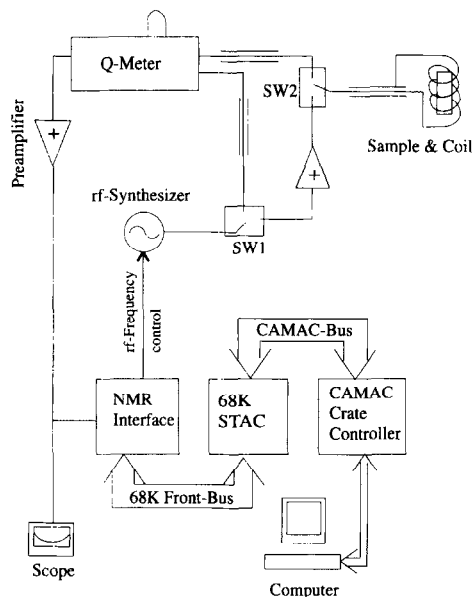


Fig. 3. Block diagram of the NMR system.

Figs. 4 and 5 show a typical proton and deuteron NMR signal of the target material (see next section).

The NMR circuit is used for selective depolarization as well. At frozen spin mode, by saturating the proton or deuteron polarization with a strong rf-signal, we can then get polarized proton or deuteron targets. As we have already discussed at the end of the Introduction, this facilitates greatly the analysis of neutron scattering data and make the spin contrast variation more versatile.

The rf-power is controlled so that the target temperature will not rise too much (normally less than 250 mK). The depolarization takes about 3 min to be carried out.

In order to depolarize all protons in the sample, the sweep area has to be large enough to cover all the protons. Some nuclei, like those in the nearby of a paramagnetic center, have a magnetic field around them which differs

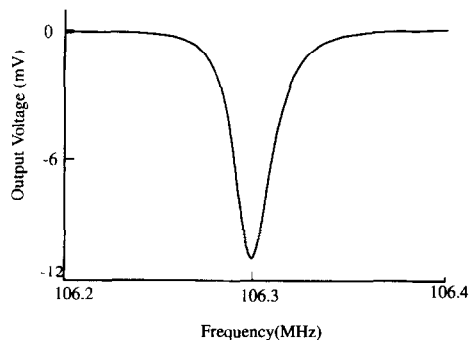


Fig. 4. A typical proton signal of the a deuterated target. The proton content in the sample is about 2%. The polarization here is 66%.

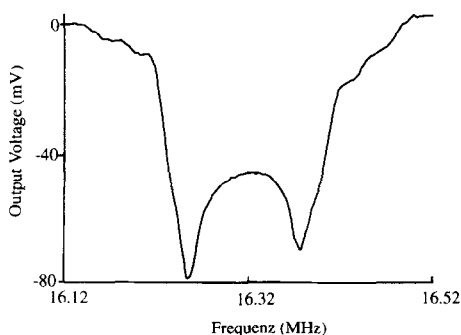


Fig. 5. A deuteron signal taken at proton polarization of 55%.

very much from the external ones exerted on the sample. As for the NMR, these nuclei behave abnormally. Since their signal can spread out over many MHzs and can not be detected by the NMR system.

However these nuclei can be seen by the neutrons. Fig. 6 shows the incoherent neutron scattering intensity of a deuteron target (see also Eq. (3)). The intensities are measured after the protons are depolarized over a sweep range of 200 kHz for 3 min. The proton NMR signal disappears afterwards. But from the intensity difference for $P_n P_1 > 0$ and $P_n P_1 < 0$ we know that the protons are still not completely depolarized, since this difference is much bigger than that from deuteron only. If we keep on depolarizing the protons every 30 min, after some hours the intensity difference decreases to the level of deuterons.

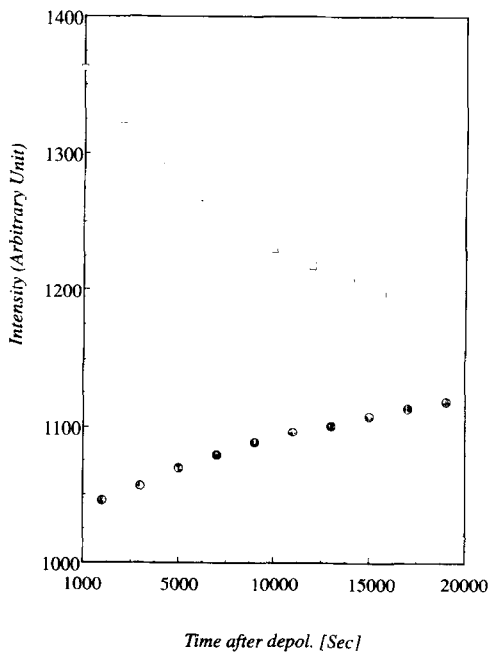


Fig. 6. Neutron scattering intensity after the proton spins are saturated and then re-saturated repeatedly every 30 min. The squares are $P_n P_1 > 0$, while the filled circles $P_n P_1 < 0$.

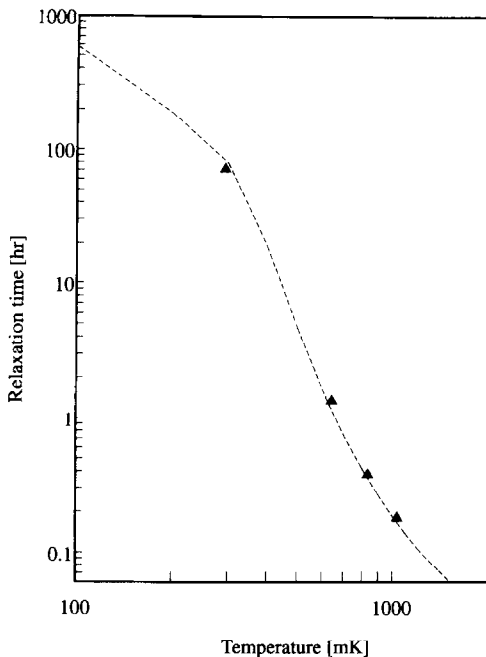


Fig. 7. Proton relaxation time of the target. The data points are measured and the dashed line is calculated with the empirical formula from de Boer et al.

This indicates that the spin polarization diffuses from abnormal protons to normal ones and then depolarized with the time. It has to be mentioned here that at frozen spin mode, the spin-lattice relaxation time T_1 is of order of some hundred hours and has hardly anything to do with the decrease of the intensity difference.

The spin diffusion can also be observed by the NMR system. The proton signal increases with time after the protons are depolarized.

To saturate all the protons at one time, the frequency sweep range has to be as large as 1.5 to 2 MHz for our sample.

2.5. The target material

The ideal environment for living matter is of no doubt aqueous. But for three reasons other components must be

added to the solvent. Firstly the target must polarize well. Secondly, the sample must be of glass form for the sake of neutron scattering. Finally the sample should have a stable form. The best material to be added to the solvent is found to be glycerol. Though the ribosomes are still alive in the water-glycerol mixture, it is always advisable from a biologist's viewpoint to have less glycerol in the solvent. The glycerol/water ratio is chosen at 11:9.

The paramagnetic centers are supplied by the EHBA-Cr(V) complex. Some other free radicals (like TEMPO) are also tested but found to be less useful for this target material. The EHBA concentration in the sample is about 1 wt.%.

The relaxation time of the target can be quite well fitted with the empirical formula [7] by de Boer et al. (see Fig. 7). A proton polarization of over 90% can be reached within 24 h. The increase and speed up of the polarization has also been observed on this material by modulating the microwave frequency. The modulation amplitude is set to ± 20 MHz. The modulation speed has been varied from 100 Hz to 10 kHz and shows no observable effect on the polarization.

3. The SANS-1 at GKSS

The polarized target station, together with the SANS-1 facility at the GKSS research center, is specialized to investigate the structure of macromolecules. Fig. 8 shows the overview of the setup of the SANS-1.

The neutron source is a 5 MW reactor equipped with a cold neutron source. The cold neutron flux at the end of the bent neutron guide is $2 \times 10^8 \text{ s}^{-1} \text{ cm}^{-1}$. The relative bandwidth of the monochromized neutrons after the neutron velocity selector is 10%. The super mirror [8] installed polarizes the neutron at an efficiency of 99% and a transmission of 40%. A Mezei-type spin flipper can flip the neutron spin direction with an efficiency of 97%. The neutron collimation can be changed from 2 to 7 m. The two dimensional neutron detector developed at GKSS (area: $55 \times 55 \text{ cm}^2$) can be moved from 0.7 to 10 m away from the sample.

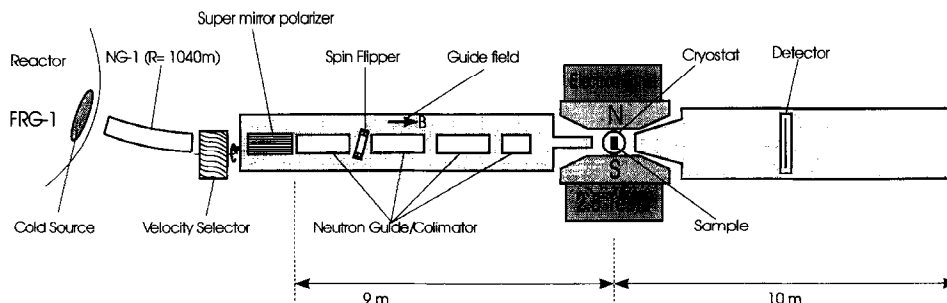


Fig. 8. Schematic overview of the SANS-1 at GKSS.

4. Conclusions

With the polarized target station built at SANS-1, GKSS, a new powerful tool has been established for the structure research [9,10]. With it we can now study macromolecules [11] which was not possible to examine before even at high flux reactors.

References

- [1] W.E. Hill, ed., *The Ribosome, Structure, Function & Evolution* (American Society of Microbiology, 1990), ISBN 1-55581-020-9.
- [2] M.S. Capel, D.M. Engelman, B.R. Freeborn, M. Kjeldgaard, L.A. Langer, V. Ramakrishnan, D.G. Schindler, B.P. Schoenborn, I.Y. Sillers, S. Yabuki and P.B. Moor, *Science* 238 (1987) 1403.
- [3] M. Abragam, *Nuclear magnetism order and disorder* (Clarendon Press, 1982) p. 430, ISBN 0-19-851294-5.
- [4] T.O. Niinikoski and F. Udo, *Nucl. Instr. and Meth.* 134 (1976) 219.
- [5] G. Court, D.W. Giffort and T.O. Niinikoski, *Proc. 2nd Workshop on Polarized Target Materials* (1980) p. 76.
- [6] A. Rijllart, A. MC68000 Stand-Alone CAMAC Microprocessor System in *Microprocessing and Microprogramming* 12 (1983) 291.
- [7] T. de Boer and T.O. Niinikoski, *Nucl. Instr. and Meth.* 114 (1974) 495.
- [8] O. Schärpf, *Physica B* 156&157 (1989) 631 and 639.
- [9] W. Knop et al., *J. Appl. Cryst.* 22 (1989) 352.
- [10] W. Knop et al., *Physica B* 174 (1991) 275.
- [11] J. Zhao and H. Stuhmann, *J. Phys.* 5(3), (1993) 233.



ELSEVIER

Magnetic coupling between ^3He and nuclei in a substrate

A possible way to polarize bulk ^3He

B. van den Brandt ^{a,*}, E.I. Bunyatova ^b, P. Hautle ^a, J.A. Konter ^a, A.I. Kovalev ^c,
S. Mango ^a

^a Paul Scherrer Institut, CH-5232 Villigen PSI, Switzerland

^b Joint Institute for Nuclear Research, Dubna, Head P.O. Box 79, 101000 Moscow, Russian Federation

^c St. Petersburg Nuclear Physics Institute, 188350 Gatchina, Russian Federation

Abstract

We have developed an apparatus which allows us to study the interaction of ^3He with powder substrates at temperatures down to 50 mK. A Stycast cell has been filled with liquid or solid ^3He , at pressures up to 65 bar, confined by fine powder that can be polarized in situ by dynamic nuclear polarization at 2.5 Tesla. A fast and accurate NMR/AFP system has been used to determine relaxation times. Different substrates have been investigated in search for polarizability and a strong enough surface interaction to eventually transmit their magnetization to bulk ^3He .

1. Introduction

It is a longstanding dream to dynamically polarize ^3He in dense form. This dream has been only partially fulfilled with the advent of optically pumped gaseous ^3He as for many applications a higher target density is required. On the other side the brute force method can produce high polarizations in solid ^3He but is only suited for a narrow class of applications.

A straightforward strategy, based on the fact that an electron spin system can couple directly to the ^3He nuclei, has been proposed by Delheij et al. [1]. If paramagnetic centers could be diluted in bulk ^3He , the method of dynamic nuclear polarization (DNP) could be applied directly to produce a ^3He polarization. However, this idea did not yet bring success.

An alternative way to dynamically polarize ^3He [2] arose from the discovery of the magnetic interaction between nuclei in a teflon substrate and ^3He spins on its surface [3]. A magnetization enhancement produced in the substrate nuclei by DNP might therefore be mediated to the ^3He in the surface layer through magnetic coupling and then transferred to the bulk liquid or solid. Schuhl et al. [4] have demonstrated the feasibility of this scheme by producing a small steady-state magnetization enhancement in the liquid ^3He .

2. The magnetic coupling of ^3He with a substrate

The van der Waals binding potential exerted by the substrate on the ^3He atoms has the effect of localizing the ^3He situated near the surface. The substrate is then separated from the liquid by at least one atomic layer adsorbed ^3He which exhibits a solid-like behaviour and a very strong magnetic coupling to the substrate.

Friedman et al. [3] discovered this phenomenon in PTFE microspheres (DLX6000 [5]), where they found the fluorine nuclei in the substrate and the ^3He nuclei adsorbed on the surface more strongly coupled to each other than either species to the lattice.

This coupling mechanism has been explained by introducing the exchange of ^3He atoms in the solid layer as a heat bath balancing the energy difference of the two Zeeman transitions [6,7]. The two kinds of spins are coupled through the modulation of the ^3He substrate nuclei dipolar interaction by exchange motion of the ^3He spins. The coupling is direct in the sense that a ^3He spin flip can occur only if a substrate spin flips in the opposite direction.

The relaxation of the liquid ^3He becomes thus entirely dominated by this surface interaction and is described by the relation [8]

$$T_1^{\text{He}} = T_{1s} \left[1 + M_L^0 / M_S^0 \right], \quad (1)$$

where T_1^{He} is the ^3He relaxation time, M_L^0 and M_S^0 are the

* Corresponding author.

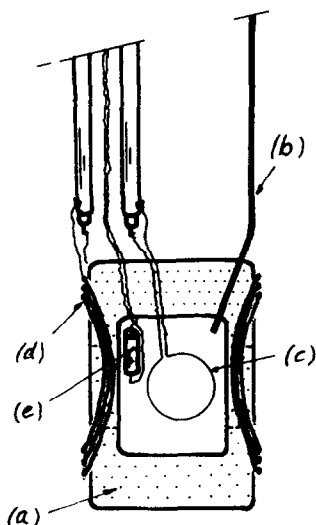


Fig. 1. Drawing of the experimental cell: (a) Stycast cell; (b) filling capillary; (c) NMR coil; (d) AFP coil; (e) resistance thermometer.

equilibrium magnetization of the liquid bulk and of the solid surface layer respectively, and

$$T_{1S} = [1/T_1 + 1/T_C]^{-1} \quad (2)$$

is the relaxation time of the monolayer, depending on the coupling time T_C , the inverse of the rate at which the two surface layers exchange magnetization. T_1 is the relaxation time that the surface layer spins alone (not seeing the substrate spins) would have.

Below the Fermi temperature ($T_F^{**} = 360$ mK) T_1^{He} even exhibits a linear temperature dependence

$$T_1^{\text{He}} = T_{1S} [1 + (N_L/N_S)(T/T_F^{**})], \quad (3)$$

(N_L/N_S) being the ratio between the number of spins in the liquid and the number of spins in the surface layer, as explained by a generally accepted model of Hammel and Richardson [7].

However only in a few substrates (DLX6000, charcoal [9], polystyrene [10]), all having a very large specific surface, a coupling time T_C short enough to detect a pronounced effect has been found.

3. Apparatus

The magnetic coupling between ^3He and nuclei in a substrate was measured in a Stycast cell (see Fig. 1), placed in the mixing chamber of our dilution refrigerator using a target holder with an integrated microwave guide [11]. The cell was situated just below the microwave horn. It was made out of two machined pieces of Stycast 1266, a material transparent both for light and for microwaves. The upper part of the cell was equipped with a 100 Ω Mat-

sushita resistance thermometer and a NMR pick-up coil, and a filling capillary of 0.7×0.5 mm stainless steel was mounted with Stycast 2850. Both parts of the cell were glued together directly after filling the cell with powder of the substrate of interest. The cell could withstand a pressure of more than 80 bar. The volume of the cell was 1 cm^3 , the filling factor was ~ 0.5 . A Helmholtz type coil was wound around the cell to allow polarization reversal by adiabatic fast passage. This AFP coil was also used to measure the relaxation times after reversal of the equilibrium polarization.

For experiments with solid ^3He a pressure of more than 29 bar is needed. Our ^3He -pressure system consists of a small gas handling system and a stainless-steel bomb with a volume of 30 cm^3 , containing active coal. Cooled to 4.2 K in a standard dewar it can be filled with ~ 0.5 mol ^3He in a few minutes. Back again at room temperature the closed volume will show pressures up to 200 bar.

4. Experiments

The experiments on DNP of ^3He carried out so far [4,9] have been more of principal nature; the achieved enhanced magnetizations were only a few times the equilibrium value. The main reason was possibly not the inefficiency of the polarizing mechanism but the polarizability of the substrate, limiting the maximum possible ^3He polarization

$$P_{\text{He}} = (\gamma_{\text{He}}/\gamma_n)P_n. \quad (4)$$

In the search for a candidate substrate we were therefore guided first by its polarizability, all the more because the coupling strength is hardly accessible in advance. Additionally the substrate surface should be large, and the mean free length d between substrate beads has to be much shorter than the spin diffusion length l in ^3He :

$$d \ll l < (DT_1)^{1/2}. \quad (5)$$

We performed tests with polyethylene, PTFE of the type DLX6000 and zeolite powders.

4.1. Polyethylene

Our first choice fell on polyethylene because former experiments had shown that it can be easily doped with a stable radical and polarized to a considerable amount [12]. In an extensive series of tests we achieved a polarization of +60% and -56% in a low density polyethylene powder¹ doped with the radical TEMPO to a nominal electron spin concentration of 2×10^{19} spins/ cm^3 (see also Ref. [13]). Even though the substrate surface was quite small

¹ Purchased from Aldrich Chemic.

due to a grain diameter of about 10 μm , and therefore the coupling to the ^3He could be expected to be weak, we considered it well suited to test and improve our apparatus. The powder was pressed into the target cell to give a filling factor of approximately 0.5. Before cooldown it was pumped shortly only to remove the air and not the TEMPO from the substrate. Afterwards the cell was filled with ^3He , which then condensed to liquid and was eventually solidified during the experiments.

To tell it at once, the ^3He magnetization was not following the polyethylene proton polarization upon irradiation with microwaves. However, we experienced an interesting behaviour of the ^3He NMR signal irrespective of the helium being liquid or solid: the shape of the signal was continuously changing with the proton polarization of the substrate. This is illustrated by Fig. 2, where the ^3He NMR signal in contact with unpolarized (i.e. TE), negative and positive polarized protons in polyethylene is shown.

It seems as if the small fraction of ^3He spins on the substrate surface is influenced by the nearby highly ordered proton spins, but the effect is masked in the NMR signal largely by the magnetization of the uninfluenced bulk nuclei.

Judging from the relaxation time of the proton system when surrounded by pure ^3He , which is not noticeably shorter than when surrounded by a mixture of ^3He - ^4He , the coupling time T_C must be very long in this substance. However no further quantitative studies were carried out in this system.

4.2. DLX6000

This substrate (now commercially available under the name MP1000) fulfills both criteria, having a short cou-

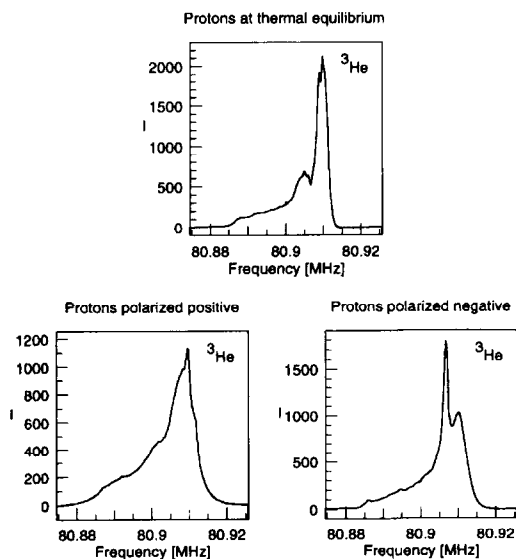


Fig. 2. The NMR signal of the ^3He (in this case solid at $p = 45$ bar) takes a different shape according to the degree and sign of the polarization of the protons in the polyethylene substrate.

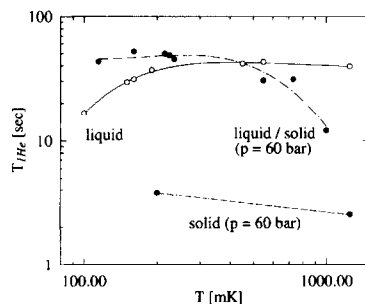


Fig. 3. Relaxation time T_1^{He} of liquid and solid ^3He confined by DLX6000 as a function of temperature.

pling time and a very large surface area. However, due to the small grain size (about 200 nm) the doping process, based on the diffusion of the TEMPO free radical into the powder, was not very successful and unpredictable. Only one out of several samples was polarizable to a small extent ($P = \pm 2.5\%$).

The sample filled into the pressure cell did not polarize at all and hence no change in the ^3He NMR signal shape could be detected upon microwave irradiation. On the other hand, the strong coupling of the substrate with the ^3He left its footprints in the temperature dependence of the relaxation time T_1^{He} of the liquid ^3He (see Fig. 3), which is in agreement with the theoretical model. Above the Fermi temperature T_1^{He} is independent of T (Eq. (1)) whereas for $T < T_F^*$ the relaxation time decreases linearly with the temperature (Eq. (3)). The values measured for the relaxation of the bulk solid ^3He are somewhat contradicting. According to Eq. (1), they should be equal to T_{1s} , which in turn is independent of T in the temperature range of our experiments [6]. However, the data points shown stem from different solidification cycles. Therefore a possible explanation for the un-expectedly long relaxation times might be that only part of the ^3He was actually solid.

Assuming a diffusion coefficient of $D = 7 \times 10^{-5} \text{ cm}^2 \text{ s}^{-1}$ in ^3He we get a diffusion length of about 0.5 mm in bulk liquid which amply fulfills Eq. (5) in the case of the DLX6000 powder. With a coupling time T_C of only a few seconds deduced from the T_1^{He} data, there is thus a good chance to achieve a sizeable polarization in the bulk liquid ^3He if only this substrate could be polarized.

This problem could be overcome by creating the necessary paramagnetic centers by γ -irradiation [14].

4.3. Zeolite

Some more qualitative experiments have been performed in zeolith crushed to a fine powder. Most probably the TEMPO radical did not enter into the cavities of the Zeolite (5–10 \AA diameter) or even blocked them because of its large molecule size. This might partly explain the fact that we could not detect any magnetic coupling of the powder with the ^3He .

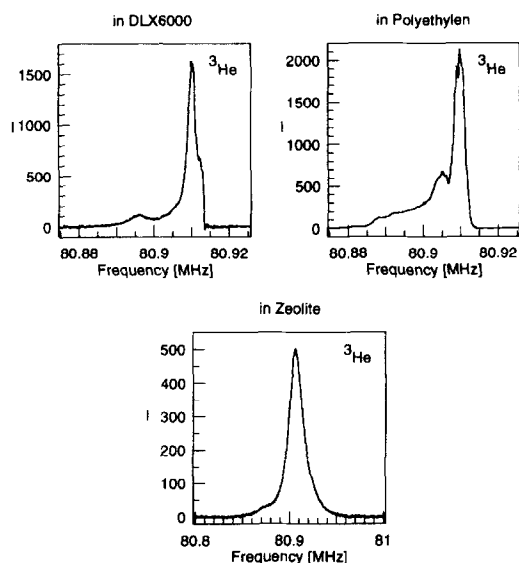


Fig. 4. NMR signal of solid ^3He ($p = 45$ bar) confined by different powders at thermal equilibrium.

Worth mentioning is however the shape of the ^3He NMR signal, which is much broader and quite different from the one observed with DLX6000 and polyethylene respectively (Fig. 4).

5. Conclusions

We have built an apparatus suited to investigate the magnetic coupling between liquid or solid bulk ^3He and a substrate under conditions normally used in dynamically polarized solid targets. Experiments with powders of polyethylene, DLX6000 and zeolite, doped with the free radical TEMPO, have been performed. An interesting connection between the ^3He NMR signal shape and the polarization of the protons in polyethylene has been observed. The substrate magnetization has not been transferred to the

bulk liquid and solid ^3He respectively. As expected, a strong coupling between the DLX6000 micropowder and liquid ^3He was measured. The relaxation and coupling parameters found in this system should allow to achieve considerable polarizations in ^3He if one would be able to dynamically polarize DLX6000 substantially. Experiments of DNP in irradiated DLX6000 are planned for the near future.

References

- [1] P.P. Delheij, H. Postma and K. Bindels, Proc. 9th Int. Symp. on High Energy Spin Physics, Bonn, 1990, eds. W. Meyer et al., (Springer, Berlin, 1991) vol. 2, p. 328.
- [2] M. Chapellier, J. Phys. Lett. (Paris) 43 (1982) L-609.
- [3] L.J. Friedman, P. Millet and R.C. Richardson, Phys. Rev. Lett. 47 (1981) 1078.
- [4] A. Schuhl, S. Maegawa, M.W. Meisel and M. Chapellier, Phys. Rev. Lett. 54 (1985) 1952.
- [5] DLX6000 is a PTFE micropowder manufactured by Dupont (diam. 200 nm).
- [6] A. Schuhl, F.B. Rasmussen and M. Chapellier, J. Low Temp. Phys. 57. (1984) 483.
- [7] P.C. Hammel and R.C. Richardson, Phys. Rev. Lett. 52 (1984) 1441.
- [8] A. Schuhl, S. Maegawa, M.W. Meisel and M. Chapellier, Phys. Rev. B 36 (1987) 6811.
- [9] L.W. Engel and K. DeConde, Phys. Rev. B 33 (1986) 2035.
- [10] F.W. Van Keuls, R.W. Singerman and R.C. Richardson, J. Low Temp. Phys. 96 (1994) 103.
- [11] B. van den Brandt, J.A. Konter and S. Mango, Nucl. Instr. and Meth. A 289 (1990) 526.
- [12] E.I. Bunyatova, Proc. 9th Int. Symp. on High Energy Spin Physics, Bonn, 1990, eds. W. Meyer et al. (Springer, Berlin, 1991) vol. 2, p. 333.
- [13] B. van den Brandt, E.I. Bunyatova, P. Hautle, J.A. Konter and S. Mango, these Proceedings (7th Workshop on Polarized Target Materials and Techniques, Bad Honnef, Germany, 1994) Nucl. Instr. and Meth. A 356 (1995) 36.
- [14] D. Suryanarayana, L. Kevan and S. Schlick, J. Am. Chem. Soc. 104 (1982) 668, and references therein.



ELSEVIER

Polarized targets at triangle universities nuclear laboratory

M.L. Seely^{a,*}, C.R. Gould^a, D.G. Haase^a, P.R. Huffman^b, C.D. Keith^a, N.R. Roberson^b,
W. Tornow^b, W.S. Wilburn^b

^a North Carolina State University, Raleigh, NC 27695, USA

Triangle Universities Nuclear Laboratory, Durham, NC 27708, USA

^b Duke University, Durham, NC 27708, USA

Triangle Universities Nuclear Laboratory, Durham, NC 27708, USA

Abstract

A summary of the polarized and aligned nuclear targets which have been constructed and used at the Triangle Universities Nuclear Laboratory is given. Statically polarized targets, typically operating at a temperature of 12 mK and a magnetic field of 7 T, have provided significant nuclear polarization in ¹H, ³He, ²⁷Al, ⁹³Nb and ¹⁶⁵Ho. A rotating, aligned ¹⁶⁵Ho target is also in use. A ³He melting curve thermometer has been developed for use in statically polarized targets. A dynamically polarized proton target is under construction.

1. Introduction

At the Triangle Universities Nuclear Laboratory, a number of polarized and aligned nuclear targets have been constructed and used in polarized neutron – polarized target scattering experiments. The nuclei which have been polarized include ¹H [1], ³He [2], ²⁷Al [3], ⁹³Nb [4] and ¹⁶⁵Ho [5]. An aligned ¹⁶⁵Ho [6] target with zero vector polarization is also in operation. A summary of the polarized and aligned targets which have been used at TUNL, including the polarization achieved and the thickness, is given in Table 1.

In a typical experiment, polarized protons or polarized deuterons are produced in the TUNL atomic beam polarized ion source [7] and are accelerated by a 10 MeV FN tandem, Van de Graaff accelerator. Polarized neutrons are produced by the ³H(p, n)³He reaction in a tritiated foil at low energies or by the ²H(d, n)³He reaction at higher energies. The flux of neutrons transmitted by the target is measured as the beam polarization is reversed at the source every 0.1 s. The quantities determined are $\Delta\sigma_L$ and $\Delta\sigma_T$; the difference between total neutron scattering cross sections with neutron spins parallel and anti-parallel to the target polarization. In the case where the neutron and target polarizations are along the beam direction (longitudinal) this difference in cross sections is designated $\Delta\sigma_L$. In the case of neutron and target spins transverse to the beam direction, the difference is designated $\Delta\sigma_T$. These

experiments have yielded information on the spin dependence of nuclear potentials [1,3,4] and on the structure of ⁴He [8]. The ability to measure transmission asymmetries in both the longitudinal and transverse direction has made it possible to unambiguously determine the central and tensor parts of the nuclear spin–spin potential [3]. The holmium target has been used to search for violations of T-reversal symmetry [9,10].

The targets used at TUNL to date have all been “brute-force” or statically polarized targets. Nuclei are polarized by cooling the sample to very low temperatures (12 mK) and applying a strong (7 T) magnetic field. (In the special case of holmium, the internal hyperfine field enables significant nuclear polarization to be obtained at more moderate fields and temperatures). A statically polarized target is practical in our experiments because the neutron beam normally imposes a negligible heat load on the target and because we are not concerned with deflection of charged particles by the strong magnetic field at the target. Almost any nucleus with nonzero spin may be polarized by this method [11]. For a nucleus having spin $\frac{1}{2}$, the polarization in a solid displaying simple paramagnetic behaviour (susceptibility following the Curie Law) is given by:

$$f_1 = \tanh(\mu B/kT), \quad (1)$$

where μ is the magnetic moment of the nucleus, B is the magnetic field and T is the temperature. The static polarizations which are expected at 10 mK and 7 T are illustrated for a variety of nuclei in Fig. 1. Statically polarized targets may employ samples which are in a dense form and do not require specialized materials or some of the other

* Corresponding author.

Table 1

A summary of the polarized and aligned targets which have been used at Triangle Universities Nuclear Laboratory

Nucleus	Method	Thickness (cm^{-2})	Polarization (alignment)	Studies
^1H	BF, 13 mK/7 T	2.0×10^{23}	50%	N–N tensor force
^1H	DNP, 0.5 K/2.5 T	6.8×10^{22}	80%	N–N tensor force
^3He	BF, 12 mK/7 T	4.3×10^{22}	38%	structure of ^4He
^{27}Al	BF, 12 mK/7 T	1.1×10^{23}	34%	spin–spin potentials
^{93}Nb	BF, 12 mK/7 T	9.9×10^{22}	50%	spin–spin potentials
^{165}Ho	BF, 140 mK/1 T	5.4×10^{22}	69%	T-reversal
^{165}Ho	Cryo. 140 mK/0 T	6.1×10^{22}	$P = 0, A = 94\%$	T-reversal

complications inherent in optically or microwave-pumped polarized targets. Target thickness is an important consideration in these experiments because the intensity of the neutron beam is much lower than that of the charged particle beam. One drawback of statically polarized targets is that it is not practical to reverse the target polarization frequently in order to cancel systematic errors. Since some systematic effects may be due to the magnetic field at the target, reversing the target polarization may not be effective in removing all systematic errors. For this reason, we are constructing a dynamically polarized proton target which will be used to continue our measurements of $\Delta\sigma_L$ and $\Delta\sigma_T$ for protons.

Statically polarized targets require accurate thermometry at temperatures near 10 mK. We have used nuclear orientation thermometers for this purpose. Recently, we

have developed a ^3He melting curve thermometer for use in the statically polarized ^1H and ^3He targets [12].

2. Statically polarized ^1H , ^{27}Al , ^{93}Nb and ^{165}Ho

The statically polarized targets at TUNL are based on a commercial dilution refrigerator (SHE model 430). This dilution refrigerator has a cooling power of $1.5 \mu\text{W}$ at 10 mK with a circulation rate of $500 \mu\text{moles/s}$. The target is mounted on a 38 cm long copper cold finger which is attached to the mixing chamber. The commercial dilution refrigerator was modified by adding a narrow, demountable tail section to the vacuum can and a demountable extension to the dewar. The tail section of the vacuum can was designed to fit through the bore of our 7 T superconducting magnet. Placing demountable seals in the vacuum can and the dewar at a level just below the mixing chamber allows access to the target without going through the laborious procedure of lowering the entire dewar and vacuum can. The magnet is a 7 T superconducting Helmholtz pair (American Magnetics Incorporated) which may be mounted to place the magnetic field either parallel or perpendicular to the beam direction. The field uniformity is 0.1% over a 1 cm diameter region at the center of the coils. A diagram of the cryostat is shown in Fig. 2.

Targets on the order of 15 cm^3 cooled to 20 mK in 12 to 24 h and reached a base temperature of 12 mK in an additional 12 to 24 h. The aluminum target, fabricated from high-purity ^{27}Al ($I = \frac{5}{2}$), measured $18 \text{ mm} \times 18 \text{ mm} \times 50 \text{ mm}$ and was threaded for attachment to the cold finger. The target was slotted to reduce eddy current heating. A vector polarization of 34% was obtained at $T = 12 \text{ mK}$ and $B = 7 \text{ T}$. The ^{93}Nb ($I = \frac{9}{2}$) target measured $18 \text{ mm} \times 18 \text{ mm} \times 38 \text{ mm}$ and was attached to the cold finger by a stainless steel compression connector. A maximum vector polarization of 50% was obtained at 12 mK and 7 T.

The statically polarized proton target employed TiH_2 as the target material and is similar to the Karlsruhe target [13]. The use of high-purity TiH_2 was found to be important in achieving good thermal conductivity at low temper-

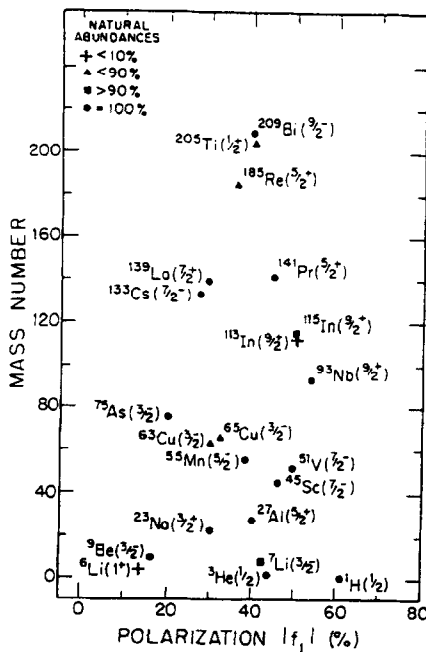


Fig. 1. The nuclear polarization f_1 obtained at $B = 7 \text{ T}$ and $T = 10 \text{ mK}$ for a variety of nuclei.

atures [14]. The TiH_2 powder was pressed into a copper form under 1.5 GPa of pressure. Reliable thermal contact between the target and the thermometers was difficult to achieve. For this reason, the product of target polarization and target thickness was determined by measuring $\Delta\sigma_T$ at 1.94 MeV. At low energies, known properties of the deuteron, along with kinematic factors, restrict the range of possible values of $\Delta\sigma_T$ [13]. Calculated values of $\Delta\sigma_T$ based on potential models, phase shift analysis and effective range parameters at 1.94 MeV all agree to within 5%. In the experiments, the cryostat temperature was allowed to stabilize and $\Delta\sigma_T$ was measured at 1.94 MeV. The energy was then increased to the desired value and the

measurement of $\Delta\sigma_T$ was repeated. While the target polarization was not calculated from the temperature, thermometry was still important in verifying that the target temperature remained constant between calibration runs at 1.94 MeV and data-taking runs at higher energies.

The polarized holmium target was used to search for P-odd T-odd effects in neutron–nucleus scattering. The holmium target was a 1.8 cm cube of single-crystal ^{165}Ho . As holmium becomes ferromagnetic below 20 K, it is possible to achieve relatively high nuclear polarizations at moderate fields and temperatures [5]. This target was operated at a temperature of 140 mK and a field of 1 T to achieve a vector polarization of 69%.

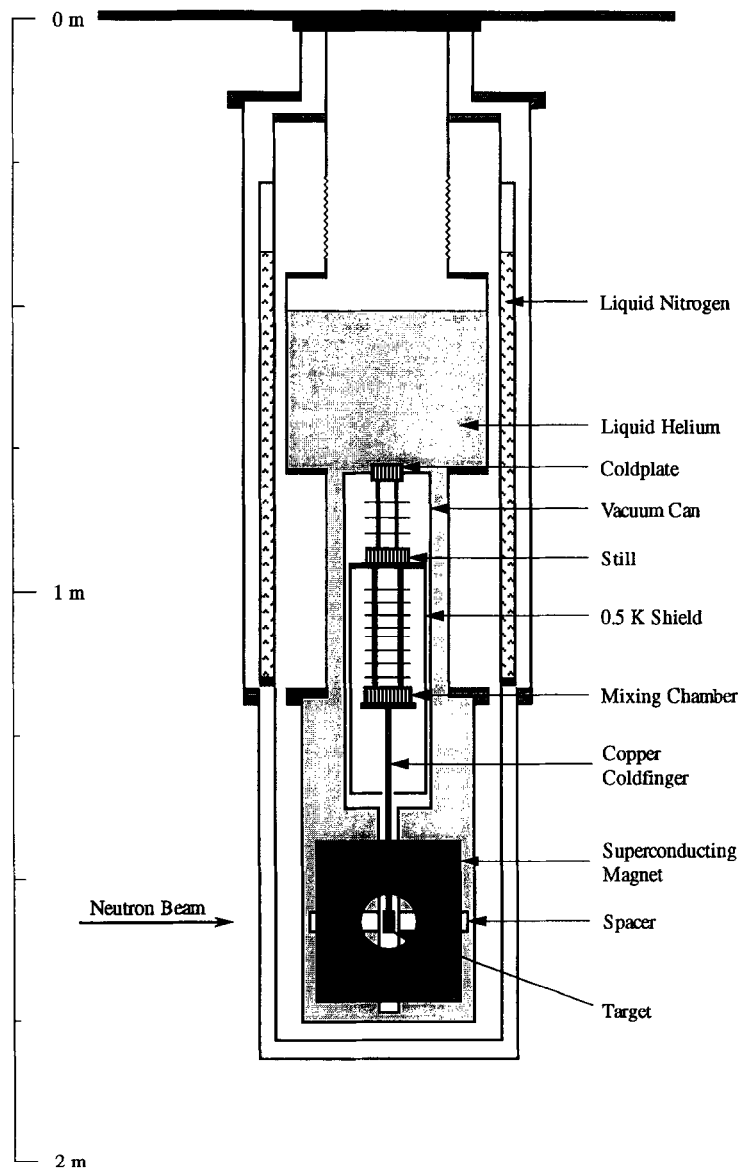


Fig. 2. The TUNL statically polarized target cryostat.

3. The polarized solid ^3He target

The polarized ^3He target employs the same SHE-430 dilution refrigerator and 7 T magnet as described above. The target cell, shown in Fig. 3, has an internal volume 11.2 cm^3 and 1.27 mm thick BeCu walls. The lower part of the target cell is fabricated from BeCu. The cap is constructed from OFHC copper in order to provide good thermal contact to the cold finger. The cell is filled with $3\text{ }\mu\text{m}$ silver powder to a filling factor of 19%. The silver powder improves the thermal conductivity of the target by approximately a factor of 5 (as compared with pure solid ^3He) and, moreover, provides for improved contact between the ^3He solid and the walls of the cell. The resulting target has a thickness of 4.3×10^{22} ^3He atoms/ cm^2 . The cell is filled through a CuNi capillary connected to a room-temperature gas handling system. The capillary is heat sunk to the dilution refrigerator at several locations and the blocked capillary technique is used to confine the ^3He sample inside the cell at a density of 0.125 g/cm^3 .

At the temperatures and pressures encountered in this target, ^3He solidifies in the paramagnetic phase. However, the magnetization of this solid deviates from the Curie law. The large zero-point motion of ^3He atoms in the lattice leads to the exchange of neighboring atoms. It has been found that an accurate model of solid ^3He in the paramagnetic phase must also include exchanges involving three

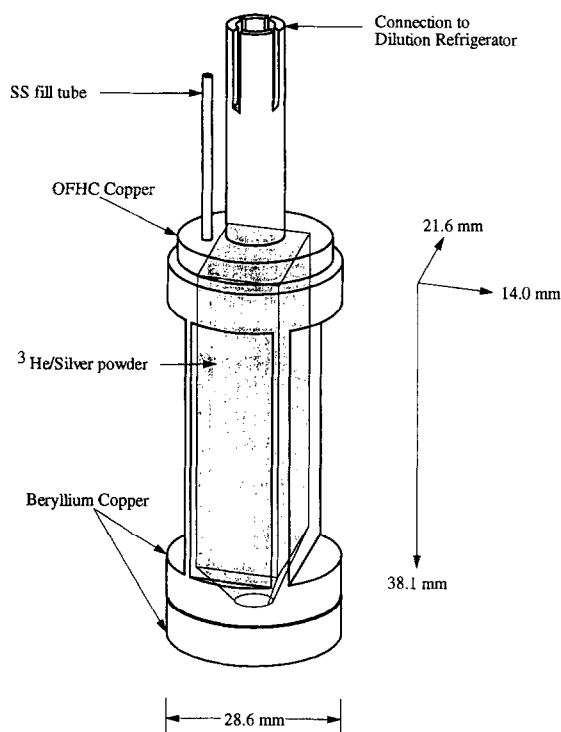


Fig. 3. The polarized solid ^3He target cell. The shaded region indicates the interior of the cell.

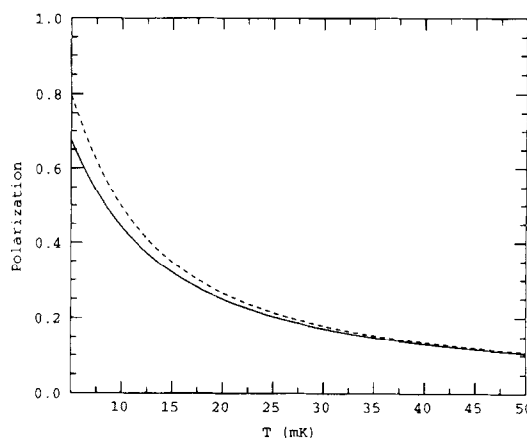


Fig. 4. The polarization of solid ^3He in a 7 T magnetic field. Solid line; the polarization is calculated using Eq. (2) with parameters obtained from Ref. [16]. Dashed line; the polarization for a simple paramagnetic solid in which the magnetic susceptibility is given by the Curie Law.

and four neighboring atoms [15]. The parameters used in this model are obtained by fitting experimental data [16]. The resulting expression for the polarization f_1 is:

$$f_1 = \tanh\left[\frac{(\mu B + \Theta f_1 + K f_1^3)}{kT}\right], \quad (2)$$

where μ is the magnetic moment of the ^3He nucleus, $\Theta/k = -1.18\text{ mK}$ and $K/k = -1.962\text{ mK}$. The magnetic moment of the ^3He nucleus is negative and the polarization is antiparallel to the external field. The quantities Θ and K are antiferromagnetic coupling constants, tending to reduce the value of the polarization below that which would be expected for a simple paramagnetic solid. A plot of the polarization calculated from this expression, along with the polarization that would be predicted for a solid obeying the Curie law, is given in Fig. 4. We have obtained a vector polarization of 38% at $T = 12\text{ mK}$ and $B = 7\text{ T}$. This target has been used to measure $\Delta\sigma_T$ in the energy range of 1.9 to 7.5 MeV. Measurements of $\Delta\sigma_L$ are presently underway.

4. Thermometry

A ^{60}Co nuclear orientation thermometer has been installed in all of the targets described above. This thermometer utilizes a $2\text{ }\mu\text{Ci}$ source mounted in a region of low magnetic field and connected to the target by a copper braid. While it is possible to operate the nuclear orientation thermometer in a strong magnetic field, its sensitivity would be reduced. An intrinsic germanium detector is located outside the dewar approximately 36 cm from the source. With a counting rate of 5 counts/s, the anisotropy was determined to 2% after one hour of counting by comparing the warm and cold counting rates. The detector

was removed from the experimental hall while the neutron beam was on target and was accurately repositioned at the end of each run to verify that the target temperature had not changed.

The desire for a continuously-reading thermometer that would be unaffected by radiation led us to develop a ^3He melting curve thermometer for use in statically polarized targets. The melting curve thermometer has been used with the ^1H and ^3He targets. The ^3He melting curve thermometer consists of a cell containing liquid and solid ^3He in equilibrium at approximately constant volume. One wall of the cell is a thin diaphragm and forms one plate of a capacitive pressure gauge. The temperature of the sample is determined by measuring the pressure in the cell. Our melting curve thermometer is of the Straty–Adams type [18]. A detailed description has been given by Keith et al. [12]. The melting curve thermometer is filled by the blocked capillary technique in a manner similar to the ^3He target. However, the melting curve thermometer is filled to a lower average density (0.118 g/cm^3) in order to insure that a solid/liquid mixture will exist at all temperatures below 0.76 K . The P vs. T curve for melting ^3He has been measured to an accuracy of better than 1% over the range of 1 mK to 770 mK [18–20]. The melting curve thermometer and the ^{60}Co nuclear orientation thermometer agreed to within 0.25 mK at temperatures around 12 mK . The sensitivity of the melting curve thermometer was $1.5\text{ }\mu\text{K}$ at 20 mK . A comparison of the two thermometers is given in Fig. 5, which records the cooling of the ^3He target from 100 mK to its base temperature.

The ^3He melting curve thermometer is somewhat sensitive to magnetic fields because magnetization of the solid decreases its entropy and depresses the melting curve. Accurate data on the melting curve is available for fields to 9 T [21]. This effect corresponds to a temperature shift of 0.35 mK/T at 15 mK . We chose to locate the melting curve thermometer in a region of low field and connect it to the target by means of a copper braid, making the field correction unnecessary.

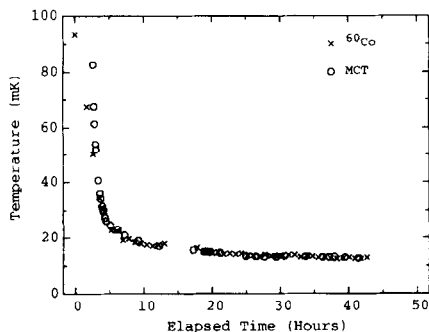


Fig. 5. Cooling curve for the ^3He target with temperatures measured by the ^{60}Co nuclear orientation thermometer (crosses) and the ^3He melting curve thermometer (circles).

5. The rotating aligned ^{165}Ho target

The aligned holmium target has been used to search for P-even T-odd terms in nucleon–nucleus scattering. The alignment axis of the target is rotated in the scattering plane. The beam polarization, transverse to the scattering plane, is reversed and the asymmetry in neutron transmission by the target is measured as a function of angle between the alignment axis and the beam direction. A term in the asymmetry varying as $\sin(2\theta)$ would indicate the presence of a T-odd term in the scattering amplitude. In order to carry out these experiments, we have constructed an aligned holmium target in which the axis of alignment may be rotated through 360° .

Holmium forms a hexagonal crystal which becomes ferromagnetic below 20 K . The electronic magnetic moments form a spiral staircase arrangement about the c axis, with the spins in neighboring basal planes inclined at 10° . In the absence of a magnetic field, the magnetizations of different domains in a bulk sample cancel, yielding zero net magnetization. The nuclear magnetic moments align with the local field, resulting in a bulk sample having zero vector polarization but a net alignment along the c axis. Our target employs a single crystal of ^{165}Ho ($I = \frac{7}{2}$) which has been cut and ground to a cylinder 2.3 cm in diameter and 2.8 cm long. The c axis is perpendicular to the axis of the cylinder. At 130 mK , the average operating temperature presently achieved, the alignment reaches 94% of its maximum value.

The dilution refrigerator employed in this target was constructed at North Carolina State University and was designed to accommodate a central shaft from the target through the vacuum can to the top mounting flange [6]. The dilution refrigerator produces $85\text{ }\mu\text{W}$ of cooling power at 110 mK with a circulation rate of $120\text{ }\mu\text{moles/s}$. The holmium target is pressed into a copper sleeve which is mounted on a stainless steel shaft approximately 30 cm below the mixing chamber. Copper braids connect the target holder to the mixing chamber, allowing the target to rotate while providing for thermal contact. The stainless steel shaft is supported by bearings which are mounted in a copper sleeve extending from the mixing chamber. Copper bellows couplings inserted in the stainless steel tube at the cold-plate and in the dewar heat sink these points by contact with the surrounding walls. The tube is driven by a stepping motor and gear reduction unit mounted outside the dewar. The angular position of the shaft is monitored by a shaft encoder. Torque on the shaft, due primarily to the copper braids, is expected to twist shaft slightly, producing a misalignment between the target and the warm end of the shaft. Tests of the rotation system with the cryostat warm confirm that the target returns to its original position to within 1° after repeated rotations. A direct check of the rotation system with the target cold is performed during each run by observing the deformation effect in holmium [22]. To within the accuracy of these

measurements, no discrepancy between the exterior shaft angle and the target angle has been observed.

6. Dynamically polarized proton target

In order to extend our measurements of $\Delta\sigma_{\perp}$ and $\Delta\sigma_{\parallel}$ for protons, we are constructing a dynamically polarized proton target. This target is a modification of the PSI design [23] employing a ^3He evaporation insert. The cryostat has been modified to accommodate a 1.4 cm square target. Butanol doped with EHBA Cr–V has been selected as the target material. While ammonia or mixtures of ammonia compounds may offer a higher fraction of polarizable protons, we wish to avoid the presence of other polarized species in the target. The target employs a 2.5 T superconducting split-coil magnet (American Magnetics Incorporated) which allows access to the target in both the longitudinal and transverse directions. The homogeneity of the magnetic field is 1 part in 10^4 over a 1 cm diameter spherical volume. The target polarization will be monitored by an NMR system of the Liverpool design [24]. A personal computer equipped with a 16 bit ADDA card will be used to control the NMR system and log both cryostat and NMR data. Interface circuits enabling computer control of the NMR frequency sweep and the monitoring of resistance thermometers were constructed in-house. In addition to the NMR measurements, the product of target polarization and thickness will be measured by measuring $\Delta\sigma_{\parallel}$ at 1 MeV. We plan to have this target in operation early in 1995.

Acknowledgements

This work was supported in part by the US Department of Energy, Office of High Energy and Nuclear Physics, under contracts DE-FG05-88-ER40441 and DE-FG05-91-ER40619.

References

- [1] W.S. Wilburn, C.R. Gould, D.G. Haase, P.R. Huffman, C.D. Keith, J.E. Koster, N.R. Roberson and W. Tornow, *Phys. Rev. Lett.* 71 (1993) 1982.
- [2] C.D. Keith, C.R. Gould, D.G. Haase, M.L. Seely, P.R. Huffman, N.R. Roberson, W. Tornow and W.S. Wilburn, *Proc. 14th Int. Conf. on Few Body Problems in Physics*, ed. F. Gross (Williamsburg, VA, 1994) to be published.
- [3] C.R. Gould, D.G. Haase, L.W. Seagondollar, J.P. Soderstrum, K.E. Nash, M.B. Schneider and N.R. Roberson, *Phys. Rev. Lett.* 57 (1986) 2371.
- [4] J.P. Soderstrum, C.R. Gould, D.G. Haase, N.R. Roberson, M.B. Schneider and L.W. Seagondollar, *Phys. Rev. C* 45 (1992) 326.
- [5] J.P. Soderstrum, C.R. Gould, D.G. Haase, L.W. Seagondollar, M.B. Schneider, and N.R. Roberson, *Phys. Rev. C* 38 (1988) 2424.
- [6] J.E. Koster, C.R. Gould, D.G. Haase and N.R. Roberson, *Nucl. Instr. and Meth. A* 313 (1992) 464.
- [7] T.B. Clegg, H.J. Karwowski, S.K. Lemieux, R.W. Sayer, E.R. Crosson, W.M. Hooke, C.R. Howell, H.W. Lewis, A.W. Lovette, H.J. Pfütznner, K.A. Sweeton and W.S. Wilburn, to be published.
- [8] C.D. Keith, C.R. Gould, D.G. Haase, N.R. Roberson, W. Tornow, G.M. Hale, H.M. Hofmann and H. Postma, *Phys. Rev. C* 50 (1994) 237.
- [9] J.E. Koster, E.D. Davis, C.R. Gould, D.G. Haase, N.R. Roberson, L.W. Seagondollar, W.S. Wilburn and X. Zhu, *Phys. Lett. B* 267 (1991) 23.
- [10] P.R. Huffman, C.R. Gould, D.G. Haase, C.D. Keith, N.R. Roberson, M.L. Seely and W.S. Wilburn, *Proc. Conf. on Intersections between Particle and Nuclear Physics* (St. Petersburg, FL 1994) to be published.
- [11] D.G. Haase, C.R. Gould and L.W. Seagondollar, *Nucl. Instr. and Meth. A* 243 (1986) 305.
- [12] C.D. Keith, C.R. Gould, D.G. Haase, N.R. Roberson and W. Tornow, *Hyperfine Interactions* 75 (1992) 525.
- [13] A. Aures, W. Heeringa, H.O. Klages, R. Maschuw, F.K. Schmidt and B. Zeitnitz, *Nucl. Instr. and Meth.* 224 (1984) 347.
- [14] TiH_2 powder supplied by H.O. Klages, KFA, Karlsruhe, Germany.
- [15] M. Roger, J.H. Hetherington and J.M. Delrieu, *Rev. Mod. Phys.* 55 (1983) 1.
- [16] H.L. Stipdonk and J.H. Hetherington, *Phys. Rev. B* 31 (1985) 4684.
- [17] E.L. Ziercher, K.I. Blum and Y. Hu, in: *Experimental Techniques in Condensed Matter Physics at Low Temperatures*, eds. R.C. Richardson and E.N. Smith (Addison-Wesley, New York, 1988) p. 293.
- [18] D.S. Greywall and P.A. Busch, *J. Low Temp. Phys.* 46 (1982) 451.
- [19] D.S. Greywall, *Phys. Rev. B* 27 (1986) 2747.
- [20] W.E. Fogel, J.C. Colwell and R.J. Soulen Jr., *Physica B* 165 (1990) 33, Melting curve data obtained through private communication.
- [21] C.C. Kranenburg, S.A.J. van de Haar, R. Jochemsen and G. Frossati, *Jpn. J. Appl. Phys.* 26 (1987) 2133.
- [22] J.E. Koster, C.R. Gould, D.G. Haase and N.R. Roberson, *Phys. Rev. C* 49 (1994) 710.
- [23] B. van den Brandt, J.A. Konter and S. Mango, *Nucl. Instr. and Meth. A* 289 (1990) 526.
- [24] G.R. Court, D.W. Gifford, P. Harrison, W.G. Heyes and M.A. Houlden, *Nucl. Instr. and Meth. A* 324 (1993) 433.



ELSEVIER

The SLAC high-density gaseous polarized ^3He target [☆]

J.R. Johnson ^{a,*}, A.K. Thompson ^b, T.E. Chupp ^c, T.B. Smith ^c, G.D. Cates ^d,
B. Driehuys ^d, H. Middleton ^d, N.R. Newbury ^d, E.W. Hughes ^e, W. Meyer ^{e,1}

^a Department of Physics, University of Wisconsin, Madison, WI 53706, USA

^b Department of Physics, Harvard University, Cambridge, MA 02138, USA

^c Randall Laboratory of Physics, University of Michigan, Ann Arbor, MI 48109, USA

^d Joseph Henry Laboratories of Physics, Princeton University, Princeton, NJ 08544, USA

^e Stanford Linear Accelerator Center, Stanford University, Stanford, CA 94309, USA

Abstract

A large-scale high-pressure gaseous ^3He polarized target has been developed for use with a high-intensity polarized electron beam at the Stanford Linear Accelerator Center. This target was used successfully in an experiment to study the spin structure of the neutron. The target provided an areal density of about 7×10^{21} nuclei/cm² and operated at ^3He polarizations between about 30% and 40% for the six-week duration of the experiment.

1. Introduction

Experiment E-142 at SLAC [1] was proposed to measure the spin-dependent structure function of the neutron by studying deep-inelastic scattering of high-energy polarized electrons from polarized neutrons. Polarized ^3He was chosen as the target material to provide the polarized neutrons for two main reasons. First, ^3He nuclear wavefunction calculations [2] indicate that the nucleus is primarily in a spatially symmetric S-state where the spins of the two protons must be anti-aligned. Thus the spin of the nucleus is mainly provided by the neutron, and so polarized ^3He is a good approximation to a polarized neutron target, diluted by the presence of the protons but with only small corrections needed due to the polarization of the protons. Second, practical ^3He polarized targets have been developed [3–10] using the technique of collisional spin-exchange with optically pumped alkali-metal vapor, typically rubidium. Using modern high-power Ti:sapphire lasers for the depopulation optical pumping of rubidium, such targets have been shown to be capable of operating effectively at high ^3He pressures (more than 10 atm [8]) and in the presence of intense electron beams [10], as

required by the SLAC experiment. A disadvantage of this technique is the weakness of the hyperfine interaction between the polarized rubidium valence electron and the ^3He nucleus, leading to typical time constants for the build-up of ^3He polarization of the order of 10 h. Thus, long ^3He spin relaxation times are required to achieve high polarization.

2. Target description

Fig. 1 shows a schematic overview of the SLAC target system. The large main Helmholtz coils have a diameter of about 1.5 m and provide a uniform magnetic field of about 20 G in the vicinity of the target cell during operation. The coils shown produced a field direction parallel (or antiparallel) to the electron beam direction, and this direction (and thus the direction of the ^3He polarization) was reversed every few hours during the experiment. Not shown is a second set of coils that produced a magnetic field (and ^3He polarization) direction transverse to the beam direction for part of the experiment. The RF drive coils are about 50 cm in diameter and, together with the small pickup coils shown, were used for NMR measurements of the ^3He polarization, as described later in this paper.

The laser shown in the figure represents one of five Ti:sapphire lasers, each pumped by a 20 W argon-ion laser and capable of delivering several watts of power at 795 nm, the wavelength of the D_1 line of rubidium. Together, the five laser systems typically produced nearly 20 W of infrared photons for optical pumping. The quarter-wave plate in each laser beam line was adjusted to

[☆] Work supported in part by Department of Energy contracts DE-AC03-76SF00515 (SLAC), DE-FG02-90ER40557 (Princeton), and DE-AC02-76ER00881 (Wisconsin); by National Science Foundation grants 8914353 and 9200621 (Michigan); and by the Bundesministerium für Forschung und Technologie (W. Meyer).

* Corresponding author.

¹ Permanent address: Universität Bonn, Bonn, Germany.

produce circularly polarized photons, and the mirrors shown were oriented so as to preserve the circular polarization.

As indicated in Fig. 1, the ^3He gas was contained in a sealed glass vessel constructed as two chambers connected by a transfer tube, for reasons discussed below. The chamber in the electron beam was a cylinder about 2.1 cm in diameter and 30 cm long, with end windows about 125 μm thick. The other chamber was about 3.7 cm diameter by 8 cm long, and was enclosed in a plastic oven connected to hot air supply and return tubes (not shown). The oven had an optically coated laser-beam entrance window on one end, and transparent plastic windows on two adjacent sides to allow observation of the rubidium fluorescence during optimization of laser steering and wavelength adjustment. The oven was operated typically at about 175°C, giving a typical rubidium vapor density of a few times 10^{14} atoms/cm 3 and a ^3He pressure in the sealed vessel of about 11 atm.

The target cell, oven, and NMR coils were required to operate in a completely evacuated beam line, to minimize backgrounds and unpolarized material intercepting the electron beam. The oven and the support structure for the NMR coils and target cell were constructed of plastic or other nonconducting material, to avoid disrupting the RF drive field during NMR measurements. The entire target structure was constructed of nonmagnetic materials so as not to degrade the uniformity of the main holding field.

3. Target design considerations

3.1. The two-chamber cell

One requirement of the target arrangement was that the optical pumping of the rubidium vapor take place away from the electron beam, since the rubidium would be depolarized through ionization by the intense beam. In principle, a single cylindrical chamber could be pumped in a location outside the experimental area, then installed in the beam line to replace another cell when the polarization of the latter has dropped too low. However, in the SLAC environment, a long access time would be required to secure the experimental area, break the beam-line vacuum, exchange the target cells, then restore the vacuum, and finally retune the accelerator. Also, the glass cell walls could darken from radiation damage and prevent repumping of the cell, the target polarization would be varying at all times, recovery time from an accidental loss of polarization could be very long, and the pressure (and hence stress) while pumping would be substantially higher for the same operating pressure in the cell. The “double cell” solves or minimizes these problems, and in principle one good cell of this design could operate for the whole experiment. In this design, the ^3He is polarized in the upper (pumping) chamber and diffuses through the transfer

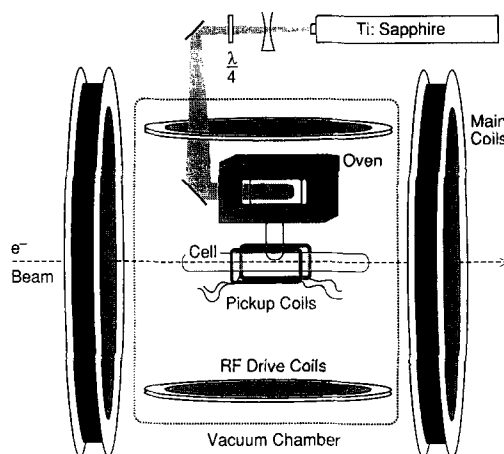


Fig. 1. Schematic overview of the SLAC ^3He polarized target. Not shown are four of five identical Ti:sapphire lasers, the argon-ion lasers used to pump the Ti:sapphire, and the optics used to combine the five laser beams. Also not shown is a second set of main magnet coils with an axis transverse to the electron beam direction.

tube to the lower (target) chamber with a time constant of about 10 min – small compared with the characteristic spin exchange and relaxation times. Due to the low thermal conductivity of glass, the target chamber remains at a low enough temperature (about 60°C) that the rubidium vapor density there is negligible. The disadvantage of this design is that the effective spin-exchange time is increased, and the cell is more difficult to construct.

3.2. Maximizing polarization

The asymptotic ^3He polarization is given by $P_{^3\text{He}} = (\gamma_{\text{SE}}/\gamma_{\text{SE}} + \Gamma)\langle P_{\text{Rb}} \rangle$, where γ_{SE} is the spin-exchange rate between the rubidium and the ^3He , Γ is the ^3He spin relaxation rate due to all other effects, and $\langle P_{\text{Rb}} \rangle$ is the average rubidium polarization. If adequate laser power reaches all parts of the pumping chamber, $\langle P_{\text{Rb}} \rangle$ can approach 100%. Since γ_{SE} is proportional to the rubidium number density, this term may be increased by increasing the oven temperature to vaporize more rubidium, but then more laser power is needed to maintain $\langle P_{\text{Rb}} \rangle$. Practical limitations are then reached due to the cost and complexity of more lasers, or to the temperature limits of the oven materials, or both. The remaining variable is then the spin relaxation rate Γ , which should be minimized.

3.3. Relaxation effects

The total ^3He spin relaxation rate is the result of several effects, here approximately $\Gamma = \Gamma_{\text{bulk}} + \Gamma_{\text{beam}} + \Gamma_{\text{field}} + \Gamma_{\text{gas}} + \Gamma_{\text{wall}}$, as identified below. The first two of these are unavoidable. Bulk relaxation results from ^3He – ^3He collisions, where a dipolar interaction couples the nuclear spin

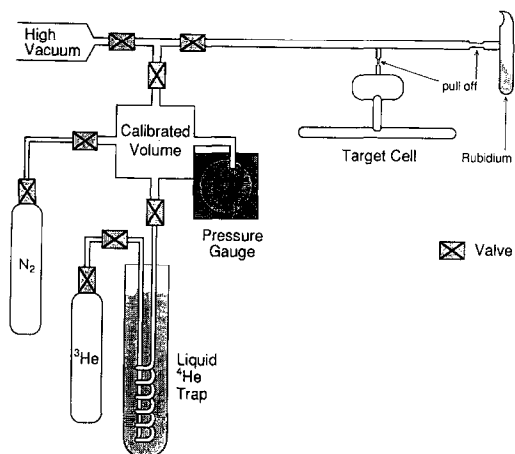


Fig. 2. Schematic diagram of the vacuum and gas filling system used for preparing target cells. Not shown is a vacuum jacket placed around the lower chamber of the cell while cooling with liquid helium.

to the orbital angular momentum of the colliding atoms. At a pressure of about 10 atm, this limits the relaxation time to approximately 75 h. Beam depolarization results from ionization and recombination of ^3He exposed to an electron beam. This was not a major effect during much of the experiment, but caused a noticeable (several percent) reduction in target polarization at the highest beam currents (about $4 \mu\text{A}$).

The remaining terms are ones over which the target builders have some control. Magnetic field inhomogeneities induce depolarization as the ^3He atoms diffuse throughout the cell volume. The solution for this target was to use large Helmholtz coils to produce the holding field, as such a design was required in any case to provide access to the target vacuum chamber. The last two effects listed are due to collisions of ^3He atoms with paramagnetic impurities in the gas mixture, and collisions with the cell walls. These relaxation effects can be minimized by careful attention to details of cell production, as discussed below.

3.4. Cell manufacture

Fig. 2 shows a diagram of the system used for preparing and filling target cells. The cell is connected to a high-vacuum system capable of 10^{-8} Torr, and baked under vacuum for up to 7 days at 450°C . A small amount of rubidium is then "chased" into the pumping chamber with a torch, and the target chamber is inclosed in a vacuum-walled enclosure through which liquid ^4He is blown. A small amount of 99.9995% pure nitrogen is introduced into the cell (this suppresses "radiation trapping" in the optical pumping process [7]) and the desired amount of high-purity ^3He is flowed through a liquid ^4He

trap into a calibrated volume, then introduced into the cell. The temperature of the target chamber is lowered enough (by the liquid ^4He blowing by) to reach a pressure below atmospheric, and the small entrance tube at the top of the pumping chamber is then sealed with a torch.

The construction of the cell itself is also critical for achieving long relaxation times. Aluminosilicate glass has been found to highly suitable for this purpose, possibly due to its relatively low porosity to ^3He . For the cells used in this experiment, commercial tubing (Corning 1720) was rinsed with nitric acid to remove possible surface contaminants, then reblown to the desired dimensions on a glass-working lathe, resulting in a very clean and microscopically smooth "fire-polished" surface. Cells constructed in this manner and filled as described above were measured to have net relaxation times up to 65 h at room temperature with no incident electron beam, or nearly the bulk limit.

4. Polarization measurement

The method chosen for measuring target polarization was the NMR technique called adiabatic fast passage, or AFP. This technique is relatively well-understood, had been used successfully in earlier work with similar targets, and was compatible with the experimental arrangement of this target. Fig. 3 shows a diagram of the apparatus used for the measurement. An RF drive field orthogonal to the main field is applied at a fixed frequency of 92 kHz, while the main holding field strength is varied from the normal value of 20 G to a maximum of 38 G, passing through resonance for ^3He at this frequency when the field is about 29 G. If the strength of the drive field and the rate of change of the main field strength are chosen correctly, essentially all of the ^3He nuclear spins flip over during this process and the target polarization ends up reversed. The precessing nuclear spins induce a signal in the small pickup coils. This signal passes through a preamplifier in such a way as to cancel common-mode noise, and is transmitted to a lock-in amplifier locked to the frequency of the drive field. An adjustable circuit ("A- ϕ Box") produces a signal used to cancel any direct pickup from the drive field. Fig. 4a shows a typical ^3He signal resulting from this procedure. The main field is then swept back to the normal value, reversing the process and restoring the polarization to the direction being pumped, while providing another measurement of the ^3He signal. Repeated measurements show that very little polarization ($< 0.1\%$) is lost in this procedure.

The method is calibrated by replacing the ^3He cell with a nearly identical cell filled with distilled water, then performing repeated measurements with the same apparatus at the same frequency. The calculable thermal equilibrium polarization of the protons in the water is very small (about 10^{-8}) at such low magnetic fields (at 92 kHz,

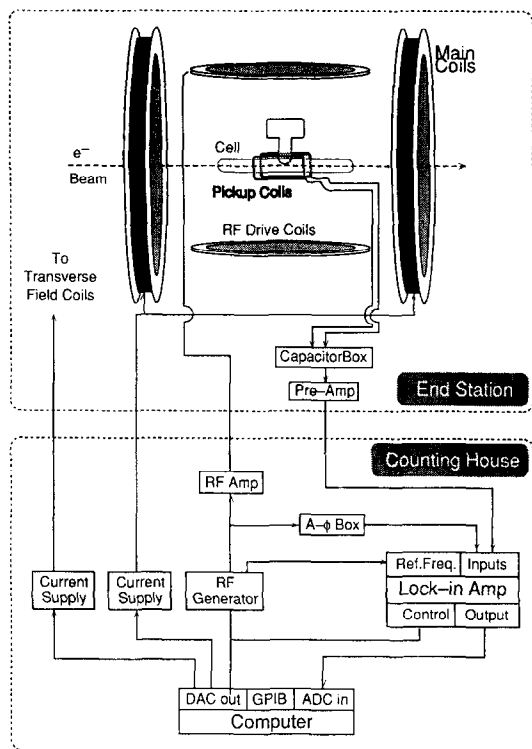


Fig. 3. Schematic diagram of the apparatus used for adiabatic fast passage NMR measurements of the target polarization.

protons are resonant at about 22 G), but the density in water is high enough to create measurable signals during AFP (less than $2 \mu\text{V}$ in this setup). Many measurements must be averaged to achieve acceptable signal-to-noise ratio, and the process is very time-consuming because the proton spin relaxation time in distilled water is about 2 s, so a substantial waiting time is required between sweeps in

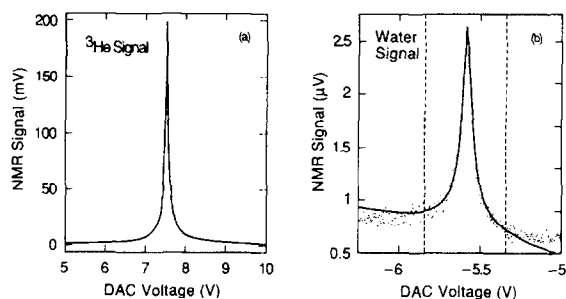


Fig. 4. (a) Typical NMR signal from the lock-in amplifier during an AFP measurement with polarized ^3He . The solid line is a fit to a theoretical line shape and cannot be distinguished from the individual data points. (b) Typical AFP signal from a water-filled calibration cell. The data points are averaged over 25 individual measurements. The solid line is a fit to a theoretical line shape with a linearly varying background. The dashed lines indicate the limits of the fit region.

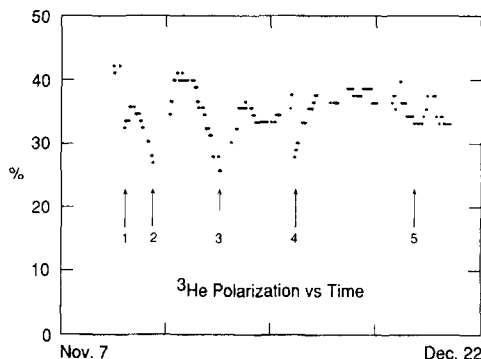


Fig. 5. Time dependence of on-line ^3He polarization measurements during the course of the experiment. Numbered arrows indicate episodes discussed in the text.

either direction. Fig. 4b shows the average of 25 proton signals from a typical water measurement.

Experimental errors in the polarization measurement can arise from several sources. The largest contribution for this experiment was from the extraction of the proton signal from water measurements, with an estimated uncertainty of $\pm 5.6\%$. The ^3He density in the target chamber was determined from measurements made during cell filling, and from temperature measurements of the two chambers of the cell during operation, and contributes an estimated uncertainty of $\pm 2.5\%$. Uncertainty in measurement of the diameter of the reblown tubing for the target chamber introduces another 2.6% error. When these are combined with several less significant effects, the overall uncertainty in the ^3He polarization during this experiment is estimated to be $\pm 7\%$, which is small compared with the statistical errors in the results of the experiment.

5. Operational experience

Fig. 5 shows the measured ^3He polarization as a function of time during the six-week experimental run. The polarization was generally maintained between about 30 and 40%, with variations primarily due to certain episodes indicated by arrows on the figure.

- 1) The first (and best) cell installed had to be removed when the plastic oven cracked and leaked due to prolonged exposure to high temperature while surrounded by vacuum. (This cell was reinstalled later with a replacement oven and finished the experiment).
- 2) The next cell had insufficient rubidium metal in the pumping chamber, and had to be removed when all the rubidium metal had migrated to the transfer tube and the rubidium vapor density dropped too low.
- 3) The next cell behaved in a way that at first appeared similar to the second cell, but instead can be attributed to a leak of ^3He , possibly due to slightly different cell construction. The evidence is that the electron scatter-

ing rates dropped linearly with the ^3He NMR signals during this episode, implying a decrease in ^3He density rather than polarization.

- 4) Some time was spent running with target polarization oriented transverse to the beam direction. The arrangement was not capable of optical pumping in this orientation, so the polarization decayed until the longitudinal orientation was restored. For the transverse running, the main holding field was provided by a second set of Helmholtz coils, as mentioned earlier.
- 5) Near the end of the experiment the beam intensity was increased, leading to additional depolarization due to ionization by the electrons.

In general, this target performed quite well considering the large size and complexity of the device compared with earlier experiments. For future running, several improvements are anticipated. Using better plastics for the oven will improve reliability and allow somewhat higher average temperatures, leading to greater rubidium vapor density and hence reduced spin-exchange times. Improvements will be made to the laser beam transport optics to increase the amount of laser power that reaches the rubidium vapor. This will increase the average rubidium polar-

ization, or maintain it in the face of higher rubidium density. Finally, with more experience in cell construction, it is expected that cells will be produced that are longer, at higher ^3He pressure, and with substantially thinner end windows, thus greatly increasing the fraction of polarizable material exposed to the electron beam.

References

- [1] P.L. Anthony et al., Phys. Rev. Lett. 71 (1993) 959.
- [2] R.M. Woloshyn, Nucl. Phys. A 496 (1989) 749.
- [3] M.A. Bouchiat, T.R. Carver and C.M. Varnum, Phys. Rev. Lett. 5 (1960) 373.
- [4] R.L. Gamblin and T.R. Carver, Phys. Rev. 138 (1965) 964.
- [5] N.D. Bhaskar, W. Happer and T. McClelland, Phys. Rev. Lett. 49 (1982) 25.
- [6] W. Happer et al., Phys. Rev. A 29 (1984) 3092; Phys. Rev. A 31 (1985) 260.
- [7] T.E. Chupp et al., Phys. Rev. C 36 (1987) 2244.
- [8] B. Larson et al., Phys. Rev. A 44 (1991) 3108; Phys. Rev. Lett. 67 (1991) 3356.
- [9] N.R. Newbury et al., Phys. Rev. Lett. 67 (1991) 3219; Phys. Rev. Lett. 69 (1992) 391.
- [10] T.E. Chupp et al., Phys. Rev. C 45 (1992) 915.